The Quantum Theory of Atoms in Molecules as an Interpretative Tool in Chemistry

by

Norberto Castillo Rijo

Submitted in partial fulfillment of the requirements
for the degree of Doctor of Philosophy

at

Dalhousie University
Halifax, Nova Scotia
May 2006

Your file Votre référence
ISBN: 978-0-494-19600-7
Our file Notre référence
ISBN: 978-0-494-19600-7

DALHOUSIE UNIVERSITY

To comply with the Canadian Privacy Act the National Library of Canada has requested that the following pages be removed from this copy of the thesis:

Preliminary Pages
- Examiners Signature Page (pii)
- Dalhousie Library Copyright Agreement (piii)

Appendices
- Copyright Releases (if applicable)

To my beloved parents, Juan Antonio Castillo Hernández and Esperanza Rijo Camacho
To my beloved grandmother, Zoila Hernández Navarro
To my beloved brother, Juan Carlos Castillo Rijo

To all my friends

To all my professors from my preuniversitary school, Mártires de Humboldt 7
To all my professors from the Department of Chemistry at Havana University
To all my professors at Dalhousie University

Tables of Contents

List of Tables

List of Figures and Schemes

Abstract

The Theory of Atoms in Molecules (AIM) developed by Bader is a wonderful extension of quantum mechanics to chemistry. It gives a quantum definition for atoms (open systems) in molecules, showing that they are bounded by zero-flux surfaces in the gradient vector field of the electron density. This remarkable result supports an important hypothesis in chemistry, which is the basis of chemistry as an experimental science: molecules are formed by the union (chemical bond) of atoms. Therefore, AIM serves to gain insight into many areas of chemistry including the characterization of the valence shells of atoms in molecular systems and the characterization of weak interactions in molecular systems. The results presented in this thesis demonstrate the use of AIM as an interpretative tool in inorganic and organic chemistry.

The valence shell of the fluorine atom in its compounds has not been fully characterized from a theoretical point of view. A detailed characterization of the valence shell charge concentration (VSCC) of fluorine through AIM is reported to provide a simple explanation for several intriguing facts in the chemistry of fluorine. Furthermore, a new empirical approach for the evaluation of fluorine-fluorine spin-spin coupling constants (J_{FF}) in aromatic compounds is proposed as well as a complete AIM characterization of these aromatic systems.

Weak interactions make great contributions and play determinant roles in the stability and energetics of important molecular systems such as polyaromatic systems and inclusion complexes of cyclodextrins. A characterization of the weak interactions in terms of AIM parameters provides insight into the chemistry of these types of molecular systems. Several weak interactions in several difluorinated polyaromatic compounds and in the inclusion complex of p-chlorophenol inside α-cyclodextrin are reported and characterized.

The concept of resonance is especially useful for systems containing delocalized electrons and has been used to explain many phenomena in chemistry. A detailed study by means of AIM of the resonance effect exhibited in systems where a halogen is adjacent to a carbon-carbon double bond is carried out. Moreover, a comparable study of the respective saturated halohydrocarbons and hydrocarbons, as well as the related unsaturated hydrocarbons is also carried out. Several observations that are consistent with the presence of the halogen resonance effect in compounds where the halogen is bonded to a carbon-carbon double bond are reported.

The thermolysis of many β-hydroxyl compounds has been studied experimentally and theoretically. A mechanism involving a six-membered cyclic transition state where the hydrogen of the hydroxyl group interacts with the oxygen of the carbonyl group has been proposed previously. The proposed mechanism is studied for a series of β-hydroxyl aldehydes. Rate constants and activation energies are reported as well as a study of the influence of tunneling on the reaction rates. The electron density at the ring critical points, population analyses by atoms in molecules (AIM) and natural bond orbital (NBO) methods, as well as atomic energy analyses, are used to gain insight into this interesting mechanism and into the effects of substituents.

List of Abbreviations and Symbols Used

Abbreviations

DFT	Density functional theory
HF	Hartree-Fock
MO	Molecular orbital
LCAO	Linear combination of atomic orbitals
STO	Slater type orbital
GTO	Gaussian type orbital
CI	Configuration Interaction
MPPT	Møller-Plesset perturbation theory
MP	Møller-Plesset
AIM	Atoms in Molecules
CC	Coupled Cluster
TST	Transition State Theory
VSEPR	Valence shell electron pair repulsion
VSCC	Valence shell charge concentration
RHS	Right-hand side of an equation
LHS	Left-hand side of an equation
NMR	Nuclear magnetic resonance spectroscopy
BCP	Bond critical point
RCP	Ring critical point
CCP	Cage critical point
IAS	Inter-atomic surface
IAM	Independent atom model
Cc	Complex conjugate
Au	Atomic units
BO	Bond order
BSSE	Basis set superposition error
NBO	Natural bond orbital
NAO	Natural atomic orbital
AO	Atomic orbital
CCA	Coupled cluster approximation
IEPA	Independent electron pair approximation
CIS	Configuration interaction single excitation
CID	Configuration interaction double excitation
FC	Frozen core
IRC	Intrinsic reaction coordinate
ZPVE	Zero-point vivrational energy
EA	Electron affinity
IP	Ionization potential
IAM	Independent atom model

Symbols

ρ	Electron density
ϕ	Atomic orbital
H	Hamiltonian
T	Kinetic energy
V	Potential energy
F	Fock operator
Ψ	Total wave function
$\mathscr{V}$	Virial
Ω	Atomic basin
ψ	Molecular orbital

Acknowledgments

I would like to thank to my supervisor Dr. Russell Boyd for all his support and for giving me the great opportunity to carry out my graduate studies in this beautiful university. I would also like to thank him for teaching me a lot of science and a lot of other things that are not pure science but they are as important as science.

There are not words to describe how grateful I am to my colleague and friend Dr. Chérif Matta, one of the persons that has contributed the most to my development as a scientist. I really enjoyed doing research with such a talented and promising scientist.

I would also like to thank the people from my group, especially Dr. Fuqiang Ban.

I would like to thank Dalhousie University and Canada for giving me the opportunity of doing my Ph.D.

I am very grateful to Dr. Lisandro Hernández de la Peña for his cooperation and useful discussions that allowed me to develop my comprehension about the fascinating world of quantum theory.

I would like to thank my Cuban friends, especially Lorenzo Vega and Gianna Alemán, for their support.

Most important, I would like to thank my family for everything in my life.

Chapter 1 Introduction

The study and calculation of atomic and molecular properties from first principles is one of the central problems of chemistry. Nowadays theory complements experiment, the results are interpreted in terms of existing theories. The interplay between experiment and theory leads to the formulation of new theories and the design of new experiments. Furthermore, theory provides insights into many areas, such as atmospheric reactions and the calculation of properties of species with a very high reactivity, that are not obtainable from experiments alone.

Theoretical chemistry is a valuable tool to deal with all those problems which are untreatable by experimental methods. The basis of theoretical chemistry is very well supported by the quantum theory developed at the beginning of the last century by Planck, Einstein, Born, Schrödinger, Dirac and Heisenberg. The great development that we enjoy today in the area of theoretical chemistry would not have been possible without the tremendous developments in computer technology. The availability of powerful computers has led to the birth of a new field known as computational chemistry. It facilitates the development of models for the interpretation of biological processes such as enzymatic reactions and photosynthesis. Furthermore, computational chemistry plays an important role today in the design of new drugs and chemical compounds as well as in the determination of structure-activity relationships. The role of computational methods in drug design and biopharmaceutical chemistry will continue to increase for the foreseeable future.

The main goal of this thesis is to apply the Atoms in Molecules (AIM) theory developed by Richard Bader to specific topics in inorganic and organic chemistry as well as to NMR.

AIM theory provides a connection between experimental chemistry and the quantum theory of electronic structure. In fact, AIM theory through its dependence on the important theorems of quantum mechanics provides a basis for many models whose origins are rooted in experimental chemistry. For example, the topology of the electron density (ρ) in terms of the gradient vector field ($\nabla\rho$) provides evidence of the main chemical concepts such as atoms, molecules and chemical bonds as well as molecular structure where the ring and cage structures are clearly defined. As a consequence, several properties of atoms in molecules, such as energy, dipole moment, etc., can be determined, and several properties of the chemical bonds such as strengths and π character (which is very important to describe the chemical behavior of unsaturated and aromatic systems) can be estimated. Furthermore, it can be said that the electron pairs of the Lewis model and valence shell electron pair repulsion model (VSEPR) find their theoretical justification in the topology of $L=-\nabla^2\rho$ (the negative of the Laplacian of the electron density). These two models still play a remarkable role in the interpretation of experimental results in inorganic and organic chemistry. The theory of atoms in molecules also recovers from a theoretical point of view the additivity and transferable properties of the functional groups of atoms in molecular systems, as evidenced by experimental results. It allows the characterization of chemical compounds into families by which organic chemistry is structured.

This thesis, apart from this introductory chapter, contains 10 more chapters and one section for the list of references. Chapter 2 is divided in two parts. The first one describes the basic aspects of quantum chemistry as well as the main ab initio methods that are used to obtain the electron density (Hartree-Fock (HF), Configuration Interaction (CI),

Coupled-Cluster (CC), Density Functional Theory (DFT) and Møller-Plesset (MP)). The second part describes briefly how to obtain the electron density from experiment (X-Ray Diffraction).

Chapter 3 presents an exhaustive discussion about the quantum theory of atoms in molecules. In this chapter, it is demonstrated that an atom defined by the theory of atoms in molecules (attractor plus its basin) is an open quantum system. Furthermore, most of the AIM parameters such as critical points (attractors, bond, ring and cage critical points), bond paths, ellipticity and interatomic surfaces are also defined. The topology of $L=-\nabla^2\rho$ and its connection with the Lewis and VSEPR models, which is one of the most useful results of AIM theory, are discussed. Finally, a list of several properties, such as atomic energy, dipole moment, atomic charge, etc., that can be obtained by AIM theory; is provided.

Chapter 4 presents a detailed characterization of the valence shell charge concentration (VSCC) of fluorine in methyl fluoride through AIM theory. The study was carried out by use of several ab initio (HF, CISD, MP2, MP3 and CCD) methods with a large basis set (6-311++G(2d,p)). Moreover, a comparison between the VSCCs of fluorine and neighboring elements in the periodic table such as carbon, nitrogen, oxygen, silicon, phosphorus, sulfur and chlorine is presented.

Chapter 5 describes a new empirical approach for the evaluation of fluorine-fluorine spin-spin coupling constants (J_{FF}) in aromatic compounds. The correlations between J_{FF} and the delocalization index calculated within the framework of AIM theory and with the fluorine-fluorine internuclear separation are investigated for a data set consisting of 33 coupling constants spread over a range of 85 Hz.

The closed-shell fluorine-fluorine bonding interaction in aromatic compounds is characterized on the basis of the electron density in Chapter 6. Furthermore, several other weak closed-shell interactions are reported and characterized including F···C, F···O and C···C interactions, hydrogen bonding, dihydrogen bonding, and hydrogen-hydrogen bonding. This study represents another example of the usefulness and richness of the bond path concept and of the theory of atoms in molecules in general.

A type of cage critical point (CCP) that has remained so far only a mathematical possibility is reported for the first time in Chapter 7. A CCP enclosed by two ring surfaces is found in a single ring in three derivatives of 1,12-difluorobenzo [c]phenanthrene. The Poincaré–Hopf relationship is satisfied in each case.

Chapter 8 reports a study of the inclusion complex of p-chlorophenol inside α-cyclodextrin (α-CD) by the theory of atoms in molecules. A quantitative comparison of some AIM properties of isolated *p*-chlorophenol (PCP) and the inclusion complex (PCP-CD) is presented and some weak interactions within the host-guest complex are characterized. Furthermore, electrophilic aromatic substitutions on the *p*-chlorophenol in the isolated state and inside α-CD are compared.

A detailed study by means of the theory of atoms in molecules of the resonance effect exhibited in systems where a halogen is adjacent to a carbon-carbon double bond is presented in Chapter 9. A comparable study of the respective saturated halohydrocarbons and hydrocarbons, as well as the related unsaturated hydrocarbons is also carried out. Furthermore, a study about the electrophilic aromatic substitution in α and β-halonaphthalenes is presented.

Chapter 10 reports a theoretical study of the thermolysis of β-hydroxyl aldehydes. The proposed mechanism for the thermolysis of several β-hydroxyl compounds, such as β-hydroxyl ketones, β-hydroxyl esters, etc., is studied for a series of β-hydroxyl aldehydes. Rate constants and activation energies are reported as well as a study of the influence of tunneling on the reaction rates. The electron density at the ring critical points, population analyses by the atoms in molecules (AIM) and natural bond orbital (NBO) methods, as well as atomic energy analyses, are used to gain insight into this interesting mechanism and into the effects of substituents.

Chapter 11 presents the global conclusions and describes the two directions for future research. The first future direction is focused mainly on an AIM study based on the negative divergence of the quantum stress tensor of the cis and trans forms of C_6H_8, $C_{10}H_{12}$ and $C_{14}H_{16}$ in order to gain insight into the conductivity properties of polyacetylene-type of systems. The second future direction is a comprehensive study of all homonuclear combinations of the first row (Li-Li, Be-Be, B-B, C-C, N-N, O-O and F-F) and the second row (Na-Na, Mg-Mg, Al-Al, Si-Si, P-P, S-S and Cl-Cl) of the periodic table, except for the noble gases, to generalize the correlation between bond lengths and ρ_{BCP}.

Chapter 2 Electron Density from Theory and Experiment.

2.1 The Electronic Problem.

The non-relativistic treatment of any problem that involves particles requires the solution of the Schrödinger equation. Most of the cases in quantum chemistry are related to the study of molecules and chemical reactions where the electrons play the main role; and to interactions that are independent of time. Thus, Chapter 2 is concerned with the solution of the time-independent Schrödinger equation:

$$\hat{H}\Psi(\mathbf{r},\mathbf{R}) = E\Psi(\mathbf{r},\mathbf{R}) \tag{2.1}$$

where **r** and **R** represent the position vectors of all electrons and nuclei, respectively. $\hat{H}$ is the Hamiltonian of the system formed by n electrons and N nuclei:

$$\hat{H} = -\sum_{i=1}^{n}\frac{1}{2}\nabla_i^2 - \sum_{A=1}^{N}\frac{1}{2M_A}\nabla_i^2 - \sum_{i=1}^{n}\sum_{A=1}^{N}\frac{Z_A}{\mathbf{r}_{iA}} + \sum_{i=1}^{n}\sum_{j>1}^{n}\frac{1}{\mathbf{r}_{ij}} + \sum_{A=1}^{N}\sum_{B>1}^{N}\frac{Z_A Z_B}{\mathbf{R}_{AB}} \tag{2.2}$$

The first two terms in equation 2.2 represent the kinetic energies of the electrons and nuclei, respectively, the other three take into account the electron-nucleus, the electron-electron and the nucleus-nucleus interactions.

With the exception of a few special cases, equation 2.1 cannot be solved exactly and therefore approximate methods based on the variational theorem and perturbation theory [1] have been developed. Thus, the ab initio methods can be classified, depending upon which method they use, into variational or perturbative methods.

2.1.1 Adiabatic Approximation.

The mass of a nucleus is much greater than the mass of an electron and therefore the electrons move at much higher speeds than nuclei. This statement, which is supported by experimental observations, leads to the adiabatic approximation, according to which the motion of the nuclei is neglected. In essence this approximation eliminates the correlation between the motion of nuclei and electrons and simplifies the solution of the time-independent Schrödinger equation [2].

Under this approximation the term that represents the kinetic energy of the nucleus can be neglected and the last term in equation 2.2 will be a constant, which does not imply any problem in the solution of the Schrödinger equation because it is shown by quantum mechanics [1] that the addition of a constant to an operator does not change its eigenfunctions; and its eigenvalues are modified by the simple summation of the constant. Then the electronic problem consists of solving the following equation:

$$\hat{H}_{elec}\,\Psi_{elec}(\mathbf{r},\mathbf{R}) = E_{elec}(\mathbf{R})\Psi_{elec}(\mathbf{r},\mathbf{R}) \tag{2.3}$$

where

$$\hat{H} = -\sum_{i=1}^{n}\frac{1}{2}\nabla_i^2 - \sum_{i=1}^{n}\sum_{j=1}^{N}\frac{Z_j}{\mathbf{r}_{ij}} + \sum_{i=1}^{n}\sum_{j>1}^{n}\frac{1}{\mathbf{r}_{ij}} = \sum_{i=1}^{n}\hat{h}_i + \sum_{i=1}^{n}\sum_{j>1}^{n}\frac{1}{\mathbf{r}_{ij}} \tag{2.4}$$

The single particle operator $\hat{h}_i$ introduced in equation 2.4 represents the kinetic energy of an electron and the potential energy in the average field of all nuclei. The electronic wave function $\Psi_{elec}(\mathbf{r},\mathbf{R})$ depends explicitly on the coordinates of all the electrons and implicitly on every fixed arrangement of nuclei.

2.1.2 The Hartree-Fock Theory.

The HF approximation [2,3], also called the independent particle model, is the ab initio method most widely used in the study of atomic and molecular electronic structure. It is a variational method where the trial function is a Slater determinant of spin orbitals and an optimization process is carried out until the spin orbitals yield the minimum value of the energy.

A Slater determinant (equation 2.5) satisfies the antisymmetry principle according to which the wave function for describing a system of fermions must change sign under the permutation of any two fermions. Fermions are all the particles with half-integer spin.

$$\Psi_{HF} = (n!)^{-\frac{1}{2}} |\psi_1(1)\psi_1(2)....\psi_N(n)| \tag{2.5}$$

ψ_i functions are the spin orbitals and n is the number of electrons in the system.

Applying the variational method and the orthonormality condition of the spin functions leads to a set of equations that are known as the Hartree-Fock equations given by

$$\hat{F}_i \psi_i = \varepsilon_i \psi_i \tag{2.6}$$

where

$$\hat{F}_i = \hat{h}_i + \sum_j v^{HF}(i) \tag{2.7}$$

$$\hat{h}_i = -\frac{1}{2}\nabla_i^2 + \sum_A \frac{Z_A}{r_{iA}} \tag{2.8}$$

$$v^{HF}(i) = \sum_j \left(2\hat{J}_j - \hat{K}_j\right) \tag{2.9}$$

$\hat{F}$ is the Fock operator and the ε_i are the orbital energies. $\hat{J}_j$ and $\hat{K}_j$ are the Coulomb and exchange operators, respectively, and in general the last term of the Fock operator represents the effective potential seen by the electrons in the i^{th} orbital

$$\hat{J}_j = \left\langle \psi_j \left| r_{12}^{-1} \right| \psi_j \right\rangle \tag{2.10}$$

$$\hat{K}_j = \left\langle \psi_j \left| r_{12}^{-1} \hat{P}_{12} \right| \psi_j \right\rangle \tag{2.11}$$

where $\hat{P}_{12}$ is the permutation operator, which acts on the right side and permutes electrons 1 and 2.

The HF equations can be only solved iteratively because they depend on the orbital ψ_j. When they are applied to atoms the solutions are the well-known atomic orbitals. However the solution of the HF equations for polyatomic systems is impractical and therefore it was suggested by Roothaan [4] to simplify the solution of the HF equations for molecules by expanding the molecular orbitals (ψ_i) in terms of a basis of atomic orbitals (ϕ_μ) which is known as the MO-LCAO approximation

$$\psi_i = \sum_{\mu}^{M} C_{\mu i} \phi_\mu \tag{2.12}$$

where M is the number of the atomic orbitals (or, more generally, a set of basis functions) and the $C_{\mu i}$ are the expansion coefficients which are determined by applying the variational method. The results are the algebraic Roothaan-Hall equations

$$\sum_{\mu}^{M} C_{\mu\nu} \left(F_{\mu\nu} - \varepsilon_i S_{\mu\nu} \right) = 0 \quad \nu = 1, 2, \ldots, M \tag{2.13}$$

$C_{\mu\nu}$, $F_{\mu\nu}$ and $S_{\mu\nu}$ are elements of the coefficient matrix, Fock matrix and overlap matrix ($\langle\phi_\mu|\phi_\nu\rangle$), respectively. The Fock matrix elements in the case of closed-shell systems are given by

$$F_{\mu\nu} = H_{\mu\nu} + \sum_{\lambda,\sigma}^{M} P_{\mu\nu}\left[(\phi_\mu\phi_\nu|\phi_\lambda\phi_\sigma) - \frac{1}{2}(\phi_\mu\phi_\lambda|\phi_\nu\phi_\sigma)\right] \tag{2.14}$$

where the matrix elements of the core Hamiltonian are given by

$$H_{\mu\nu} = \left\langle \phi_\mu \left| -\frac{1}{2}\nabla^2 + \sum_A \frac{Z_A}{\mathbf{r}_{1A}} \right| \phi_\nu \right\rangle \tag{2.15}$$

and $P_{\lambda\sigma} = \sum_{i=1}^{occ} 2C_{\lambda i}C_{\sigma i}$ is an element of the density matrix.

2.1.2.1 MO-LCAO and Basis Functions.

In all MO calculations the selection of the atomic orbitals used to expand the molecular orbitals is very important. There are two main criteria used to select the basis set; the first one consists of how many terms in the expansion are required to get an accurate representation of the molecular orbital and the second one is purely related to the efficient evaluation of the two-electron integrals [2].

The two types of atomic orbitals that have been used the most widely are the Slater-type atomic orbitals [5] (STO) and the Gaussian-type atomic orbitals [6] (GTO). The STO functions, which take the form $e^{-\xi r}$, are more physical because they are more closely related to the exact solution of the Schrödinger equation for the hydrogen atom. Thus, they are much better than the GTO functions with respect to the first criterion. However they are expensive computationally. On the other hand the GTO functions, which are of

the form $e^{-\alpha r^2}$, do not describe very well the atomic orbitals in regions close and far from the nucleus, but their mathematical properties for calculating integrals make them extremely efficient [2] with respect to the second criterion. The GTO functions conduce to a rapid integral evaluation due to the Gaussian product theorem, which states that the product of two GTOs on two different centers is a third GTO on a center between the first two centers.

The solution that has been proposed for this dilemma is to represent the STO (ϕ) of the molecular expansion as a linear combination of primitive Gaussian (g) type functions that are all of the same type (i.e., s, p, d, ...). This is known as a contraction scheme and it is represented by equation 16:

$$\phi_\mu = \sum_{p=1}^{L} d_{p\mu} g_p(\alpha_{p\mu}) \tag{2.16}$$

where L is the length of the contraction, $d_{p\mu}$ and $\alpha_{p\mu}$ are the contraction coefficient and exponent, respectively. All these parameters are defined and obtained by using a specific contraction scheme at the atomic level.

A minimal basis set uses the least number of basis functions to describe the atomic orbital (contraction scheme, STO-LG). The most used minimal basis set is STO-3G in which the STOs are expanded in three primitive Gaussian functions. These types of basis sets are inexpensive and they are applied to calculations of quite large molecules. However, minimal basis sets are not sufficiently flexible to yield accurate results. For some purposes, minimal basis sets provide useful qualitative information.

Most of the calculations undertaken today use the split-valence basis sets (commonly referred to as Pople basis sets) where the number of basis functions per atom is increased.

For example, the double-zeta split-valence basis set 6-31G indicates that each atomic core orbital is described by a single contraction of six GTO primitives, and each valence shell orbital is described by two contractions (basis functions), an inner one with three primitives and an outer with one primitive (splitting of the valence shell). Split-valence basis sets allow for more flexibility in the description of the valence electrons than minimal basis sets. Additional flexibility in the basis set is acquired by further division of the valence shell as in the case of 6-311G (an example of a triple-zeta split-valence basis set).

The Pople basis set notations described above can be modified to extend the accuracy of the calculation by adding polarization functions, e.g., 6-311G(d,p): d primitives are added to atoms other than hydrogen and p primitives are added to hydrogen as well. Polarization functions (functions of higher angular momentum) account for the distortion of the atomic orbitals in the molecular environment (displacement of charge away from the nucleus) to provide additional flexibility. Another modification in this notation accounts for the inclusion of diffuse functions, e.g., 6-311++G(d,p): a single plus sign indicates that diffuse functions (s and p) are added to atoms other than hydrogen and the second plus implies that diffuse s functions are added to the basis set for hydrogen. These functions allow the orbital to occupy a larger region in space, and are particularly useful to describe systems such as anions where the electrons are loosely bound.

2.1.3 Electron Correlation.

The HF approximation has been shown to be successful in the description of many molecular systems, however when high accuracy is required this method presents severe

limitations. In particular the HF method is inadequate for the calculation of ionization potentials, dissociation energies, excited states and transition states energies.

In essence the HF model is an independent particle model which neglects the correlation between electrons. Therefore the creation of new methods that include the electronic correlation effect is necessary in order to obtain results in agreement with experiment.

The correlation energy for a system is defined as the difference in energy between its exact non-relativistic energy and the energy calculated by the HF method in the limit of a complete basis set. However the most widely used definition of correlation energy is that given by Löwdin [7] where the correlation energy for a system is defined with respect to a specific Hamiltonian, and it is the difference between the eigenvalue of the Hamiltonian and the expectation value obtained by using the HF approximation.

There are two ways of introducing the electronic correlation effect within the framework of the variational method. The first one is to construct a wave function as a linear combination of Slater determinants; configuration interaction and coupled-cluster methods are examples of this approach. The second one is through the Hamiltonian where accurate Hamiltonians are constructed; the density-functional methods belong to this approach.

The perturbation methods provide an alternative approach to the treatment of the electronic problem, based on perturbation techniques to solve the Schrödinger equation which include by themselves correlation effects. The Møller-Plesset perturbation method is the most widely used method of this type in quantum chemistry.

2.1.3.1 Configuration Interaction.

The CI method is conceptually the simplest ab initio method that takes into account the correlation effect between electrons [2,8]. The key idea of this method is to use as the trial wave function a linear combination of Slater determinants and to determine the coefficients by the variational method.

The CI wave function can be written in the following way:

$$|\Psi_0\rangle = C_{HF}|\Psi_{HF}\rangle + \sum_{i,a} C_i^a |\Psi_i^a\rangle + \sum_{i<j}\sum_{a<b} C_{ij}^{ab} |\Psi_{ij}^{ab}\rangle + \ldots \qquad (2.17)$$

where $|\Psi_i^a\rangle$ represents the single excitations in which an occupied orbital "i" has been substituted by a non-occupied orbital "a". The $|\Psi_{ij}^{ab}\rangle$ represent the double excitations. The expansion continues with higher order excitations.

In principle, if the linear combination 2.17 is not truncated and the basis set is complete, the obtained energies will be exact not only for the ground state but also for the excited states. When the complete series of determinants with a specific basis set is used, the method is called *full CI.*

In practice, to carry out a full CI calculation is almost impossible because of the high computational cost. Therefore to limit the number of determinants, taking into account the purposes and the level of accuracy of the calculation is required. For instance the CIS method (takes into account only single excitations) is used to calculate molecular electronic spectra (UV). The CID method takes into account only double excitations, and as was shown by Watson [9] in 1960, includes some of the correlation energy.

Unfortunately, the truncation of the CI expansion has the size-consistency problem, which in essence means that the energy calculation of a system where two molecules are

infinitely separated (no interaction) is not the same as if the two molecules were calculated as independent systems. To deal with this problem there must be included in the expansion higher levels of excitation even though they make very small contributions to the energy and other properties.

2.1.3.2 Pair and Coupled-pair theories.

There are two main reasons for the success of the pair and coupled-pair theories in the solution of the electronic problem. The first reason is related to the fact that the Hamiltonian, equation 2.4, only contains one and two–electron operators. The second one has to do with the Pauli principle; it requires that only electrons with opposite spin can occupy the same point in space.

The correlation energy by using a full CI wave function and applying the intermediate normalization [2] is:

$$E_{corr} = \sum_{a<b} \sum_{i<j} C_{ij}^{ab} \left\langle \Psi_{HF} \left| \hat{H} \right| \Psi_{ij}^{ab} \right\rangle \tag{2.18}$$

where the C_{ij}^{ab} are the double excitation coefficients that appear in the equation 2.17. The correlation energy expression can be written as:

$$E_{corr} = \sum_{i<j} e_{ij} \quad , \text{ where } \quad e_{ij} = \sum_{a<b} C_{ij}^{ab} \left\langle \Psi_{HF} \left| \hat{H} \right| \Psi_{ij}^{ab} \right\rangle \tag{2.19}$$

represents the contribution of all the possible excitations of every pair of spin-orbitals. Even though this decomposition simplifies the problem to a sum of contributions of spin orbital pairs, it is necessary that all the full CI wave function coefficients be known in order to be able to calculate C_{ij}^{ab}.

The independent electron pair approximation (IEPA) developed separately by Sinanoglu [10] and Nesbet [11] provides a suitable scheme to calculate approximately the energy of every electron pair independently. Therefore the C_{ij}^{ab} can be calculated without knowing all full CI wave function coefficients under the IEPA.

The IEPA consists of the construction of a wave function specific for every electron pair by using the simple approach of neglecting the other electron pairs in the system and considering the possible excitations of a particular electron pair

$$\left|\Psi_{ij}\right\rangle = \left|\Psi_{HF}\right\rangle + \sum_{a<b} C_{ij}^{ab} \left|\Psi_{ij}^{ab}\right\rangle \tag{2.20}$$

The energy of the system represented by the above wave function is:

$$E_{ij} = \left\langle \Psi_{HF} \left| \hat{H} \right| \Psi_{HF} \right\rangle + e_{ij} = E_{HF} + e_{ij} \tag{2.21}$$

The procedure to calculate the energy of every electron pair (E_{ij}) is the linear variation method. It consists of expanding the Hamiltonian operator in the subspace of Ψ_{HF} and all the double excitations of the equation 2.20, solving a matrix eigenvalue problem to obtain the lowest eigenvalue.

The IEPA does not suffer from the size-consistency problem (see CI section) and it is not a variational method; thus, it leads to overestimation of correlation energies. Also, it has a deficiency which apart from neglecting the interaction between electron pairs makes the method more limited; it is not invariant under unitary transformations of degenerate molecular orbitals.

Cizek and Paldus [12] developed an alternative that incorporates the correlation between electron pairs, called the coupled-cluster approximation (CCA). In essence this method

considers the double, quadruple, sextuple, etc, excitations (even excitations) from the full CI wave function.

$$|\Psi_0\rangle = C_{HF}|\Psi_{HF}\rangle + \sum_{i<j}\sum_{a<b} C_{ij}^{ab}|\Psi_{ij}^{ab}\rangle + \sum_{i<j<r<s}\sum_{a<b<c<d} C_{ijrs}^{abcd}|\Psi_{ijrs}^{abcd}\rangle \ldots \quad (2.22)$$

The main approach of this method is to represent the higher excitation coefficients such as quadruples, sextuples, etc, as products of double excitation coefficients, a fact that is true in non-interacting systems [2]. Because of this assumption, carrying out a similar procedure to IEPA leads to a set of nonlinear equations, which make the method computationally expensive.

Finally, CCA is one of the most rigorous methods in quantum chemistry giving extremely good results for those systems whose sizes allow the application of the method. Moreover, unlike IEPA, it does not have the size-consistency problem and it is invariant under a unitary transformation.

2.1.3.3 Density Functional Theory.

The electron density (ρ) plays a very important role in the comprehension of the electrostatic forces, which are responsible for the formation and stability of the molecules. A key event in the development of the density functional theory occurred with the formulation of the theorems [13] of Hohenberg and Kohn in 1964.

From the form of the electronic Hamiltonian, equation 2.4, it is not difficult to realize that all the properties of a system are determined by the number of electrons and their external potential

$$v(\bar{r}) = -\sum_{I=1}^{N} \frac{Z_I}{|\bar{r} - \bar{R}_I|} \quad (2.23)$$

Therefore, the first Hohenberg and Kohn theorem states that the external potential is determined unequivocally by ρ. Moreover, ρ determines the number of electrons in a system and thus ρ also defines the kinetic energy $T(\rho)$, potential $V(\rho)$ and total energy $E(\rho)$ of the system:

$$E[\rho] = T[\rho] + V_{ne}[\rho] + V_{ee}[\rho] = \int v(\bar{r})\rho(\bar{r})d\bar{r} + F_{HK}[\rho] \tag{2.24}$$

where

$$F_{HK}[\rho] = T[\rho] + V_{ee}[\rho] = T[\rho] + J[\rho] + E_{xc}[\rho] \tag{2.25}$$

$F_{HK}[\rho]$ is an universal functional because it only depends on the internal Hamiltonian, which is the same for all the systems with the same number of electrons. $J[\rho]$ and $E_{xc}[\rho]$ are the repulsion between electrons and exchange terms, respectively.

The second Hohenberg and Kohn theorem states that for any trial $\tilde{\rho}$ where $\int \tilde{\rho}(\bar{r})d\bar{r} = n$, the ground state energy that is determined by $\tilde{\rho}$ will be always higher than the real ground state energy of the system.

$$E_0 \leq E[\tilde{\rho}] \tag{2.26}$$

However, obtaining an expression for the universal functional is extremely difficult, and the search for this universal functional, or at least the best approximation to it, is one of the fundamental goals in the development of better DFT methods.

Many models, which can be traced to the work of Thomas and Fermi [13], attempt to provide an explicit formulation of the universal functional (TF and related models), including those by Ludena [14] and Perdew [15]. However another kind of approach arose from the initial idea of Kohn and Sham [16]. They proposed to calculate the kinetic energy $T(\rho)$ of the system as if they were close noninteracting particles and to include the

difference in the exchange term E_{xc} [ρ]. Therefore the electron density is expressed in terms of new orbitals (ψ)

$$\rho(\bar{r}) = \sum_{i=1}^{n} |\psi_i(\bar{r})|^2 \tag{2.27}$$

which are obtained by the solution of the following set of single particle equations

$$\left[-\frac{1}{2}\nabla^2 + \mathrm{v}_{eff}(\bar{r})\right]\psi_i = \varepsilon_i \psi_i \tag{2.28}$$

where

$$\mathrm{v}_{eff}(\bar{r}) = \mathrm{v}(\bar{r}) + \int \frac{\rho(\bar{r}')}{|\bar{r} - \bar{r}'|} d\bar{r}' + \frac{\delta E_{xc}}{\delta \rho(\bar{r})} \tag{2.29}$$

It must be stressed that the exact form of E_{xc} [ρ] is still unknown, and the propositions of different approaches for this term characterize the many different DFT methods (B3LYP [17,18], B3P86 [17,18], B3PW91 [17,18], etc).

From the computational point of view, the DFT methods are the most efficient methods that take into account the electron correlation. Furthermore, DFT methods offer great advantages for very big systems such as polymers, proteins, etc. DFT methods account for about 90 percent of the published applications to biological molecules and materials science.

2.1.3.4 Møller-Plesset Theory.

The Møller-Plesset perturbation theory (MPPT) uses Rayleigh and Schrödinger perturbation theory [19], to solve electronic structure problems. In this theory the Hamiltonian is divided in two parts:

$$\hat{H} = \hat{H}^{(0)} + \delta \hat{V} \tag{2.30}$$

where $\hat{H}^{(0)}$ is the zero-order approximation to the real Hamiltonian of the system, and its eigenfunctions and eigenvalues are known. $\hat{V}$ represents the perturbation to the system or the perturbing Hamiltonian, and δ is the order parameter in terms of which the energy and wave functions are expanded (n represents the energy state that is being analyzed, for instance if n=0 it is the ground state, n=1 refers to the first excited state, and so on):

$$E_n = E_n^{(0)} + \delta E_n^{(1)} + \delta^2 E_n^{(2)} + \ldots \tag{2.31}$$

$$\left|\Psi_n\right\rangle = \left|\Psi_n^{(0)}\right\rangle + \delta\left|\Psi_n^{(1)}\right\rangle + \delta^2\left|\Psi_n^{(2)}\right\rangle + \ldots \tag{2.32}$$

The expressions for the zero, first and second-order corrections to the energy are given by

$$E_n^{(0)} = \left\langle n^{(0)}\left|\hat{H}\right|n^{(0)}\right\rangle \tag{2.33}$$

$$E_n^{(1)} = \left\langle n^{(0)}\left|\hat{V}\right|n^{(0)}\right\rangle \tag{2.34}$$

$$E_n^{(2)} = \sum_{m\neq n} \frac{\left\langle n^{(0)}\left|\hat{V}\right|m^{(0)}\right\rangle\left\langle m^{(0)}\left|\hat{V}\right|n^{(0)}\right\rangle}{E_n^{(0)} - E_m^{(0)}} \tag{2.35}$$

$n^{(0)}$ and $m^{(0)}$ are the known eigenfunctions of $\hat{H}^{(0)}$.

Essentially, the MPPT assumes the perturbation as the difference between the real Hamiltonian and the HF Hamiltonian

$$\hat{H}^{(0)} = \sum_{i=1}^{n} \hat{F}(i) = \sum_{i=1}^{n} \left[\hat{h}(i) + v^{HF}(i)\right] \tag{2.36}$$

$$\hat{V} = \sum_{i=1}^{n}\sum_{j>i}^{n} r_{ij}^{-1} - \sum_{i=1}^{n} v^{HF}(i) \tag{2.37}$$

The Hartree-Fock wave function is taken as the zero-order approximation, and δ is assumed equal to 1. Thus the HF energy is obtained by summing the zero and first-order corrections of the Rayleigh-Schrödinger perturbation theory.

It is necessary to point out again that MPPT is not a variational method such as Hartree-Fock, CI and DFT.

2.1.4 Geometry Optimization

All the ab initio methods described above provide an expression within the adiabatic approximation for the energy of the system depending upon the position of all the nuclei in the system. This function is known as the potential energy surface.

In order to carry out a reliable geometry optimization it is very important to choose a good initial guess for which the SCF equations are solved and the energy gradient of each of the nuclear coordinates is constructed [19]. The directions of highest decrease are indicated by the energy gradients, and they define the variation of the structure with respect to the nuclear coordinates of the system. The procedure is repeated until a stationary point is reached, or in other words, when the energy gradient of each nuclear coordinate is zero. Some of the best known methods to explore the potential energy surface in order to find stationary points are: Fletcher-Powell, quasi-Newton (Berny Optimization), DFP (Davidson-Fletcher-Powell) and Newton-Raphson [20].

The characterization of the stationary points in this potential energy surface is carried through the so called Hessian matrix, which is an array of the second derivatives of the energy with respect to all the nuclear coordinates. The diagonal elements are the second derivatives with respect to the same nuclear coordinate and the off-diagonal terms are the crossed second derivatives. A stationary point is a minimum if all the eigenvectors produced by the diagonalization of the Hessian matrix are positive. When the stationary point exhibits one, and only one, negative curvature it is a transition state. Points with

more than one negative curvature are not important in chemistry. In practice, the equilibrium structures (minima in the potential energy surface) are distinguished from transition states (first-order saddle points) by an analysis of the harmonic vibrational frequency [21]. For example, equilibrium structures exhibit all real frequencies, whereas transition states exhibit exactly one imaginary frequency.

2.2 Electron Density from Experiment (X-Ray Difraction).

Crystallinity is a highly ordered three-dimensional state whereof a macroscopic substance is constructed of a large number of species. These species can be one or more types of atoms, molecules, ions or even a complex assembly of molecules. In all crystals there is a volume element which is representative of the whole system. It is called unit cell. The unit cells can be viewed as the bricks from which the crystal is built. In general, they are characterized by six parameters, three axial lengths (*a, b, c*) and three interaxial angles (α, β, γ) [22,23].

A crystal exhibits a three-dimensional periodic electron density where the electron density of the unit cell is repeated through the whole lattice. Therefore, defining *p*, *q* and *r* as the unit cell dimensions, the electron density in a crystal has the following property [22]:

$$\rho(x+p, y+q, z+r) = \rho(x, y, z) \tag{2.38}$$

When a diffraction experiment is carried out, a simple inverse relationship between the spacing in the real lattice and the spacing of the reflections is observed. Therefore, it is not difficult to calculate the dimensions of the unit cell in crystalline materials by the analysis of the spacings in the reflections. This new space of the reflections is called

reciprocal lattice because of the relationship with the real lattice; h, k and l are its discrete set of coordinates and they run from -∞ to ∞ as x, y and z. Thus, the electron density can be related to a function in the reciprocal space by a Fourier series in the following way:

$$\rho(x,y,z)=\frac{1}{V}\sum_{h}\sum_{k}\sum_{l}F(h,k,l)\ \exp[-2\pi i(hx+ky+lz)] \tag{2.39}$$

where V is the volume of the unit cell and the expansion coefficients $F(h,k,l)$ are the structure factors. The intensity of the reflections can be measured by the diffraction experiment, and they are equal to the square of the structure factors $F(h,k,l)$.

An expression for the structure factors $F(h,k,l)$ can be obtained by applying the inverse Fourier transform to equation 2.39. It will be a function in the reciprocal space, which depends on the electron density in the real space.

$$F(h,k,l)=\int_{V}\rho(x,y,z)\exp[2\pi i(hx+ky+lz)]dxdydz \tag{2.40}$$

Therefore, the structure factors can be obtained from theory by substituting model electron density in equation 2.40. It is exactly in this way in which the refinement of structures in crystallography is carried out, by comparing the structure factors obtained through model densities and through experiment. A residual factor (*R-factor*) is defined to measure quantitatively the difference between both ways

$$R-factor=\frac{\sum\left\|F_{observed}\right|-\left|F_{calculated}\right\|}{\sum\left|F_{observed}\right|} \tag{2.41}$$

An accurate experimental electron density is achieved when the *R-factor* obtained is less than 0.002.

The first approach that was implemented to produce model densities was based on the independent atom model (IAM), where molecules are approximated as the superposition

of spherical atomic densities. It is known as the promolecule approximation. There are several assumptions inside this approximation. For example, no electronic excitations and transfer of charge between atoms is allowed, as well as the spherical atomic symmetry is conserved. The most difficult task is to build the density within the unit cell, for example, to define the position and number of atoms in the unit cell. This is carried out by analyzing the chemical information of the crystal, specifically what types of atoms form the crystal. Therefore, under the promolecule approximation the expression for $F(h,k,l)$ (Equation 2.40) will be in terms of atomic densities, and it can be written by assuming the atoms centered at x_j, y_j and z_j such as [22]:

$$\begin{aligned} x' &= x - x_j \\ y' &= y - y_j \\ z' &= z - z_j \end{aligned} \tag{2.42}$$

in this new form:

$$F(h,k,l) = \sum_j \exp\left[2\pi i\left(hx_j + ky_j + lz_j\right)\right]\left\{\int_{V_j} \rho_j(x',y',z') \exp\left[2\pi i(hx'+ky'+lz')\right]dx'\,dy'\,dz'\right\} \tag{2.43}$$

which can be written as follows:

$$F(h,k,l) = \sum_j f_i \exp\left[2\pi i\left(hx_j + ky_j + lz_j\right)\right] \tag{2.44}$$

where

$$f_j = \int_{V_j} \rho_j(x',y',z') \exp\left[2\pi i(hx'+ky'+lz')\right]dx'\,dy'\,dz' \tag{2.45}$$

f_j is known as the atomic scattering factor, and it is calculated by quantum mechanical methods. The values of f_j depends on the type of atoms and on the Bragg angle, and they are tabulated in Volume II of the International Tables for X-ray Crystallography.

The breaking of spherical symmetry of the atoms due to the interaction with the other atoms or by the formation of a chemical bond introduces significant errors in the elucidation of the structure using the promolecule approximation. Therefore, this approximation leads to acceptable results for heavy atoms where the core electrons dominate the scattering of the X-rays relative to the valence electrons and the distortion of the electron density from the spherical symmetry is not severe [25]. In the case of light atoms, the distortion is considerable and the results using the promolecule approximation are in general inaccurate [24,25], specifically for hydrogen atoms where an acceptable determination of their positions is not possible.

To consider the deformation of the electron density due to the interaction with the other atoms of the systems or by the formation of chemical bonds, aspherical multipolar formalisms have been developed [24,26,27]. One of the most used is the formalism of Hansen and Coppens [24,25,27,28], where the atomic electron density is expressed as a sum of three terms.

$$\rho_{ato} = P_{core}\rho_{core} + P_{valence}\kappa^3\rho_{valence}(\kappa r) + \sum_{l=0}^{l_{max}} \kappa'^3 R_l(\kappa' r) \sum_{m=0}^{l} P_{lm\pm} d_{lm\pm}(\theta,\varphi) \qquad (2.46)$$

The first and second terms account for the contribution of the core electrons and the valence electrons, respectively. The third term accounts for the valence deformation. The P's refer to population coefficients and they satisfy the following condition:

$$P_{core} + P_{valence} + \sum_{m=0}^{l} P_{lm\pm} = \text{total number of electrons of the atom or ion} \qquad (2.47)$$

The ρ_{core} and $\rho_{valence}$ for light atoms or ions are calculated using the Hartree-Fock method, whereas for heavy atoms or ions the relativistic Hartree-Fock method is used to account for relativistic effects [24,25,27,28]. R_l is a Slater radial function with energy optimized

exponents, and the parameter κ scales the coordinates to provide radial contraction or expansion flexibility to the valence shell. The $d_{lm\pm}$ are density-normalized real spherical harmonic functions expressed in polar coordinates which describe the aspherical features of the density. Substituting equation 2.46 into equation 2.45, an expression for the aspherical multipolar atomic scattering factor (f_j) is obtained. Thus, the structure factor $F(h,k,l)$ expressed as a function of these new scattering factors results in the following equation:

$$F(h,k,l) = \sum_j \left[P_{j,core} f_{j,core}(H) + P_{j,valence} f_{j,valence}(H/\kappa) \right.$$

$$\left. + 4\pi \sum_{l=0}^{l_{max}} \sum_{m=0}^{l} P_{lm\pm} i^l \langle j_i \rangle d_{lm\pm}(\beta,\gamma) \right] \exp\left[2\pi i\left(hx_j + ky_j + lz_j\right)\right] T_j(h,k,l) \quad (2.48)$$

where $f_{j,core}$ and $f_{j,valence}$ are the Fourier transforms of $\rho_{j,core}$ and $\rho_{j,valence}$, respectively, $\langle j_l \rangle$ is the l^{th} –order Fourier-Bessel transform of R_l, and the $d_{lm\pm}$ are spherical harmonics expressed in reciprocal space polar coordinates. The T_j(h,k,l) are the temperatures which are introduced to measure the extent to which every atom j oscillates around the position specified in the model due to thermal vibrations. The use of this aspherical model of atomic density makes a significant contribution to the refinement of chemical structures determined by the X-ray diffraction experiment.

Chapter 3 The Quantum Theory of Atoms in Molecules.

3.1 The Topology of the Electron Density.

Open systems are those systems that can interchange charge and momentum with their surroundings. Quantum mechanics establishes the properties of open systems when they are bounded by a zero-flux surface in the gradient vector field of the electron density ($\nabla\rho$, Equation 3.1). From elementary calculus the gradient ∇ of a scalar function, $\rho(\mathbf{r})$ in this case, at a point in space is a vector pointing in the direction in which $\rho(\mathbf{r})$ undergoes the greatest rate of increase and having a magnitude equal to the rate of increase in that direction.

$$\nabla\rho = \mathbf{i}\frac{d\rho}{dx} + \mathbf{j}\frac{d\rho}{dy} + \mathbf{k}\frac{d\rho}{dz} \tag{3.1}$$

In essence the theory of Atoms in Molecules (AIM) developed by Bader [29] is a wonderful extension of quantum mechanics to chemistry. It gives a quantum definition for atoms (open systems) in molecules, showing that they are bounded by a zero-flux surface in the gradient vector field of the electron density. Therefore, it is the topology of a physical observable, the electron density, that determines the boundaries of an atom in a molecule, which in turn determine its shape and its properties. This remarkable result supports an important hypothesis in chemistry, which is the basis of chemistry as an experimental science: molecules are formed by the union (chemical bond) of atoms.

When the electron density is analyzed in molecules (it could be from experiment or from theoretical calculation), specifically the plot of $\nabla\rho$, it shows trajectories coming from infinity and terminating at nuclei or points where $\nabla\rho$ is equal to zero. Indeed the

trajectories of $\nabla\rho$ come from and terminate in regions or points where $\nabla\rho = 0$ (infinity and critical points). It should be borne in mind that ρ is a function in three dimensions, and $\nabla\rho$ has to be zero in the three dimensions in these critical points [29,30].

The forces exerted by the nuclei on the electron density dominate the topology of it, thus, the electron density exhibits a maximum at the position of each nucleus. The nuclei are considered as attractors of $\nabla\rho$, and the regions in the space that contain one attractor and are enclosed by a surface of zero flux formed for all the trajectories of $\nabla\rho$ that originate and terminate in points where $\nabla\rho = 0$, except the position of the nuclei (attractors), are called basins (Ω). These basins contain all the trajectories of $\nabla\rho$ that terminate at the contained attractor coming from any point in the space. Therefore the analysis of $\nabla\rho$ produces a partitioning of the total space of a molecular system into subspaces formed by one attractor (nucleus) and its respective basin. Each subspace defines an atom in the AIM theory.

Any critical point in the electron density distribution is characterized by its rank and signature [29,30]. The characterization of a critical point is carried through the so-called Hessian matrix evaluated at the critical point in question. The Hessian matrix is a 3×3 array of nine second derivatives of ρ where the diagonal elements are the second derivatives in the same direction and the off-diagonal terms are the crossed second derivatives (Equation 3.2).

$$\mathbf{A}(\mathbf{r}_c) = \begin{pmatrix} \frac{\partial^2\rho}{\partial x^2} & \frac{\partial^2\rho}{\partial x\partial y} & \frac{\partial^2\rho}{\partial x\partial z} \\ \frac{\partial^2\rho}{\partial y\partial x} & \frac{\partial^2\rho}{\partial y^2} & \frac{\partial^2\rho}{\partial y\partial z} \\ \frac{\partial^2\rho}{\partial z\partial x} & \frac{\partial^2\rho}{\partial z\partial y} & \frac{\partial^2\rho}{\partial z^2} \end{pmatrix}_{\mathbf{r}=\mathbf{r}_c} \tag{3.2}$$

Since the Hessian matrix is real and symmetric, it can be diagonalized to give the associated Hessian matrix. Essentially the procedure of diagonalization is equivalent to finding the eigenvectors that define the axes of a new coordinate system where the off-diagonal elements of the Hessian matrix are zero. It should be kept in mind that in three dimensions there can be points where the $\nabla\rho = 0$ in two dimensions, which will make the Hessian matrix diagonal in two dimensions. The only critical points of interest are those which make the Hessian matrix diagonal in three dimensions. This associated matrix is denoted by $\mathbf{\Lambda}(\mathbf{r}_c)$ and it is given by:

$$\Lambda = \begin{pmatrix} \frac{\partial^2\rho}{\partial x^2} & 0 & 0 \\ 0 & \frac{\partial^2\rho}{\partial y^2} & 0 \\ 0 & 0 & \frac{\partial^2\rho}{\partial z^2} \end{pmatrix}_{\mathbf{r}'=\mathbf{r}_c} = \begin{pmatrix} \lambda_1 & 0 & 0 \\ 0 & \lambda_2 & 0 \\ 0 & 0 & \lambda_3 \end{pmatrix} \tag{3.3}$$

where λ_1, λ_2 and λ_3 are the eigenvalues of the associated Hessian matrix (the curvatures of the density with respect to the new coordinate system). An important property that has to be mentioned is that the trace of the Hessian matrix is invariant to rotations of the coordinate system.

The rank of a critical point is determined by the number of non-zero eigenvalues (or curvatures) of the associated Hessian matrix evaluated at the critical point, and the signature is the algebraic sum of the signs of the eigenvalues. A positive eigenvalue indicates that the function is a minimum in the direction defined by its associated eigenvector, and a negative sign indicates the opposite. In most molecular systems, ρ is antisymmetric with respect to the bond critical points. Thus, the behavior of ρ in the direction defined by an eigenvector and in the opposite direction to it is different. For

example, the direction defined by a positive eigenvector indicates the largest increase of a function (ρ); in the opposite direction ρ also increases but not as in the direction defined by the eigenvector (A function only presents the same behavior in both directions when it is symmetric with respect to the evaluated point.)

Bond critical points have rank = 3 and signature = -1, and are denoted by (3,-1). The eigenvector with a positive sign represents the direction in which ρ is a minimum, it defines a trajectory in $\nabla\rho$ that links the two nuclei of the atoms. This trajectory is known as a bond path. It represents a line of maximum density between the bound nuclei and it can be considered as a universal indicator of bonding. The set of trajectories that terminate at a bond critical point (and at a ring critical point depending upon molecular system) define the interatomic surface (IAS) that separates the basins of the neighboring atoms. An interatomic surface is one of zero-flux in the gradient vector field of the electron density since it is formed by all the trajectories of $\nabla\rho(\mathbf{r})$ that do not terminate at the position of the nuclei. This property is the necessary and sufficient condition for the development of the theory of atoms in molecules from first principles. A more detailed analysis about this important condition will be provided in the next section.

Even though the electron density at the center of a nucleus is zero, each nucleus defines the terminus of the $\nabla\rho$ trajectories. The nuclei represent local maxima in the electron density and are classified as (3,-3) critical points.

All the topological properties of the electron density in the molecular systems discussed above are clearly illustrated in Figure 3.1.

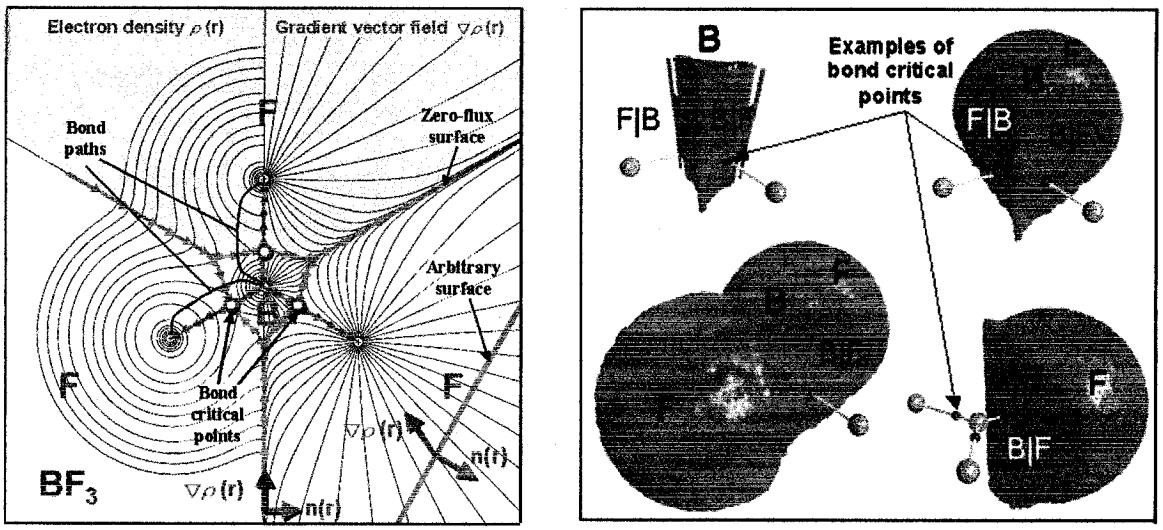

(a) (b)

Figure 3.1 Topological characterization of the electron density in BF_3 molecule (included with the permission of Dr. Chérif Matta).
(a) Bond critical points, bond paths, contour map of the electron density, $\nabla\rho$ trajectories and interatomic surfaces.
(b) A three-dimensional view of the interatomic surfaces.

However, not all the (3,-3) critical points are nuclei. In clusters of lithium and sodium (3,-3) critical points have been found at the bond midpoint [29]. These maxima are called non-nuclear attractors, and they exhibit a small value of ρ relative to the nuclei. Therefore, the nuclei in these clusters of lithium and sodium are not linked by a BCP but two BCPs and a non-nuclear attractor. The BCPs are exhibited between each nuclei and the non-nuclear attractor, and they appear on the trajectories of ∇ρ that connect each nucleus with the non-nuclear attractor. The electronic charge is loosely and delocalized in regions dominated by the non-nuclear attractors and it can be useful to explain the conducting properties of clusters of metals.

Ring critical points are characterized by rank=3 and signature =1 and denoted by (3,+1). The two positive eigenvalues define a surface formed by all the trajectories of $\nabla\rho$

generated at the ring critical point; this surface is called the ring surface. The ring critical point is present in all the structures where the bond paths form a ring, therefore the existence of this critical point is the necessary theoretical condition to classify the structure of a certain compound as a ring. Cage critical points are denoted by (3, +3) and are inside the volume engulfed by two or more ring surfaces.

The Poincaré–Hopf relationship defines a algebraic relation between all the critical points that can coexist in a molecule and it is given by:

$$n - b + r - c = 1 \tag{3.4}$$

where n stands for number of attractors, b for the number of bond critical points (BCP), r for the number of RCPs, and c for the number of CCPs. The set {n, b, r, c} for a given molecular system is known as the characteristic set of that system. Equation 3.4 holds for a non-periodic system such as an isolated molecule or molecular complex. The violation of the Poincaré–Hopf equality means that a further search for the missing critical point(s) is necessary [29,30].

One important parameter of the AIM theory is the ellipticity [29,30] of a bond, which is defined as (λ_1/λ_2) -1, where λ_1 and λ_2 are the two negative curvatures at the bond critical point in decreasing order of magnitude. Curvature at a certain point gives an idea of how a function decreases or increases in the vicinity of this point. A small negative curvature indicates a small decreasing of the function, and a small positive curvature indicates a small increasing of the function; the opposite when their values are great. Therefore small negative curvatures represent high accumulation of charge through the axis defined by the corresponding eigenvalue, and specifically, the eigenvector with λ_2 curvature defines the direction of highest concentration of ρ. Thus, the ellipticity serves to quantify how ρ

is preferentially distributed in the perpendicular plane to the bond formed by the two axes, which at the same time are defined by the two eigenvectors with negative curvatures λ_1 and λ_2. In other words, the ellipticity is a suitable parameter to determine the π character of the bonds.

Probably the AIM result that contains the most chemical information is the Laplacian [29,31,32] of ρ ($\nabla^2\rho$), especially the (3, -3) critical points on the topology of the negative of the Laplacian. It should be kept in mind that the characterizations of charge concentrations in terms of critical points is always carried out through L, which is equal to $-\nabla^2\rho$, to make the analysis of the results easier. The Laplacian of the electron density is the trace of the Hessian matrix, and it is given by:

$$\nabla^2\rho(\mathbf{r}) = \nabla\cdot\nabla\rho(\mathbf{r}) = \frac{\partial^2\rho(\mathbf{r})}{\partial x^2} + \frac{\partial^2\rho(\mathbf{r})}{\partial y^2} + \frac{\partial^2\rho(\mathbf{r})}{\partial z^2} \tag{3.5}$$

The Laplacian of the electron density ($\nabla^2\rho$) plays a central role in analyzing and understanding the reactivity and geometry of compounds [29]. In regions where $\nabla^2\rho<0$ the charge is locally concentrated, whereas in regions where $\nabla^2\rho>0$ the charge is locally depleted. A chemical reaction is defined by AIM theory as the interaction between regions of charge concentration with regions of charge depletion. The line of approach of the two reactants is one that minimizes $|\nabla^2\rho_1 - \nabla^2\rho_2|$.

AIM studies of the Laplacian also exhibit shell structure for isolated atoms [29,48]. The valence shell of an atom is divided into two regions. The outer region exhibits positive values of $\nabla^2\rho$ whereas the inner one presents negative values of $\nabla^2\rho$. This inner region is called the valence shell charge concentration (VSCC).

It can be said that the electron pairs of the Lewis model find their theoretical justification in the topology of L or in other words the topology of L describes the valence shells of atoms in molecules in such a way that is consistent with the Lewis model. This model is frequently used to predict geometries and the stability of compounds as well as reaction paths.

The critical points in L are obtained in the same way as those of ρ, through the diagonalization of the Hessian matrix [29,30]. The most important critical points in the topology of L are those characterized by rank=3 and signature =-3 denoted by (3, -3) and by rank=3 and signature=-1 denoted by (3, -1). The (3, -3) critical points are maxima and correspond to the points of highest concentration of charge. These local maxima in three dimensions in L can be considered to represent the electron pairs of atoms in molecules of the Lewis model, which is the basis of the valence shell electron pair repulsion model (VSEPR) for the prediction of molecular geometries [29]. The (3, -1) critical points are known as link points and can be associated with the bond critical points in the topology of ρ. The link points are maxima in the two dimensions perpendicular to a line that joins two (3, -3) critical points in L topology and a minimum along this line.

3.2 The Zero-Flux Surface and Proper Open Quantum Systems

A zero-flux surface in the gradient vector field of the electron density is a surface (S) where a normal vector $\mathbf{n}(\mathbf{r})$ to the surface is orthogonal to the gradient vector field $\nabla\rho(\mathbf{r})$ at every point on the surface. This boundary condition is defined by the following equation:

$$\nabla\rho(\mathbf{r})\cdot\mathbf{n}(\mathbf{r})=0 \qquad \forall \quad \mathbf{r}\in S(\Omega,\mathbf{r}) \tag{3.6}$$

where Ω refers to the atomic basin. This equation plays a central role in the quantum theory of atoms in molecules because it is the necessary condition for the definition of an atom as a proper open quantum system. In general, the atomic surface consists of an intersection of a number of interatomic surfaces that produces a partitioning of the molecular space into a disjoint set of mono-nuclear regions (atomic basins). This is a consequence of the fact that each nucleus acts as an attractor in the gradient vector field of the electron density. Thus, those trajectories of $\nabla\rho$ (**r**) that do not terminate at the position of the nuclei form the interatomic surfaces, separating one atomic basin from the other and having the condition of zero-flux surface in the $\nabla\rho$ (**r**) field [29,30].

A molecule can be viewed as a collection of atoms linked by bond paths as was explained in the last section. Therefore, atoms can be considered as subsystems of the molecular system. In the quantum mechanical description of subsystems, the analysis of the bounded surfaces that limit one subsystem from the others has to be taken into account. For example, consider the following expression:

$$\nabla^2(\Psi^*\Psi) = \nabla\cdot\left[(\nabla\Psi^*)\Psi + \Psi^*(\nabla\Psi)\right]$$

$$= (\nabla^2\Psi^*)\Psi + \Psi^*(\nabla^2\Psi) + 2\nabla\Psi^*\cdot\nabla\Psi \qquad (3.7)$$

By doing some transformations on equation 3.7 and substituting $\Psi^*\Psi$ by ρ, one obtains:

$$-\left[\Psi\nabla^2\Psi^* + \Psi^*\nabla^2\Psi\right] = 2\nabla\Psi^*\cdot\nabla\Psi - \nabla^2\rho \qquad (3.8)$$

Multiplying both sides of equation 3.8 by $-\hbar^2/4m$ and summing for the "*i*" electrons in the system, it is obtained the following expression is obtained for the many-electron case:

$$-\frac{\hbar^2}{4m}\sum_i\left[\Psi\nabla_i^2\Psi^* + \Psi^*\nabla_i^2\Psi\right] = \frac{\hbar^2}{2m}\sum_i\nabla_i\Psi^*\cdot\nabla_i\Psi - \frac{\hbar^2}{4m}\sum_i\nabla_i^2\rho \qquad (3.9)$$

The electrons are fermions (semi-integer spin), therefore Ψ has to be antisymmetrized. Moreover, the electrons are indistinguishable particles, thus, N times the average of an one-electron operator is equal to the average of a sum of N one-electron operators. The average of each one-electron operator term in equation 3.9 is obtained by integrating over the space coordinates of all the electrons but one, and summing over all the spins [29,30]. This mode of integration will be denoted by $\int d\tau'$, and it will be used elsewhere in this chapter. As was explained above, the result of the integration is then multiplied by the number of electrons to obtain:

$$-\frac{\hbar^2}{4m} N \int d\tau' \left[\Psi \nabla_i^2 \Psi^* + \Psi^* \nabla_i^2 \Psi\right] = \frac{\hbar^2}{2m} N \int d\tau' \nabla_i \Psi^* \cdot \nabla_i \Psi - \frac{\hbar^2}{4m} N \int d\tau' \nabla_i^2 \rho \qquad (3.10)$$

Where the LHS term and the first RHS term are kinetic energy densities, and they are denoted by K (**r**) and G (**r**), respectively. The second RHS term is a function of the Laplacian of the electron density, and it is denoted by L (**r**). Since $\nabla\rho$ (**r**) vanishes at infinity, $\nabla^2\rho$ (**r**), which is equal to $\nabla\cdot\nabla\rho$ (**r**), also vanishes. Therefore, an integration of equation 3.10 over all space will cancel L (**r**) and will result in the equality $K = G = T$, where K is the Schrödinger kinetic energy, G is the gradient kinetic energy and T is the well defined kinetic energy. However, integration of equation 3.10 over an arbitrary subsystem Ω

$$K(\Omega) = G(\Omega) - \frac{\hbar^2}{4m} N \int_{\Omega} d\tau' \nabla \cdot \nabla \rho = G(\Omega) - L(\Omega) \qquad (3.11)$$

would result in a non-physical result (K (Ω) $\neq$ G (Ω)), and the kinetic energy of the subsystem (T (Ω)) would not be well-defined if the bounding surface of Ω does not satisfy the condition of zero-flux surface in the $\nabla\rho$ (**r**) field. In order to make this

statement clearer, the volume integral of equation 3.11 can be transformed to a surface integral using the divergence theorem of Gauss.

$$K(\Omega) = G(\Omega) - \frac{\hbar^2}{4m} N \oint dS(\Omega, \mathbf{r}) \nabla\rho \cdot \mathbf{n}(\mathbf{r}) \tag{3.12}$$

Therefore, S has to be a zero-flux surface in the $\nabla\rho$ (**r**) field to obtain a well defined kinetic energy ($K(\Omega) = G(\Omega) = T(\Omega)$).

Bader and Beddall in 1972 obtained a remarkable result by studying the behavior of the kinetic energy density [33]. They demonstrated that when the electron density of a proper open system is transferable, the kinetic energy density is equally transferable. However, it is necessary to prove that the virial theorem applies to an atom in a molecule to state that the total energy of this atom E (Ω) is also transferable. The virial theorem in general establishes that the average kinetic energy of a system (or subsystem) is equal to the negative of the average of the total energy of the system. In the case of an atom in a molecule it will be enunciated in the following way:

$$T(\Omega) = -E(\Omega) \tag{3.13}$$

In consequence, the electron density determines the form of an atom in a molecule and its contribution to the total molecular energy. It means that two atoms with similar distributions of the electron density in their basins will contribute similar amounts to the total energy [29,30].

Another consequence of application of the virial theorem on a subsystem, which in this case is an atom in a molecule, is that the total energy of the molecule (and the kinetic energy) can be partitioned into additive atomic contributions.

$$E = -\sum_{\Omega} E(\Omega) \tag{3.14}$$

Therefore, the additivity and transferability are two fundamental properties that the empirical atoms exhibit, and they are consequences of the fulfillment of the virial theorem on an atom in a molecule. The demonstration of the virial theorem on an atom in a molecule will be presented in section 3.4.

3.3 The Coincidence of the Topological Atom and the Quantum Atom

The mathematical requirement for Hermiticity of an operator $\hat{A}$ is

$$\int \Psi^* \left(\hat{A}\Psi\right) d\tau = \int \left(\hat{A}\Psi\right)^* \Psi d\tau \tag{3.15}$$

where Ψ can be all the functions defined in the space of functions in which $\hat{A}$ is defined. The non-Hermiticity of an operator's average over subsystem consists of one the most important distinctions, in a quantum mechanical sense, between a subsystem and its total system. The formation of fluxes in property currents across the surface defining its boundaries is responsible for the lost of Hermiticity. An atom is a subsystem of the molecular system, and it can exchange fluxes of properties (energy, etc) with the surroundings through its bounding surface. Therefore, all the operators, when they are integrated over the basin of an atom (Ω), lose their Hermiticity. This statement is made clear using the Heisenberg equation of motion, which determines the evolution of an operator $\hat{A}$ over time:

$$\frac{d\left\langle \hat{A} \right\rangle}{dt} = \frac{i}{\hbar} \left\langle \Psi \middle| \left[\hat{H}, \hat{A}\right] \Psi \right\rangle + \left\langle \partial \hat{A} / \partial t \right\rangle \tag{3.16}$$

where the first LHS term is the commutator of the Hamiltonian and the observable $\hat{A}$ (property). Suppose that $\hat{A}$ does not have an explicit dependence on time to make the derivation easier, thus, the second RHS term is zero.

The commutator term of equation 3.15 can be rewritten in the following way:

$$\left\langle \Psi \middle| \left[\hat{H}, \hat{A}\right] \Psi \right\rangle = \left\langle \Psi \middle| \hat{H}\hat{A} \middle| \Psi \right\rangle - \left\langle \Psi \middle| \hat{A}\hat{H} \middle| \Psi \right\rangle \tag{3.17}$$

Utilizing the Hermiticity property ($\left\langle a \middle| \hat{A} \middle| b \right\rangle = \left\langle b \middle| \hat{A} \middle| a \right\rangle^*$) and the Schrödinger equation $\hat{H}|\Psi\rangle = E\Psi$, one obtains:

$$\begin{aligned} \left\langle \Psi \middle| \left[\hat{H}, \hat{A}\right] \Psi \right\rangle &= \left\langle \hat{H}\Psi \middle| \hat{A}\Psi \right\rangle - \left\langle \Psi \middle| \hat{A}E \middle| \Psi \right\rangle \\ &= E\left\langle \Psi \middle| \hat{A} \middle| \Psi \right\rangle - E\left\langle \Psi \middle| \hat{A} \middle| \Psi \right\rangle = 0 \end{aligned} \tag{3.18}$$

Therefore, when the integration is performed over the whole space the commutator will be always equal to zero whether Ψ is an eigenfunction of the operator $\hat{A}$ or not. In other words, the Hamiltonian and $\hat{A}$ do not have to commute to obtain the average of the commutator over the whole space equal to zero. But this average can no longer be assumed when it is integrated over any subsystem:

$$\left\langle \Psi \middle| \left[\hat{H}, \hat{A}\right] \Psi \right\rangle_\Omega = \left\langle \Psi \middle| \hat{H}\hat{A}\Psi \right\rangle_\Omega - \left\langle \Psi \middle| \hat{A}\hat{H}\Psi \right\rangle_\Omega \neq 0 \tag{3.19}$$

To continue with the derivation in a simple way, assume that $\hat{H}$ describes the motion of a single particle under the influence of a scalar potential $\hat{V}(\mathbf{r})$:

$$\hat{H} = -\left(\frac{\hbar^2}{2m}\right)\nabla^2 + \hat{V}(\mathbf{r}) \tag{3.20}$$

This does not cause loss of generality since the many-electron case can be obtained by the insertion of $N\int \mathrm{d}\tau'$. The potential energy operator in $\hat{H}$ is a real quantity, and it does not involve derivatives. Therefore, its contribution in the average commutator 3.19 will be canceled out. Rewriting equation 3.19:

$$\left\langle \Psi \middle| \left[\hat{H},\hat{A}\right] \middle| \Psi \right\rangle_{\Omega} = \frac{\hbar^2}{2m}\int_{\Omega} d\mathbf{r}\left[\left(\nabla^2\Psi^*\right)\hat{A}\Psi - \Psi^*\nabla^2\left(\hat{A}\Psi\right)\right]$$

$$= \frac{\hbar^2}{2m}\int_{\Omega} d\mathbf{r}\nabla\cdot\left[\left(\nabla\Psi^*\right)\hat{A}\Psi - \Psi^*\nabla\left(\hat{A}\Psi\right)\right] \tag{3.21}$$

Transforming the volume integral into a surface integral using Gauss' theorem yields:

$$\left\langle \Psi \middle| \left[\hat{H},\hat{A}\right] \middle| \Psi \right\rangle_{\Omega} = \oint dS(\Omega,\mathbf{r})\left\{\frac{\hbar^2}{2m}\left[\left(\nabla\Psi^*\right)\hat{A}\Psi - \Psi^*\nabla\left(\hat{A}\Psi\right)\right]\right\}\cdot\mathbf{n}(\mathbf{r}) \tag{3.22}$$

which is equivalent to:

$$\left\langle \Psi \middle| \left[\hat{H},\hat{A}\right] \middle| \Psi \right\rangle_{\Omega} = -i\hbar\oint dS(\Omega,\mathbf{r})\mathbf{j}_A\cdot\mathbf{n}(\mathbf{r}) \tag{3.23}$$

where $\mathbf{j}_A$ is the quantum mechanical current density for the observable $\hat{A}$ through the surface, and it is defined by the following equation:

$$\mathbf{j}_A(\mathbf{r}) = \frac{\hbar}{2mi}\left[\Psi^*\nabla\left(\hat{A}\Psi\right) - \left(\nabla\Psi^*\right)\left(\hat{A}\Psi\right)\right] \tag{3.24}$$

As can be seen in equation 3.23, the commutator term $\left\langle \Psi \middle| \left[\hat{H},\hat{A}\right] \middle| \Psi \right\rangle_{\Omega}$ does not vanish for an open system, and it depends on the quantum mechanical current density for the observable in question through the surface. This result demonstrates clearly the difference between the open systems and the closed systems where this commutator is equal to zero. In order to yield a physical (real-observable) result, equation 3.23 should be rewritten

adding the complex conjugate terms to each side of the equation and dividing by two to compensate for this summation:

$$\frac{1}{2}\left\{\frac{i}{\hbar}\left\langle\Psi\left|\left[\hat{H},\hat{A}\right]\right|\Psi\right\rangle_{\Omega}+cc\right\}=\frac{1}{2}\left[\oint dS(\Omega,\mathbf{r})\mathbf{j}_{A}\cdot\mathbf{n}(\mathbf{r})+cc\right] \tag{3.25}$$

Thus, whenever $\hat{H}$ and $\hat{A}$ do not commute, there is a flux in the property density of A across the surface defined by the surface term in equation 3.25. Note that if $\hat{A}$ is equal to 1, the quantum mechanical current density will be expressed as

$$\mathbf{j}(\mathbf{r})=\frac{\hbar}{2mi}\left[\Psi^{*}\nabla\Psi-\Psi\nabla\Psi^{*}\right] \tag{3.26}$$

Schrödinger in 1926 considered the one electron system "Hydrogen Atom" to obtain the time-independent Schrödinger equation ($\hat{H}|\Psi\rangle=E\Psi$) [34]. He stated that the wave function (Ψ) which describes the hydrogen atom has to be such a function that makes the "Hamilton integral" ($\int d\tau\left\{\hbar^{2}T(q,\partial\Psi/\partial q)+\Psi^{2}V\right\}$) of the system stationary with the normalization constraint $\int\Psi^{2}d\tau=1$. $T(q,\partial\Psi/\partial q)$ is the kinetic energy, and V is the potential energy ($-e^2 / r$). Therefore, the energy functional ($J[\Psi]$) for this one electron system is defined by:

$$J[\Psi]=\int d\tau\left[\frac{\hbar^{2}}{2m}\nabla\Psi^{*}\cdot\nabla\Psi+\left(\hat{V}+\lambda\right)\Psi^{*}\Psi\right] \tag{3.27}$$

where the constant λ is the Lagrange multiplier for the constraint on Ψ, which is identified with the negative of the total energy of the system ($E = -\lambda$).

The statement of Schrödinger can be rewritten in the following way: the wave function (Ψ) to describe the system has to make the functional $J[\Psi]$ a minimum or the

infinitesimal variation of this functional ($\delta J[\Psi]$) equal to zero. This generalization to the many-electron system is straightforward.

However, a variational definition was needed for a subsystem in order to describe the quantum mechanics of an atom in a molecule. Such a generalization of the Schrödinger's derivation was carried out by Srebrenik and Bader [35,36]. They defined a corresponding energy functional for a subsystem Ω:

$$G[\Psi,\Omega]=\int_{\Omega} d\mathbf{r}\left[\frac{\hbar^2}{2m}\nabla\Psi^*\cdot\nabla\Psi+\left(\hat{V}-E\right)\Psi^*\Psi\right]=\int_{\Omega} d\mathbf{r} f(\Psi,\nabla\Psi) \tag{3.28}$$

A variation (infinitesimal change denoted by δ) of G [Ψ,Ω], which is a function of both Ψ (Ψ^*) and ∇Ψ ($\nabla\Psi^*$), has to include the variation of the bounding surface. Ψ and Ψ^* are treated as independent variables, therefore, cc terms will appear in the final expression for the variation of the functional:

$$\delta G[\Psi,\Omega]=\int_{\Omega} d\mathbf{r}\left[\left(\frac{\partial f}{\partial\Psi}\right)\partial\Psi+\left(\frac{\partial f}{\partial\nabla\Psi}\right)\partial\nabla\Psi\right]+\oint dS(\Omega,\mathbf{r}) f\times\delta S(\Omega,\mathbf{r})+cc \tag{3.29}$$

By doing several transformations equation 3.29 can be shown to yield [35]:

$$\delta G[\Psi,\Omega]=\int_{\Omega} d\mathbf{r}[H\Psi-E\Psi]\delta\Psi+\oint dS(\Omega,\Psi)\left[\left(\frac{\hbar^2}{2m}\right)\nabla\Psi^*\cdot\mathbf{n}(\mathbf{r})\delta\Psi+f\times\delta S(\Omega,\mathbf{r})\right]+cc \tag{3.30}$$

Consider a system where the bounding surface is at ∞ (total system). Thus, the second RHS term vanishes by requiring that there is no electron density at **r** = ∞, and then, Ψ and ∇Ψ are equal to zero. Therefore, for such a system equation 3.30 is reduced to:

$$\delta G[\Psi,\Omega]=\int_{\Omega} d\mathbf{r}\left[H\Psi^*-E\Psi^*\right]\delta\Psi+cc \tag{3.31}$$

$\delta G[\Psi,\Omega]$ must be equal to zero to make the Hamilton integral of the system stationary, as was stated by Schrödinger in 1926. In consequence, the bracketed term in this equation must vanish, and it will yield the two conjugate Schrödinger equations:

$$\hat{H}\Psi = E\Psi \qquad \text{and} \qquad \hat{H}\Psi^* = E\Psi^* \tag{3.32}$$

Therefore, it can be concluded that the first term in Eq. 3.31 will not contribute to δG for a subsystem as well as a total system (system with the bounding surface at ∞) because Schrödinger's equation applies at any point of variation. Thus, at any point of variation equation 3.30 is reduced to:

$$\delta G[\Psi,\Omega] = \oint dS(\Omega,\mathbf{r})\left[\left(\frac{\hbar^2}{2m}\right)\nabla\Psi^* \cdot \mathbf{n}(\mathbf{r})\delta\Psi + f(\Psi,\nabla\Psi)\times\delta S(\Omega,\mathbf{r})\right] + cc \tag{3.33}$$

Equation 3.33 shows that the variation of the energy functional does not vanish. It depends on two terms involving its bounding surface. However, this equation is not useful to obtain a general physical result because the second surface term cannot be calculated. Therefore, an alternative expression for $f(\Psi,\nabla\Psi)$ involving the Hamiltonian operator $\hat{H}$ is formulated where the complex conjugate term is taken into account, thus, $f(\Psi,\nabla\Psi)$ appears twice in the equation. Also, using equation 3.10, which relates the two forms of kinetic energy density, rewritten for the one-electron case, one has:

$$2f(\Psi,\nabla\Psi) = \left[\left(\hat{H}\Psi\right)^*\Psi + \Psi^*\hat{H}\Psi\right] - 2E\Psi^*\Psi + 2\left(\frac{\hbar^2}{4m}\right)\nabla^2\left(\Psi^*\Psi\right) \tag{3.34}$$

and since Schrödinger's equations are applicable, equation 3.34 is simplified to:

$$f(\Psi,\nabla\Psi) = \left(\frac{\hbar^2}{4m}\right)\nabla^2\rho(\mathbf{r}) \tag{3.35}$$

Substituting this expression in equation 3.33, yields:

$$\delta G[\Psi,\Omega]=\oint dS(\Omega,\mathbf{r})\left[\left(\frac{\hbar^2}{4m}\right)\left(2\nabla\Psi^*\cdot\mathbf{n}(\mathbf{r})\delta\Psi+\delta S(\Omega,\mathbf{r})\nabla^2\rho\right)\right]+cc \qquad (3.36)$$

This is an important result which clarified the physical interpretation of our problem because it shows that the variation of the energy functional depends on the Laplacian of the electron density. However, it is not possible to make further progress in obtaining a general variational principle from this expression 3.36 for an arbitrary region in the space. Therefore, we need to restrict our subsystem Ω to satisfy a particular variational constraint on the form of the open system. It is demonstrated next that equation 3.36 is transformed into the atomic statement of the hypervirial theorem for such a subsystem. A trial function Φ is used to introduce the variational constraint.

Before proceeding with the demonstration we should recall that the topological definition of an atom implies the zero-flux surface condition (equation 3.6). In other words, an atom is a region of space bounded by a surface satisfying the zero-flux condition.

A region $\Omega(\Phi)$ is defined in terms of the trial function Φ that is bound by a zero-flux surface in $\nabla\rho_\Phi$, where the trial density is defined as:

$$\rho_\Phi = \int d\mathbf{r}\ \Phi^*\Phi \qquad (3.37)$$

$\Omega(\Phi)$ is required to be continuously deformable into the region $\Omega(\Psi)$, which is the region associated with the atom, as Φ tends to Ψ. In consequence, the region $\Omega(\Phi)$ represents the atom in the system which is described by the trial function Φ, and $\Omega(\Psi)$ represents the atom when the system is in the state described by Ψ. Therefore, we have to impose the variational constraint for $\Omega(\Phi)$ at all stages of variations, which is:

$$\int_{\Omega(\Phi)}\nabla^2\rho_\Phi(\mathbf{r})d\mathbf{r}=0 \qquad (3.38)$$

In other words, it means that all admissible Φ fulfill condition 3.38, which implies that:

$$\delta\left[\int_{\Omega(\Phi)}\nabla^2\rho_\Phi(\mathbf{r})d\mathbf{r}\right]=0 \tag{3.39}$$

Similar to equation 3.29, the variation 3.39 requires a variation in the surface of Ω as well as the variation of the integrand. Therefore, the variation in the surface Ω has to be equal to the negative of the variation of the integrand, or vice versa, in order to obtain 3.39 equal to zero:

$$\frac{\hbar^2}{4m}\oint dS(\Omega,\mathbf{r})\delta S(\Omega,\mathbf{r})\nabla^2\rho(\mathbf{r})=-\frac{\hbar^2}{4m}\int_\Omega d\mathbf{r}\delta\left[\nabla^2\rho(\mathbf{r})\right] \tag{3.40}$$

$$=-\frac{\hbar^2}{4m}\int_\Omega d\mathbf{r}\nabla\cdot\left[\nabla\Psi^*\delta\Psi+\Psi^*\nabla\delta\Psi\right] \tag{3.41}$$

$$=-\frac{\hbar^2}{4m}\oint dS(\Omega,\mathbf{r})\left[\nabla\Psi^*\delta\Psi+\Psi^*\nabla\delta\Psi\right]\cdot\mathbf{n}(\mathbf{r}) \tag{3.42}$$

as can be seen the change from volume integral in 3.41 to surface integral in 3.42 was performed utilizing the Gauss' theorem. Then, substituting the RHS of equation 3.42 into 3.36, yields:

$$\delta G[\Psi,\Omega]=\frac{\hbar^2}{4m}\oint dS(\Omega,\mathbf{r})\left[\left(\nabla\Psi^*\right)\delta\Psi-\Psi^*\delta(\nabla\Psi)\right]\cdot\mathbf{n}(\mathbf{r})+cc \tag{3.43}$$

Equation 3.43 is a statement of a physical principle because it shows that the Schrödinger's energy functional can be expressed in terms of the surface integral of the quantum mechanical current density (equation 3.26). For example, the variation of equation 3.26 yields:

$$\delta\ \mathbf{j}(\mathbf{r})=\frac{\hbar}{2mi}\left[\Psi^*\delta(\nabla\Psi)-\left(\nabla\Psi^*\right)\delta\Psi\right] \tag{3.44}$$

Therefore, the Schrödinger's energy functional can be rewritten to show clearly its dependence on the quantum mechanical current density (**j** (**r**)) by substituting 3.44 in 3.43:

$$\delta G[\Psi,\Omega] = -\frac{i\hbar}{2}\oint dS\,(\Omega,\mathbf{r})\delta\mathbf{j}(\mathbf{r})\cdot\mathbf{n}(\mathbf{r}) + cc \tag{3.45}$$

However, the equivalence between the expression for the variation of the subsystem energy functional ($\delta G[\Psi,\Omega]$) and the variational derivation of the hypervirial theorem for an atom in a molecule has not been demonstrated to this point. For this purpose, we need to consider the variation of Ψ to be generated by the action of an operator on itself. Schwinger uses infinitesimal unitary transformations, which apply separately to the observables and the state function of the system, to generate all possible physical changes in the mechanics of a quantum system [37]. The operator for an infinitesimal unitary transformation and its inverse (its Hermitian conjugate) are given by:

$$\hat{U} = \hat{1} - \frac{i\varepsilon}{\hbar}\hat{G} \qquad \text{and} \qquad \hat{U}^{-1} = \hat{1} + \frac{i\varepsilon}{\hbar}\hat{G} \tag{3.46}$$

where ε is an infinitesimal and $\hat{G}$ is any linear Hermitian operator (observable), which is referred to be the generator of the infinitesimal transformation. The effect of these unitary transformations defined by 3.46 on Ψ and Ψ^* generates the infinitesimal variations represented by 3.47:

$$\delta\Psi = -\frac{i\varepsilon}{\hbar}\hat{G}\Psi \qquad \text{and} \qquad \delta\Psi^* = \frac{i\varepsilon}{\hbar}\hat{G}\Psi^* \tag{3.47}$$

Then, it is convenient to define a quantum mechanical current density for the property associated with the operator $\hat{G}$ since the variation of Ψ and Ψ^* ($\delta\Psi$ and $\delta\Psi^*$) is generated by $\hat{G}$. The expression for this quantum mechanical current is given by:

$$\mathbf{j}_G(\mathbf{r}) = \frac{\hbar}{2mi}\left[\Psi^*\nabla\left(\hat{G}\Psi\right) - \left(\nabla\Psi^*\right)\left(\hat{G}\Psi\right)\right] \tag{3.48}$$

and now the expression for the variation of the energy functional in terms of $\mathbf{j}_G(\mathbf{r})$ is:

$$\delta G[\Psi, \Omega] = -\frac{\varepsilon}{2}\oint dS\,(\Omega, \mathbf{r})\delta\mathbf{j}_G(\mathbf{r})\cdot\mathbf{n}(\mathbf{r}) + cc \tag{3.49}$$

By comparing 3.49 with the expression derived previously for a subsystem statement of the hypervirial theorem (Equation 3.25), we can write:

$$\delta G[\Psi,\Omega] = -\frac{\varepsilon}{2}\left\{\frac{i}{\hbar}\left\langle\Psi\right|\left[\hat{H},\hat{G}\right]\left|\Psi\right\rangle_\Omega + cc\right\} \tag{3.50}$$

This is a remarkable result, and it is known as the atomic statement of the principle of stationary action for a stationary state. It applies to a system with its bounding surface at infinity (total system) and also to all the open systems in which the bounding surface satisfies the zero-flux condition in the gradient of the vector field of the charge density. Therefore, it can be applied to an isolated atom, an atom in a molecule and to any linked atoms or grouping of atoms. Thus, it can be said that the zero-flux condition expressed in equation 3.6 makes possible the definition of the topological atom as a quantum system.

As the main conclusion of this section we can say that the topological atoms have been proved from first principles to be proper open quantum systems. Therefore, they can be identified with the atoms of chemistry since the principle of stationary action establishes for the proper open quantum system that their properties are additive and transferable [38]. The additivity property is expressed by the following equation:

$$M = \sum_\Omega M(\Omega) \tag{3.51}$$

where M is any molecular property and $M(\Omega)$ is the corresponding additive atomic counterpart. This result is precisely what makes the theory of atoms in molecules so

powerful, the coincidence in properties between the topological atom and the atoms in chemistry or, in other words, the connection between experimental chemistry and the quantum theory of electronic structure of chemical systems. In experimental chemistry there are many instances where the values of several properties, such as the heat of formation, the electric polarizability or the magnetic susceptibility, can be expressed in terms of additive group contributions. This additivity is also exhibited by using the definition of group by the theory of atoms in molecules in theoretical calculations. For example, calculations in linear hydrocarbons have demonstrated that the total energy of the hydrocarbons can be expressed as a sum of the energies of the methyl and methylene groups [29]. This additivity principle is satisfied to within experimental accuracy. Furthermore, the linear hydrocarbons are examples where the density distribution of an atom or group is essentially transferable between systems [29]. In conclusion, the quantum theory of atoms in molecules recovers the ancient concept of atoms as the building blocks of matter.

3.4 The Atomic Virial Theorem

The virial theorem of an atom is derived using the atomic statement of the principle of stationary action, which was presented in last section. Equating 3.49 and 3.50 to put it in a more general way, we obtain:

$$\left\{\frac{i}{\hbar}\left\langle\Psi\left|\left[\hat{H},\hat{G}\right]\right|\Psi\right\rangle_{\Omega}+cc\right\}=\left[\oint dS(\Omega,\mathbf{r})\mathbf{j}_{G}(\mathbf{r})\cdot\mathbf{n}(\mathbf{r})+cc\right] \tag{3.52}$$

The virial operator $\hat{\mathbf{r}}\cdot\hat{\mathbf{p}}$, where $\hat{\mathbf{r}}$ and $\hat{\mathbf{p}}$ are the position and momentum operators for a single electron, is used as the generator of the infinitesimal unitary transformation

($\hat{G} = \hat{\mathbf{r}} \cdot \hat{\mathbf{p}}$). Therefore, we obtain for the LHS term of 3.52 by inserting $\hat{\mathbf{r}} \cdot \hat{\mathbf{p}}$, evaluating the commutator and multiplying by *N*/2 to the both sides of the resultant equation by *N*/2, the following:

$$\left(\frac{N}{2}\right)\left\{\frac{i}{\hbar}\left\langle\Psi\middle|\left[\hat{H}, \hat{\mathbf{r}} \cdot \hat{\mathbf{p}}\right]\middle|\Psi\right\rangle_{\Omega} + cc\right\} = -2N\left(\frac{\hbar^2}{4m}\right)\int_{\Omega} d\tau \int d\tau' \left[\Psi^* \nabla^2 \Psi + \left(\nabla^2 \Psi^*\right)\Psi\right]$$

$$+ N \int_{\Omega} d\tau \int d\tau' \Psi^* \left(-\mathbf{r} \cdot \nabla \hat{V}\right)\Psi$$

$$= 2T(\Omega) + \mathscr{V}_b(\Omega) \tag{3.53}$$

The first term of the RHS of 3.53 is twice the average electronic kinetic energy of the atom $T(\Omega)$ defined in equations 3.10 and 3.11. The second term is the integrated value of the virial of the Ehrenfest force acting on an electron in the basin of the atom Ω, which in other words is the average effective potential field felt by an electron in an atom Ω.

Now working on the RHS term of 3.52, we evaluate the surface integral and multiply by *N*/2 to yield:

$$\frac{N}{2}\left[\oint dS(\Omega, \mathbf{r}) \mathbf{j}_{\hat{\mathbf{r}} \cdot \hat{\mathbf{p}}}(\mathbf{r}) \cdot \mathbf{n}(\mathbf{r}) + cc\right] =$$

$$= -\frac{N\hbar^2}{4m} \oint dS(\Omega, \mathbf{r}) \int d\tau' \Psi^* \nabla\left(\mathbf{r} \cdot \nabla\Psi\right) - \nabla\Psi^* \left(\mathbf{r} \cdot \nabla\Psi\right) + \Psi\nabla\left(\mathbf{r} \cdot \nabla\Psi^*\right) - \nabla\Psi\left(\mathbf{r} \cdot \nabla\Psi^*\right)$$

$$= -\oint dS(\Omega, \mathbf{r}) \mathbf{r} \cdot \tilde{\sigma}(\mathbf{r}) \cdot \mathbf{n}(\mathbf{r}) - \frac{\hbar^2}{4m} \oint dS(\Omega, \mathbf{r}) \nabla\rho(\mathbf{r}) \cdot \mathbf{n}(\mathbf{r}) \tag{3.54}$$

The identity $\nabla\left(\mathbf{r} \cdot \nabla\Psi\right) = \nabla\Psi + \mathbf{r} \cdot \nabla\nabla\Psi$ was used to obtain the final result. The second term of the RHS of equation 3.54 is $L(\Omega)$, as defined in equation 3.11 in section 3.2. The negative of the first term on the RHS of equation 3.54 is labeled $\mathscr{V}_s(\Omega)$, and it is the virial

of the Ehrenfest forces exerted on the surface of the atom Ω. The quantum stress tensor $\ddot{\sigma}(\mathbf{r})$ is defined for the many-electron case as:

$$\ddot{\sigma}(\mathbf{r}) = -N\frac{\hbar^2}{4m}\int d\tau'\left\{\Psi^*\nabla(\nabla\Psi)+\nabla(\nabla\Psi^*)\Psi+\nabla\Psi^*\nabla\Psi-\nabla\Psi\nabla\Psi^*\right\} \tag{3.55}$$

which can be reduced to the one-electron case by performing the integration and dividing by *N*. The quantity $\ddot{\sigma}(\mathbf{r})\cdot\mathbf{n}(\mathbf{r})$ is the outwardly directed force per unit of the surface, and $\mathbf{r}\cdot\ddot{\sigma}(\mathbf{r})\cdot\mathbf{n}(\mathbf{r})$ is the virial of this force, which integrated over the surface yields the virial of the Ehrenfest forces exerted on the surface of the atom Ω:

$$\mathscr{V}_S = \oint dS(\Omega,\mathbf{r})\mathbf{r}\cdot\ddot{\sigma}(\mathbf{r})\cdot\mathbf{n}(\mathbf{r}) \tag{3.56}$$

Equating equations 3.53 and 3.54, and taking into account that for an atom $L(\Omega) = 0$ (second term of the RHS of 3.54) since its bounding satisfies the zero-flux condition in the gradient of the vector field of the charge density, one obtains:

$$-2T(\Omega) = \mathscr{V}_b(\Omega)+\mathscr{V}_S(\Omega) = \mathscr{V}(\Omega) \tag{3.57}$$

$\mathscr{V}(\Omega)$ is the total atomic virial, and it has two contributions; one from the basin and the other one form the bounding surface, which is the expected physical result for a proper open system.

The electronic energy of an atom $E_e(\Omega)$ can be defined by:

$$E_e(\Omega) = T(\Omega)+\mathscr{V}(\Omega) \tag{3.58}$$

where $T(\Omega)$ is the well defined kinetic energy of an atom as was mentioned in section 3.2 and $\mathscr{V}(\Omega)$ is the total atomic virial. For a system in electrostatic equilibrium where there are no external forces acting on the nucleus of each basin Ω, the virial of the system is

equal to the potential energy (V) of the system. Therefore, equations 3.57 and 3.58 can be re-expressed under this condition in the following ways:

$$-2T(\Omega)=V(\Omega) \tag{3.59}$$

$$E(\Omega)=E_e(\Omega)=T(\Omega)+V(\Omega)=-T(\Omega) \tag{3.60}$$

where $V(\Omega)$ can be referred to now as the potential energy of atom Ω and $E(\Omega)$ is the total energy of atom Ω.

Equation 3.58 is a remarkable result. The equation represents a quantum mechanical spatial partitioning of all of the interactions in a molecule: electron-electron, electron-nuclear and nuclear-nuclear into a sum of atomic contributions (equation 3.14). Specifically, we just need to calculate the well-defined kinetic energy of each atom in the molecule to obtain the total energy of the molecule.

3.5 Atomic Properties

The atomic average of an observable $\hat{A}$ under the quantum theory of atoms in molecules is given by:

$$A(\Omega)=\left\langle \hat{A}\right\rangle_{\Omega}=\frac{N}{2}\int_{\Omega}d\tau\int d\tau'\left[\Psi^{*}\hat{A}\Psi+\left(\hat{A}\Psi\right)^{*}\Psi\right] \tag{3.61}$$

But we can define the corresponding property density for an observable $\hat{A}$, as:

$$\rho_A(r)==\frac{N}{2}\int d\tau'\left[\Psi^{*}\hat{A}\Psi+\left(\hat{A}\Psi\right)^{*}\Psi\right] \tag{3.62}$$

and rewrite the expression for the average of a property A over an atomic basin Ω as:

$$A(\Omega)=\int_{\Omega}d\tau\rho_A(\mathbf{r}) \tag{3.63}$$

Some atomic properties calculated by the theory of atoms in molecules are presented below:

1- The atomic electron population ($N(\Omega)$) is obtained by setting $\hat{A} = \hat{1}$ in which case $\rho_A(\mathbf{r}) \rightarrow \rho(\mathbf{r})$ to yield:

$$N(\Omega) = \int_{\Omega} \rho(\mathbf{r}) d\tau \tag{3.64}$$

2- The net atomic charge ($q(\Omega)$) is calculated obviously by subtracting $N(\Omega)$ from the nuclear charge Z_Ω.

$$q(\Omega) = Z_\Omega - N(\Omega) \tag{3.65}$$

3- The atomic volume ($\upsilon(\Omega)$) is the region of space enclosed by the intersection of the bounding surface of the atom and an envelope of the charge density of some value. The commonly value used for this envelope is $\rho = 0.001$ atomic units (au).

4- The average of the radial distance of an electron from the nucleus of the atom is calculated by setting $\hat{A} = r_\Omega$:

$$r(\Omega) = \int_{\Omega} r_\Omega \rho(\mathbf{r}) d\tau \tag{3.66}$$

5- The atomic dipolar polarization ($\mathbf{M}(\Omega)$), which is also known as the first atomic electrostatic moment, is obtained by averaging the vector $\mathbf{r}_\Omega$, with the center of the coordinate system at the position of the nucleus, over the charge density of the atom:

$$\mathbf{M}(\Omega) = -e \int_{\Omega} \mathbf{r}_\Omega \rho(\mathbf{r}) d\tau \tag{3.67}$$

$\mathbf{M}(\Omega)$ is a three-dimensional vector, and it can be decomposed into its three components (x, y, z) in the following way:

$$\mathbf{M}(\Omega) = -e\int_{\Omega}\mathbf{r}_{\Omega}\rho(\mathbf{r})d\tau = \begin{pmatrix}\mathbf{M}_x\\ \mathbf{M}_y\\ \mathbf{M}_z\end{pmatrix} = \begin{pmatrix}-e\int_{\Omega}x\rho(\mathbf{r})d\mathbf{r}\\ -e\int_{\Omega}y\rho(\mathbf{r})d\mathbf{r}\\ -e\int_{\Omega}z\rho(\mathbf{r})d\mathbf{r}\end{pmatrix} \tag{3.68}$$

M (Ω) provides a measure of the extent and direction of the dipolar polarization, which in essence measures the departure from spherical symmetry of the atom in question.

3.6 Closing Remarks.

Figure 3.2 shows a summary scheme of Chapters 2 and 3.

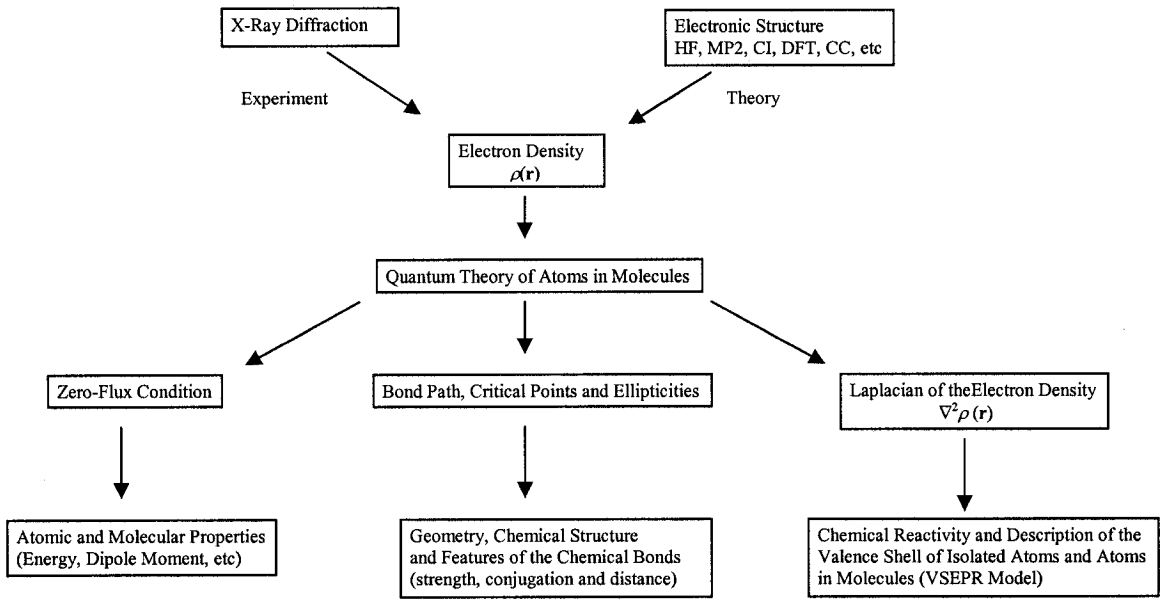

Figure 3.2 Summary scheme of Chapters 2 and 3 (taken and modified with the permission of the author from the Ph.D thesis of Dr. Chérif Matta [24]).

Chapter 4 A Theoretical Study of the Fluorine Valence Shell in Methyl Fluoride

4.1 Introduction

The chemistry of fluorine has fascinated chemists since its isolation in 1886 by Moissan after nearly 74 years of continuous effort [39]. This interesting halogen is the most electronegative element having the highest primary ionization potential (IP) and the smallest atomic radius (r_{cov}). However there is a curious anomaly between the fluorine and chlorine atoms, the electron affinity (EA) of the chlorine atom is greater than that of the fluorine atom, but fluorine is more electronegative than chlorine. This fact is rationalized in inorganic chemistry books by the small size of the fluorine atom and the resultant high concentration of charge that makes it difficult to accept another electron [40,41]. Table 4.1 summarizes these features of fluorine by providing some atomic properties of the halogen atoms [40]: the covalent or atomic radius, the ionic radius, the van der Waals radius, the ionization potential, the electron affinity and the electronegativity.

Table 4.1. Some atomic properties of the group 17 elements.

Element	r_{cov} (Å)	r_{X^-} (Å)	r_{vdw} (Å)	IP (eV)	EA (eV)	Electronegativity[a]
F	0.71	1.36	1.50	17.4	3.4	3.90
Cl	0.99	1.81	1.90	13.0	3.6	2.95
Br	1.14	1.95	2.00	11.8	3.4	2.62
I	1.33	2.16	2.10	10.4	3.1	2.52

(a) Mulliken-Jaffé values in Pauling units [40].

The quantum theory of atoms in molecules (AIM) provides a consistent framework to characterize bonding and the finer details of molecular electron density distributions [29]. The Laplacian of the electron density ($\nabla^2\rho$) plays a central role in AIM theory and yields valuable information on bonding through its topology, especially via the critical points in L ($L=-\nabla^2\rho$). As was discussed in Chapter 3, the analysis of L provides insight into many features of isolated atoms and atoms within molecules. For example, the characterization of the valence shell charge concentration (VSCC) of the fluorine atom in its compounds through AIM theory provides a simple explanation for the weakness of the F-F bond in F_2, which is explained traditionally by the repulsion between the lone-pairs of each fluorine atom [40,41]. The VSCC has also been shown to account for the geometry of the H_2F^+ ion ($\angle HFH=114^\circ$) [42] and the HF polymer ($\angle HFH=110^\circ$) [42]. Also, it explains the very high coupling constant J_{FF} that exists in compounds where the fluorine atoms are separated by more than three bonds but are close spatially. This fact is explained through the so-called through-space FF coupling [43,44,45,46].

There are several publications that describe the valence shell through AIM theory in isolated atoms [29,47,48,49] and in covalent molecules [29]. In view of the importance of fluorine, the scarcity of literature discussions on the VSCC of this element in its compounds is surprising. In their study of the topology of the Laplacian distribution of the F_2 molecule, Chan and Hamilton [50] located areas of charge concentration in the valence shell of fluorine. They also showed that bond formation has little effect on the valence shell shape of the fluorine atom. Gillespie et al. [51] in their study on fluorides of transition metals also showed charge concentration in the valence shell of fluorine. However, in each case the regions of charge concentration in the valence shell of fluorine

were not characterized as (3, -3) critical points of the negative of the Laplacian. Bader [29] discussed this anomaly of L in fluorine, which is exhibited in almost all of the cases studied so far. In fact, hydrogen fluoride is the only molecule in which Bader reports a bonded maximum in the VSCC of fluorine [29]. It is interesting that a Hartree-Fock/AIM study by Oliferenko et al. reports four (3, -3) critical points in the L topology of the fluorine atom in CH_3F, three non-bonded maxima and one bonded maximum [52]. The small basis set used by these workers (3-21G) casts doubt as to the physical reality of their findings, however.

In the light of these apparent inconsistencies, a detailed characterization of the VSCC of fluorine in CH_3F through AIM theory was carried out, with an emphasis on the global maxima in L and the critical points that link these maxima. Moreover, the VSCCs of carbon and silicon in CH_4 and SiH_4, respectively, were examined as well as nitrogen, oxygen, phosphorus, sulfur and chlorine in their methyl compounds in order to compare with the fluorine case.

4.2 Computational Details

The optimization of the molecular geometry of CH_3F and characterization of the VSCC of the fluorine atom was performed with several ab initio methods (CISD, MP2, MP3 and CCD) and the 6-311++G(2d,p) basis set. All calculations were performed with the GAUSSIAN 98 program [53].

The CISD/6-311++G(2d,p) level of theory was used to carry out the VSCC comparison with the other compounds. The location of the maxima of L and characterization of the critical points as well as the calculation of the atomic populations were carried out using

the EXTREME and PROAIM programs belonging to the AIMPAC program package [54]. The graphs were obtained by using Molden [55]. Gauss View 2.1 was used to visualize the locations of the maxima and link points.

4.3 Results and Discussion

4.3.1 Characterization of the Fluorine Valence Shell in CH_3F.

Figure 4.1 summarizes some of the main results for CH_3F. The most heavily shaded regions in Figure 4.1(a) represent the areas of charge concentration in a HCF plane. Figure 4.1(b) shows a graphical representation of the non-bonded maxima (indicated by small lines) and link points (indicated by dots) on fluorine. Figure 4.1(c) shows a three-dimensional plot of L in a HCF plane.

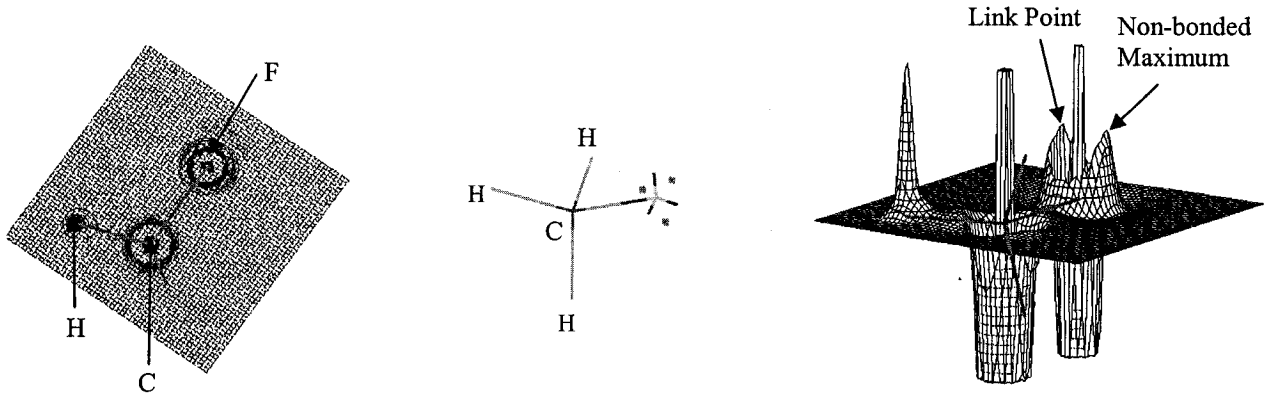

Figure 4.1. Characterization of the fluorine valence shell in CH_3F.
(a) Contour map of L in a HCF plane.
(b) Graphical representation of the maxima (indicated by small lines) and link points (indicated by dots) on fluorine.
(c) Relief plot of L in a HCF plane.

As can be seen in Figure 4.1(b), the maxima in the VSCC of the fluorine atom assume a tetrahedral spatial arrangement. Moreover the optimized structure is a staggered conformation, corresponding to less interaction between the maxima of L and the carbon-hydrogen bonds. The link points are eclipsed with respect to the hydrogen atoms. These results are consistent with the VSEPR model [42].

Table 4.2 provides the distances of the maxima and the link points to the fluorine atom (the radius) as well as the electron density (ρ) and the negative of the Laplacian at the maxima and at the link points for the fluorine atom in CH_3F as computed with four levels of theory. There are no appreciable differences between the three maxima and between the three link points and, therefore, we only report the maximum and the link point of L indicated in Figure 4.1(c).

Table 4.2. Characterization of non-bonded maxima (non-bonded charge concentrations) and link points for the VSCC of fluorine in CH_3F by several ab initio methods with the 6-311++G(2d,p) basis set.

Method	Non-bonded maxima			Link points		
	r (Å)	$-\nabla^2\rho$ (au)	ρ (au)	r (Å)	$-\nabla^2\rho$ (au)	ρ (au)
CISD	0.3028	9.468	1.4954	0.3028	9.421	1.4940
CCD	0.3027	9.474	1.4954	0.3028	9.428	1.4941
MP2	0.3027	9.477	1.4953	0.3028	9.432	1.4940
MP3	0.3028	9.472	1.4954	0.3028	9.426	1.4941

As can be seen in Table 4.2, the four methods yield remarkably similar results. This is another example of the well-documented insensitivity of AIM analysis to the level of theory [29]. The non-bonding surface of maximum concentration of charge in the VSCC of fluorine in CH_3F can be considered as a hemisphere of radius 0.303 Å with an almost

constant value of $\nabla^2\rho$ and ρ on its surface. This negligible distortion of the VSCC of fluorine induced by bonding is consistent with the findings of Chan and Hamilton about the distortion of the fluorine VSCC by the formation of the F_2 molecule [50].

The CH_3F results are anomalous in the sense that there is no bonded maximum in the fluorine VSCC (it has only been reported for the HF molecule [29]). To appreciate this point it is helpful to consider the results for CH_3Cl, in which a bonded maximum of the chlorine VSCC lies on the line joining chlorine and carbon. This position for the bonded maximum is consistent with the simple picture presented by the VSEPR model because it minimizes the interaction with the non-bonded electron pairs. A unique feature of CH_3F is the presence of a (3, +1) critical point in the fluorine VSCC on the direct line that joins fluorine and carbon, 0.336 Å from F with L=3.51 au and ρ=1.059 au. The distances between nitrogen and oxygen and their bonded maxima in CH_3NH_2 and CH_3OH, respectively, are greater by 0.045 Å and 0.041 Å than the distances between oxygen and nitrogen and their non-bonded maxima. This fact suggests a difference in the fluorine case around 0.036 Å. Hence, this (3, +1) critical point is located approximately at the expected position for the bonded maximum of the fluorine VSCC. The eigenvector analysis shows that the eigenvector with a negative eigenvalue (which indicates that L is a maximum in this direction) is on the line that joins fluorine and carbon. Therefore, L is a minimum in both perpendicular directions to this line. Figure 4.2 characterizes the (3,+1) critical point of the fluorine VSCC in CH_3F with respect to the eigenvector directions. Figure 4.2(a) shows a graphical representation of CH_3F and Figure 4. 2(b) illustrates the location of the (3,+1) point and the eigenvector directions.

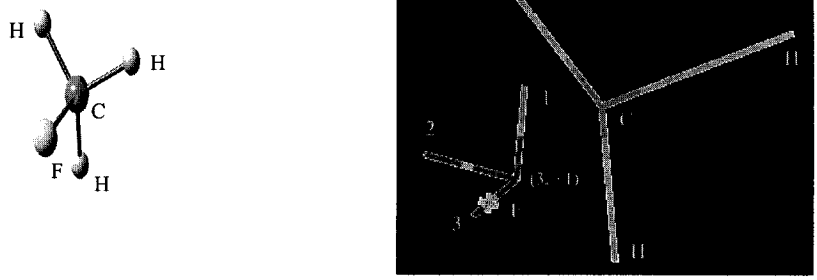

(a) (b)

Figure 4.2. Characterization of the (3,+1) critical point of the fluorine valence shell in CH_3F with respect to eigenvector directions.
(a) Molecular graph of CH_3F.
(b) Locations and directions of the eigenvectors at the (3,+1) critical point in L. Eigenvector 3 has a negative eigenvalue.

The AIM results are insensitive to the level of theory and therefore, appreciable changes in the VSCC of fluorine at even higher levels of theory are not expected. For a bonded maximum to appear in the VSCC of fluorine in CH_3F, link points on the ∇L trajectories that link the bonded maximum with the non-bonded maxima must also exist. The VSCC of fluorine is very compact and characterized by large charge concentration and electron density and therefore it lacks the flexibility required for the appearance of these necessary link points on the ∇L trajectories. Thus, a (3, +1) critical point will be found instead of a bonded maximum because it will be a maximum in the line that connects fluorine and carbon, but it will be a minimum in the perpendicular directions to this line. These perpendicular directions are tangents to the ∇L trajectories that connect this (3,+1) critical point with the non-bonded maxima (Figure 4.2).

4.3.2 VSCC Comparison.

Figure 4.3 summarizes results for CH_4, CH_3NH_2, CH_3OH, CH_3PH_2, CH_3SH and CH_3Cl. The most heavily shaded regions in Figure 4.3(a) represent the areas of charge concentration, the outer one being the valence shell charge concentration (VSCC). Figure 4.3(b) shows a graphical representation of the non-bonded maxima of L topology indicated by small lines and Figure 4.3(c) shows the link points in a HCX plane. The three-dimensional plot of L in a HCX plane Figure 4.3(c) indicates the locations of bonded and non-bonded maxima as well as the locations of the link points.

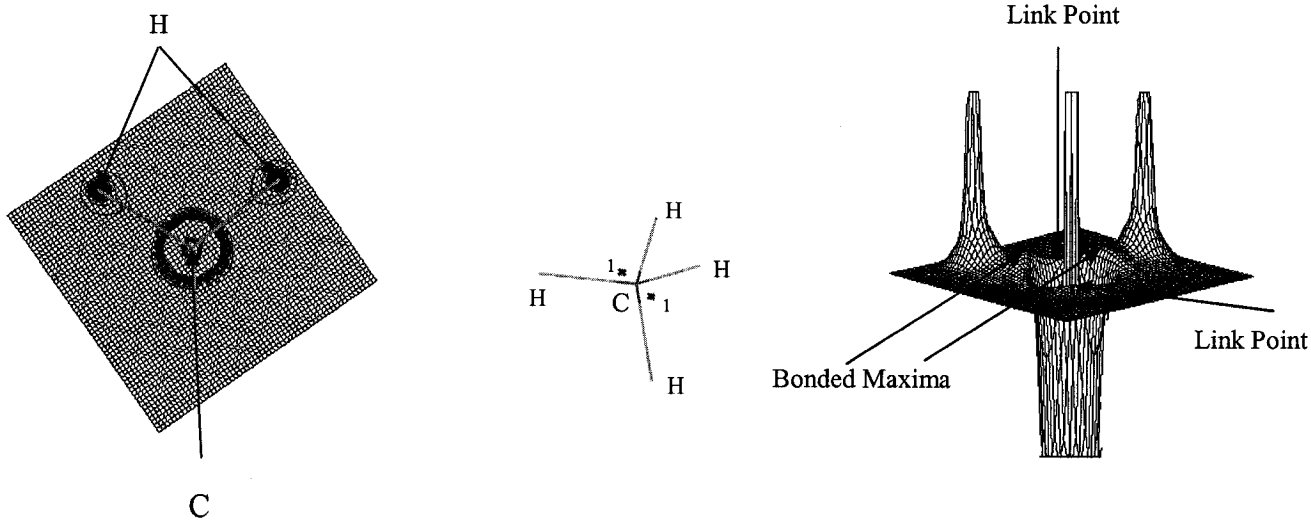

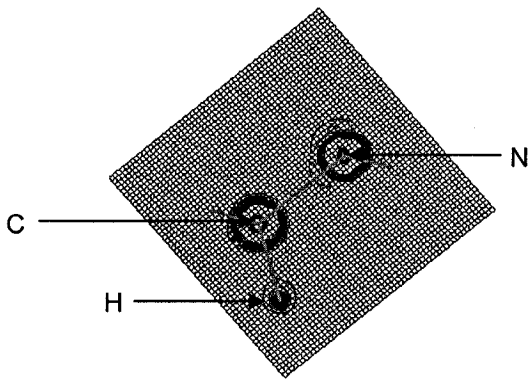
N
C
H

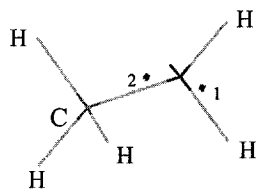
H
H
C
H
H
2
1

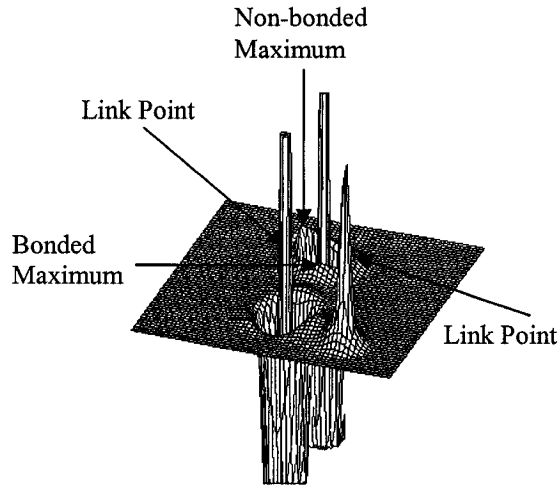
Non-bonded
Maximum
Link Point
Bonded
Maximum
Link Point

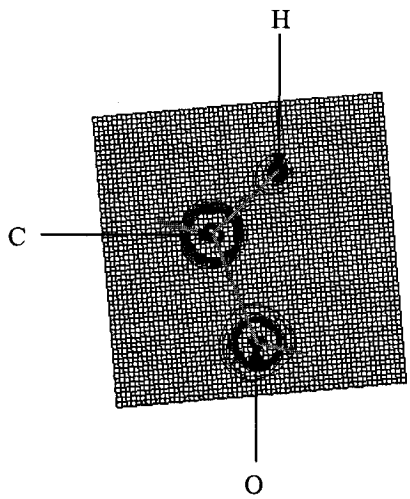
H
C
O

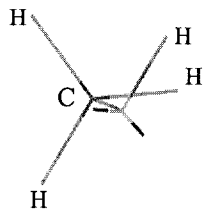
H
H
C
H
H

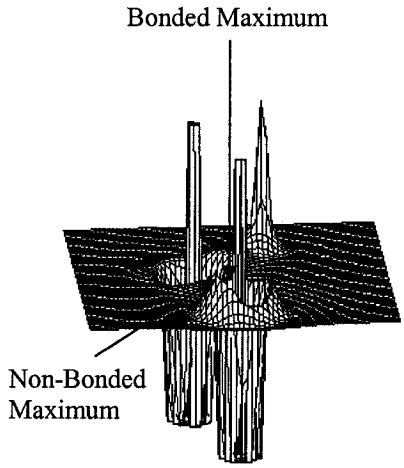
Bonded Maximum
Non-Bonded
Maximum

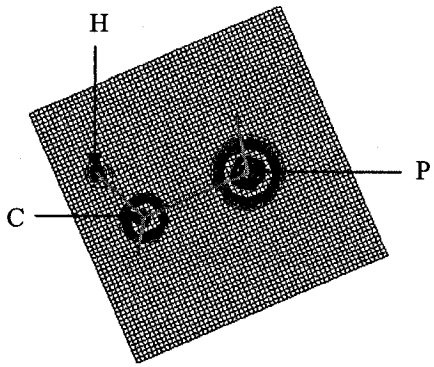
H
C
P

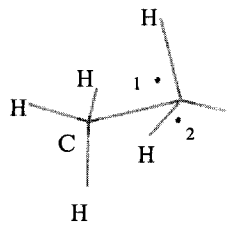
H
H
H
C
H
H
1
2

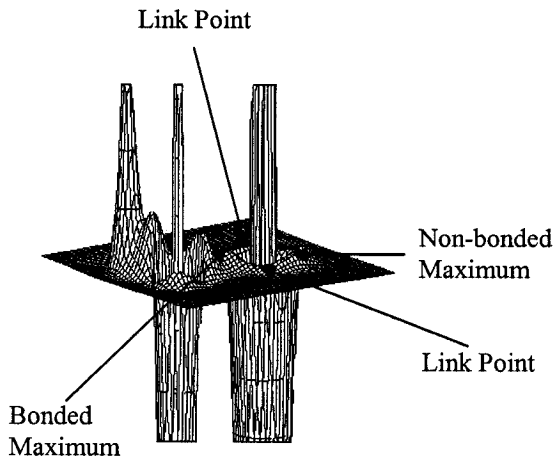
Link Point
Non-bonded
Maximum
Link Point
Bonded
Maximum

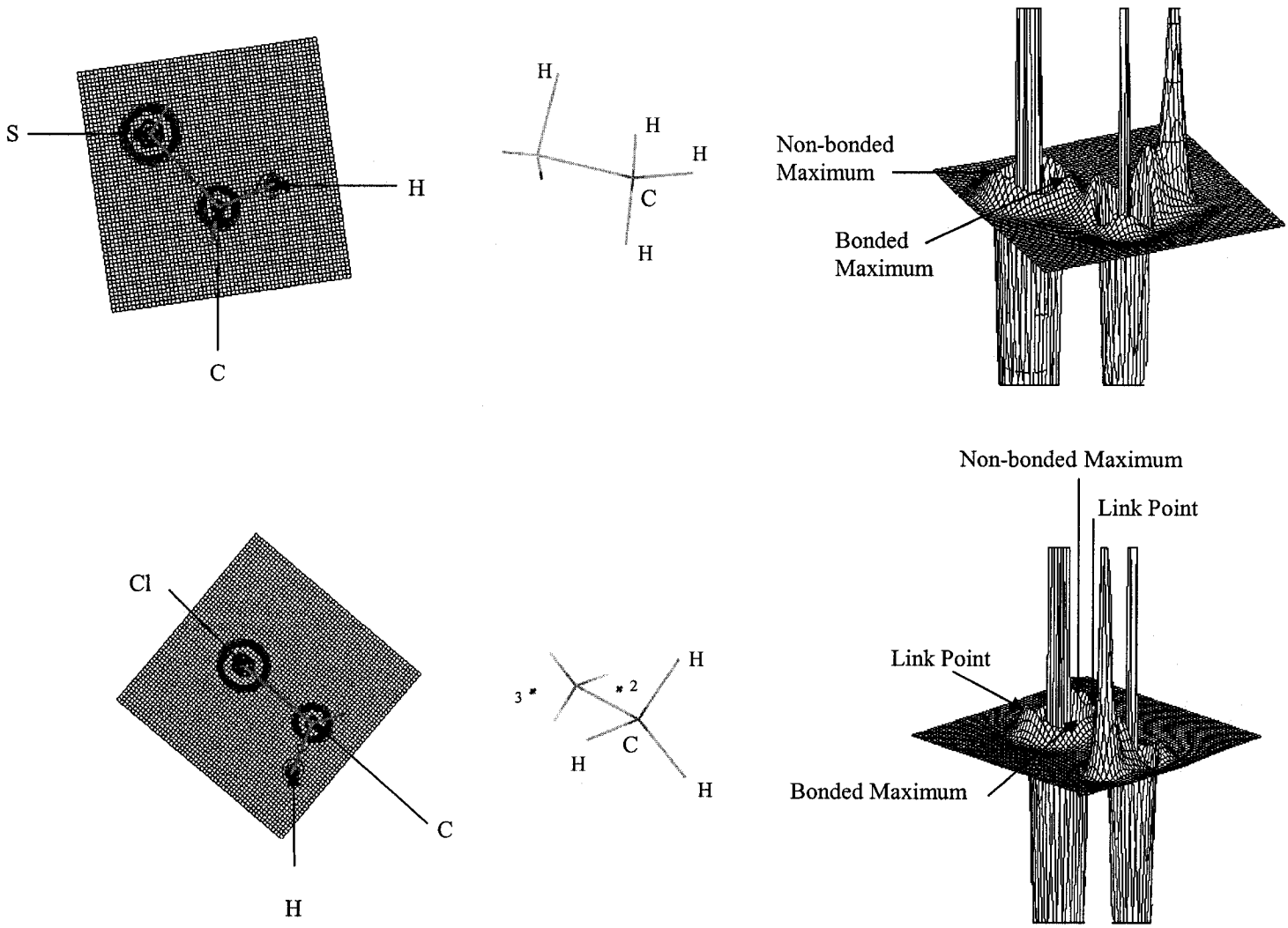

Figure 4.3. Characterization of the valence shells of carbon, nitrogen, oxygen, phosphorus, sulfur and chlorine in CH_3X, where X=H, NH_2, OH, PH_2, SH and Cl.

(a) Contour map of L in a HCX plane.

(b) Graphical representation of the non-bonded maxima indicated by small lines, the bonded maxima are on the lines that connect the atoms. Graphical representation of the link points in a HCX plane that are shown in part (c):

1- links two bonded maxima.

2- links one bonded maximum and one non-bonded maximum.

3- links two non-bonded maxima.

(c) Three-dimensional plot of L in a HCX plane.

All the optimized structures shown in Figure 4.3(b) are staggered conformations, which minimize the interaction between the maxima and the hydrogen-carbon bonds. In the figure, the link points are minima of L in the line that connects two maxima, and maxima in the two perpendicular directions to this line. Therefore, the locations of the link points must represent the least electrostatic interaction with the other maxima in the system. Figure 4.3 shows that all the compounds exhibit two link points in the HCX plane except CH_3OH and CH_3SH. Because of the symmetry of CH_4, CH_3NH_2, CH_3PH_2 and CH_3Cl molecules, the link points in the HCX plane minimize the interaction with the rest of the bonded and non-bonded maxima (bonded and non-bonded electron pairs). In the cases of CH_3OH and CH_3SH, the link points were not found in the HCX plane because it does not represent the least electrostatic interaction with the bonded maximum directed toward the hydrogen atom and the non-bonded maximum. All these results are consistent with the VSEPR model as was also shown in the CH_3F case.

Tables 4.3 and 4.4 describe VSCC of carbon, nitrogen, oxygen, fluorine, phosphorus, sulfur and chlorine atoms at the CISD/6-311++G(2d,p) level in their respective compounds. Table 4.3 provides the radius and area of the maxima, the angles between them as well as the negative of the Laplacian and ρ values at the maxima for the compounds (the calculation of area between maxima is very well explained in page 266 of Bader's book [29]). Table 4.4 describes all the found link points for the same compounds in terms of distances to the nucleus, ρ and $-\nabla^2\rho$

Table 4.3. Characterization of bonded maxima and non-bonded maxima for the VSCCs of nitrogen, oxygen, fluorine, silicon, phosphorus, sulfur and chlorine atoms by CISD/6-311++G(2d,p) in CH_3X.

CH_3-X													
	Bonded maxima (b)							Non-bonded maxima (nb)					
X	# b	r (Å)	ρ (au)	$-\nabla^2\rho$ (au)	Angle (°) < bAb	Area (Å^2)	Angle (°) < bAnb	#nb	r (Å)	ρ (au)	$-\nabla^2\rho$ (au)	Angle (°) < nbAnb	Area (Å^2)
H	4[a]	0.528	0.295	1.23	109.5[c]	0.740							
NH_2	2[a]	0.437	0.476	2.12	107.6[ac]	0.504[a]	111.1[ac]	1	0.392	0.579	2.87		0.414[d]
	1[b]	0.436	0.442	1.67	108.3[abc]	0.503[b]	110.3[b]						
OH	1[a]	0.378	0.735	3.16	105.2[ab]	0.355[a]	105.6[ac]	2	0.341	0.968	5.62	130.6	0.327
	1[b]	0.380	0.690	2.53		0..353[b]	103.8[bc]						
F	NOT FOUND							3	0.303	1.495	9.47	116.1[c]	0.251
PH_2	CHARGE TRANSFER							1	0.760	0.136	0.36		1.653
	1[b]	0.815	0.155	0.33	98.3[c]	1.610	119.7						
SH	1[a]	0.760	0.222	0.68	102.2	1.393	105.9[ac]	2	0.685	0.202	0.63	129.7	1.343
	1[b]	0.727	0.194	0.46		1.282	106.4[bc]						
Cl	1[b]	0.661	0.248	0.57	104.8[c]	1.070		3	0.626	0.276	0.88	113.7[c]	1.064

a- Bonded charge concentration between the heavy atom and hydrogen.
b- Bonded charge concentration between the heavy atom and carbon.
c- Average angle
d- The area was calculated by assuming the bonded maximum (not found) lies on the direct line between fluorine and carbon.
e- As the VSCC of the phosphorus does not exhibit a bonded maximum in the P-H bond at this level of theory, the angles and area of the charge concentrations were calculated by assuming imaginary bonded maxima on the direct line between phosphorus and each hydrogen.

Table 4.4. Characterization of the link points for the VSCC of nitrogen, oxygen, fluorine, phosphorus, sulfur and chlorine atoms by CISD/6-311++G(2d,p).

CH_3-X				
Link Points				
X	# L	r_A (Å)	ρ (au)	$-\nabla^2\rho$ (au)
H	4	0.521	0.207	0.19
NH_2	1[b]	0.420	0.452	1.38
	1[c]	0.423	0.438	1.35
	1[d]	0.429	0.418	0.87
	2[e]	0.430	0.412	0.87
OH	1[a]	0.345	0.898	4.55
	2[b]	0.369	0.754	2.91
	2[c]	0.378	0.694	2.52
	1[e]	NOT FOUND		
F	3[a]	0.303	1.494	9.42
PH_2	1[c]	0.802	0.095	0.08
SH	1[a]	0.697	0.172	0.41
	2[b]	0.714	0.164	0.26
	2[c]	0.714	0.162	0.27
	1[e]	NOT FOUND		
Cl	3[a]	0.627	0.275	0.86
	3[c]	0.652	0.227	0.40

a- Link point between non bonded charge concentrations.
b- Link point between hydrogen bonded charge concentration and non-bonded charge concentration.
c- Link point between carbon bonded charge concentration and non-bonded charge concentration.
d- Link point between hydrogen bonded charge concentration and hydrogen bonded charge concentration.
e- Link point between hydrogen bonded charge concentration and carbon bonded charge concentration.

As can be seen in Table 4.3, the fluorine atom presents the smallest radius of the non-bonded maxima. It also presents the highest values of the negative of the Laplacian and ρ, being almost twice the negative of the Laplacian and ρ values of the oxygen atom that has the second highest. These results are expected; it is well known experimentally that fluorine is the smallest atom of the atoms considered herein [40,41], and as a consequence it has a large concentration of charge in its valence shell. The angle analysis

shows the tetrahedral form of the valence shell of the fluorine atom and the rest of the analyzed elements in their respective compounds.

The analysis of maxima and link points serves to characterize the distortion of the VSCC by the formation of a bond. As was seen in the above section, the maxima and link points in the fluorine valence shell in CH_3F present very similar radii, ρ and $-\nabla^2\rho$ values. Otherwise, the VSCC of carbon is considerably perturbed by the formation of the four hydrogen carbon bonds and is very far from the spherical surface of constant values of ρ and $-\nabla^2\rho$ that exist in the isolated carbon atom [29]. The non-bonded part of the VSCC of chlorine in CH_3Cl is close to a sphere of constant ρ and $-\nabla^2\rho$ on its surface. It is similar to that of fluorine in shape but considerably larger in radius and is approximately one order of magnitude lower in ρ and $-\nabla^2\rho$. Generalizing, the distortion of the VSCC due to the bond formation decreases in the order of carbon, nitrogen, oxygen and fluorine in the second period of the periodic table, and in the order of silicon, phosphorus, sulfur and chlorine in the third period of the periodic table.

As an aside, it should be noted that transfer of charge from phosphorus to hydrogen was found in CH_3PH_2. This result is not expected because charge transfer in PH_3 at the HF/6-21G(d,p) level is not observed [29]. However, a calculation on PH_3 at the CISD/6-311++G(2d,p) level was carried out and yielded the same behavior as in the CH_3PH_2 case. The transfer of charge from phosphorus toward hydrogen connected to phosphorus is noted by a large value of atomic population in these hydrogen atoms ($N_H(\Omega)$ =1.602) and by the lack of bonded maxima between phosphorus and hydrogen atoms. This result is consistent with the fact that PH_3 is a strong reducing agent [41].

Finally, it is important to note that all attempts to reproduce the results of Oliferenko [52] were unsuccessful. In particular, bonded maxima in the fluorine VSCC of CH_3F were not located (Table 4.5).

Table 4.5. Characterization for the fluorine VSCC in CH_3 in terms of charge concentrations (bonded and non-bonded maxima) and link points at the HF/3-21G, HF/6-31++G(d,p) and MP2/6-311++G(2d,2p) levels of theory.

	Non-bonded maxima			Link Points		
	r_{max} (Å)	$-\nabla^2\rho$ (au)	ρ (au)	r_{max} (Å)	$-\nabla^2\rho$ (au)	ρ (au)
HF/3-21G	0.301	7.64	1.50	0.301	7.63	1.50
HF/6-31++G(d,p)	0.293	11.65	1.56	0.293	11.61	1.56
MP2/6-311++G(2d,2p)	0.303	9.48	1.50	0.303	9.43	1.49

4.4 Conclusions

The valence shell charge concentration (VSCC) of fluorine in CH_3F has been characterized by AIM theory at several levels of theory. The AIM results are remarkably insensitive to the level of theory (CISD, CCD, MP2 and MP3). The fluorine VSCC exhibits three clearly defined non-bonded maxima in L. Analysis of the angles indicates a tetrahedral form for these maxima and it supports the geometric structures of H_2F^+ ion and HF polymer. The link points are at the same distance from the nucleus as the maxima with almost the same ρ and $-\nabla^2\rho$ values. The non-bonding surface of maximum concentration of charge in the VSCC of fluorine in CH_3F can be considered to be a semi-sphere of constant electron density and charge concentration. Therefore, it can be stated that the formation of the carbon-fluorine bond in CH_3F has little effect on the fluorine VSCC.

Instead of finding a bonded charge concentration in CH_3F, a (3, +1) critical point in L approximately localized at the expected position for the bonded charge concentration was found. This is contrary to an earlier report [52]. On the other hand, the locations of the maxima and link points are consistent with the VSEPR model in all the analyzed compounds, including the (3,+1) critical point in the fluorine VSCC.

The fluorine VSCC is the most compact, with considerably larger values of ρ and $-\nabla^2\rho$ than the other atoms. These observations are consistent with the suggestion that the surprisingly long bond in the F_2 molecule is due to the strong electrostatic interaction that exists between the non-bonded electron pairs (non-bonded maxima) of the two fluorine atoms. Also, this characterization supports the lower electron affinity of fluorine relative chlorine. The chlorine VSCC is larger with lower values of ρ and $-\nabla^2\rho$ than that of fluorine, which makes the acceptance of an electron easier. Finally, this characterization of the fluorine VSCC supports the explanations given for the so-called through-space FF coupling where the coupling between the fluorine atoms depends on the locations of the electron pairs on the fluorine atoms.

Chapter 5 Fluorine-Fluorine Spin-Spin Coupling Constants in Aromatic Compounds: Correlations with the Delocalization Index and with the Internuclear Separation

5.1 Introduction

In view of its importance in the elucidation of long-range interactions in organic and bioorganic rigid molecules (see, for example, Gakh et al. [56] and references therein), the fluorine-fluorine coupling constant (J_{FF}) is a particularly interesting property to calculate. In general, the Fermi contact interaction is the dominant mechanism by which spin information is transmitted between nuclei with spin I=½ (such as ^{1}H, ^{13}C, ^{15}N and ^{19}F) and thus determines, in large part, the magnitude of their *J*-coupling interaction (also known as scalar spin coupling) [57,58,59]. The electron density at or near such a nucleus is perturbed to favor an antiparallel orientation of electron spins with respect to the spin of the nucleus. In other words, near a spin ½ nucleus, there is a net excess of α- or β-spin density. This spin information is then transmitted through space by means of the mechanism of exchange which embodies the Pauli exclusion principle. When a second nucleus senses this perturbation in its immediate vicinity, it responds by adopting either a parallel or antiparallel orientation which differs in energy and thus leads to an energy splitting observed as the *J*-coupling constant. The coupling constant can be positive or negative depending on whether the state with antiparallel or parallel nuclear spins is the lower in energy, respectively.

In general, the calculation of *J*-coupling constants is not trivial [60,61,62]. The prediction of NMR properties, especially coupling constants, usually requires very large basis sets with at least triple-zeta quality and supplemented with diffuse and polarization functions.

One important factor to consider is the behavior of the basis set near and at the nuclei, since that is where the Fermi contact interaction takes place. The electron density exhibits marked maxima at the positions of the nuclei, maxima that constitute cusps if one neglects the finite nuclear size, as is the common practice in quantum chemistry. The presence of nuclear cusps poses a challenge to contracted Gaussian basis functions and necessitates the use of a large number of primitives and/or the use of Slater-type basis functions. This problem is encountered specifically in the calculation of spin-spin coupling and does not arise, for instance, in the calculation of nuclear shielding constants [60]. The convergence of spin-spin coupling constants with the extension of the basis set has been analyzed at the multiconfigurational self-consistent-field level for HF and H_2O. It was found that only correlation-consistent basis sets augmented with tight *s* functions converge smoothly and yield accurate indirect nuclear spin-spin couplings [63]. Additional challenges arise from the high computational costs associated with the calculation of the other interactions contributing to the scalar coupling constant, namely, the paramagnetic spin-orbit, diamagnetic spin-orbit, and spin-dipolar interactions [60,61,62].

The calculation of the coupling constants involving fluorine is generally more problematic than for other nuclei in view of the possible relative importance of contributions other than the Fermi contact interactions in some of its compounds [64,65,66]. These difficulties led several groups to propose empirical approaches for the fast estimation of *J*-coupling constants such as J_{FF} correlations with distance [67,68] or with properties derived from the topology of the electron density [69]. The primary goal of this chapter is to describe an alternative empirical model, but with foundations in

physics, which has the potential to provide a fast prediction of the J_{FF} coupling constants. The standard Pople basis sets that behave well *on average* (as opposed to specifically at the position of the nuclei) are used, and thus a major problem in the calculation of spin-spin coupling constants is circumvented.

5.2 Theory of Delocalization of Electrons

The extent of spatial localization or delocalization of electrons has long been known to be determined by the Fermi hole [70]. The Fermi hole is the physical manifestation of the Pauli exclusion principle, it measures the extent of same-spin density exclusion at a point $\mathbf{r}_2$ given a reference electron present at $\mathbf{r}_1$ [70]. If the density of the Fermi hole is localized near the reference point, then all other same-spin electrons are excluded from this region, and the reference electron is *localized* at $\mathbf{r}_1$. In contrast, if the Fermi hole is spread into a region around $\mathbf{r}_2$ far from $\mathbf{r}_1$, the location of the reference electron, then there is a significant reduction in the probability of finding other same-spin electrons in the vicinity of $\mathbf{r}_2$, which implies that the reference electron is "smeared" or *delocalized* between $\mathbf{r}_1$ and $\mathbf{r}_2$. In Hartree-Fock (H-F) theory the Fermi hole is equal to the exchange density (the quantity in the curly brackets in equation 5.1) divided by the corresponding spin-density $\rho^{\sigma}(\mathbf{r})$. Thus, the Fermi hole is given by [68]:

$$h^{\sigma}(\mathbf{r}_1,\mathbf{r}_2) = -\sum_i \sum_j \left\{ \phi_i^*(\mathbf{r}_1)\phi_j(\mathbf{r}_1)\phi_j^*(\mathbf{r}_2)\phi_i(\mathbf{r}_2) \right\} / \rho^{\sigma}(\mathbf{r}_1) \qquad (5.1)$$

where $\sigma = \alpha$ or β, the double-sum runs over σ-spin orbitals ϕ. The Fermi hole, when integrated over all space of the second electron, yields -1e corresponding to the complete removal of one electronic charge. At $\mathbf{r}_1=\mathbf{r}_2$ this quantity reduces to $-\rho^{\sigma}(\mathbf{r}_1)$ and thus excludes same-spin density from the position of electron 1. When the exchange density

$(\rho^{\sigma}(\mathbf{r}_1)h^{\sigma}(\mathbf{r}_1,\mathbf{r}_2))$ is integrated over all space with respect to the coordinates of both electrons it yields $-N^{\sigma}$, the negative of the total number of σ-electrons, i.e., the total Fermi correlation of σ-spin electrons. If now the integration is performed over a bounded region of space, it will yield the total Fermi correlation within this region denoted by $F^{\sigma}(A,A)$ and given by [70]:

$$\begin{aligned} F^{\sigma}(A,A) &= \int_A d\mathbf{r}_1 \int_A d\mathbf{r}_2 \rho^{\sigma}(\mathbf{r}_1) h^{\sigma}(\mathbf{r}_1,\mathbf{r}_2) \\ &= -\sum_i \sum_j \int_A d\mathbf{r}_1 \int_A d\mathbf{r}_2 \left\{ \phi_i^*(\mathbf{r}_1)\phi_j(\mathbf{r}_1)\phi_j^*(\mathbf{r}_2)\phi_i(\mathbf{r}_2) \right\} \\ &= -\sum_i \sum_j S_{ij}^{\,2}(A) \end{aligned} \tag{5.2}$$

where $S_{ij}(A)=S_{ji}(A)$ denotes the overlap of a pair of spin orbitals over a region A. The limiting value of $F^{\sigma}(A,A)$ is $-N^{\sigma}(A)$, the negative of the σ-spin population of A, implying a complete localization of N σ-electrons within A since these electrons do not exchange with electrons outside A. The total number of electrons localized within A is called the *localization index*, λ(A), and is given by [71]:

$$\lambda(A) = \left|F^{\alpha}(A,A)\right| + \left|F^{\beta}(A,A)\right| \tag{5.3}$$

The limit of total localization, where the localization index equals the total electron population contained within A, i.e., $\lambda(A)= N(A)$, can never be reached as the electrons will always be delocalized to some extent outside of region A.

The measure of electron delocalization from region A to region B is determined by [71]:

$$\begin{aligned} F^{\sigma}(A,B) &= \int_A d\mathbf{r}_1 \int_B d\mathbf{r}_2 \rho^{\sigma}(\mathbf{r}_1) h^{\sigma}(\mathbf{r}_1,\mathbf{r}_2) \\ &= -\sum_i \sum_j \int_A d\mathbf{r}_1 \int_B d\mathbf{r}_2 \left\{ \phi_i^*(\mathbf{r}_1)\phi_j(\mathbf{r}_1)\phi_j^*(\mathbf{r}_2)\phi_i(\mathbf{r}_2) \right\} \\ &= -\sum_i \sum_j S_{ij}(A)\, S_{ji}(B) \end{aligned} \tag{5.4}$$

in which it is clear that $F^{\sigma}(A,B)=F^{\sigma}(B,A)$. The total extent of exchange between two regions A and B is given by the delocalization index $\delta(A,B)$ which measures the number of electron pairs shared between A and B and which is given by [71]:

$$\delta(A,B) = 2\left|F^{\alpha}(A,B)\right| + 2\left|F^{\beta}(A,B)\right| \tag{5.5}$$

When these ideas are used in conjunction with the theory of atoms in molecules (AIM), a theory which defines atomic regions (basins) in a molecule unambiguously, one can then quantify localization of electrons within an atom or between two atoms in a molecule [71]. The AIM theory is well-known and has been extensively reviewed in Chapter 3. Here it is sufficient to recap that the quantum condition defining the boundary of an atomic basin in a molecule is given by $\nabla\rho(\mathbf{r})\cdot\mathbf{n}(\mathbf{r}) = 0$ for all $\mathbf{r}$ on the surface [29] where $\nabla\rho(\mathbf{r})$ is the gradient of the electron density ρ, and $\mathbf{n}(\mathbf{r})$ is a vector normal to the surface.

The relationship between the hydrogen-to-hydrogen delocalization index δ(H,H) and the experimental proton-proton spin–coupling constants (J_{HH}) has been recently investigated [72]. It has been shown that J_{HH} is linearly correlated with δ(H,H). The theoretical basis for this correlation is the proportionality of δ(H,H) determined over the volume of two *hydrogen atoms* to the product of the electron spin densities at the positions of the two *protons,* a product proportional to the coupling constant. Thus, the expression relating the Fermi contact contribution to the coupling constant between two nuclei $J_{nn'}$ to the exchange between the positions of the two nuclei is given by [73]:

$$J_{nn'} = -\frac{2}{3h}\left(\frac{16\pi\beta\hbar}{3}\right)^2 \gamma_n \gamma_{n'} \frac{1}{\Delta E} \sum_i \sum_j \left\langle \phi_i(\mathbf{r}_1)\delta(\mathbf{r}_{1n})\phi_j(\mathbf{r}_1)\right\rangle \left\langle \phi_j(\mathbf{r}_2)\delta(\mathbf{r}_{2n'})\phi_i(\mathbf{r}_2)\right\rangle \tag{5.6}$$

in standard notation, where $\delta(\mathbf{r}_{kn})$ is a Dirac δ function which picks out the value at $\mathbf{r}_{kn}=0$, i.e., at the position of nucleus n, in any integration over the coordinates of the k^{th} electron.

The contribution described by equation 5.6 is termed the "contact term" because it is evaluated at the nuclei [73].

If, as in the case of hydrogen, one assumes that density at a fluorine nucleus is, on average, proportional to the density within the basin of the fluorine atom one can then write [72]:

$$\left\langle \phi_i(\mathbf{r}_1)\delta(\mathbf{r}_{1n})\phi_j(\mathbf{r}_1)\right\rangle\left\langle \phi_j(\mathbf{r}_2)\delta(\mathbf{r}_{2n'})\phi_i(\mathbf{r}_2)\right\rangle \propto \left\langle \phi_i(\mathbf{r}_1)\phi_j(\mathbf{r}_1)\right\rangle_{\mathrm{F}}\left\langle \phi_j(\mathbf{r}_2)\phi_i(\mathbf{r}_2)\right\rangle_{\mathrm{F'}} \equiv S_{ji}(\mathrm{F})S_{ij}(\mathrm{F'}). \tag{5.7}$$

Expression 5.7 is a reasonable approximation in the case of proton spin-spin coupling since the basin of the hydrogen atom is primarily described by spherically symmetric *s*-functions, which is not the case for the fluorine atom. Thus, there is no *a priori* reason to assume that equation 5.7 will apply to fluorine or to any atom other than hydrogen. Quite to the contrary, one would expect that the approximation in equation 5.7 will generally fail for non-hydrogen atoms due to the presence of basis functions with non-zero angular momentum in a primary (rather than polarizing) role. These non-zero angular momentum functions increase the contributions of the other terms responsible for the *J*-coupling, namely, the paramagnetic spin-orbit, the diamagnetic spin-orbit, and the spin-dipolar interactions. It is therefore quite surprising that the approximation in equation 5.7 appears to hold for fluorine-fluorine coupling, as will be shown phenomenologically in this chapter.

The correlation between the experimental $J_{\mathrm{FF'}}$ and δ(F,F') was studied for the 30 aromatic fluorine derivatives (and 35 coupling constants) shown in Figure 5.1.

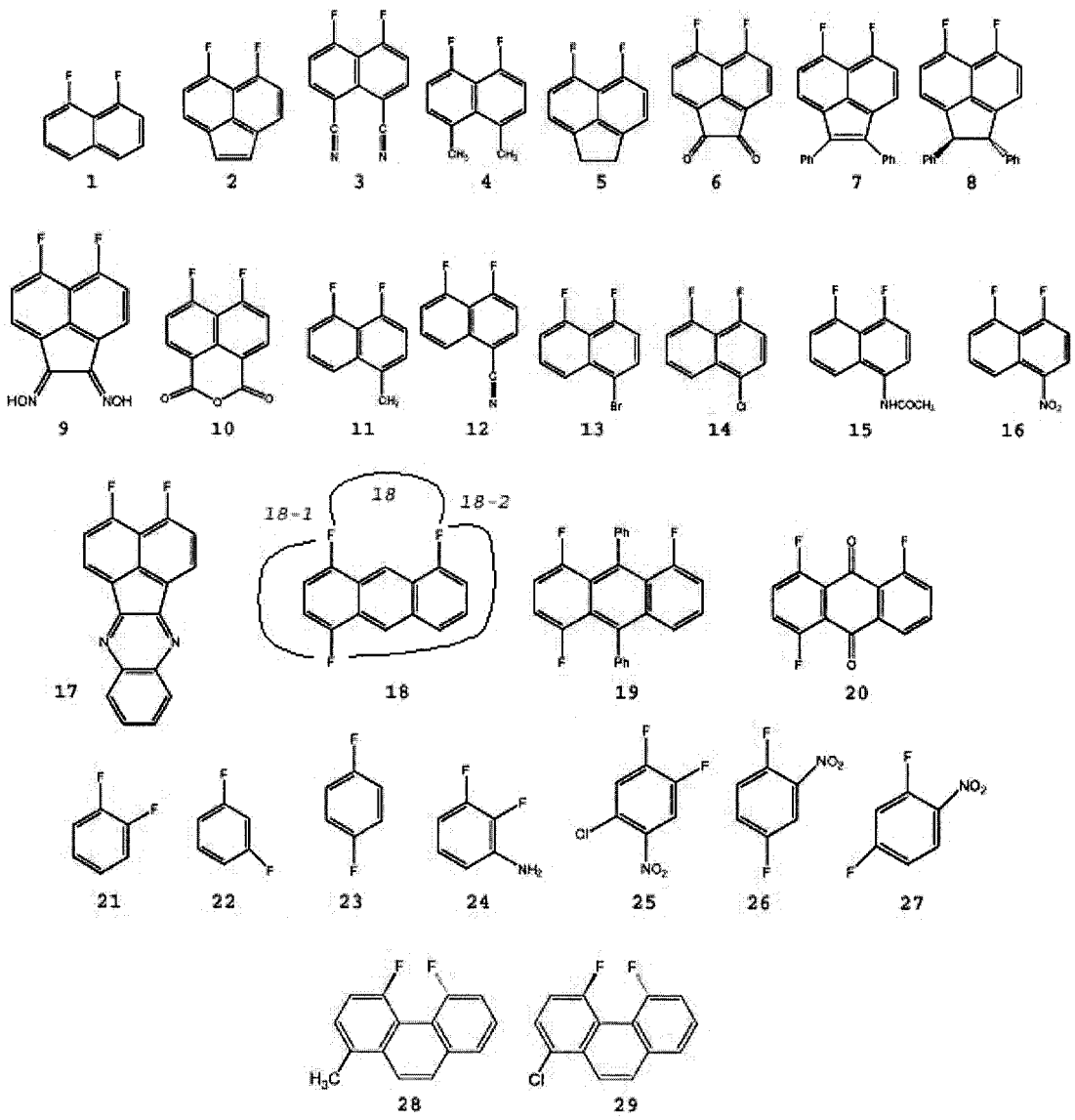

Figure 5.1. Chemical structures of the compounds constituting the data set employed in this study. For compounds (**18-20**), the three different F-F coupling interactions exist. These are labeled on the chemical structure of compound **18** in italics, and the same labeling convention applies to compounds **19** and **20**. The labeling of these interactions corresponds to that used in Table 5.1.

While strictly speaking, the above formalism only acquires physical meaning within the context of HF theory and can be readily extended to configuration interaction (CI) theories [71], delocalization indexes calculated from Kohn-Sham (KS) orbitals [74] are used herein. It has been shown on a number of occasions that delocalization indexes obtained using KS orbitals exhibit similar numerical values and trends as those obtained from HF and are systematically slightly higher than those obtained from CI wavefunctions. (See Poater et al. [75] and references therein).

5.3 Computational Details

The geometries of all molecules have been fully optimized at the B3LYP/6-31G(*d*) level. Single-deterimant KS "wavefunctions" were obtained at the B3LYP/6-311++G(*d*,*p*)//B3LYP/6-31G(*d*) level. The resulting wavefunctions were then integrated using the PROAIM suite of programs [54] to obtain the atomic overlap matrices, which were then processed using AIMDELOC [76] to obtain the delocalization indexes. All electronic structure calculations were performed using the Gaussian 03 package [53]. Statistical analyses were carried out using the Minitab [77] and the Origin [78] packages.

5.4 Results and Discussion

Large spin-spin coupling between two fluorine atoms separated by more than three bonds but which are spatially close is known as "through space coupling". Ernst and Ibrom proposed that the magnitude of J_{FF} is related to the distance of separation of the two coupled fluorine atoms in a simple way [67]:

$$J_{FF} \approx a\, e^{b\, d_{FF}} \tag{5.8}$$

where a and b are the fitting constants, and b<0. Mallory and coworkers [68] reported a strong correlation (r^2=0.991) of the form of equation 5.8 for several 1,8-difluoronaphthalenes. These workers included 13 data points in the fitting, all chosen from a set of 18 closely related derivatives of 1,8-difluoronaphthalenes. Significantly, however, five compounds which could not be fitted to the above equation were excluded from the fitting. The authors argue that the origin of this correlation is the sidewise overlap of the fluorine 2p orbitals [68]. (See also [43]). In a more recent study, Peralta et al. [65] concluded that the inability of fittings to equation 5.8 to accommodate these five outliers is due to significant contributions from terms other than the Fermi contact term, especially the paramagnetic spin-orbit coupling. These authors predict that enlarging the data set is not likely to improve the regression model described in equation 5.8 [65].

A different approach was recently adopted by Alkorta and Elguero who relied on the theory of atoms in molecules to predict J_{FF} coupling constants from the total electron density at the bond critical point (ρ_{BCP}) [69]. These workers report a strong linear correlation between the coupling constants and ρ_{BCP} (r^2=0.983), but their expression also includes a term proportional to the cosine of the dihedral angle F-C...C-F as a second regressor. Alkorta and Elguero used a very small data set in their regression (only 6 data points) leading to an elevated ratio of parameters to data points (1:3). Their approach, while certainly very appealing, depends on the presence of a bond path linking the two fluorine atoms, which often occurs in these compounds when the F-F distance and angular orientations are favorable for F-F bonding. It is not clear how one can use their expression when there is no bond path linking the nuclei in question. In contrast, the delocalization index discussed in section 5.2 has a nonvanishing value between any two

atoms in a molecule whether bonded or not, i.e., whether they share a bond path and an interatomic zero-flux surface (equation 5.1) or not. In the case when two atoms do share a bond path, the delocalization index has been shown to provide the basis for the definition of a bond order [71,79,80]. The delocalization index between atoms sharing a bond path has also been shown to be highly correlated with several bond properties including ρ_{BCP} [79].

In this chapter, a new empirical approach that incorporates and extends the data sets used in previous related studies [68] is followed. Thus, the selected data sets included Mallory et al.'s set of 1,8-difluoronaphthalenes [68], benzene derivatives, compounds with three and four fused rings including those where the coupling occurs through an intervening phenyl ring or oxygen atom [81] (compounds **19** and **20**, respectively).

The purely geometrical correlation was tested first. A total of 35 data points were fitted to an expression of the same form as equation 5.8, and the following result was obtained:

$$J_{FF} = 7.897 \times 10^{7}\, e^{-5.461 \times d_{FF}} \qquad (5.9)$$

where J_{FF} is in Hz and F-F interatomic distances are in Å and which yields a calculated-experimental linear relationship with r^2=0.94, SD=8.55, and an average absolute deviation of 7.25 Hz. Figure. 5.2 displays the correlation between J_{FF} calculated from equation 5.9 and experimental F-F distances.

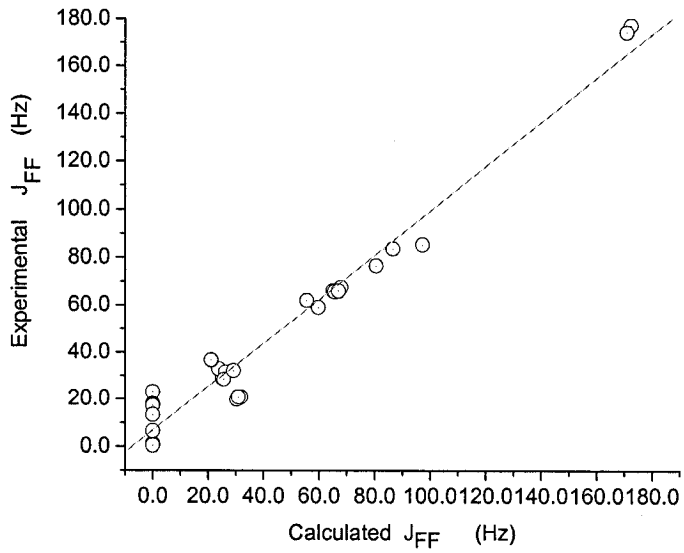

(a)

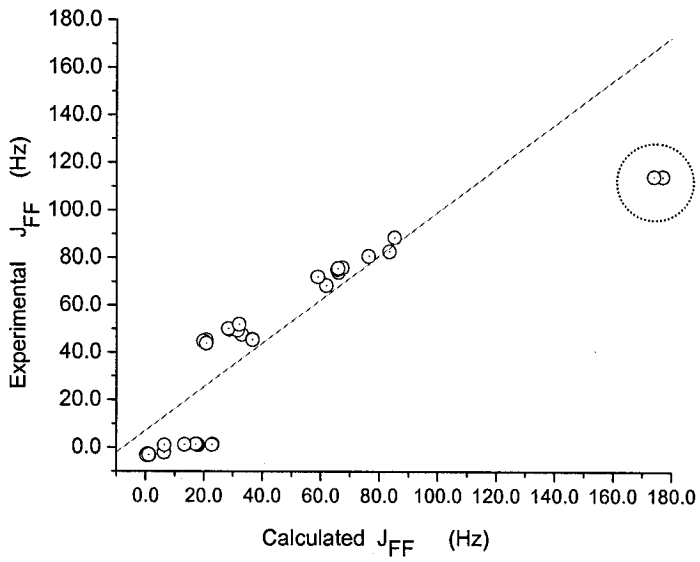

(b)

Figure 5.2. The correlation between J_{FF} calculated from equation 5.9 and experimental F-F distances. (a) A plot of experimental J_{FF} coupling constants versus those calculated from equation 5.9, which uses the F-F distance (d_{FF}) as the sole predictor. The plot corresponds to the following fit: $J_{FF}^{Exptl.} = 6.89+0.92\times J_{FF}^{Calc.}$. [$r^2$=0.96, SD=8.35, n=35]. (b) A plot of experimental J_{FF} coupling constants versus those calculated from equation 5.11 which uses the delocalization indexes (δ(F,F')) as the sole predictor (outliers are encircled). The plot corresponds to the following fit: $J_{FF}^{Exptl.} = 0.37+1.00\times J_{FF}^{Calc.}$. [$r^2$=0.77, SD=20.58, n=35].

As one can see from the figure and the statistical indicators, the correlation is excellent. The ability of distance alone to predict the experimental values with such a high correlation coefficient is quite surprising, as mentioned at the beginning of this section, due to the contribution of terms other than the Fermi term in the coupling interaction [65]. The correlation of J_{FF} coupling constants with the delocalization indexes was also attempted, despite not knowing *a priori* whether the approximation embodied in equation 5.7 would hold in the case of the F-F coupling. If the approximation holds as in the case of proton-proton coupling, then one expects a linear correlation of the form [72]:

$$J_{FF} \approx a + b \times \delta(F,F') \tag{5.10}$$

where a and b are constants. Fitting the 35 data points to the linear model of equation 5.10 leads to:

$$J_{FF} = -3.284+1303\times \delta(F,F') \tag{5.11}$$

where J_{FF} is in Hz, r^2=0.77, SD=20.58, and the mean absolute deviation between the calculated and experimental J_{FF} coupling constants is 14.66 Hz. The presence of two outlying data points (See Figure 5.2(b)) reduces the overall quality of the fit. If one excludes the two outliers from the correlation, one obtains a regression equation (a=3.696, b=959.953) for which the fit is improved substantially with higher correlation coefficient, a standard deviation cut by half (r^2=0.85, SD=10.38, n=33), and an average absolute deviation of 8.35 Hz. The two outliers are data collected from difluorophenanthrene derivatives **28** and **29** where the two fluorine atoms are located in the bay region. In view of the larger size of fluorine (compared to hydrogen), these molecules are highly twisted to accommodate the two fluorine atoms in the bay region. The lack of space around the fluorine is likely to cause significant departure from spherical symmetry of its electron

density distribution. When the electron density of an atom adopts a nonspherical distribution, the basin integral can no longer be assumed to be proportional to the density at the nucleus. Thus, in cases of crowded fluorine atoms, the working assumption behind equation 5.11, namely equation 5.7, is no longer valid which provides an explanation for the irregular behavior of the coupling constants of compounds such as **28** and **29**.

Within the exponential model, the correlation with internuclear distance provides better statistics than the correlation with the delocalization index. The two models, however, are not independent (though not collinear) and one finds:

$$\delta(\mathrm{F},\mathrm{F}') = 29.337 \times \mathrm{e}^{-2.422 \times d_{\mathrm{FF}}} \tag{5.12}$$

in which distances are in Å. Figure 5.3 shows the correlation between the delocalization index calculated directly and that calculated using the fit in equation 5.12.

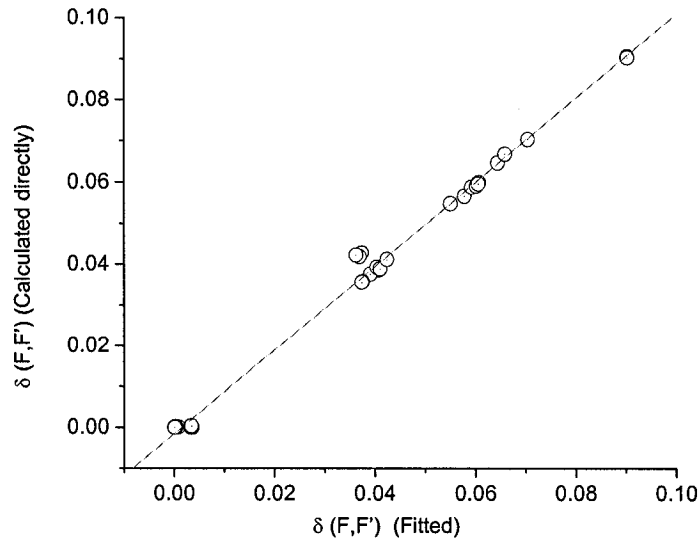

Figure 5.3. Delocalization indices (δ(F,F')) calculated directly and those obtained through the exponential fit with distance (Equation 13).
$\delta(F,F') = -0.0015+1.0232\times\delta(F,F)^{fitted}$ [r^2=1.00, SD=0.0022, n=35].

Using 33 data points (after excluding the two ouliers around J_{FF}~170) and combining the two regressors into one model leads to:

$$J_{FF} = 10.5 - 1216\, e^{-d_{FF}} + 2509\times\delta(F,F') \qquad (5.13)$$

which is exponential with respect to distance and linear with respect to the delocalization indexes, and where J_{FF} is in Hz and d_{FF} is in Å. Equation 5.13 leads to a good agreement between calculated and experimental J_{FF} as can be seen from the statistics, Table 5.1, and Figure 5.4 and a relatively small mean absolute deviation (4.05 Hz).

Table 5.1. A comparison of calculated and experimental J_{FF} spin coupling constants in Hz, listed along with the internuclear separations in Å, and the delocalization indexes.

F-F Interaction	d_{FF}	$10^2 \times *(F,F')$	J_{FF} Exptl.[(a)]	J_{FF} Calc.[(b)]	Residuals
1	2.5810	5.78	59.00	63.51	4.51
2	2.7721	3.74	36.70	28.24	8.46
3	2.5128	6.59	83.50	77.22	6.28
4	2.4916	7.04	85.20	86.53	1.33
5	2.7357	4.10	28.40	34.50	6.10
6	2.7314	4.03	31.50	32.53	1.03
7	2.7702	3.75	36.60	28.43	8.17
8	2.7394	4.06	28.80	33.86	5.06
9	2.7120	4.24	32.10	36.05	3.95
10	2.5943	5.50	61.90	57.74	4.16
11	2.5638	6.02	65.60	67.79	2.19
12	2.5655	5.92	66.10	65.57	0.53
13	2.5573	6.07	67.40	68.58	1.18
14	2.5589	6.05	66.50	68.17	1.67
15	2.5600	6.06	65.90	68.43	2.53
16	2.5262	6.44	76.40	74.89	1.51
17	2.7497	3.90	33.00	30.71	2.29
18	4.9276	0.02	1.10	2.31	1.21
18-1[(c)]	5.4703	0.34	22.80	13.82	8.98
18-2[(c)]	7.3578	0.01	1.10	9.99	8.89
19	5.1923	0.09	6.40	5.91	0.49
19-1[(c)]	5.4523	0.36	23.00	14.30	8.70
19-2[(c)]	7.4881	0.00	1.30	9.89	8.59
20	5.2054	0.04	0.80	4.85	4.05
20-1[(c)]	5.4290	0.33	18.10	13.40	4.70
20-2[(c)]	7.4983	0.01	0.40	9.96	9.56
21	2.6964	3.73	20.80	22.16	1.36
22	4.7034	0.33	6.50	7.71	1.21
23	5.4435	0.36	17.60	14.27	3.33
24	2.7049	3.69	19.80	21.76	1.96
25	2.7016	3.62	20.80	19.81	0.99
26	5.4438	0.36	17.20	14.19	3.01
27	4.6706	0.34	13.40	7.75	5.65
28[(d)]	2.3884	9.02	174.0		
29[(d)]	2.3868	9.02	177.0		

(a) Experimental values were collected from References [68,81,82,83]
(b) Calculated according to equation 5.13.
(c) More than one J_{FF} coupling interaction exists in the molecule. Labels of these interactions are indicated on the structural diagram of compounds **18-20** in Figure 5.1.
(d) Outliers, not included in the fitting, see text.

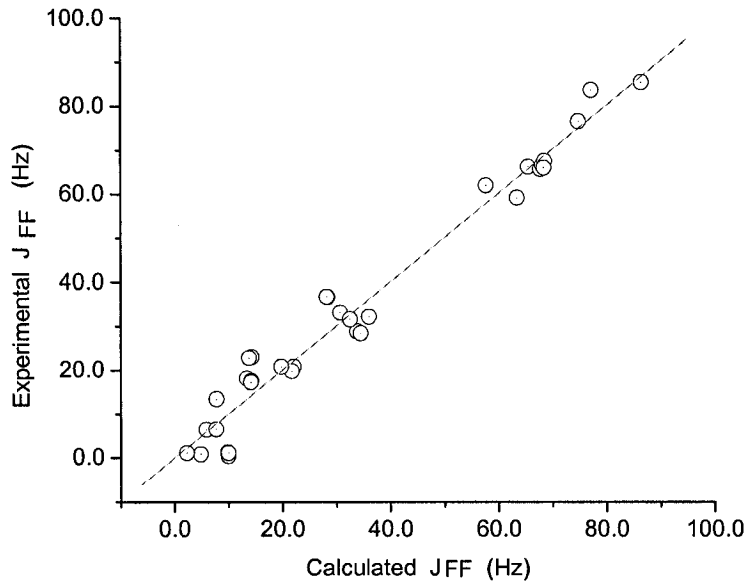

Figure 5.4. A plot of experimental J_{FF} coupling constants versus those calculated from eqn. 5.13 which uses both the F-F distance (d_{FF}) and the delocalization indexes (δ(FF)) as predictors. The plot corresponds to the following fit: $J_{FF}^{Exptl.} = 0.02+1.00\times J_{FF}^{Calc.}$ [r^2=0.96, SD=5.15, n=33].

5.5 Conclusions

Contrary to expectations, both the internuclear distance and the delocalization index yield strong correlations with the experimental J_{FF} coupling constants, except in compounds with crowded fluorine atoms. The correlations described in this chapter span a wide range of coupling constants (84 Hz) and a variety of aromatic compounds, including ones with phenyl groups or oxygen atoms intervening between the coupled fluorine atoms and also including fluorines that are *meta* and *para* with respect to each other in a ring. When the two descriptors are combined, they yield a regression model capable of accurately reproducing the experimental J_{FF} coupling constants.

Chapter 6 The Characterization of a Closed-Shell Fluorine-Fluorine Bonding Interaction in Aromatic Compounds on the Basis of the Electron Density

6.1 Introduction

Halogen-halogen "short contacts" of the type C-X···X-C (where X = F, Cl, Br, or I) and contacts of the type C-X···O, C-X···N , C-X···H-(C,N,O) or C-F···M (metal) have long been known in X-ray crystallographic structures [84-89]. In the crystallographic literature, a short contact between two atoms A and B usually signifies that the A···B distance is less than the sum of their van der Waals radii [90]. More recently, several authors have reported weak closed-shell bonding interactions between halogens on the basis of the topological properties of the electron density. For example, Tsirelson et al. have described a closed-shell bonding interaction between chlorine atoms belonging to neighboring molecules in solid molecular chlorine crystals, the interaction that enables solid chlorine to exist in the crystalline form [91]. Bach, Lentz and Luger [92] have described weak intermolecular C-F···O and C-F···F-C bonding interactions in an electron density study of crystalline pentafluorobenzoic acid at 110 K and using multipolar refinement. In a recent theoretical study, Grabowski et al. [93] reported evidence for the presence of intramolecular C-F···F-C and C-F···H-C bonding interactions based on the topology of the electron density in fluorinated styrenes. In another recent work, Alkorta and Elguero [69] found a correlation between the calculated electron density at the C-F···F-C bond critical point and the through-space fluorine-fluorine spin-spin coupling constant J_{FF} in six fluorinated organic compounds. The same group has also studied the geometries, bond properties, and interaction energies of several classes of non-classical bonding interactions involving halogens by means of density functional theory (DFT) and

second-order Møller-Plesset perturbation theory (MP2) calculations [94]. Recently, correlations of the fluorine-fluorine spin-spin coupling constants with the spatial separation and with the electron delocalization between the two fluorine atoms have been reported (Chapter 5, [95]). During the course of the investigation, it was found that relatively strong through-space coupling constants occur in those instances where the two fluorine atoms are linked by a bond path. In all these studies, however, the F···F bonding was either examined for a very limited number of molecules or was not the main focus of the investigation. The ubiquity of the F···F bonding interaction, thus, calls for a systematic examination, which is the purpose of this chapter. Furthermore, several other interesting closed-shell bonding interactions, which are described herein, were found in the course of the present investigation.

The properties of the electron (and energy) densities at the BCP have been shown to succinctly characterize bonding interactions in an unambiguous manner [29]. Thus, the electron density at the BCP (ρ_{BCP}) provides a measure of the strength of the bonding (or of the bond order) between two atoms [96,97]. Generally, $\rho_{BCP} > 0.20$ au for shared or polar interactions and < 0.10 au for closed-shell interactions, such as ionic and hydrogen bonding and the interactions examined in this chapter.

The sign of the Laplacian of the electron density at the BCP, $\nabla^2\rho_{BCP}(\mathbf{r})$, indicates whether the bonding is of the closed-shell or open-shell type. In a shared interaction, density is accumulated between the nuclei and concentrated along the bond path so that ρ_{BCP} is large and $\nabla^2\rho_{BCP} < 0$ (since the two negative curvatures dominate the small magnitude of the positive curvature). An example of a shared interaction is the C-H bonding for which $\rho_{BCP} = 0.29$ au and $\nabla^2\rho_{BCP} = -1.1$ au. For a closed-shell interaction density is removed

from the region of contact of the two atoms and hence ρ_{BCP} is small and $\nabla^2\rho_{BCP} > 0$, an example being the hydrogen bond N-H···O=C for which ρ_{BCP} = 0.01 au and $\nabla^2\rho_{BCP}$ = +0.03 au. Polar bonding as in C-X (e.g. X=O,N,F,···) exhibits significant charge accumulation between the nuclei typical of shared interactions, but in these cases the Laplacian can be of either sign (for example, in this study the $C^{+0.5}$-$F^{-0.6}$ bond is characterized by ρ_{BCP} = 0.26 au and $\nabla^2\rho_{BCP}$ = +0.14 au). Polar bonding is dominated by charge transfer, and the BCP falls in the region bordering the core of the electropositive atom, unlike shared but non-polar bonding. These observations lead to the development of a powerful model that predicts atomic and group electronegativity based on the location of the BCP along the bond path [98,99].

Energy densities at the BCP determined by the one-electron density matrix (as opposed to the density, its diagonal element) summarise the mechanics of a bonding interaction. As was discussed in Chapter 3, the AIM theory defines a potential energy density experienced by an electron at position vector **r**, also known as the virial field $\mathscr{V}(\mathbf{r})$. The virial field is the average effective potential field felt by an electron in a many-particle system. This field is negative everywhere and when integrated over all space yields the total potential energy of a molecule in an equilibrium geometry. For a stationary state, the virial theorem may be expressed locally [29]:

$$\left(\frac{\hbar^2}{4m}\right)\nabla^2\rho(\mathbf{r}) = 2G(\mathbf{r}) + \mathscr{V}(\mathbf{r}) \tag{6.1}$$

Since it is always true that $G(\mathbf{r})>0$ and $\mathscr{V}(\mathbf{r})<0$, the local statement of the virial theorem ties in the kinetic and potential energy densities to a term proportional to the Laplacian of the electron density. When the theorem is applied locally at the BCP, interactions for

which $\nabla^2\rho_{BCP} < 0$ are dominated by a local lowering of the potential energy, while those for which $\nabla^2\rho_{BCP} > 0$ are dominated by a local excess in the kinetic energy as measured by the 2:1 ratio required for the satisfaction of Equation 6.1. Cremer and Kraka [100] suggested the use of the electronic energy density:

$$H(\mathbf{r}) = G(\mathbf{r}) + \mathscr{V}(\mathbf{r}) \tag{6.2}$$

evaluated at a BCP ($H_{BCP} = G_{BCP} + \mathscr{V}_{BCP}$) to compare the kinetic and potential energies on an equal footing. The electronic energy density yields the total electronic energy when integrated over all space. H_{BCP} assumes negative values for all interactions with significant sharing of electrons, its magnitude reflecting the "covalent character" of the interaction [100].

The presence of a bond path is always stabilizing and is mirrored by a "shadow" path, the virial path, which is a line of maximally negative potential energy density in space linking the nuclei of the two bonded atoms [101]. The appearance of a bond path upon a conformational change entails a local lowering of the energy of the system, even when this fact is disguised by a rise in the total energy caused by other energetic changes in the molecule. For example, it has been shown recently that the twisting of biphenyl is driven by the destabilization of the two carbon atoms connecting the two rings in the planar conformation rather than due to a "steric non-bonded repulsion" between the ortho-hydrogen atoms [102]. In the planar conformation, the ortho-hydrogen atoms are linked by a hydrogen-hydrogen bond path and each is stabilized by 7 kcal/mol as a result. In the planar conformation, the destabilization of the two carbon atoms linking the phenyl rings exceeds the stabilization due to the H···H interaction by a net ~2 kcal/mol when compared to the twisted equilibrium geometry [102]. Similar hydrogen-hydrogen bonding has been

shown to be a ubiquitous stabilizing interaction in angular polycyclic aromatic hydrocarbons and in several other organic molecules [102]. As another example, the 1,3-diaxial interaction in monosubstituted cyclohexanes has also been shown to reside in a more subtle energetic balance than in the one offered in a typical organic textbook: The origin of the energetic destabilization in monosubstituted cyclohexane resides in the carbon skeleton, which overrides the energetic stabilization due to the close H···H contacts [103]. It is concluded that a study of atomic energies complements the characterization of the bonding since it allows one to uncover the local-atomic energies and their changes. Finally, and as already mentioned, the electron density determined at the BCP, $\rho_{BCP}(\mathbf{r})$, is a measure of the strength of bonding between the two atoms and, thus, is related to the bond order (BO). An exponential relationship has been proposed to describe this relationship [29]:

$$BO = \exp\left[a(\rho_{BCP} - b)\right] \tag{6.3}$$

where a and b are constants characterizing each specific type of bonding. The bond order signifies the number of electron pairs *shared* between the two bonded atoms. In the previous chapter the sharing of electrons between two atoms was measured by the delocalization index which is the magnitude of the exchange of the electrons in the basin of atom A with those in the basin of atom B [71]. The delocalization index is defined between any two atoms in a molecule, but for atoms sharing a bond path and an IAS, that is, bonded atoms, it has been shown to be a measure of the bond order [71,80]. The bond order is, thus, reflected in both the total electron density at the BCP and the delocalization index between the two bonded atoms. These two measures have been found to be highly correlated in the case of strong C-C bonding in polycyclic aromatic

hydrocarbons [79]. Thus, one can calibrate Equation 6.3 using the delocalization index rather than arbitrarily assigned bond orders [79]:

$$\delta(A,B) = \exp\left[a(\rho_{BCP} - b)\right] \tag{6.4}$$

6.2 Computational Details

The geometries of all molecules have been optimized without constraints at the B3LYP/6-31G(*d*) level, and frequencies were calculated at that level to ensure that local minima have been located. Single-determinant Kohn-Sham "wavefunctions" [16] were obtained at the B3LYP/6-311++G(*d*,*p*)//B3LYP/6-31G(*d*) level. All electronic structure calculations were performed using the Gaussian 03 package [53]. The resulting electron densities were analyzed using the AIMPAC suite of programs [54] to obtain the bond and atomic properties and to prepare the contour and gradient vector field plots. The molecular graphs were plotted using AIM 2000 [104,105]. The AIMDELOC [76] program was used to calculate the delocalization indices from the atomic overlap matrices. Statistical analyses and correlations were carried out using the Origin 6.1 [78] and the Polymath 5.1 [106] packages.

6.3 Results and Discussion

6.3.1 Optimized Geometries and F-F Internuclear Separations

Figure 6.1 displays the set of molecules included in this study. All F···F and other closed-shell interactions are depicted by faint lines. Compounds **1**-**17** are all derivatives of 1,8-difluoronaphthalene (1,8-DFN), the numbering scheme of which is depicted in Figure 6.2.

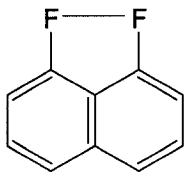

1

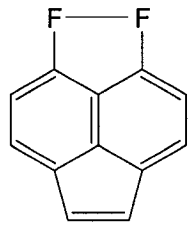

2

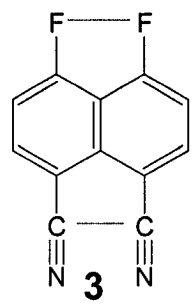

3

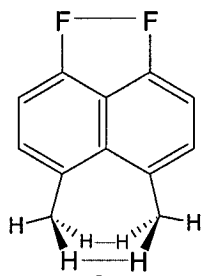

4

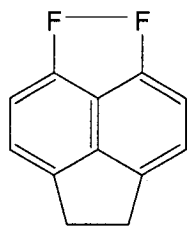

5

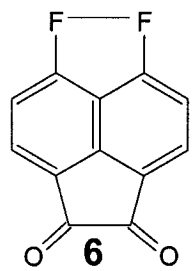

6

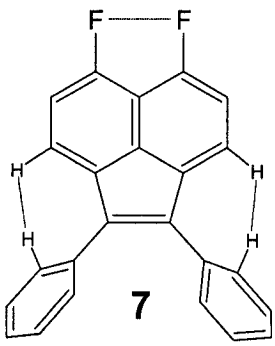

7

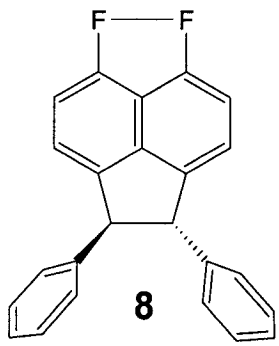

8

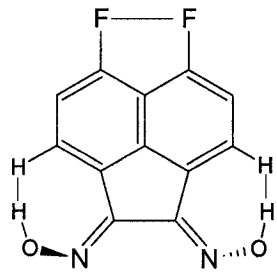

9

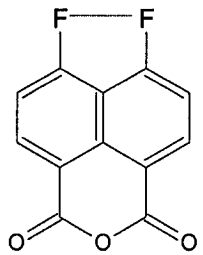

10

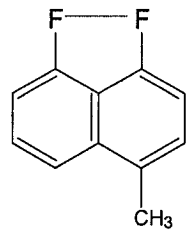

11

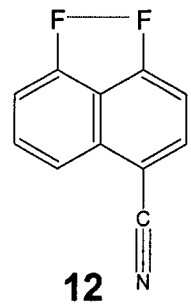

12

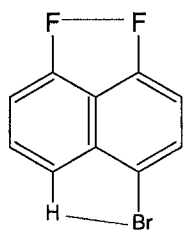

13

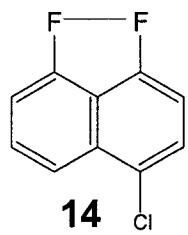

14

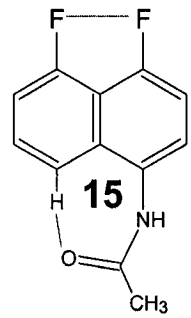

15

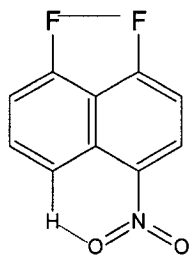

16

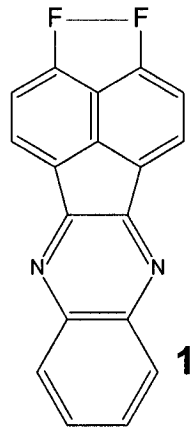

17

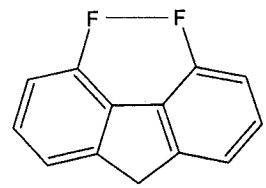

18

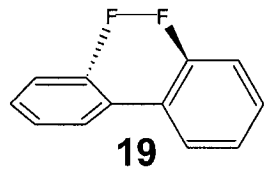

19

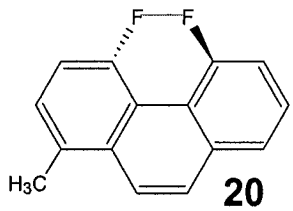

20

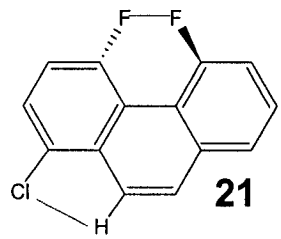

21

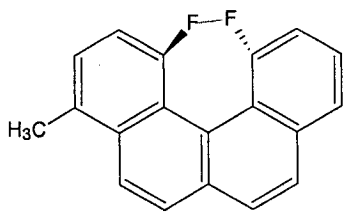

22

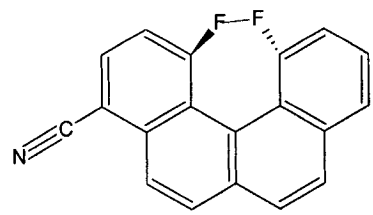

23

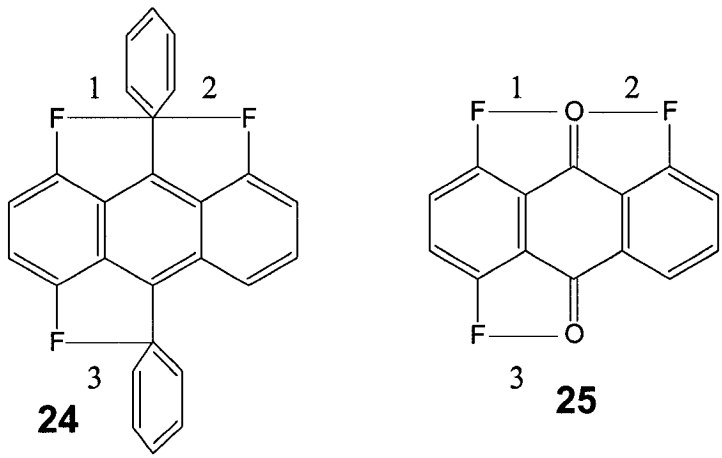

Figure 6.1. Chemical structures of the compounds constituting the data set employed in this study. Closed-shell bonding interactions are denoted by faint lines.

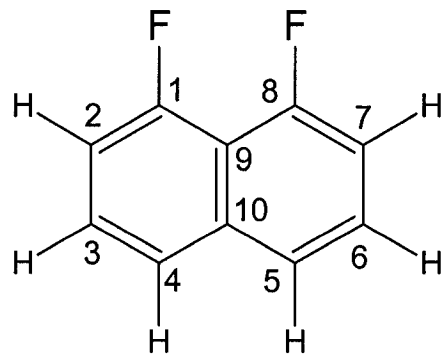

Figure 6.2. Numbering scheme for the naphthalene ring system used in this study exemplified with the 1,8- difluoronaphthalene molecule.

Contrary to what one might expect, the substituents have a significant effect on the F-F distance. The F-F distance falls within the range from 2.492Å (in compound **4**) to 2.772Å (in compound **2**) spanning almost 0.3Å. This distance depends on the nature of

the substituents at positions 4 and 5 positions of naphthalene. Thus, in compound **4**, the naphthalene ring distorts to accommodate the bulky 1,4-dimethyl substituents, while in **2** the two fluorines are pulled apart due to the geometrical necessity of accommodating the five-membered ring.

The geometry of the naphthalene skeleton in **1-17** can be viewed as a "pair of scissors" formed by the C1-C10 and C8-C10 axes pivoting around the C1-C10-C8 angle. In the parent compound 1,8-DFN (compound **1**), this angle is 62° but in **4** it is only 60° with a consequent shortening of the F-F distance. At the other extreme, the C1-C10-C8 angle opens to 66° in compound **2** since the C4-C10-C5 moiety is part of a five-membered ring, driving the two fluorine atoms apart to their maximal separation. The other molecules fall in between these two extremes. In all cases, the scissors angle turns out to be an excellent predictor of the F-F separation in compounds **1-17**, as can be seen in Figure 6.3.

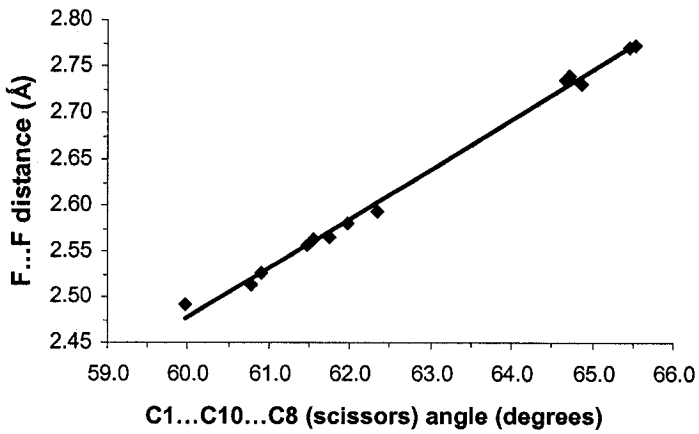

Figure 6.3. Regression plot showing the strong predictive power of the scissors angle (the C1-C10-C8 angle) and the F···F distance.

Compounds **1-17** are characterized by planar naphthalene ring systems and two C-F bonds that are coplanar with the naphthalene rings and essentially parallel to each other. In contrast, compounds **18-23** are no longer derivatives of naphthalene and the two C-F bonds are no longer parallel. Compounds **19-23** further differ in that their two C-F bonds are also no longer coplanar since these are highly crowded molecules which twist to accommodate the two proximal fluorine atoms. No F···F bond paths are present in **24** and **25** which thus do not exhibit F···F bonding interactions. Instead, F···C and F···O bond paths were found in these two compounds and will be discussed separately in section 6.3.6.

6.3.2 The F···F Bond Path

As was mentioned in Chapter 3, the bond path is a unique and universal indicator of bonding interactions. Bonding is an all or nothing phenomenon, but wherever a bond path links two nuclei it is always locally stabilizing in an equilibrium geometry. In general the set of bond paths defining a molecular structure, the molecular graph, reproduces the conventional Lewis structure. In addition, one of the major advantages of the bond path as an indicator of bonding is that it is capable of detection of weak interactions of any type: van der Waals, hydrogen bonding, dihydrogen bonding, etc. The literature is rich with descriptions of topologically characterized non-conventional bonding. Examples of bonding interactions which were reported on the basis of the topology of the electron density include: (1) the bonding between two equivalent or similar closed-shell hydrogen atoms (C-H···H-C), better termed hydrogen-hydrogen bonding interaction [102] to distinguish it from the dihydrogen bonding in which one hydrogen atom plays the role of the acceptor in the hydrogen bonding [93,107,108]; (2) bonding involving two non-

equivalent hydrogen atoms or dihydrogen bonding ($X\text{-}H^{\delta+}\cdots H^{\delta-}\text{-}Y$) [109,110,111]; (3) a plethora of hydrogen bonding interactions [94,112-118]; (4) Cl···Cl closed-shell interactions in crystalline chlorine [91]; (5) a N=O···O=N closed-shell interaction [119]; (6) weak F···O and F···F' intra- and intermolecular interactions [92,94]; (7) intramolecular F···F interactions [69,93]; (8) metallic closed-shell interaction between two Mn atoms [120]; and (9) several closed-shell O···O and O···C interactions [120]. The absence of a bond path has also been shown to be a decisive indicator for the lack of bonding despite an unusually close spatial arrangement of a closed-shell carbon atom to a titanium atom [121].

In this chapter one of these examples of a closed-shell interaction is described in detail, an interaction which we show to be ubiquitous in crowded fluorinated compounds: the F···F bonding interaction.

Figure 6.4(a) is a contour map of the electron density of 1,8-difluoronaphthalene (1,8-DFN) in the molecular plane, Figure 6.4(b) is the corresponding gradient vector field showing the lines of steepest ascent in the electron density, and Figure 6.4(c) is a plot of the Laplacian showing regions of charge concentration and charge depletion. Superimposed on these plots are the sets of bond paths linking the nuclei as well as the intersections of the interatomic zero flux surfaces with the molecular plane (some of these surfaces are indicated with arrows in the figure). Some atomic basins are highlighted in color in Figure 6.4 to highlight their respective forms. Basins F1 and F8, which share a bond path also share an IAS of zero-flux, are highlighted in yellow in the figure. F1 shares an IAS with F8 and with C1, and F8 shares an IAS with F1 and C8. The IAS from now on will be denoted by the vertical bar " | " between the two bonded

atoms sharing that surface. For example, the IAS between F1 and C1 will be denoted by "F1|C1" when we refer to the side of the surface facing the F1 basin and "C1|F1" to the side facing the C1 basin. The C1 atomic basin is surrounded by three IASs corresponding to its three bonding interactions: C1|F1, C1|C2, and C1|C9. The atomic basin of C1 extends to infinity tailing between the F1 and H2 basins but ends abruptly at the line where the basins of F1, C1, C9, C8, and F8 all meet. In contrast, Figure 6.4 shows that the basin of C4, also highlighted in yellow, surrounds the H4 basin (in the plane of the figure) and extends to infinity on both sides. The same is true by symmetry for C5 and H5. Thus, unlike F1 and F8 which share an IAS, H4 and H5 are separated by the tailing atomic basins of C4, C5, and C10. From this discussion, it is also clear that the basins of C9 and C10 differ in a fundamental way: C9 is the only internal atom with finite boundaries totally enclosed within this molecule, while C10 and all other atomic basins are external atoms extending to infinity.

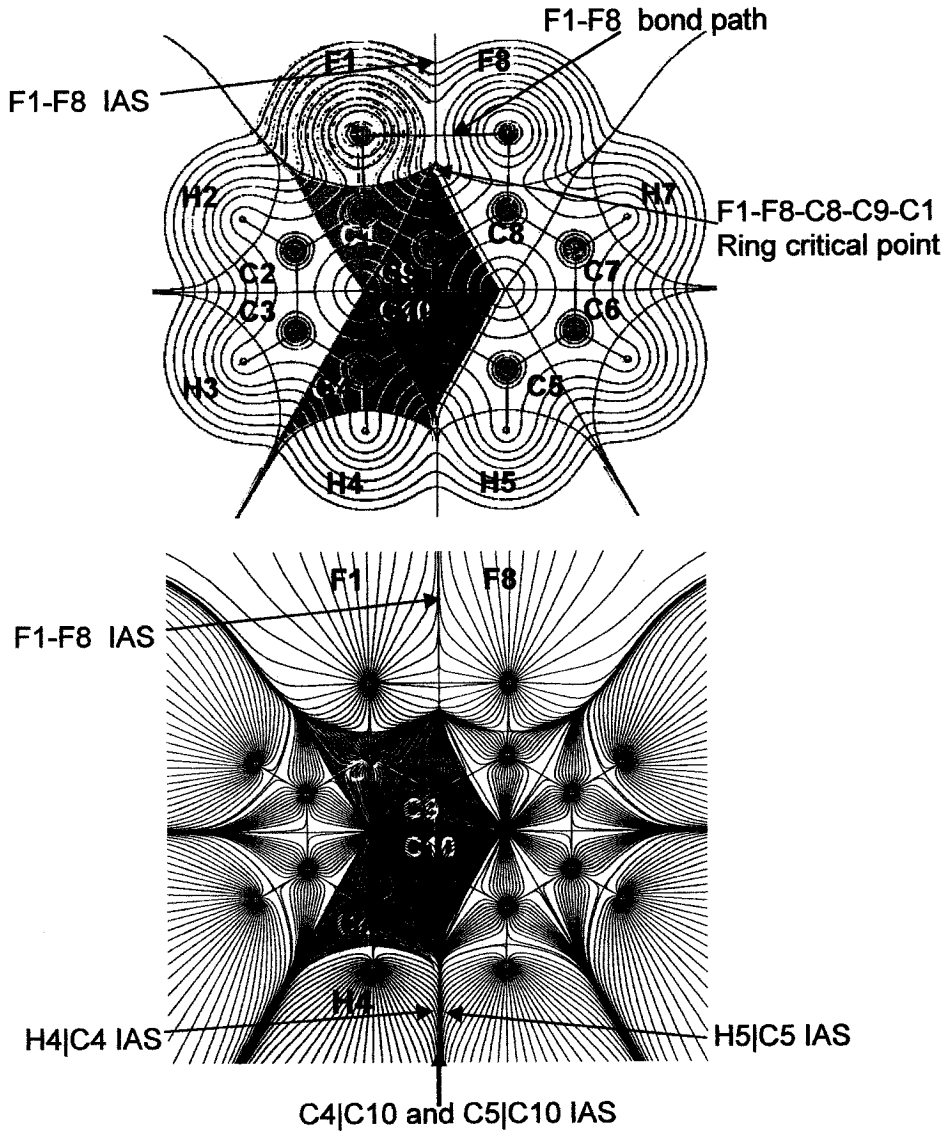
F1-F8 bond path
F1-F8 IAS
F1
F8
H2
H7
F1-F8-C8-C9-C1
Ring critical point
C1
C8
C2
C7
C3
C6
H3
C5
H4
H5
F1-F8 IAS
F1
F8
H4|C4 IAS
H5|C5 IAS
C4|C10 and C5|C10 IAS
Typical
closed-shell
interaction
F1
F8
Highly polar
interaction
Typical
shared
interactions
H4
H5

Figure 6.4. (a) Electron density contour plot of 1,8-difluoronaphthalene in the molecular plane. The set of contours from outside going inwards have the values of: 0.001, 0.002, 0.004, 0.008, 0.02, 0.04, 0.08, 0.2, 0.4, 0.8, 2.0, 4.0, 8.0, 20.0, 40.0, and 80.0 au. (b) Gradient vector field corresponding to the contour plot. (c) Laplacian plot in the molecular plane. Solid contours denote regions of charge concentration where $\nabla^2\rho(\mathbf{r})<0$ and dashed contours denote regions of charge depletion $\nabla^2\rho(\mathbf{r})>0$. Contours levels increase or decrease from a zero contour in steps: ±0.001, ±0.002, ±0.004, ±0.008, ±0.02, ±0.04, ±0.08, ±0.2, ±0.4, ±0.8, ±2.0, ±4.0, ±8.0, ±20.0, ±40.0, ±80.0 au. Several atoms have been colored for the easy distinction of the form of their atomic basins.

A comparison of the Laplacian plot Figure 6.4(c) shows that the F···F interaction exhibits the same characteristics of typical closed-shell interactions (See Figure 7.15, on page 294 of Bader's book [29]). The Laplacian plots of closed-shell and shared interactions differ radically. Thus, for a shared interaction, the valence shell charge concentration (VSCC) of two atoms fuse into a continuous region of charge concentration between the atoms. In a closed-shell interaction, on the other hand, the valence shells for the atoms are clearly defined inside the basin of the two bonded atoms. The reader is asked to compare the bonding region between the two fluorine atoms in Figure 6.4(c) with that between any two carbon atoms or any carbon atom and its bonded hydrogen atom.

The F···F bond paths have been traced in all compounds **1-23** as can be seen from their molecular graphs plotted in Figure 6.5(a, b). Figure 6.5(c) depicts the molecular graphs of compounds **24** and **25**, which show closed-shell weak interactions of the type F···C (in **24**) and F···O (in **25**), interactions which will be discussed in section 6.3.6 below.

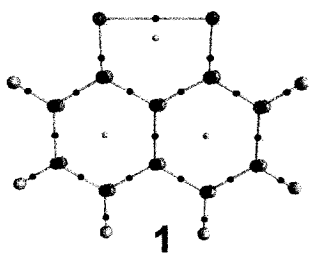

1

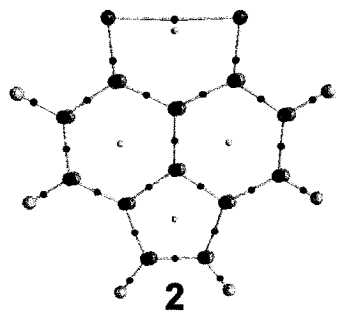

2

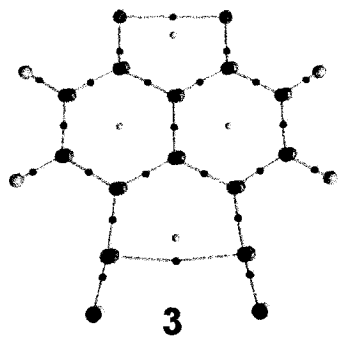

3

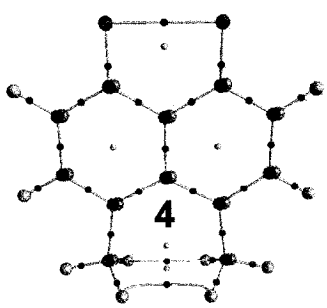

4

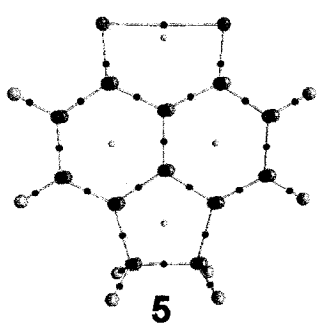

5

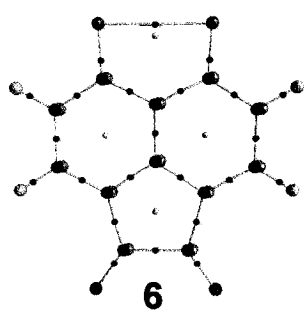

6

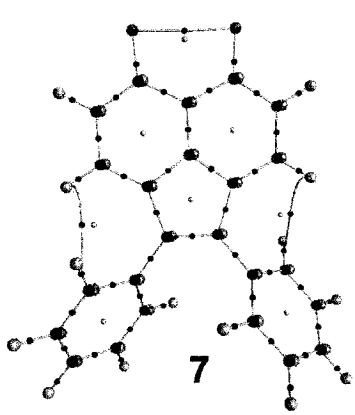

7

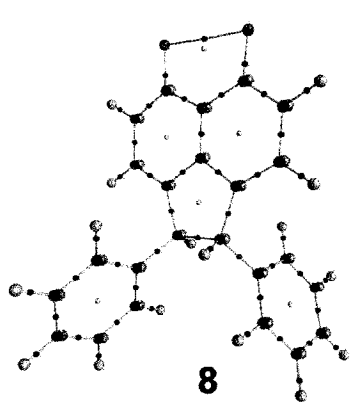

8

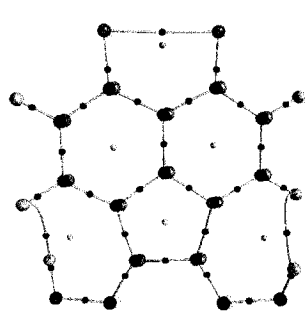

9

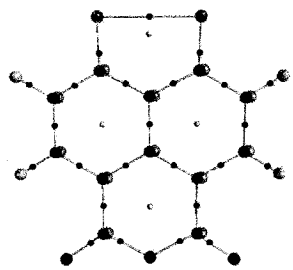

10

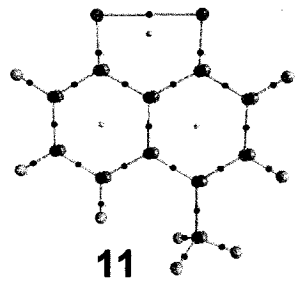

11

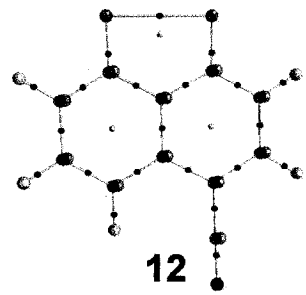

12

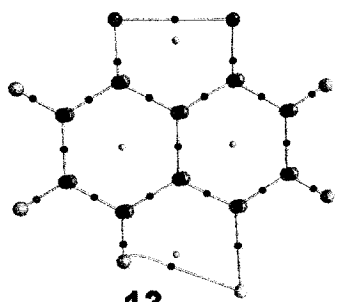

13

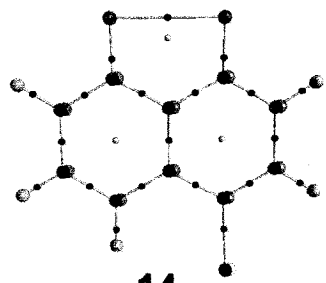

14

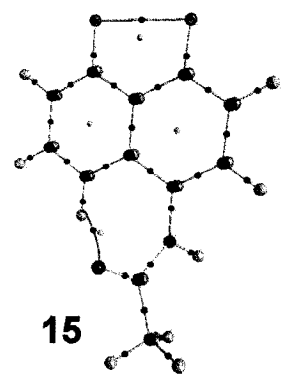

15

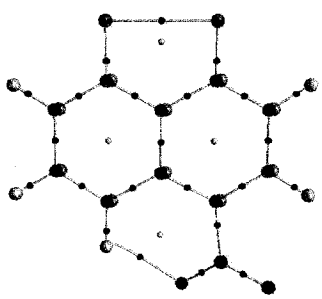

16

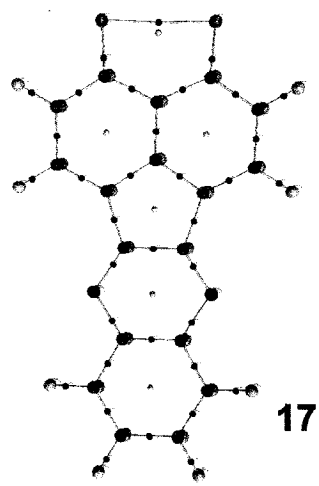

17

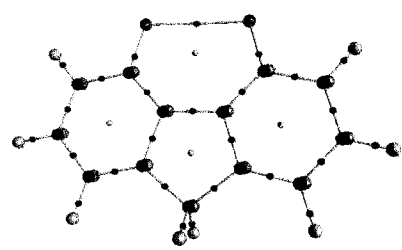

18

(a)

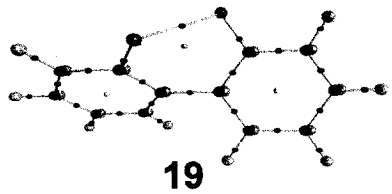

19

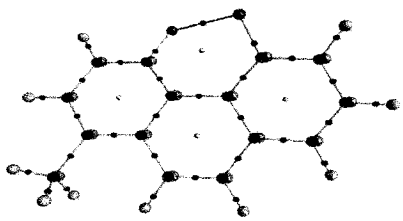

20

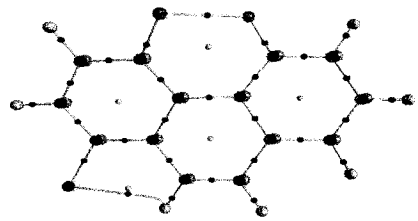

21

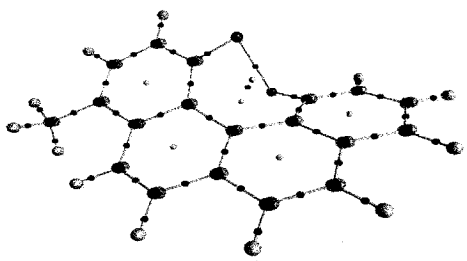

22

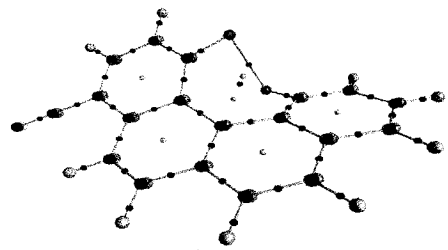

23

(b)

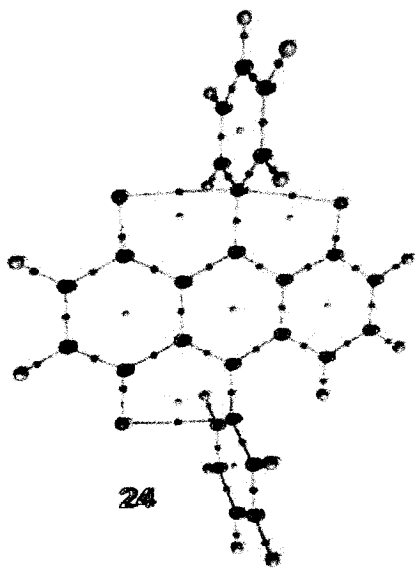

24

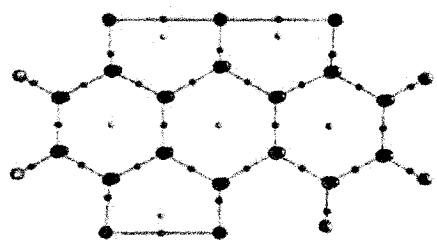

25

(c)

Figure 6.5. Computed molecular graphs of the set of compounds presented in Figure 6.1. Red dots on bond paths are the bond critical points (BCP), yellow dots are the ring critical points (RCP), and green dots are cage critical points (CCP). Spheres denote the positions of atoms: C = dark grey, O = red, N = dark blue, H = grey, F = golden yellow, Cl = green, Br = light grey (the reader is encouraged to also refer to Figure 6.1 to identify the different atoms and bonds). The planes of some of the molecules have been tilted to show the structure more clearly, which results in the distortion of the proportions caused by perspective projection (e.g. some symmetry equivalent parts may appear to have different sizes). Also, the molecular graphs of different compounds are not necessarily plotted to the same scale. (a) Compounds in which the F···F bond is essentially co-planar with the molecular plane, (b) crowded twisted molecules, (c) compounds devoid of F···F bonding but involving F···C and F···O closed-shell interactions.

In all cases the corresponding ring critical point(s) has (have) also been located and the Poincaré-Hopf (P-H, equation 3.4) relationship verified [29]. Compounds **22** and **23** have been found to possess an unusual topology with highly twisted α-helical rings formed as a result of the F···F bonding interaction that gives rise to two ring critical points and a cage critical point. The P-H relationship has also been verified for these highly unusual ring topologies. The interesting topology of these rings is known to be a mathematical possibility [29] but not found previously in an actual molecular system to the best of our knowledge. This topic will be the subject of the next chapter [122].

6.3.3 Characterization of the F···F Bonding Interaction

Table 6.1 lists the bond properties of the F···F interactions in compounds **1-23**.

Table 6.1. F···F bond properties. All entries are in atomic units except bond lengths, and bond path lengths (BPL) which are in Å, δ(F,F') is the number of electron pairs shared between the two bonded fluorine atoms, and ε is dimensionless.

Cpd.	δ(F,F')	*r*FF'	BPL	ρ_{BCP}	$\nabla^2\rho_{BCP}$	G_{BCP}	$\mathscr{V}_{BCP}$	H_{BCP}	λ_1	λ_2	λ_3	ε
1	0.0578	2.5810	2.5816	0.0146	0.0645	0.0152	-0.0142	0.0010	-0.0150	-0.0137	0.0931	0.0930
2	0.0374	2.7721	2.7743	0.0096	0.0434	0.0100	-0.0091	0.0009	-0.0092	-0.0055	0.0582	0.6639
3	0.0659	2.5128	2.5133	0.0169	0.0766	0.0178	-0.0165	0.0013	-0.0178	-0.0170	0.1114	0.0474
4	0.0704	2.4916	2.4921	0.0178	0.0813	0.0189	-0.0175	0.0014	-0.0188	-0.0183	0.1183	0.0280
5	0.0410	2.7357	2.7370	0.0104	0.0463	0.0108	-0.0100	0.0008	-0.0101	-0.0072	0.0636	0.4121
6	0.0404	2.7314	2.7328	0.0104	0.0467	0.0108	-0.0100	0.0008	-0.0102	-0.0071	0.0640	0.4402
7	0.0375	2.7702	2.7721	0.0096	0.0435	0.0100	-0.0092	0.0009	-0.0092	-0.0056	0.0584	0.6570
8	0.0406	2.7394	2.7407	0.0103	0.0461	0.0107	-0.0099	0.0008	-0.0100	-0.0070	0.0631	0.4347
9	0.0424	2.7120	2.7132	0.0109	0.0484	0.0113	-0.0105	0.0008	-0.0107	-0.0079	0.0671	0.3624
10	0.0550	2.5943	2.5949	0.0141	0.0624	0.0146	-0.0137	0.0010	-0.0145	-0.0129	0.0897	0.1199
11	0.0602	2.5638	2.5643	0.0152	0.0672	0.0158	-0.0148	0.0010	-0.0156	-0.0145	0.0974	0.0763
12	0.0592	2.5655	2.5660	0.0151	0.0669	0.0157	-0.0147	0.0010	-0.0156	-0.0144	0.0969	0.0828
13	0.0607	2.5573	2.5578	0.0154	0.0684	0.0160	-0.0150	0.0010	-0.0159	-0.0148	0.0991	0.0737
14	0.0605	2.5589	2.5595	0.0153	0.0680	0.0160	-0.0150	0.0010	-0.0158	-0.0148	0.0986	0.0728
15	0.0606	2.5600	2.5605	0.0153	0.0679	0.0159	-0.0149	0.0010	-0.0158	-0.0147	0.0984	0.0759
16	0.0644	2.5262	2.5267	0.0164	0.0739	0.0173	-0.0161	0.0012	-0.0172	-0.0163	0.1075	0.0519
17	0.0391	2.7497	2.7513	0.0100	0.0451	0.0104	-0.0096	0.0008	-0.0097	-0.0064	0.0612	0.5193
18	0.0605	2.3884	2.6318	0.0130	0.0557	0.0131	-0.0124	0.0008	-0.0143	-0.0133	0.0833	0.0759
19	0.0460	2.3872	2.6736	0.0118	0.0522	0.0123	-0.0115	0.0008	-0.0111	-0.0106	0.0740	0.0469
20	0.0902	2.4916	2.3884	0.0222	0.1085	0.0247	-0.0222	0.0025	-0.0260	-0.0251	0.1597	0.0350
21	0.0902	2.4875	2.3872	0.0223	0.1088	0.0247	-0.0223	0.0025	-0.0261	-0.0252	0.1601	0.0341
22	0.0644	2.6730	2.4927	0.0177	0.0864	0.0197	-0.0178	0.0019	-0.0170	-0.0137	0.1170	0.2422
23	0.0650	2.6311	2.4886	0.0178	0.0870	0.0198	-0.0179	0.0019	-0.0172	-0.0140	0.1182	0.2330
Max.	0.0902	2.7721	2.7743	0.0223	0.1088	0.0247	-0.0091	0.0025	-0.0092	-0.0055	0.1601	0.6639
Min.	0.0374	2.3872	2.3872	0.0096	0.0434	0.0100	-0.0223	0.0008	-0.0261	-0.0252	0.0582	0.0280
Avg.	0.0569	2.5991	2.6000	0.0144	0.0659	0.0153	-0.0141	0.0012	-0.0149	-0.0130	0.0938	0.2121
SD	0.0146	0.1146	0.1151	0.0036	0.0188	0.0042	0.0038	0.0005	0.0046	0.0053	0.0285	0.2056

In all cases, it is clear that this is a closed-shell interaction:

(1) The F···F internuclear distance is in the range of ~2.39 Å to ~2.77 Å, in other words generally smaller than (or close to) twice the van der Waals radius of fluorine (2.7 Å) [90] and thus can be classified as "close contact" [88]. In all cases, the curvature of the bond path is rather small, as can be seen visually in Figure 6.5(a,b) or from the difference between the geometric bond length and the bond path length (BPL), Table 6.1, with a maximal difference of ~ 0.08% of the bond length.

(2) ρ_{BCP} ranges from *ca.* 0.022 to 0.010 au, values an order of magnitude smaller than that for a typical covalent bond. The small value of ρ_{BCP} for the F···F bonding is similar to moderate hydrogen bonding for which ρ_{BCP} ranges from ~0.034 au in H3N···HF to ~0.007 au in HCl···HF [114].

(3) $\nabla^2\rho > 0$ since the Laplacian is dominated by λ_3, the positive curvature tangent to the bond path, for such a closed-shell interaction (compare the magnitudes on λ_3 with those of λ_1 and λ_2 in Table 6.1). $\nabla^2\rho$ ranges from ~ +0.11 to +0.04 au indicating very little sharing between the two atomic basins, which leads one to anticipate small delocalization between the basins of the two fluorine atoms.

(4) The delocatization index δ(F,F') indicates indeed very little sharing between the atomic basins of the two fluorine atoms. In the absence of charge transfer between two bonded atoms, one can equate the delocalization index between them to a bond order [71,80]. There is little or no charge transfer between the two fluorine atoms in these compounds (even when the two fluorine atoms are not equivalent by symmetry), and therefore the delocalization index can be interpreted as the F···F bond order. From Table 6.1, we can see that the largest bond order in **20** is only ~0.09, i.e., only 0.09 pair of electrons is shared between the two fluorine atoms, but this value can be as low as 0.04 pair for compound **2**. The delocalization indices have been previously shown to depend on both the internuclear separation and the angular disposition of the two F-C bonds [95].

(5) As stated in the introduction, the total energy density (Equation 6.2) evaluated at the BCP (H_{BCP}) is negative when significant sharing of electrons dominates the interaction. In these cases, the potential energy density dominates the kinetic energy

density at the BCP. From Table 6.1, one can see that the F···F interaction is dominated by the kinetic energy density (which is positive everywhere) and H_{BCP} is therefore always positive for this interaction as anticipated for a closed-shell interaction with little sharing of electrons.

(6) For weak interactions, the ellipticity indicates the stability of the bond critical point with respect to small geometrical changes such as those occurring during molecular vibration. From Table 6.1, the values of ε fall between ~0.66 and ~0.03, indicating relatively stable critical points, which can also be concluded on the basis of the relatively large distance between the F···F BCPs and their respective ring critical point ensuing from the bonding. (The separation between the RCP and the BCP is typically around 0.7 Å.)

From the above considerations, it is concluded that a weak F···F bonding interaction exists in these compounds, an interaction which exhibits the hallmarks of a typical weak closed-shell bonding interaction.

6.3.4 Correlations Among the F···F Bond Properties

The properties characterizing the F···F bonding reported in Table 6.1 are highly correlated among themselves within the range of bond lengths studied (2.3-2.8 Å). Some of those correlations are displayed in Figures 6.6-6.9.

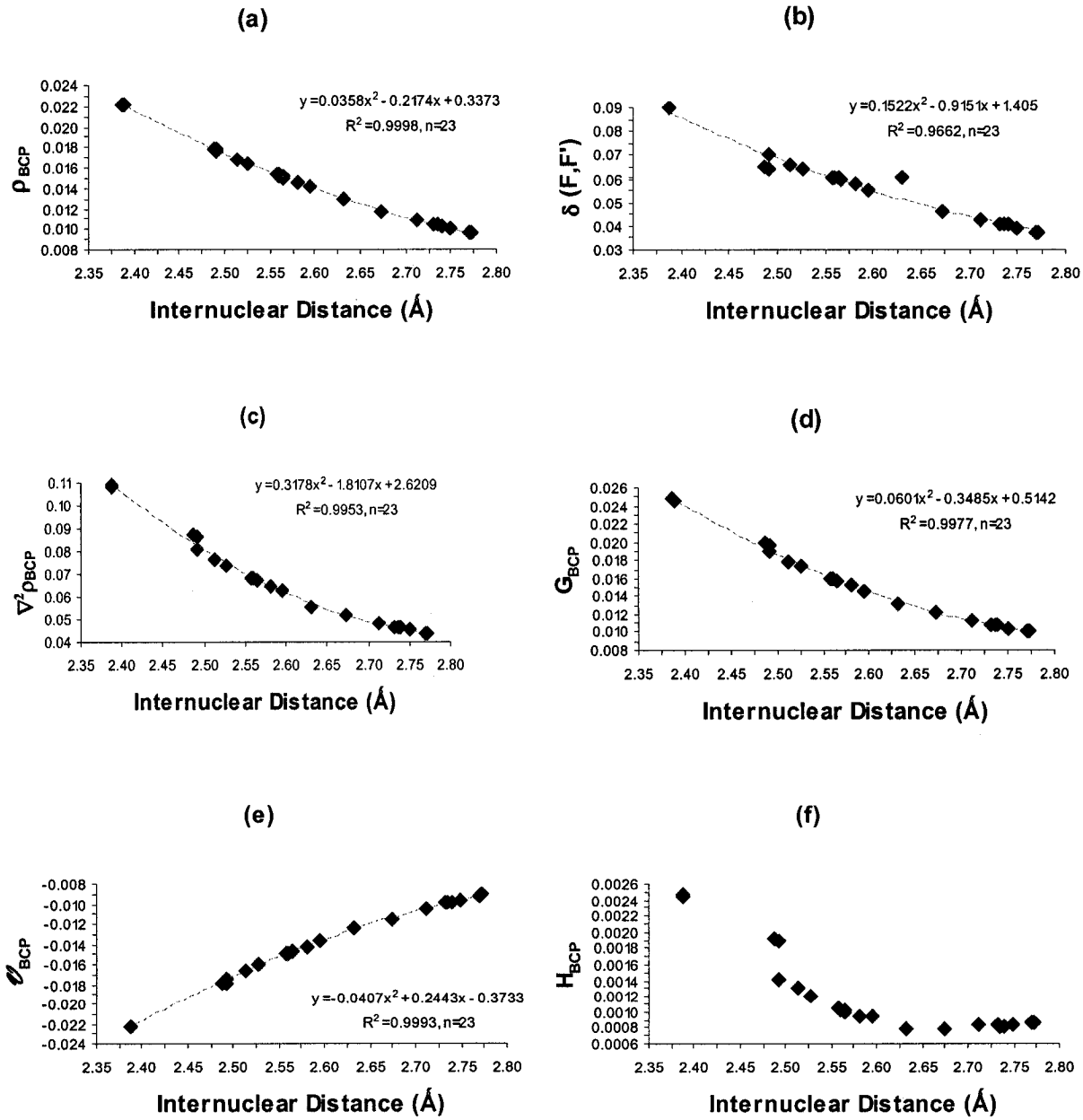

Figure 6.6. A series of plots representing the dependence of (a) ρ_{BCP}, (b) δ(F,F'), (c) $\nabla^2\rho_{BCP}$, (d) G_{BCP}, (e) $\mathscr{V}_{BCP}$, and (f) H_{BCP} on the internuclear separation. All quantities in the plots are in atomic units except the internuclear distance which is in Å. No fit or statistical output is given for poor or irregular correlations.

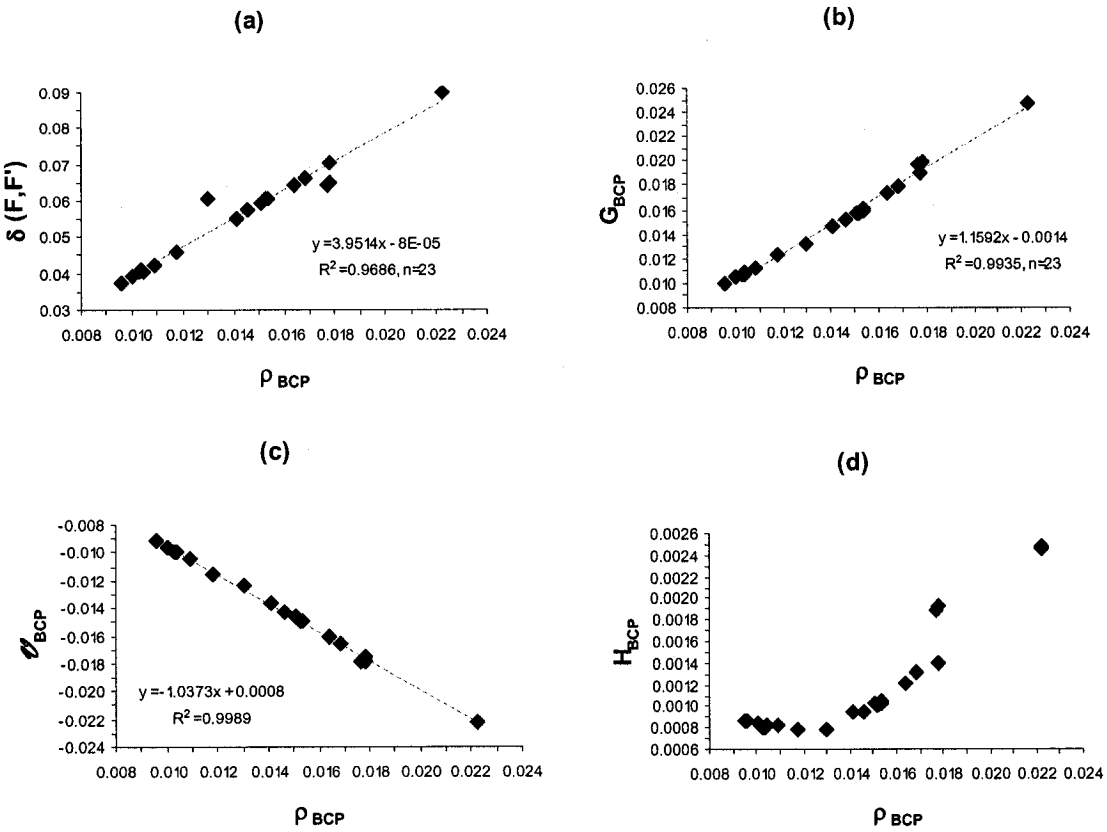

Figure 6.7. A series of plots representing the dependence of (a) δ(F,F'), (b) G_{BCP}, (c) $\mathscr{V}_{BCP}$, and (c) H_{BCP} on ρ_{BCP}. All quantities in the plots are in atomic units. No fit or statistical output is given for poor or irregular correlations.

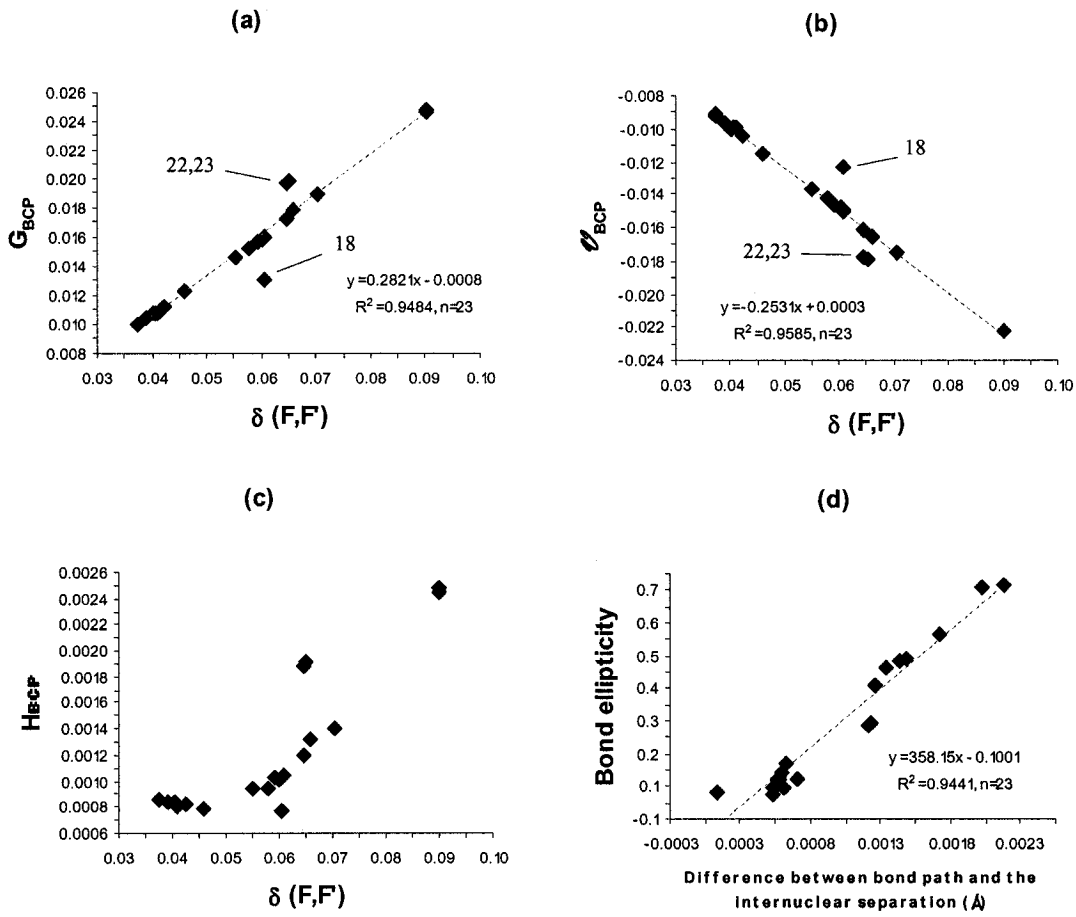

Figure 6.8. A series of plots representing the dependence of (a) G_{BCP}, (b) $\mathscr{V}_{BCP}$, and (c) H_{BCP} on the delocalization index between the two bonded fluorine atoms (δ(F,F')). All quantities in plots (a-c) are in atomic units. No fit or statistical output is given for poor or irregular correlations. The outliers have been indicated by the respective compound numbers in (a) and (b). Plot (d) shows the correlation between a measure of the departure of the bond path from linearity (the difference between the internuclear separation and the bond path length, in Å) and the bond ellipticity.

Figure 6.6 shows the correlation between the internuclear distance (bond length) and several properties. From this figure it is clear that ρ_{BCP} of this weak closed-shell F···F interaction decreases with distance, Figure 6.6(a). Figure 6.6(b) shows that the

delocalization index decreases with distance in a similar manner as ρ_{BCP}. Figure 6.6(c) shows a decrease in the Laplacian at the BCP as a function of the internuclear distance. The effects of the intenuclear distance on the energy densities at the BCP are displayed in Figure 6.6(d-f). The kinetic energy density at the BCP decreases with the internuclear distance (Figure 6.6(d)), but the potential energy density shows an opposing trend as it becomes less stabilizing with an increase in the distance (Figure 6.6(e)). The behavior of the total energy is dominated by the behavior of the kinetic energy, which decreases with increasing internuclear distance (Figure 6.6(f)).

Figure 6.7 shows the correlation of the electron density at the BCP with the delocalization index (Figure 6.7(a)) and with the energy densities (Figure 6.7(b-d)). The delocalization index increases linearly with ρ_{BCP} indicating the more delocalization the more the accumulation of electron density at the BCP. The kinetic energy density increases with increasing ρ_{BCP} (Figure 6.7(b)) while the potential energy density becomes more negative with ρ_{BCP} (Figure 6.7(c)). There is a net increase in the total energy density at the BCP as ρ_{BCP} increases.

Figure 6.8(a-c) displays the correlation between the delocalization index and the energy densities. Since ρ_{BCP} and δ(F,F') are highly positively correlated linearly (Figure 6.7(a)), the energetic trends of δ(F,F') are similar to those for ρ_{BCP} plotted in Figure 6.7(b-d). From Figure 6.7(b-d) and Figure 6.8 one concludes that the more accumulation of electron density there is at the BCP, the more electron delocalization there is between the two fluorine atoms, and the more the interaction is dominated by the kinetic energy density. Thus, while an increase in delocalization and in ρ_{BCP} is accompanied by an increasingly stable potential energy density (more negative), this stabilization is

overwhelmed by the increase in the kinetic energy density for the F···F closed shell interaction. These trends are the reverse of those described for a typical strong shared interaction such as the C-C bond where the total energy at the BCP drops with increasing electron delocalization as well as with increasing electron accumulation at the BCP (see Figure 1(h) of Ref. 79). This shows a fundamental difference in behavior between a weak closed-shell interaction such as the F···F bonding and a typical shared interaction.

Finally, Figure 6.8(d) shows the correlation between the difference in the bond path length and the bond path (the departure of the bond path from linearity) and the ellipticity. The plot shows a strong linear correlation between the two quantities indicating that the larger the departure from linearity the larger the ellipticity.

Finally, the data to Equation 6.4 were fitted to uncover whether the exponential relationship which was shown to hold for strong covalent bonding [79], still holds in the case of the weak F···F closed-shell interaction. The following fitted equation was obtained:

$$\delta(\mathrm{F,F'}) = \exp\left[64.2532(\rho_{BCP} - 0.0595)\right] \tag{6.5}$$

which yields r^2=0.959, showing that the relationship holds even for this weak F···F interaction. The values of δ(F,F') calculated from Equation 6.5 are plotted against those calculated directly in Figure 6.9.

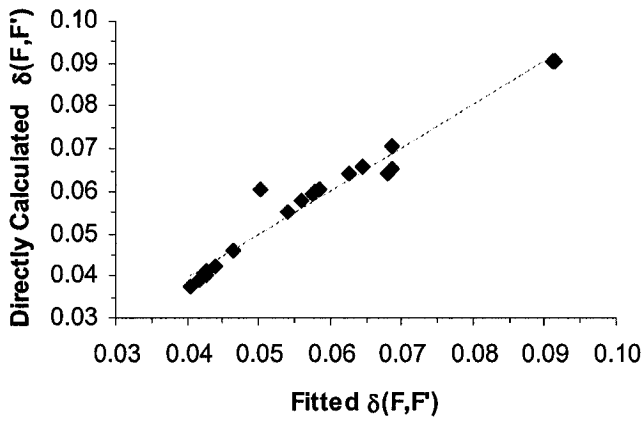

Figure 6.9. A plot of the values of δ(F,F') calculated from ρ_{BCP} via Eqn (6.5) versus δ(F,F') calculated directly.

6.3.5 The Energetic Consequences of F···F Bonding

As mentioned in the introduction, it is a general finding of the theory of atoms in molecules that all bonding interactions are associated with a *local* stabilization even when the absence of such bonding in an isomer results in a lower *total* energy. To obtain an estimate of the stabilizing contribution of a F···F bonding interaction, we compare the atomic energies in each of the two isomers: 1,8-difluoronaphthalene (1,8-DFN), which contains one F···F bond path, and 1,5-difluoronaphthalene (1,5-DFN) which is devoid of such an interaction.

The total energy of 1,8-DFN, the one containing the F···F bonding interaction, is actually higher than the 1,5-DFN isomer by 3.5 kcal/mol. A comparison of the corresponding atomic energies (Equation 3.60) in the two isomers explains this rather unexpected result. This comparison is given in the top panel of Figure 6.10. In the upper-left box of the figure (1,5-DFN), a relative atomic energy is defined as the difference between the

energy of the atom in question and the energy of *the most stable atom of the same element* in the molecule. One can see that in 1,5-DFN, C1 (and the symmetry equivalent C5) are the least stable carbon atoms in this molecule each being ~178 kcal/mol less stable than atoms C9 or C10. The destabilization of C1 and C5 is due to a significant loss of electron population (~0.46 e) to the neighboring more electronegative fluorine atom, as can be seen from the comparison of atomic charges in the lower-left box of Figure 6.10 for this molecule.

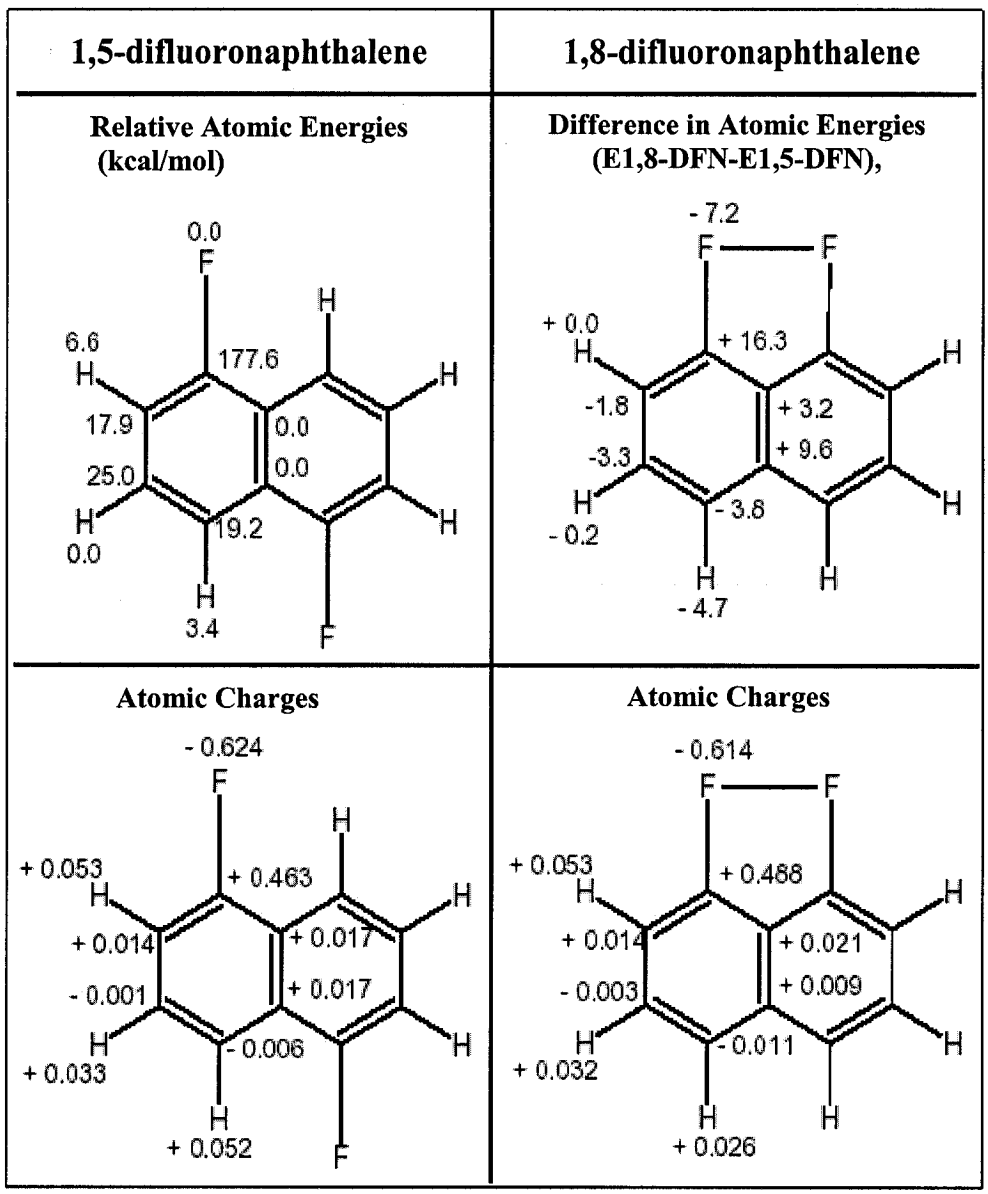

Figure 6.10. Comparison of the relative atomic energies (top panel) and atomic charges (lower panel) between the two isomers: 1,5-difluoronaphthalene (1,5-DFN) devoid of F···F interaction and 1,8-difluoronaphthalene (1,8-DFN) in which an F···F interaction occurs. The relative energies shown on the upper-right box for 1,5-DFN are given in kcal/mol and were calculated for each element taking the most stable atom of that element as the one with zero-relative atomic energy. The energies given for the 1,8-DFN isomer (upper-right box) are the difference between the atomic energy in that isomer and the corresponding atom in 1,5-DFN, given in kcal/mol. In 1,5-DFN, the absolute energies of a fluorine atom is -100.38453 au, that of the most stable carbon C9 (or C10) is -38.08982 au, and that of the most stable hydrogen H3 (or H6) is -0.61007 au. The total energy of 1,5-DFN is -584.53192 au and that of 1,8-DFN is -584.52637 au. The lower panel compares the AIM charges of the two isomers (in au).

From the figure one also finds that in 1,5-DFN, C1 and C5 are the only atoms other than the two fluorine atoms with an appreciable net charge. The same is true about the charge distribution in 1,8-DFN as can be seen from the lower-right box of Figure 6.10.

The upper-right box of Figure 6.10 displays the difference in the atomic energy between the two isomers defined as:

$$\Delta E(\Omega) = E_{1,8\text{-DFN}}(\Omega) - E_{1,5\text{-DFN}}(\Omega), \tag{6.6}$$

where Ω is a pair of equivalent atoms in the two isomers. The comparison shows that the fluorine atoms involved in the F‴F interaction in 1,8-DFN are more stable (as expected) than the corresponding ones in 1,5-DFN by 7.2 kcal/mol each. In other words, the F‴F interaction contributes ~14 kcal/mol of stabilization to 1,8-DFB over 1,5-DFB. The overall destabilization of 1,8-DFN with respect to its isomer can be traced to the carbon skeleton, particularly C1 (and its symmetry equivalent C8) which is destabilized by 16.3 kcal/mol, C10 which is destabilized by 9.6 kcal/mol, and C9 which is destabilized by 3.2 kcal/mol. A bookkeeping of the differences in the atomic energies of the remaining atoms in the molecule (which are more stable in 1,8-DFN) yields the total energy differences between the two isomers, i.e. $\sum_{all\ atoms} \Delta E(\Omega) = +3.4$ kcal/mol. The energetic destabilization of carbons 1, 8, 9 and 10 in 1,8-DFN with respect to 1,5-DFN can be the result of higher charge separation and more significant geometrical distortion of the ring system in 1,8-DFN to accommodate the two fluorine atoms in a relatively small space.

One cannot refer to the destabilization of C1,C9 and C10 in 1,8-DFN relative to the corresponding atoms in 1,5-DFN as the result of a steric repulsion since there are no forces operating in an equilibrium geometry. It must be also cautioned from the erroneous identification of the *local* stabilization energy of ~14 kcal/mol associated with the

formation of a F···F bond path as a "bond energy": It is not. It is what it is: a local stabilization energy. In fact, one cannot define a bond energy for the F···F bond in these compounds since this bond cannot be broken without the concurrent breaking of other bonds in the molecule.

To obtain an estimate for the F···F bond energy, an MP2(full)/6-31+G(d) geometry optimization for a fluoromethane dimer was performed, in head-to-head C_{3v} geometry (H_3C-F···F-CH_3). The calculation reveals that there is no net binding since a geometry optimization started with a F-F separation of 1.5 Å results in an ever increasing monomer-monomer separation. In a previous study, the interaction energy in the F-F...F-H dimer has been found to be ~-0.3 kcal/mol at three very different levels of theory (B3LYP/6-31G(d), B3LYP/6-311++G(d,p), and MP2/6-311++G(d,p)) and after correcting for basis set superposition error (BSSE) [94]. The bond properties reported for the F-F...F-H complex at the MP2 level (rFF'=2.713 Å, ρ_{BCP}=0.0073 au, $\nabla^2\Delta_{BCP}$=0.0389 au) [94] compare well with one of the weakest F...F interactions reported in the present study, the interaction in compound **2** (See Table 6.1).

6.3.6 Other Non-conventional Closed-Shell Bonding Interactions

An examination of Figure 6.5 shows, besides the F···F bonding interactions, several other non-conventional bonding interactions revealed by the presence of bond paths. The bond properties of these interactions are collected in Table 6.2.

Table 6.2. Bond properties of non-conventional weak bonding interactions. All entries are in atomic units except bond lengths and bond path lengths (BPL) which are in Å, and ε is dimensionless.

Cpd.	A···B	*r*FF'	BPL	ρ_{BCP}	$\nabla^2\rho_{BCP}$	G_{BCP}	K_{BCP}	$\mathscr{V}_{BCP}$	H_{BCP}	λ_1	λ_2	λ_3	ε
24	F···C1	2.5997	2.6031	0.0175	0.0668	0.0155	-0.0011	-0.0144	0.0012	-0.0142	-0.0124	0.0933	0.1450
24	F···C2	2.6147	2.6184	0.0170	0.0648	0.0151	-0.0011	-0.0139	0.0012	-0.0137	-0.0119	0.0904	0.1522
24	F···C3	2.6126	2.6144	0.0169	0.0641	0.0149	-0.0011	-0.0138	0.0011	-0.0131	-0.0124	0.0896	0.0578
25	F···O1	2.5844	2.5850	0.0169	0.0722	0.0165	-0.0016	-0.0149	0.0016	-0.0166	-0.0154	0.1042	0.0833
25	F···O2	2.6211	2.6218	0.0157	0.0657	0.0151	-0.0013	-0.0138	0.0013	-0.0152	-0.0136	0.0945	0.1153
25	F···O3	2.6022	2.6029	0.0163	0.0689	0.0158	-0.0014	-0.0143	0.0015	-0.0159	-0.0144	0.0992	0.0992
3	C···C	2.8528	2.8767	0.0113	0.0385	0.0081	-0.0016	-0.0065	0.0016	-0.0085	-0.0052	0.0522	0.6455
13	H···Br	2.7108	2.8155	0.0133	0.0478	0.0100	-0.0019	-0.0081	0.0020	-0.0105	-0.0059	0.0643	0.7767
21	H···Cl	2.6095	2.7508	0.0136	0.0551	0.0113	-0.0025	-0.0089	0.0025	-0.0113	-0.0047	0.0710	1.4149
15	H···O	2.6615	2.8019	0.0085	0.0333	0.0070	-0.0014	-0.0056	0.0014	-0.0049	-0.0018	0.0399	1.6971
16	H···O	2.1344	2.1919	0.0208	0.0818	0.0176	-0.0029	-0.0147	0.0029	-0.0235	-0.0202	0.1255	0.1584
4	$H^{\delta+}\cdots H^{\delta-}$	2.1087	2.4115	0.0117	0.0430	0.0087	-0.0020	-0.0067	0.0020	-0.0107	-0.0049	0.0586	1.1876
7	$H^{\delta+}\cdots H^{\delta-}$	2.5062	3.4469	0.0065	0.0245	0.0048	-0.0013	-0.0035	0.0013	-0.0025	-0.0022	0.0293	0.1513
9	H···H	1.9128	2.1240	0.0145	0.0531	0.0112	-0.0020	-0.0092	0.0021	-0.0150	-0.0103	0.0784	0.4562

A glance at the table reveals that these bonding interactions are weak to very weak, having ρ_{BCP} ranging from ~0.02-0.01 au. All of these interactions exhibit positive values for H_{BCP} as well as positive Laplacians at the BCP and can therefore be classified as closed-shell interactions. In all cases, these weak interactions result in ring(s) closure with the concurrent appearance of the ring critical point(s). The satisfaction of the Poincaré-Hopf relationship has been verified for each molecular graph as mentioned previously. We shall now discuss each class separately.

6.3.6.1 F···C and F···O Interactions

Mallory et al. [81] describe two very interesting derivatives of anthracene (**24**, **25**) exhibiting unusually high fluorine-fluorine spin-spin coupling constants despite the presence of an intervening phenyl group in **24** and a carbonyl oxygen in **25**. (See structures **24** and **25** in Figure 6.1 and the corresponding molecular graphs in Figure 6.5(c)). The three unusual bond paths traced in these two compounds have been labeled clockwise as bond 1, 2 and 3 (Figure 6.1). A comparison of all the bond properties of these six bonds reveals a striking similarity, even between the F···C and the F···O sets of bonds. Perhaps the most significant difference between the two sets is the difference between the internuclear distance and the bond path length. The difference averages to 0.003Å for the F···C set and only 0.001Å for the F···O set. The F···C set is therefore characterized by more curved bond paths, as can be also discerned by visual inspections of the molecular graphs of **24** and **25** in Figure 6.5(c). Alkorta, Rozas, and Elguero reported an interaction energy of -0.67 kcal/mol in the F-F...OH_2 complex at the MP2/6-311++G(d,p) level of theory after BSSE correction. The bond properties of this complex (rFF'=2.641 Å, ρ_{BCP}=0.0221 au, $\nabla^2\Delta_{BCP}$=0.0534 au) [94] are comparable with the F...O bond properties we reported in Table 6.1 for compound **25**. This similarity is particularly interesting because in the F-F...OH_2 complex the F...O distance is free to vary with no geometric constraints imposed by the rigidity of the molecular frame unlike in compound **25**. The same group also report the results for the F-F...CO complex which at the BSSE-corrected MP2 level are (rFF'=3.005 Å, ρ_{BCP}=0.0062 au, $\nabla^2\Delta_{BCP}$=0.0268 au) [94], values indicating a significantly weaker interaction than the ones reported here. Alkorta et al. reported a -0.33 kcal/mol for the F-F...CO interaction [94].

6.3.6.2 C···C Interaction

The two *sp*-carbon atoms in compound **3** are separated by only ~2.9 Å, much less than the twice the van der Waals radius of carbon (3.5 Å) [88]. The atoms are found to be bonded by a weak closed-shell interaction exhibiting a significantly curved bond path. The curvature of the bond path can be discerned from the molecular graph in Figure 6.5(a) as well as from the relatively large difference between the bond path length and the internuclear distance (~0.01 Å).

6.3.6.3 C-H···X (X=Cl, Br), C-H···O=X (X=C, N), and C-H···H-X (X=C, O) Interactions

The last class of weak closed-shell bonding interaction found in this series of molecules includes hydrogen bonding (in compounds **13**, **15**, **16**, and **21**), dihydrogen bonding (in compound **9**), and hydrogen-hydrogen bonding (in compounds **4**, and **7**). These provide further examples of such interactions already known and fully characterized in the literature [102,107-111,113,114,117,118].

6.4 Conclusions

The F···F bonding interaction is likely to occur in polyfluorinated aromatic compounds when the F-F internuclear separation is 2.3-2.8 Å despite the relative orientation of the two C-F internuclear axes and whether these are coplanar with the ring system or not. The presence of such bonding in 1,8-difluoronaphthalene (1,8-DFN) has been shown to impart *ca.* 14 kcal/mol of stabilization *locally*, i.e., to the two fluorine atoms involved in the bonding. The molecule is, however, *less* stable than its isomer 1,5-

difluoronaphthalene (1,5-DFN) by ~ 3 kcal/mol, an isomer that lacks this bonding interaction. The resolution of this apparent inconsistency is brought about by an atom-by-atom comparison of atomic energies between the two isomers. The estimate of the stabilization energy of the F···F bonding was obtained by comparing the atomic energies of the fluorine atoms in 1,8-DFN with the corresponding energies of the fluorine atoms in 1,5-DFN, which lacks this interaction. Each of the fluorine atoms participating in the F···F interaction is 7.2 kcal/mol more stable than the corresponding fluorine atom in the isomer devoid of F···F bonding. On the other hand, the comparison also reveals that four carbon atoms in 1,8-DFN are significantly less stable than their counterparts in 1,5-DFN. The sum of these relative atomic stabilization and destabilization energies over all the atoms in the two isomers yields the net difference between the total molecular energies of the two isomers (1,8-DFN is 3 kcal/mol less stable than the 1,5-DFN). Thus, the local stabilization associated with the F···F bond path should *not* be mistakenly identified as a bond energy since the later implies a bond dissociation. It is impossible to achieve the dissociation of an F···F bond in this series of molecules without the concurrent dissociation of other bonds.

Several other interesting non-classical closed-shell interactions have also been found and characterized in these compounds including F···C, F···O, C···C bonding as well as several variants of hydrogen bonding, dihydrogen bonding and hydrogen-hydrogen bonding.

The present work is yet another testimonial as to the usefulness, power, and richness of the bond path concept [123] and of the theory of atoms in molecules [29] in general.

Chapter 7 The First Example of a Cage Critical Point in a Single Ring: A Novel Twisted α-Helical Ring Topology

7.1 Introduction

Several crystallographic studies report short halogen-halogen contacts [84,87-89,124-126 and references therein]. Weak closed-shell bonding interactions between halogens have also been described on a number of occasions on the basis of the topological properties of the electron density [69,91-93,95,127]. Only recently, the intramolecular fluorine-fluorine closed-shell bonding has been characterized in detail on the basis of the topology of the electron density [127]. In the present chapter, this closed-shell bonding interaction will be denoted by the symbol F-F. This interaction, when present in a difluorinated polycylcic aromatic hydrocarbon (PAH), often results in the closure of an intramolecular ring [127]. In most of the difluorinated PAHs previously studied, these rings are flat or depart little from planarity and exhibit a single characteristic ring critical point (RCP). In contrast, when the F-F bonding is present between two sterically crowded fluorine atoms (as in the compounds depicted in Figure 7.1), the resulting ring is highly puckered. This marked departure from planarity gives rise to a very unusual, yet mathematically possible, topology of the ring's electron density. Instead of exhibiting a single RCP, such a highly twisted ring is characterized by the emergence of *two ring critical points and a cage critical point* (CCP). The emergence of the CCP together with the appearance of the additional RCP are necessary for the satisfaction of the Poincaré-Hopf relationship (equation 3.4).

In this chapter, the first example of an actual molecular system where a cage is bounded by two ring surfaces is reported. This type of characteristic set remained only a

possibility until now, as stated in 1990 by Bader on page 37 of his book [29]: "*While it is mathematically possible for a cage to be bounded by only two ring surfaces, the minimum number found in an actual molecule so far is three, as in bicyclo [1.1.1] pentane, for example.*" To our knowledge, this statement (which was restated in 2000 [128]) remained true to the time of writing of the present chapter.

7.2 Computational Details

The geometries of the three molecules have been fully optimized at the B3LYP/6-31G(*d*) level, and the frequencies were calculated at that level to ensure that local minima have been located as evidenced by the lack of imaginary frequencies. Single-deterimant KS "wavefunctions" were obtained at the B3LYP/6-311++G(*d,p*)//B3LYP/6-31G(*d*) level. All electronic structure calculations were performed using the Gaussian 03 package [51]. Molecular graphs, envelope maps, and bond properties were obtained using AIM2000 [104,105]. Gradient vector field plots were prepared using Morphy98 [129,130].

The characteristic set of critical points for each one of the three compounds studied in this work satisfies the Poincaré-Hopf relationship (Equation 3.4).

7.3 Results and Discussion

A case study of 1,12-difluorobenzo[*c*]phenanthrene (**I**) and two of its derivatives (4-methyl derivative (**II**), and 4-cyano derivative (**III**)) are presented. These derivatives are included in the study to ensure that this novel ring topology can survive upon inducing steric and electronic asymmetry into the polycyclic aromatic hydrocarbon backbone, a fact confirmed by our observations as described below. Figure 7.1 displays the atom

numbering scheme used in this chapter along with the chemical structures of the three compounds.

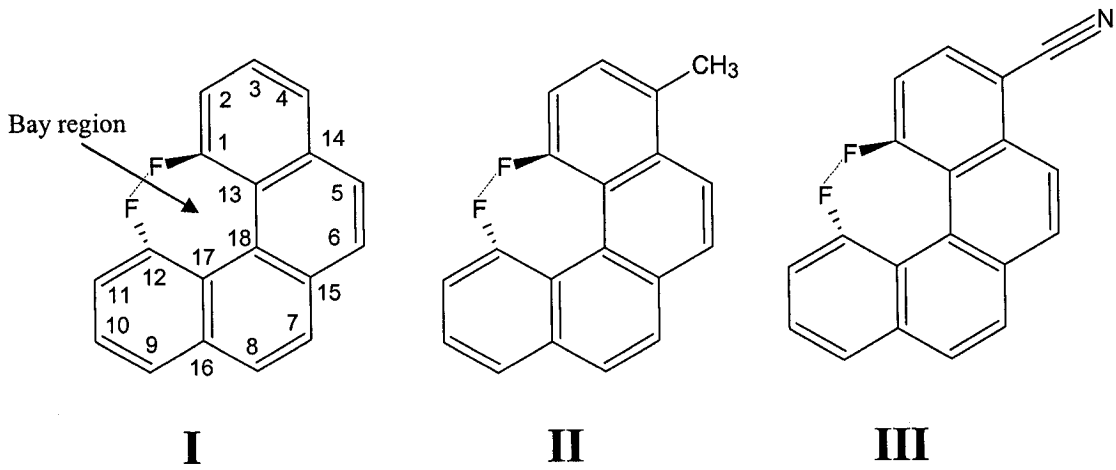

I **II** **III**

Figure 7.1. 1,12-Difluorobenzo[*c*]phenanthrene (**I**), the parent compound with the numbering scheme, 4-methyl-1,12-difluorobenzo[*c*]phenanthrene (**II**), and 4-cyano-1,12-difluorobenzo[*c*]phenanthrene (**III**).

All three compounds exhibit the same unusual topology in the bay region: a cage critical point enclosed by two ring surfaces in the same ring (Figure 7.2).

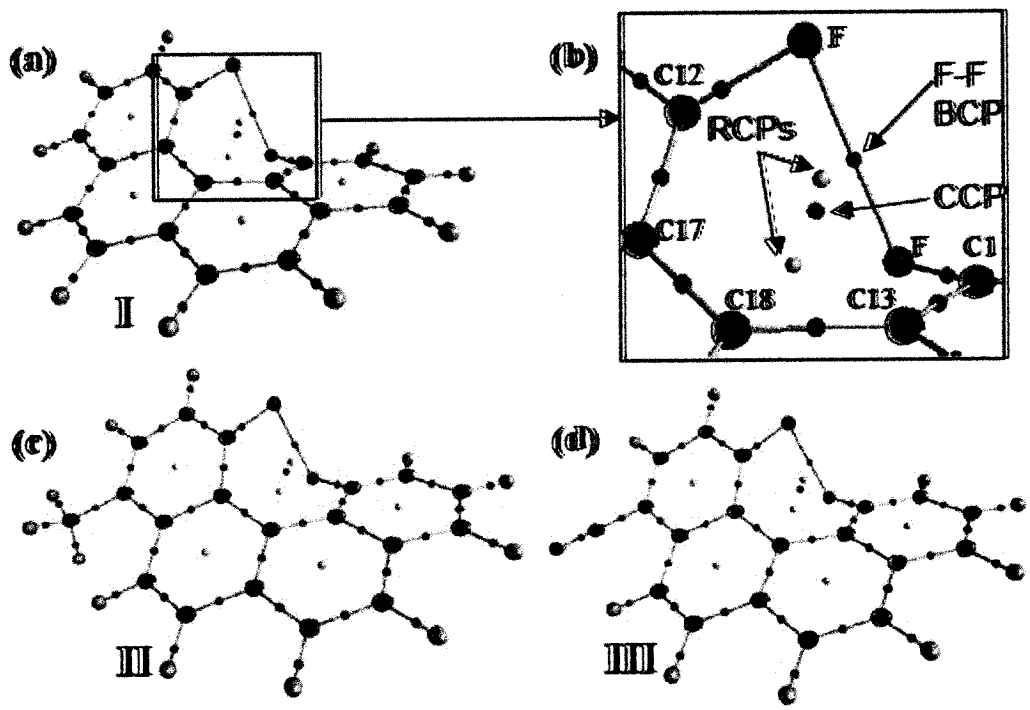

Figure 7.2. Molecular graphs (set of bond paths and critical points) of the three molecules defined in Fig. 7.1 **I** (a), **II** (c), and **III** (d). (b) represents a blow-up of the region of interest showing the bay region ring involving the two fluorine atoms. *Colour code for atoms (large spheres):* Carbon (black), hydrogen (gray), fluorine (gold), nitrogen (blue). *Colour code for critical points (small spheres):* Bond critical points (BCPs, red), ring critical points (RCPs, yellow), and cage critical points (CCPs, green).

The molecular frames of these molecules are highly strained to accommodate the two fluorine atoms in the bay region. As a result, the aromatic ring system in each of these molecules adopts a distinctive staircase α-helical geometry. Each one of the four fused six-membered rings (6-MR) belonging to the polycylic aromatic hydrocarbon (PAH) is slightly twisted as a consequence of this general α-helical geometry. Each one of these 6-MRs belonging to the PAH backbone has a single ring critical point as is usually the case for the overwhelming majority of ring systems. On the other hand, the 7-MR closed

by the F-F bonding and involving the two fluorine atoms and C1, C13, C18, C17, and C12 is highly puckered and is characterized by two ring critical points and a cage critical point, Figure 7.2(b). The cage critical point appears in the fold created by two ring surfaces, an upper and a lower, each with its own ring critical point. The visual inspection of Figure 7.2 also demonstrates that the substituents at position 4 have a negligible effect on the spatial disposition of the three critical points arising in the 7-MRs. The plane of the gradient vector plot presented in Figure 7.3(a) contains the two fluorine nuclei, the F-F bond critical point, the cage critical point and the two carbon nuclei C18 and C15 which all fall on the C_2-axis of **I**.

(a)

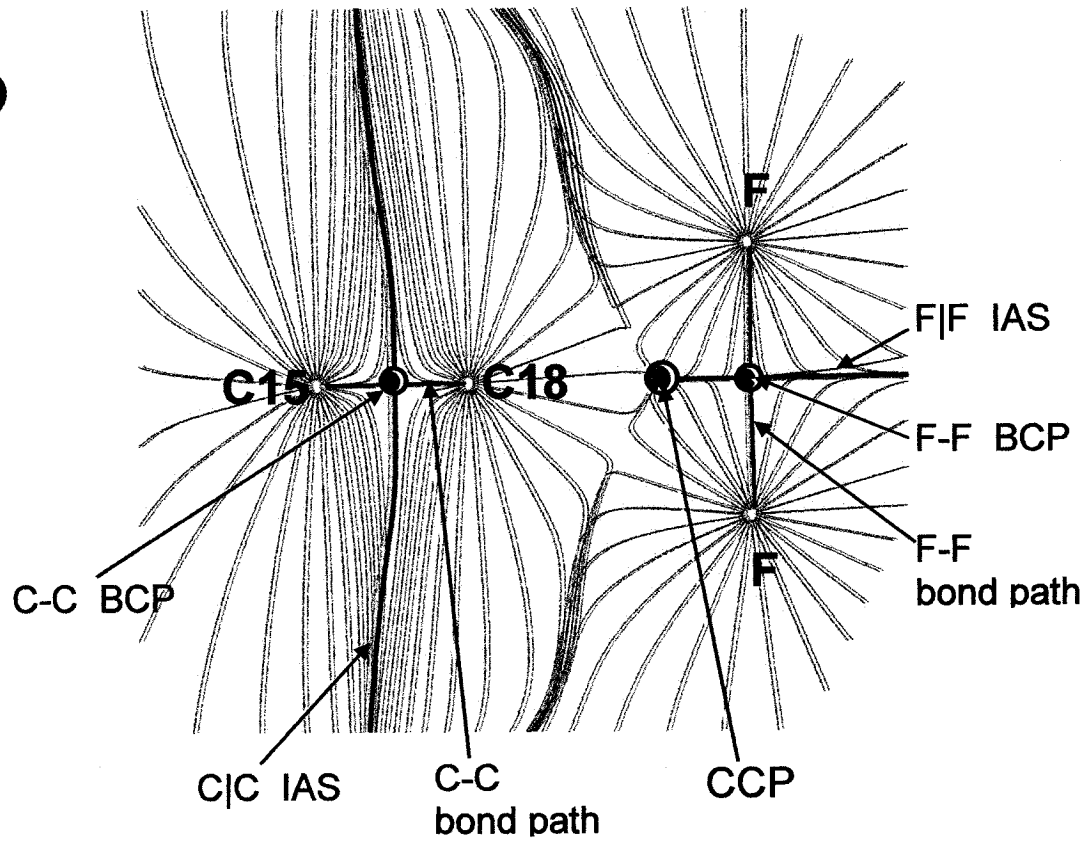
F
F|F IAS
C15
C18
F-F BCP
F-F
bond path
F
C-C BCP
C|C IAS
C-C
bond path
CCP

(b)

Figure 7.3. (a) A gradient vector field map showing the $\nabla\rho$ trajectories in the plane defined by the two fluorine atoms and C18 (C15 also falls on this plane) for the 1,12-difluorobenzo[*c*]phenanthrene molecule. For clarity, two representations of the molecular graph of this molecule indicating the plane in question are displayed in (b). In the gradient vector field plot, the thick line joining the C15 and C18 atoms as well as the two fluorine atoms are the bond paths linking these pairs of nuclei. The intersections of the interatomic zero-flux surfaces (IAS) with the plane of the plot are also displayed. In (a), the red circles are the bond critical points (BCPs) and the green circle represent the cage critical point (CCP). There is no ring critical point in the plane of the plot. As can be seen from the two representations of the molecular graph in (b), the two ring critical points (indicated by the small yellow circles) are located above and below the plane of the plot (a).

Moreover, the bond paths of the F-F and of the C18-C15 bonding interactions also fall in the plane of the plot of Figure 7.3 and are denoted by the thick black lines connecting the bonded nuclei. The red circles in the figure indicate the positions of the bond critical points. The intersection of the interatomic surfaces separating these two pairs of bonded atoms and the plane of the drawing are also depicted in Figure 7.3(a) as thick lines crossing the bond paths at the corresponding bond critical points. For clarity, the plane of the gradient vector field plot (Figure 7.3(a)) is also shown in light gray on two views of the molecular graph of I in Figure 7.3(b).

All the $\nabla\rho$ trajectories in Figure 7.3(a) originate at infinity except the set which originates at the cage critical point and terminates at each of the two fluorine nuclei, at the F-F bond critical point, or at the nucleus of C18. The $\nabla\rho$ trajectories originating at the cage critical point and terminating at each of the two ring critical points are not shown since the two ring critical points are out of the plane of this plot, one at one side of the plane and the other on the opposite side (left part of Figure 7.3(b)). There are no trajectories coming from infinity that reach the cage critical point since such a point is completely enclosed in the molecular space.

When two atoms are bonded, i.e. their nuclei are linked by a bond path, the bond path defines the unique axis of the BCP and the two atoms share an interatomic *surface*. In a ring, the axis of a RCP is defined by the line created by the intersection of the interatomic surfaces of the atoms forming the ring. Thus, the atoms in a ring all share a *line*. Finally, atoms in a cage all meet at a *point*, the CCP, where all their interatomic surfaces intersect [131].

Figure 7.4 displays another view of the molecular graph of **I**, but this time also including the two unique trajectories linking the cage critical point to the two ring critical points, on the two ring surfaces. The broken line connecting these three critical points is the line where all the interatomic surfaces intersect, each RCP-CCP segment representing a ring axis.

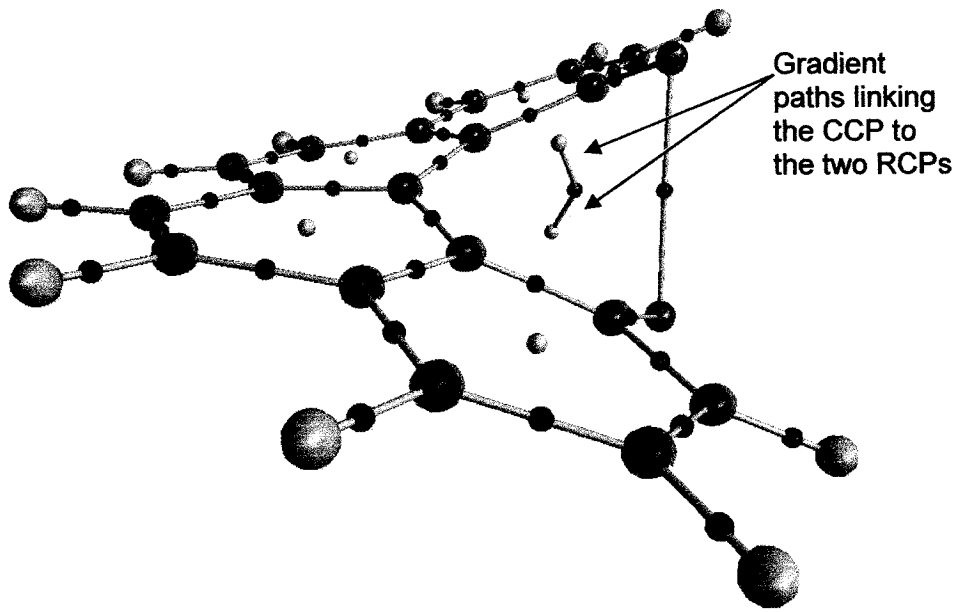

Figure 7.4. Another representation of the molecular graph of **I** but with the gradient paths linking the two ring critical points to the cage critical points also displayed. *Colour code for atoms (large spheres):* Carbon (black), hydrogen (gray), fluorine (gold), nitrogen (blue). *Colour code for critical points (small spheres):* Bond critical points (BCPs, red), ring critical points (RCPs, yellow), and cage critical points (CCPs, green).

Table 7.1 summarizes the geometry of the 7-MR topological features in terms of the distance matrix relating the cage critical point, the two ring critical points, and one set of symmetry unique nuclear critical points (one half of the ring, the other being equivalent by a 180° rotation around the C_2-axis).

Table 7.1. Distance matrix defining the location of the cage critical point and the two ring critical points in relation to other key critical points in a symmetry-unique half of the seven-membered ring. (All distances are in angstroms).

	CCP	**RCP1**	**RCP2**	**BCP (F-F)**	**F(1)**	**C1**	**C13**
CCP	0						
RCP1	0.606	0					
RCP2	0.608	1.148	0				
BCP (F-F)	0.885	1.225	1.226	0			
F(1)	1.553	2.065	1.416	1.268	0		
C1	1.629	1.802	1.728	1.734	1.355	0	
C13	1.669	1.542	1.758	2.333	2.389	1.415	0
C18	1.724	1.631	1.630	2.609	2.911	2.541	1.450

One can see from the table that the CCP is appreciably distant from the two RCPs (by 0.6 Å) and from the F-F BCP (by 0.9 Å). The latter BCP is also well separated from the two RCPs (by 1.2 Å). These observations indicate a topologically stable set of critical points, since when they are in close proximity (for example, 0.1-0.2 Å) they may annihilate each other during small geometrical changes akin to molecular vibrations.

Table 7.2 shows clearly the general trend of the electron density, which decreases in the order of BCP > RCP > CCP.

Table 7.2. Local properties of the electron density and of the energy densities at the cage critical point, the ring critical points, and the F-F bond critical point in compounds I, II, and II. All data are in atomic units.

	$\rho(\mathbf{r})$	$\nabla^2(\mathbf{r})$	$G(\mathbf{r})$	$V(\mathbf{r})$	$H(\mathbf{r})$
CCP					
I	0.0083	0.0515	0.0101	-0.0074	0.0027
II	0.0086	0.0538	0.0106	-0.0078	0.0028
III	0.0086	0.0538	0.0106	-0.0078	0.0028
iii[(a)]	0.0083	0.0533	0.0103	-0.0072	0.0031
RCC					
I	0.0099	0.0490	0.0101	-0.0079	0.0022
II[(b)]	0.0103	0.0515	0.0106	-0.0084	0.0023
III[(b)]	0.0101	0.0507	0.0104	-0.0082	0.0022
iii[(a)]	0.0100	0.0515	0.0105	-0.0080	0.0022
BCP(F-F)					
I	0.0161	0.0768	0.0176	-0.0161	0.0016
II	0.0177	0.0864	0.0197	-0.0178	0.0019
III	0.0178	0.0870	0.0198	-0.0179	0.0019
iii[(a)]	0.0185	0.0881	0.0211	-0.0203	0.0009

(a) Lower case Roman (iii) refers to compound III but for an electron density calculated with a smaller basis set (B3LYP/6-31G(d)) than the remainder of the data, all calculated at the B3LYP/6-311++G(*d,p*) level of theory as detailed in the "Computational Method" section.

(b) Since compounds **II** and **III** are less symmetric than the parent compound **I**, the two ring critical points, while very similar, are not symmetry-equivalent. The differences between the properties of two non-equivalent RCPs were found to be too small (in the third decimal) to warrant separate listing. We report averages in these cases.

The Laplacian exhibits a decreasing order of charge concentration BCP > CCP > RCP. An examination of the kinetic energy density reveals that electrons move faster at the BCP than at either the two RCPs or the CCP. From the table one also can conclude that substitutions in the PAH carbon skeleton appear to have minimal effects on the property densities determined at the critical points characterizing the 7-MR. In order to assess the sensitivity of the newly found unusual ring topology to basis set, the electron density of **III** using a much smaller basis set (6-31G(d)) than the rest of the work presented here (6-

311++G(d,p)) has been also analyzed. The density of III obtained with the small basis set is denoted by **iii**. The analysis of **iii** reveals that the topology and geometric arrangement of the critical points in the 7-MR is preserved with very little change. Furthermore, the individual property densities also exhibit a marked basis set insensitivity as can be gleaned from Table 2 by comparing the entries for **III** and **iii**.

7.4 Conclusions

A novel topological feature in ring systems is presented for the first time: A cage critical point arising within the fold of two ring surfaces belonging to a single ring of bonded atoms. The molecules in which this feature is observed are highly crowded difluorinated polycyclic aromatic hydrocarbons in which the two fluorine atoms are in close spatial proximity which leads to the appearance of a bond path linking their nuclei. The appearance of the F-F bond path leads to the closure of a highly puckered seven-membered ring in which two ring surfaces enclose a cage critical point. To the best of the author's knowledge, this is the first report of this type of cage critical point in a molecular system.

Chapter 8 The Host-Guest Inclusion Complex of p-Chlorophenol inside α-Cyclodextrin: An Atoms in Molecules Study

8.1 Introduction

Since their discovery in 1891 by Villiers [132], cyclodextrins have stimulated research in many fields. Moreover, they are used in many industries including the pharmaceutical, biotechnology, food and cosmetics sectors [133]. This popularity is due to the fact they are seminatural products that do not pose environmental risks [133].

Cyclodextrins (CD) are cyclic oligosaccharides which form a cavity with hydrophobic character on the inside and hydrophilic properties on the outside [133-135]. The best known are the α-CD, β-CD and γ-CD which contain six, seven and eight glucopyranose units, respectively. Modified cyclodextrins are effective templates for use in the chemical synthesis of a large variety of molecular hosts. By suitable modifications it is possible to design cyclodextrins to host a particular guest, which in turn leads to new areas of supramolecular chemistry [133,134].

Modifications to the cyclodextrins result in a wide range of photochemical reactions, which can be utilized in light harvesting molecular devices and photochemical frequency switchers [136,137]. Furthermore, modified cyclodextrins in solution can be used as molecular, temperature and pH sensors, and on surfaces cyclodextrins form semi-permeable membranes and electrodes [138-144].

In this chapter a study of the inclusion complex of *p*-chlorophenol inside α-cyclodextrin (α-CD) by the theory of atoms in molecules (AIM) is reported [29,30] that is based on the topological properties of the electron density, denoted by ρ. A quantitative

comparison of some AIM properties of isolated *p*-chlorophenol (PCP) and the inclusion complex (PCP-CD) is used, and some weak interactions within the host-guest complex are characterized. Furthermore, the electrophilic aromatic substitution on the *p*-chlorophenol in the isolated state and inside α-CD is compared.

8.2 Results and discussion

As was explained in Chapter 3, a chemical bond (or interaction) between two atoms is defined in AIM theory by the existence of a bond critical point (BCP) between the two atoms and a bond path (trajectory of $\nabla\rho$), which contains the bond critical point and links the two atoms. Weak interactions are characterized by low values of ρ at the BCP. The goal of this chapter is to gain insight into the interactions between the guest compounds and the cyclodextrins in inclusion complexes using AIM. This type of study can be useful to predict qualitatively the solubility of compounds inside cyclodextrins by analyzing their interactions with the cyclodextrin and to provide some qualitative information on the strength of the bonding from the electron density at the BCP. One of the first quantitative discussions of the relationships between AIM parameters and bond energies was given for hydrogen bonding about twenty years ago by Boyd and Choi [96,97], whose studies show strong correlations between some AIM parameters such as ρ and $\nabla^2\rho$ at the BCP and the hydrogen-bond energies.

For convenience the X-ray diffraction structure [145] of PCP-CD is used for the calculations. A full geometry optimization would be computationally too expensive. Single-determinant Kohn-Sham "wavefunctions" were obtained at the B3LYP/6-31+G(d) level for PCP, with the same geometry that it has inside α-CD, and also for the inclusion

complex (PCP-CD). Therefore, this study does not consider the geometry changes in PCP produced by the inclusion in α-CD. The electronic structure calculations were performed using the Gaussian 03 package [53], and the molecular graphs were obtained using AIM 2000 [104].

Figure 8.1 shows clearly the bond (BCP) and ring (RCP) critical points, as well as the bond paths in the case of the isolated PCP. Figure 8.2 illustrates the molecular graph for PCP inside α-CD.

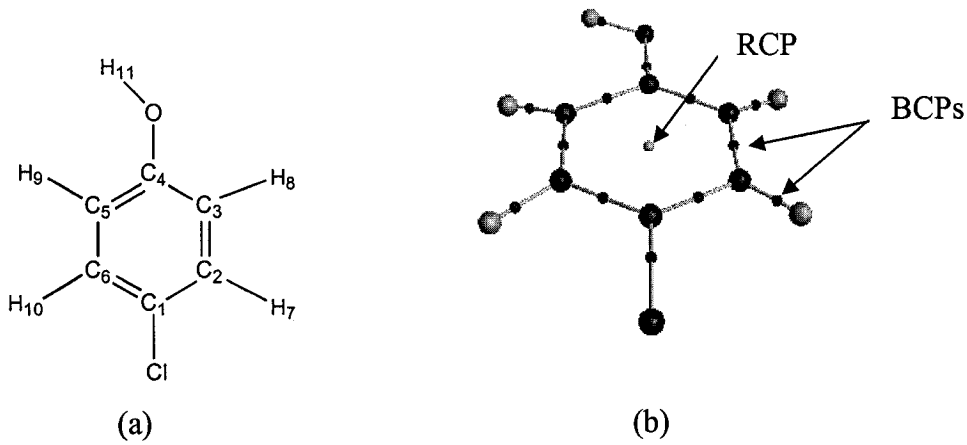

(a) (b)

Figure 8.1. *p*-Chlorophenol
(a) The numbering scheme used in this study in *p*-chlorophenol.
(b) The molecular graph of *p*-chlorophenol.

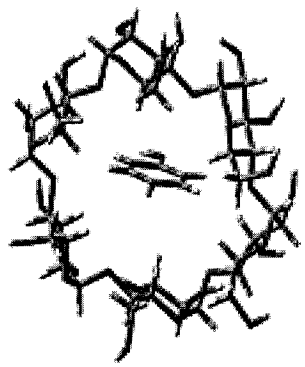

(a)

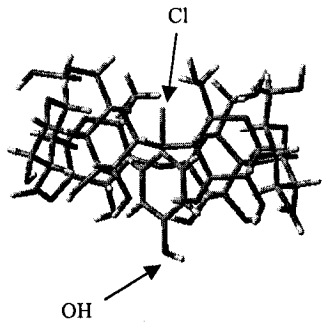

(b)

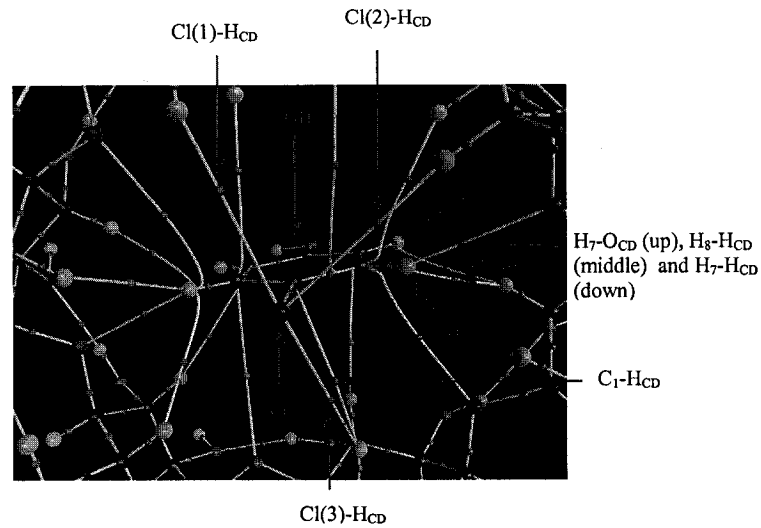

(c)

Figure 8.2. The inclusion complex of p-chlorophenol with the α-cyclodextrin.
(a) The *p*-chlorophenol inside the α-cyclodextrin viewed from above.
(b) Side view of the *p*-chlorophenol inside the α-cyclodextrin.
(c) The molecular graph of *p*-chlorophenol inside the α-cyclodextrin (the ring and cage critical points are not shown to illustrate more clearly the weak interactions between the *p*-chlorophenol and the α-cyclodextrin).

The molecular graph of PCP inside α-CD is essentially unchanged from that of isolated PCP, although many gradient trajectories that connect the nuclei of PCP and the nuclei of α-CD can be observed. The gradient trajectories correspond to the weak interactions between PCP and α-CD. For clarity, only the bond critical points are shown in the inclusion complex (ring and cage critical points have been omitted).

Table 8.1 lists the electron density (ρ), the negative of the Laplacian* and ellipticities (ε) at some BCPs. Table 8.2 characterizes the RCPs in terms of ρ and $-\nabla^2\rho$.

Table 8.1. Electronic properties at some bond critical points of *p*-chlorophenol in the isolated state (PCP) and inside α-cyclodextrin (PCP-CD) (in atomic units).

PCP	ρ	$-\nabla^2\rho$	ε	PCP-CD	ρ	$-\nabla^2\rho$	ε
C_1-Cl	0.2038	0.3164	0.0519	C_1-Cl	0.2019	0.3134	0.0572
C_4-OH	0.2803	0.3560	0.0192	C_4-OH	0.2817	0.3915	0.0197
O-H	0.3552	1.9155	0.0176	O-H	0.3552	1.9218	0.0175
C_1-C_2	0.3138	0.8563	0.2256	C_1-C_2	0.3131	0.8499	0.2269
C_2-C_3	0.3157	0.8646	0.2028	C_2-C_3	0.3154	0.8591	0.1995
C_3-C_4	0.3329	0.9935	0.2321	C_3-C_4	0.3332	0.9960	0.2254
C_2-H_7	0.3927	2.0213	0.0082	C_2-H_7	0.3945	2.0389	0.0076
C_3-H_8	0.3885	1.9734	0.0121	C_3-H_8	0.3900	2.0000	0.0104

Table 8.2. Electronic properties at the ring critical point of *p*-chlorophenol in the isolated state (PCP) and inside α-cyclodextrin (PCP-CD) (in atomic units).

	ρ	$-\nabla^2\rho$
PCP	0.0214	-0.1733
PCP-CD	0.0217	-0.1727

* Positive values of $-\nabla^2\rho$ indicate concentration of charge, whereas negative values indicate depletion of charge.

Analysis of the bond critical points shows that there is no trend in the effect on the AIM properties of PCP due to inclusion in the α-CD. For example, PCP exhibits BCPs in the C_1-C_2 and C_2-C_3 bonds with higher values of ρ and $-\nabla^2\rho$ in the isolated state than inside α-CD, whereas the opposite is observed for the BCP of the C_2-H_7 bond.

The ellipticity provides a measure of the π character of a bond [29]. As in the cases of ρ and $-\nabla^2\rho$, there is no trend in the effect on the ellipticities of the bonds of PCP by the inclusion in α-CD. For example, the ellipticity of the C_1-C_2 bond in PCP is lower than that of the inclusion complex PCP-CD, whereas the ellipticity of the C_3-C_4 bond is higher in the isolated compound. In general, it can be concluded that the α-CD has a negligible effect on the π character of PCP.

The electron density at the RCP is slightly higher in the inclusion complex than in isolated PCP. Additional insight into the structure is provided by $-\nabla^2\rho$. In particular, the isolated PCP exhibits a slightly more negative value of $-\nabla^2\rho$ than the inclusion complex. This indicates a greater depletion of charge around the RCP in the isolated state than that inside the cavity. Therefore, encapsulation of PCP by α-CD increases ρ at the RCP and makes the charge around the RCP less depleted.

8.2.1 Topological characterization of the weak interactions

Figure 8.2 shows several bond paths connecting the hydrogen and oxygen atoms of the α-CD with all atoms of PCP with the exception of the hydroxyl group and its bonded carbon (C_4) and H_9. These four atoms are not sufficiently inside the α-CD to produce a weak interaction with the cavity (Figure 8.2 (b)). Table 8.3 provides ρ and $-\nabla^2\rho$ at the

"BCPs" for the weak interactions exhibited by chlorine (Cl(1)-H_{CD}, Cl(2)-H_{CD} and Cl(3)-H_{CD}) and its bonded carbon of the benzene ring (C_1-H_{CD}).

Table 8.3. Electronic properties at the "bond critical points" of the weak interactions of chlorine and C_1 of the *p*-chlorophenol with the α-cyclodextrin in the inclusion complex (in atomic units).

PCP-CD	ρ	$-\nabla^2\rho$
Cl(1)-H_{CD}	0.0038	-0.0124
Cl(2)-H_{CD}	0.0044	-0.0148
Cl(3)-H_{CD}	0.0032	-0.0112
C_1-H_{CD}	0.0032	-0.0104

Figure 8.2 also illustrates clearly the unusual topology exhibited by the hydrogen atoms bonded to C_2 and C_6 (H_7 and H_{10}) in the benzene ring. For example, there are five bond paths that connect H_{10} with the nuclei of the α-CD. Three of them are weak interactions with hydrogen atoms of the cavity (2.4 Å average distance) whereas the other two are with two oxygen atoms that connect two glucopyranose units (2.85 Å average distance). Comparison with Table 8.1 shows that ρ and $-\nabla^2\rho$ are two and one order of magnitude less with opposite sign (typical of a closed-shell interaction [29]), respectively, than those for the BCPs between the atoms of the PCP. Therefore, they are classified as weak interactions.

8.2.2 Electrophilic aromatic substitution

Bader and Chang in 1989 [146] carried out a study on the electrophilic aromatic substitution in substituted benzenes based on the Laplacian values at the link points in the valence shell of the carbon. These points, which by definition link the bonded charge concentrations in the valence shell of the carbon, indicate that the charge concentration is

a maximum in both directions perpendicular to the path that connects these two maxima and a minimum along this line [29]. Thus, the link points exhibit the second highest charge concentration of the VSCC (valence shell charge concentration) of the atom. Their study predicts the observed directing and activating-deactivating effects of a substituent in the electrophilic aromatic substitution. Following this idea, Castillo and Boyd (next chapter) in their work on the resonance effect in α and β-halogen naphthalenes corroborated the results of Bader and Chang. The relative location of these saddle points in benzene derivatives are over and under the plane of the ring. Therefore, it is reasonable to think of them as possible sites for electrophilic attack. Figure 8.3 illustrates the location of these link points in benzene derivatives. Table 8.4 provides $-\nabla^2\rho$ at the link points for C_2 and C_3 (the values reported are the averages between the above and below the plane carbon-carbon link points).

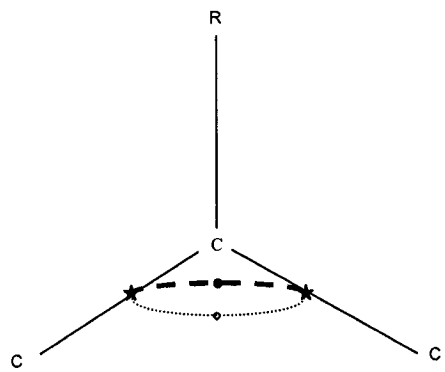

Figure 8.3 Atomic graph describing the link points of the VSCC of a carbon in benzene derivatives. The maximum charge concentrations and the link points are denoted by asterisks and dots, respectively. The solid link line is in the plane, the dashed link line is above the plane and the gray link line is below the plane. R represents an atom or a group of atoms.

Table 8.4. $-\nabla^2\rho$ at the carbon-carbon link points for C_2 and C_3 of *p*-chlorophenol in the isolated state (PCP) and inside α-cyclodextrin (in atomic units).

	C_2	C_3
PCP	0.1484	0.1705
PCP-CD	0.1493	0.1620

The hydroxyl group is a stronger *ortho*-directing group than chlorine, and, therefore, the C_3 position is more activated for electrophilic attack than the C_2 position. As can be seen in Table 8.4, $-\nabla^2\rho$ at the carbon-carbon link points is consistent with this experimental fact [157]; C_3 exhibits a higher value of $-\nabla^2\rho$ at the carbon-carbon link points than C_2 for both systems. Similar results are obtained for the C_5 and C_6 positions. It can be seen that the α-CD has a clear effect on the $-\nabla^2\rho$ at those link points. The α-CD increases $-\nabla^2\rho$ at the link point of C_2 and decreases $-\nabla^2\rho$ considerably at the link point of C_3. Thus, the effect of encapsulation of PCP by α-CD is to make C_3 a little less reactive relative to C_2 with respect to electrophilic aromatic substitution.

However, the hydrogens of the benzene ring, which are the leaving groups in the electrophilic aromatic substitution and play a determinant role in the mechanism of the electrophilic aromatic substitution [147], are attracted to the cavity by weak interactions. This fact has to be considered in order to arrive at a general conclusion about the electrophilic aromatic substitution in PCP-CD. Table 8.5 illustrates the values of ρ at the "BCP" of the weak interactions exhibited by the hydrogens bonded to C_2 and C_3 (H_7 and H_8), respectively.

Table 8.5. Electron density at the "bond critical points" of the weak interactions between the hydrogens H_7 and H_8 of the *p*-chlorophenol and the α-cyclodextrin (in atomic units).

PCP-CD	ρ
H_7-O_{CD}	0.0088
H_7-H_{CD}	0.0041
H_8-H_{CD}	0.0043

H_7 exhibits two weak interactions with one oxygen (H_7-O_{CD}, 2.50 Å) and one hydrogen (H_7-H_{CD}, 2.46 Å) of α-CD, whereas H_8 exhibits only one weak interaction (H_8-H_{CD}, 2.39 Å) with the same hydrogen (Figure 8.2). H_7-H_{CD} exhibits a similar value of ρ at its "BCP" as H_8-H_{CD}. Therefore, the strength of these two weak interactions is assumed to be similar on the basis of the results of Boyd and Choi [96,97]. H_7 has an additional weak interaction with O_{CD}, which exhibits a similar distance between the atoms and almost double the value of ρ at the "BCP" than the two weak interactions mentioned above. Therefore, H_7 is more strongly bonded to α-CD than H_8 and it is reasonable to suggest that the leaving of H_7 should be easier than that of H_8.

It is predicted on the basis of the analysis of $-\nabla^2\rho$ at the link points and the bonding interactions exhibited by the hydrogen-leaving groups with α-CD that the C_2 position in PCP-CD is more favorable with respect to electrophilic aromatic substitution than in PCP. A similar prediction with respect to electrophilic aromatic substitution at C_3 cannot be made due two opposing factors: encapsulation of PCP by α-CD decreases $-\nabla^2\rho$ at the link

points but also it produces several weak interactions between hydrogen-leaving groups and α-CD which facilitate the leaving of the hydrogen and accelerates the reaction.

It is also predicted on the basis of the analysis of $-\nabla^2\rho$ at the link points and the bonding interactions exhibited by the hydrogen-leaving groups with α-CD that the ratio between p-chlorophenol substituted at C_2 and C_3 is greater in PCP-CD than in PCP. The facts that the C_3 position is more accessible to electrophilic attack (Figure 8.2 (b)) and that the α-CD can be considered to be a competing site were not considered in this study.

8.3 Conclusions

Single-determinant Kohn-Sham "wavefunctions" were obtained at the B3LYP/6-31+G(d) level for PCP, with the same geometry that it has inside α-CD, and also for the inclusion complex (PCP-CD). The analysis of the bond critical points of PCP shows that there is no trend in the effect on the AIM properties of PCP due to inclusion in the α-CD. The analysis of the RCP shows that the encapsulation of PCP by α-CD increases ρ at the RCP and makes the charge around the RCP less depleted. Furthermore, several weak interactions between PCP and α-CD were found and characterized.

The analysis in terms of link points of the VSCC of carbons and the bonding interactions exhibited by the hydrogen-leaving groups with α-CD shows that the C_2 position of p-chlorophenol in PCP-CD is more favorable than in PCP with respect to electrophilic aromatic substitution (the same prediction holds for the C_6 position). Furthermore, the ratio between *p*-chlorophenol substituted at C_2 and C_3 is predicted to be greater in PCP-CD than in PCP.

Chapter 9 An Atoms in Molecules Study of the Halogen Resonance Effect.

9.1 Introduction.

The electronic structure of certain classes of molecular species cannot be adequately described by a single Lewis structure. In some cases, the actual electronic structure is a weighted average of two or more Lewis structures, called resonance structures, and the molecule is known as a resonance hybrid. The concept of resonance is especially useful for systems containing delocalized electrons and has been used to explain many phenomena in chemistry including several types of reactions and the stability and physical properties of compounds.

The experimental observation that electrophilic substitution at the *ortho* and *para* positions of halobenzenes (C_6H_5X) is more facile than at the *meta* position is readily rationalized by a halogen resonance effect. Thus, interaction of a halogen lone pair with the p atomic orbitals that form the delocalized system of π bonds leads to the halonium ion structures shown in Scheme 9.1. It is impossible to draw an equivalent resonance structure for the intermediate formed by electrophilic substitution at the *meta* position of a halobenzene.

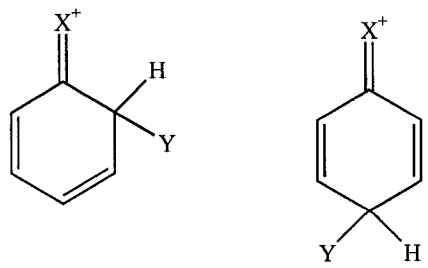

(a) (b)

Scheme 9.1. Resonance structures for the intermediates formed by electrophilic aromatic substitution of Y^+ at the *ortho* (a) and *para* (b) positions of a halobenzene.

Support for the standard interpretation of the experimental results is provided by MO calculations [148], which clearly show a large contribution of the halogen to the π bonding MOs. A similar effect is not observed in haloaliphatic compounds. In this chapter the first analysis of the halogen resonance effect by use of the theory of atoms in molecules (AIM) is reported.

9.2 The Theory of Atoms in Molecules and Resonance.

The AIM theory uses well-defined quantities derived from the electron density to provide valuable insight into the electronic structures and properties of molecules [29,30,128]. Bader and Stephens [70] have studied the resonance effect in terms of $F^{\alpha}(\Omega,\Omega')$ and $F^{\beta}(\Omega,\Omega')$, which are the delocalization functions of electrons with α and β spin, respectively, between the basins of two atoms, Ω and Ω' (Equation 5.1). The relationship between the delocalization index and bond order in the characterization of a chemical bond has been discussed previously [71,79,80,121].

Bader et al. [149] used $F^{\alpha}(\Omega,\Omega')$ to quantify the contribution of each resonance structure in acyclic and cyclic hydrocarbons as well as the effect of substituents on delocalization in aromatic systems. More recently, González and Mosquera [150] reported a similar study in pyrimidinic bases but in terms of the delocalization index ($\delta(\Omega,\Omega')$) (Equation 5.2).

Several other authors have used AIM to study the resonance effect in many different types of systems. For example, Okulik et al. have used AIM parameters to study the "three-center two-electron bonds" exhibited by isobutonium [151] and n-butonium [152] cations. Grabowski [153,154] and Gilli et al. [155] have used AIM analysis in terms of

the electron density and the Laplacian at the bond critical points to explore the resonance-assisted hydrogen bonds in malonaldehyde and ketohydrazone-azoenol systems, respectively. Also, Borbulevych et al. [156] used the AIM theory to analyze substituent effects in 4-nitroaniline derivatives.

In this chapter a detailed AIM study of systems where the halogen is adjacent to a carbon-carbon double bond is presented. Moreover, a comparable study of the respective saturated halohydrocarbons and hydrocarbons as well as the related unsaturated hydrocarbons has been carried out. The molecules included in this study are shown in Scheme 9.2, where X=F, Cl and Br.

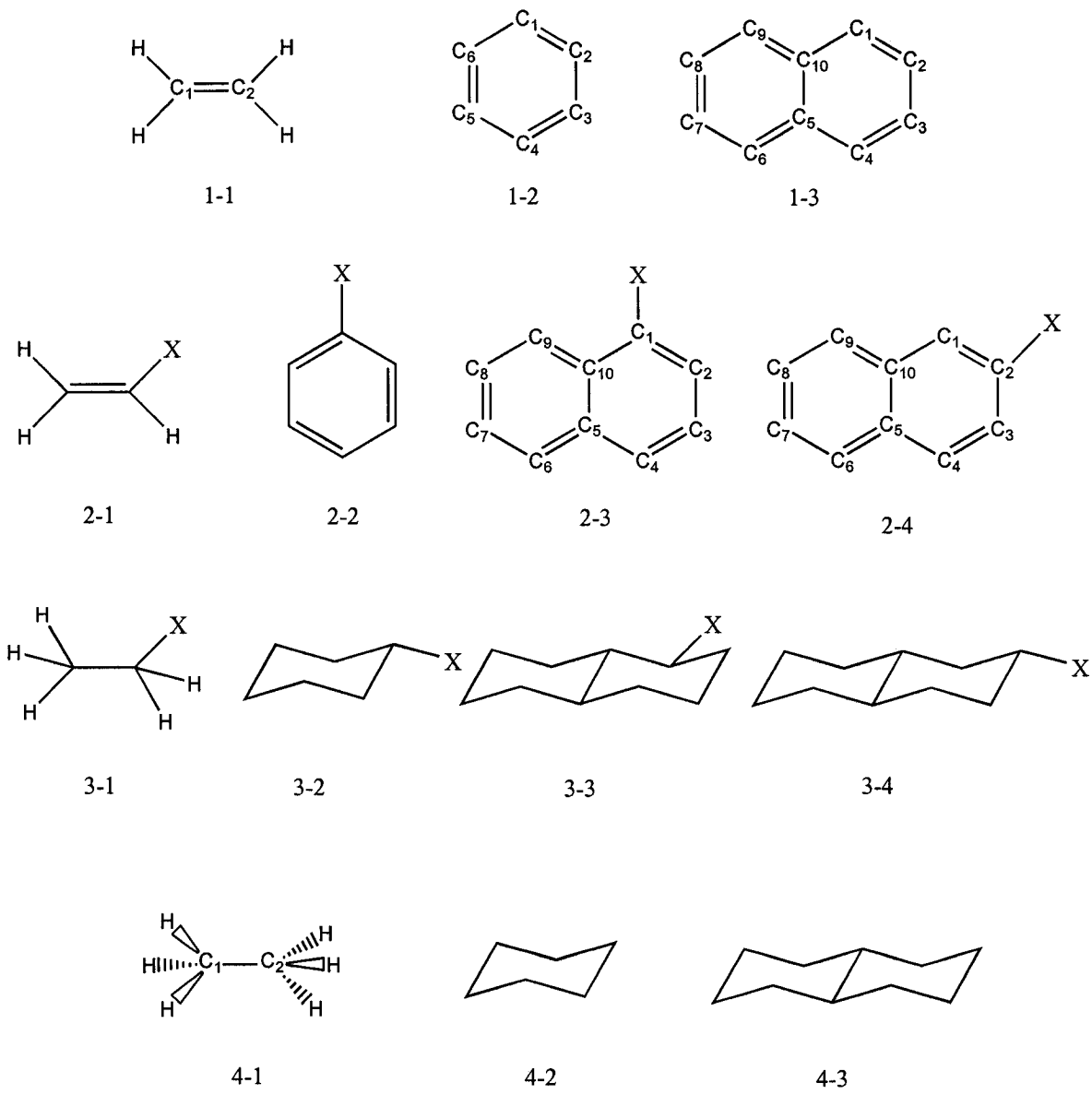

Scheme 9.2. Chemical structures of compounds included in this study, where X=F, Cl and Br.

The first series consists of ethene (1-1), benzene (1-2) and naphthalene (1-3). The second series consists of their four monohalo derivatives. The third series consists of the saturated analogues of series 2, while the fourth series consists of the unsubstituted parent compounds of the third series. The emphasis of our study is on bond critical points,

ellipticities, Laplacian topology, delocalization indexes and population analysis for the main atoms and bonds associated with the resonance effect.

A secondary purpose of this chapter is to perform an AIM study of electrophilic aromatic substitution in the halonaphthalenes in order to complement Bader and Chang's earlier study of benzene [146]. An analysis of the link points of the carbon valence shell charge concentrations (VSCCs) of the ring is used to predict the directing and activating-deactivating effects of halogens in naphthalene.

9.3 Computational Details

All molecules were fully optimized at the B3LYP/6-311++G(d,p) level using the Gaussian 03 package [53]. The characterization of the bond and ring critical points as well as the maximum charge concentrations was carried out using the EXTREME program while the atomic populations were performed by PROAIM. Both programs belong to the AIMPAC package [54]. The AIMDELOC program was used to obtain the delocalization indexes [76].

9.4 Results and Discussion

9.4.1 Valence shell characterization of chlorine in compound series two and three.

The characterization of the valence shell was carried out in terms of the (3,-3) critical points of L ($L=-\nabla^2\rho$), which represent the bonded and non-bonded maximum charge concentrations in the VSCC of an atom in a molecule. The locations of the (3,-3) critical points of L provide theoretical support for the bonded and non-bonded electron pairs of

the Lewis model [157-159]. Figure 9.1 illustrates the locations of the (3,-3) critical points in the valence shell of chlorine in compound series two and three. The position of each (3,-3) critical point is indicated by a vector whose origin is at the chlorine nucleus. In order to illustrate the distortion of the VSCC in each case, Figure 9.2 shows the contour map of the Laplacian for the plane that contains the halogen and the two carbons of chloroethane and chloroethene.

Figure 9.1 shows clearly that the chlorine VSCC exhibits two non-bonded maxima in series two and three non-bonded maxima in series three. Moreover, the missing non-bonded maxima in series two are positioned optimally to delocalize the π cloud of the carbon-carbon double bonds. Figure 9.1 also illustrates that the other two non-bonded maxima are in the σ plane of the carbon-carbon double bonds, which is a favorable location for the delocalization of the missing non-bonded maximum charge concentration into the π cloud. Furthermore, Figure 9.2 shows contour lines connecting the VSCC of chlorine with the VSCC of carbon in chloroethene, signifying a greater distortion of the VSCCs of chlorine and carbon in chlorethene than in chloroethane. This suggests a greater sharing of electrons in the chlorine-carbon bond of chloroethene than in chloroethane, and also suggests that the halogen resonance effect is a donor effect.

Table 9.1 describes the VSCC of chlorine in compound series two and series three in terms of several electronic properties.

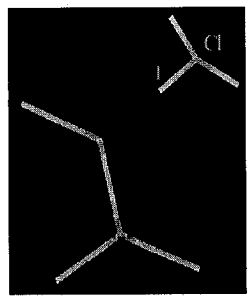

(a)

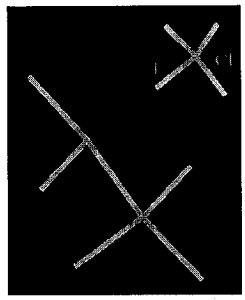

(b)

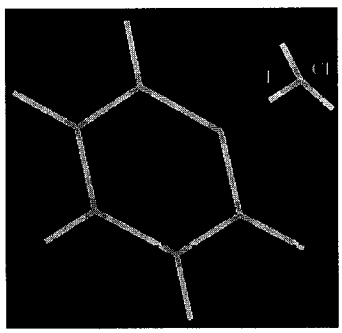

(c)

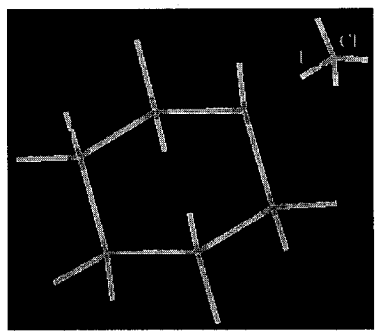

(d)

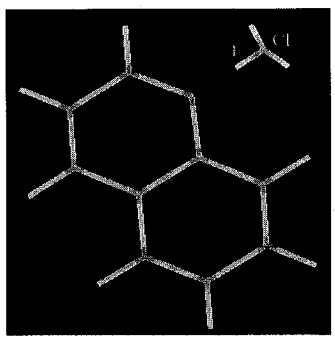

(e)

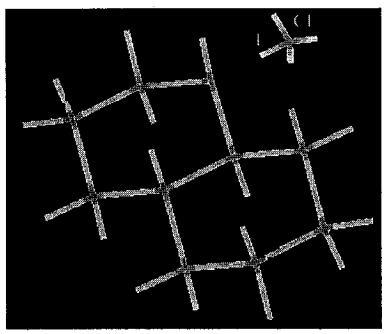

(f)

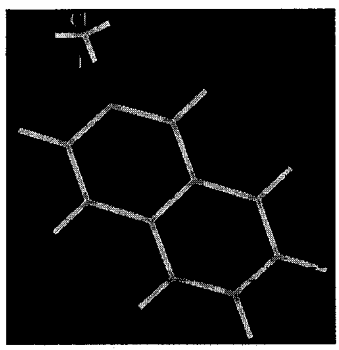

(g)

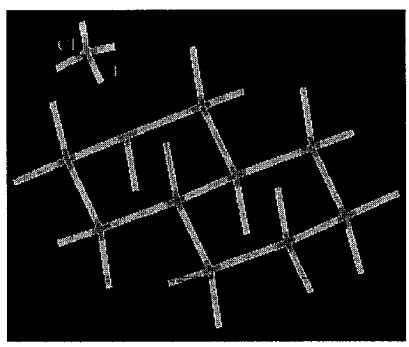

(h)

Figure 9.1. Location of the maximum charge concentrations of the VSCCs of chlorine in compound series two and series three. In each molecule the bonded maximum charge concentration is directed toward the carbon atom bonded to chlorine and is labeled by 1. Representations are as follows: (a) 2-1, (b) 3-1, (c) 2-2, (d) 3-2, (e) 2-3, (f) 3-3, (g) 2-4 and (h) 3-4

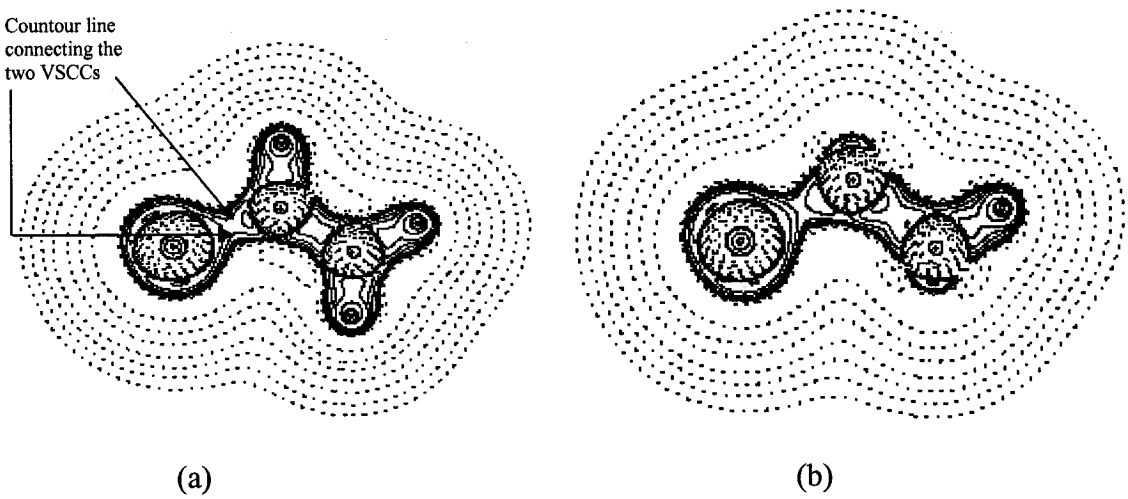

(a) (b)

Figure 9.2. Contour map of the Laplacian of the electron density in the plane that contains the chlorine and the two carbons. (a) Chloroethene and (b) Chloroethane. The chlorine nucleus is on the left side in both cases.

Table 9.1. Characterization of the maximum charge concentrations in the VSCCs of chlorine in compound series two and series three in terms of the number of bonded maxima (#b), the number of non-bonded maxima (# nb), radius (r), $-\nabla^2\rho$, ρ and average angles between non-bonded maxima.[a]

Molecule	Bonded Maxima				Non-bonded Maxima				
	# b	r	$-\nabla^2\rho\times10^1$	$\rho\times10^1$	# nb	r	$-\nabla^2\rho\times10^1$	$\rho\times10^1$	Angle (nb-nb)
2-1	1	1.271	6.18	2.55	2	1.185	8.52	2.78	152.4
						1.185	8.50	2.78	
3-1	1	1.265	5.76	2.45	3	1.187	8.31	2.76	115.2
						1.187	8.31	2.76	
						1.187	8.30	2.76	
2-2	1	1.271	6.09	2.53	2	1.185	8.47	2.78	153.1
						1.185	8.47	2.78	
3-2	1	1.261	5.74	2.45	3	1.188	8.19	2.75	115.5
						1.188	8.21	2.75	
						1.188	8.21	2.75	
2-3	1	1.271	6.03	2.52	2	1.185	8.47	2.78	153.4
						1.185	8.49	2.78	
3-3	1	1.258	5.73	2.51	3	1.187	8.21	2.75	115.1
						1.188	8.19	2.75	
						1.187	8.21	2.75	
2-4	1	1.271	6.08	2.53	2	1.185	8.47	2.78	153.7
						1.185	8.47	2.78	
3-4	1	1.261	5.73	2.45	3	1.188	8.19	2.75	115.3
						1.188	8.21	2.75	
						1.187	8.21	2.75	

a- Radius in angstroms, $-\nabla^2\rho$ and ρ in atomic units and angles in degrees.

The radii, $-\nabla^2\rho$ and ρ at the bonded maximum charge concentration of the chlorine VSCC are larger in series two than in series three. The same trend holds for the non-bonded maximum charge concentrations, with the exception of the radii, which are slightly larger in series three than in series two. The radii of the non-bonded maximum charge concentrations are smaller in series two than series three, whereas $-\nabla^2\rho$ and ρ continue being larger. The decrease of the angle from series two to series three, indicates the change of the chlorine VSCC from trigonal planar to tetrahedral. All these results

support the fact that one non-bonded maximum is delocalized into the π cloud of the double bonds in series two.

9.4.2 Comparison of the fluorine and bromine valence shells with chlorine in compound series two and series three.

The bonded maximum charge concentrations of the VSCCs of fluorine and bromine in series two and series three were not found at the level of theory used in this study. The results are listed in Table 9.2. It is possible that the maxima would be found at higher levels of calculation since it is known that the use of triplet-zeta basis set is the minimum requirement to obtain consistent and topologically stable graphs of the Laplacian [160]. The non-bonded maxima charge concentrations for fluorine and bromine have similar characteristics to that of chlorine. For example, the VSCCs for the two atoms exhibit two non-bonded maxima in series two, whereas there are three non-bonded maxima in series three. Also, the non-bonded maximum charge concentrations in series two are in a favorable location for the delocalization of the missing non-bonded maximum charge concentration into the π cloud. The radius of the non-bonded maximum charge concentration increases from series two to series three, whereas $-\nabla^2\rho$, ρ and the angles decrease. A decrease of almost 75% percent in the $-\nabla^2\rho$ value for the non-bonded maximum charge concentration in the bromine case is noteworthy. This result is expected because bromine is considerably larger than chlorine and fluorine, and any displacement of the same amount of electron charge involves larger volumes. Therefore, the concentration of ρ decreases more significantly than in the cases of chlorine and fluorine.

Table 9.2. Characterization of the non-bonded maximum charge concentrations in the VSCCs of fluorine and bromine in series two and series three in terms of the number of non-bonded maxima (# nb), radius (r), $-\nabla^2\rho$, ρ and average angles between non-bonded maxima.[a]

	Non-bonded Maxima										
	Fluorine					Bromine					
Molecule	# nb	r	$-\nabla^2\rho\times10^2$	$\rho\times10^1$	Angle (nb-nb)	Molecule	# nb	r	$-\nabla^2\rho$	ρ	Angle (nb-nb)
2-1	2	0.569	9.34	1.52	157.0	2-1	2	1.567	0.82	1.65	158.9
		0.569	9.31	1.52				1.568	0.82	1.65	
3-1	3	0.571	9.06	1.50	116.2	3-1	3	1.574	0.21	1.62	117.1
		0.571	9.06	1.50				1.574	0.19	1.62	
		0.571	9.07	1.50				1.574	0.19	1.62	
2-2	2	0.569	9.28	1.52	155.7	2-2	2	1.567	0.76	1.65	159.8
		0.569	9.28	1.51				1.567	0.76	1.65	
3-2	3	0.571	9.00	1.50	116.6	3-2	3	1.577	0.16	1.61	117.3
		0.571	8.98	1.50				1.576	0.03	1.61	
		0.571	9.00	1.50				1.576	0.03	1.61	
2-3	2	0.569	9.26	1.52	156.1	2-3	2	1.566	0.94	1.66	159.8
		0.569	9.26	1.52				1.566	0.77	1.65	
3-3	3	0.571	9.01	1.50	116.0	3-3	3	1.576	0.11	1.61	116.7
		0.571	8.96	1.50				1.578	0.29	1.60	
		0.571	8.98	1.50				1.575	0.09	1.62	
2-4	2	0.569	9.28	1.52	156.6	2-4	2	1.567	0.79	1.65	159.3
		0.569	9.28	1.52				1.567	0.77	1.65	
3-4	3	0.571	8.97	1.50	116.6	3-4	3	1.577	0.16	1.61	117.2
		0.571	9.00	1.50				1.576	0.03	1.61	
		0.571	9.00	1.50				1.576	0.03	1.61	

a- Radius in angstroms, $-\nabla^2\rho$ and ρ in atomic units and angles in degrees.

9.4.3 Characterization of the bonded maximum charge concentrations of the carbons connected to halogens.

As was shown above, the VSCCs of the halogens are significantly altered by the resonance effect. Hence, it can be expected that the VSCCs of the carbon atoms joined to the halogen will also exhibit detectable modifications. Therefore, the VSCCs of these

carbon atoms for series two and series three with the three different halogens are analyzed. Table 9.3 provides the results for the bonded maximum charge concentration of the carbon bonded to the halogens.

Table 9.3. Characterization of the carbon-halogen bonded maximum charge concentrations in the VSCC of the carbon connected to the halogen (fluorine, chlorine or bromine) in terms of radius, $-\nabla^2\rho$ and ρ for series two and series three.[a]

Fluorine				Chlorine				Bromine			
Molecule	r	$-\nabla^2\rho\times10^1$	$\rho\times10^1$	Molecule	r	$-\nabla^2\rho\times10^1$	$\rho\times10^1$	Molecule	r	$-\nabla^2\rho\times10^1$	$\rho\times10^1$
2-1	1.043	3.47	2.63	2-1	1.035	4.99	2.13	2-1	1.027	4.81	2.02
3-1	1.053	2.64	2.29	3-1	1.054	3.84	1.89	3-1	1.049	3.53	1.79
2-2	1.044	3.51	2.62	2-2	1.034	4.95	2.11	2-2	1.026	4.80	2.01
3-2	1.052	2.45	2.23	3-2	1.054	3.61	1.85	3-2	1.049	3.33	1.75
2-3	1.045	3.43	2.61	2-3	1.035	4.84	2.10	2-3	1.027	4.68	1.99
3-3	1.054	2.37	2.21	3-3	1.055	3.53	1.83	3-3	1.050	3.20	1.73
2-4	1.044	3.51	2.62	2-4	1.034	4.94	2.11	2-4	1.026	4.80	2.01
3-4	1.053	2.44	2.23	3-4	1.055	3.59	1.84	3-4	1.050	3.31	1.75

a- Radius in angstroms, $-\nabla^2\rho$ and ρ in atomic units.

As can be seen in the table, the systems with the resonance effect (series two) exhibit smaller radii and greater values of $-\nabla^2\rho$ and ρ at the maximum charge concentration of the carbon bonded to the halogen than those without the resonance effect (series three). This fact can be explained by the delocalization of the non-bonded charge concentration in the carbon-halogen bond. The resonance effect plays a similar role in the unsaturated aliphatic halohydrocarbon to that of the aromatic halohydrocarbon. There are no appreciable differences with respect to radius, $-\nabla^2\rho$ and ρ between the haloethene (2-1), the halobenzene (2-2) and the halonaphthalenes (2-3 and 2-4), respectively. Fluorine

produces the smallest value of $-\nabla^2\rho$ and the largest value of ρ at the bonded maximum charge concentration of the carbon bonded to the halogen.

The carbon connected to the halogen in series two and series three in terms of the bonded charge concentration contained in the carbon-carbon bond are analyzed in order to investigate the halogen resonance effect on the carbon-carbon double bond in series two. Also, the respective bonded charge concentrations of the carbons for the non-halogen systems (series one and series four) are characterized to make illustrative comparisons. Table 9.4 provides the results.

Table 9.4. Characterization of the carbon-carbon bonded maximum charge concentrations in the VSCCs of the carbon connected to the halogen (fluorine, chlorine or bromine) in terms of radius, $-\nabla^2\rho$ and ρ for all four series.[a]

Fluorine				Chlorine				Bromine			
Molecule	r	$-\nabla^2\rho$	$\rho\times10^1$	Molecule	r	$-\nabla^2\rho$	$\rho\times10^1$	Molecule	r	$-\nabla^2\rho$	$\rho\times10^1$
1-1	0.987	1.14	3.53	1-1	0.987	1.14	3.53	1-1	0.987	1.14	3.53
2-1	0.958	1.28	3.71	2-1	0.968	1.21	3.63	2-1	0.970	1.19	3.61
3-1	0.966	1.03	2.94	3-1	0.970	0.98	2.88	3-1	0.971	0.97	2.88
4-1	0.996	0.82	2.68	4-1	0.996	0.82	2.68	4-1	0.996	0.82	2.68
1-2	0.983	1.06	3.25	1-2	0.983	1.06	3.25	1-2	0.983	1.06	3.25
2-2	0.958	1.20	3.43	2-2	0.965	1.13	3.34	2-2	0.967	1.11	3.32
3-2	0.962	1.05	2.96	3-2	0.966	1.00	2.91	3-2	0.967	0.99	2.90
4-2	0.991	0.85	2.72	4-2	0.991	0.85	2.72	4-2	0.991	0.85	2.72
1-3 (C_1)	0.982	1.09	3.34	1-3 (C_1)	0.982	1.09	3.34	1-3 (C_1)	0.982	1.09	3.34
2-3	0.957	1.23	3.52	2-3	0.965	1.15	3.43	2-3	0.967	1.13	3.41
3-3	0.962	1.05	2.96	3-3	0.965	1.00	2.92	3-3	0.966	0.99	2.90
4-3 (C_1)	0.991	0.85	2.72	4-3 (C_1)	0.991	0.85	2.72	4-3 (C_1)	0.991	0.85	2.72
1-3 (C_2)	0.983	1.08	3.34	1-3 (C_2)	0.983	1.08	3.34	1-3 (C_2)	0.983	1.08	3.34
2-4	0.957	1.23	3.51	2-4	0.966	1.15	3.43	2-4	0.968	1.13	3.41
3-4	0.962	1.05	2.96	3-4	0.966	1.00	2.91	3-4	0.967	0.99	2.90
4-3 (C_2)	0.991	0.85	2.72	4-3 (C_2)	0.991	0.85	2.72	4-3 (C_2)	0.991	0.85	2.72

a- Radius in angstroms, $-\nabla^2\rho$ and ρ in atomic units.

The VSCC of the carbon connected to the halogen in series two and series three exhibits a bonded maximum charge concentration contained in the carbon-carbon bond with smaller radii than the non-halogen systems (series one and series four). The radii are even smaller in cases where the halogen resonance effect exists (series two). Moreover, series two exhibits the greatest values of $-\nabla^2\rho$ and ρ at these bonded maximum charge concentrations. The values of $-\nabla^2\rho$ and ρ for non-halogen unsaturated systems (series one) are in between the two types of halogen systems (series two and series three). Fluorine produces smaller radii and larger values of $-\nabla^2\rho$ and ρ in its compounds than chlorine and bromine. Slight differences are found between unsaturated aliphatic and aromatic compounds in terms of $-\nabla^2\rho$ and ρ values. For example, ethane (1-1) and chloroethene (2-1) exhibit larger radii and greater values of $-\nabla^2\rho$ and ρ than benzene (1-2) and chlorobenzene (2-2), respectively.

9.4.4 Characterization of the carbon-halogen and carbon-carbon bonds.

It is well established that the electronic properties at the bond critical point provide extensive information about a chemical bond [29]. Therefore, the characterization of the bond critical points at the carbon-halogen bond in series two and series three for the three halogens in terms of ellipticity, ρ and $-\nabla^2\rho$ is carried out. The bond critical point at the carbon-carbon bond was also characterized and a comparison with the carbon-carbon bonds in series one and series four was carried out. The data in Table 9.5 indicate that the ellipticities of carbon–halogen bonds are greater in systems where the resonance effect

exists. For example, the ellipticity of the carbon–chlorine bond in chloroethene* (2-1) is 5.09×10^{-2} au (atomic unit), which is greater than the 1.40×10^{-2} au exhibited in chloroethane (3-1). Moreover, the ellipticities are greater in halogen unsaturated aliphatic systems (2-1) than in halogen aromatic systems (2-2, 2-3 and 2-4) for chlorine and bromine. The opposite behavior is observed for fluorine.

Table 9.5. Ellipticity (ε), ρ and $-\nabla^2\rho$ of the carbon-halogen (fluorine, chlorine and bromine) bonds for series two and series three.[a]

	Fluorine				Chlorine				Bromine			
Molecule	Bond	$\varepsilon\times10^2$	$\rho\times10^1$	$-\nabla^2\rho\times10^1$	Bond	$\varepsilon\times10^2$	$\rho\times10^1$	$-\nabla^2\rho\times10^1$	Bond	$\varepsilon\times10^2$	$\rho\times10^1$	$-\nabla^2\rho\times10^1$
2-1	C-F	7.36	2.49	1.44	C-Cl	5.09	1.94	2.84	C-Br	6.22	1.57	1.47
3-1	C-F	3.25	2.23	0.37	C-Cl	1.40	1.67	1.87	C-Br	1.26	1.36	1.05
2-2	C-F	6.58	2.48	1.21	C-Cl	5.61	1.91	2.72	C-Br	6.37	1.55	1.44
3-2	C-F	1.02	2.18	0.63	C-Cl	0.86	1.61	1.64	C-Br	0.85	1.31	0.92
2-3	C-F	5.66	2.47	1.31	C-Cl	5.73	1.90	2.64	C-Br	6.38	1.53	1.39
3-3	C-F	0.46	2.16	0.64	C-Cl	0.90	1.60	1.58	C-Br	0.76	1.28	0.84
2-4	C-F	6.12	2.48	1.20	C-Cl	5.71	1.91	2.72	C-Br	6.47	1.55	1.45
3-4	C-F	1.17	2.18	0.65	C-Cl	0.90	1.61	1.63	C-Br	0.86	1.31	0.91

a- ε, ρ and $-\nabla^2\rho$ in atomic units.

The electron density at the bond critical point is also greater in systems where the halogen resonance effect is present (series two). Fluorine produces the greatest value of ρ at the bond critical point. There are no appreciable differences between halogen unsaturated aliphatic and halogen aromatic systems in terms of ρ at the carbon-halogen bond critical point. Similar behavior is observed for $-\nabla^2\rho$ except that chlorine produces the greatest values. $-\nabla^2\rho$ values for halogen unsaturated aliphatic systems are slightly greater than those of halogen aromatic systems for the three halogens.

* The direction of the eigenvector associated with the less negative eigenvalue is parallel to the π plane in chloroethene

Table 9.6 shows that series two exhibits greater values of ellipticities in the carbon-carbon double bond than series one. For example, the ellipticity at the carbon-carbon double bond in fluoroethene (2-1) is 4.20×10^{-1} au, which is greater than the 3.32×10^{-1} au exhibited in ethene (1-1). This observation can be explained by the delocalization of one non-bonded maximum charge concentration by the resonance effect through the carbon-halogen bond, which contributes to an increase in the electron density in the π plane of the whole system.

Table 9.6. Ellipticity (ε), ρ and $-\nabla^2\rho$ of the carbon-carbon bond adjacent to the halogen for all four series.[a]

Fluorine				Chlorine				Bromine			
Molecule	ε	$\rho\times10^1$	$-\nabla^2\rho\times10^1$	Molecule	ε	$\rho\times10^1$	$-\nabla^2\rho\times10^1$	Molecule	ε	$\rho\times10^1$	$-\nabla^2\rho\times10^1$
1-1	3.3210^{-1}	3.44	10.27	1-1	3.3210^{-1}	3.44	10.27	1-1	3.3210^{-1}	3.44	10.27
2-1	4.2010^{-1}	3.52	10.72	2-1	3.7910^{-1}	3.47	10.37	2-1	3.6810^{-1}	3.47	10.34
3-1	4.1510^{-2}	2.54	6.13	3-1	1.6710^{-2}	2.48	5.8	3-1	9.3710^{-3}	2.48	5.78
4-1	2.2410^{-5}	2.41	5.49	4-1	2.2410^{-5}	2.41	5.49	4-1	2.2410^{-5}	2.41	5.49
1-2	2.0010^{-1}	3.08	8.59	1-2	2.0010^{-1}	3.08	8.59	1-2	2.0010^{-1}	3.08	8.59
2-2	2.6110^{-1}	3.17	9.1	2-2	2.3210^{-1}	3.1	8.65	2-2	2.2410^{-1}	3.1	8.6
3-2	4.3810^{-2}	2.53	6.03	3-2	2.0710^{-2}	2.47	5.7	3-2	1.4010^{-2}	2.47	5.67
4-2	6.6110^{-3}	2.39	5.31	4-2	6.6110^{-3}	2.39	5.31	4-2	6.6110^{-3}	2.39	5.31
1-3	2.4210^{-1}	3.2	9.13	1-3	2.4210^{-1}	3.2	9.13	1-3	2.4210^{-1}	3.2	9.13
2-3	3.0910^{-1}	3.28	9.58	2-3	2.7710^{-1}	3.21	9.14	2-3	2.6910^{-1}	3.2	9.08
3-3	4.4510^{-2}	2.53	6.04	3-3	2.4410^{-2}	2.48	5.73	3-3	1.5210^{-2}	2.46	5.65
4-3	5.9710^{-3}	2.4	5.34	4-3	5.9710^{-3}	2.4	5.34	4-3	5.9710^{-3}	2.4	5.34
1-3	2.4210^{-1}	3.2	9.13	1-3	2.4210^{-1}	3.2	9.13	1-3	2.4210^{-1}	3.2	9.13
2-4	3.1310^{-1}	3.28	9.59	2-4	2.8110^{-1}	3.22	9.17	2-4	2.7210^{-1}	3.21	9.12
3-4	4.3010^{-2}	2.53	6.04	3-4	1.9910^{-2}	2.48	5.72	3-4	1.3110^{-2}	2.47	5.69
4-3	5.9710^{-3}	2.4	5.34	4-3	5.9710^{-3}	2.4	5.34	4-3	5.9710^{-3}	2.4	5.34

a- ε, ρ and $-\nabla^2\rho$ in atomic units.

ρ and $-\nabla^2\rho$ at the bond critical point of the carbon-carbon double bond are slightly greater in series two than in series one, with fluorine yielding the greatest differences. Moreover,

the carbon-carbon bond in series two exhibits considerably greater values of ρ and $-\nabla^2\rho$ at the bond critical point than those in series three. For example, fluoroethene (2-3) exhibits values of 3.52 au and 10.72 au (ρ and $-\nabla^2\rho$), which are greater than the 2.54 au and 6.13 exhibited in fluoroethane, respectively. These facts can be only explained by the halogen resonance effect.

Furthermore, Figure 9.3 shows the contour map of the electron density in the plane that contains the halogen and the two carbons in chloroethane and chloroethene. Greater distortion of the 0.2 au contour line in chloroethene than that of chloroethane is clearly evident. Therefore, the halogen resonance effect produces a greater amount of charge in the area between the two atoms, which further demonstrates the donor character of the halogen resonance effect.

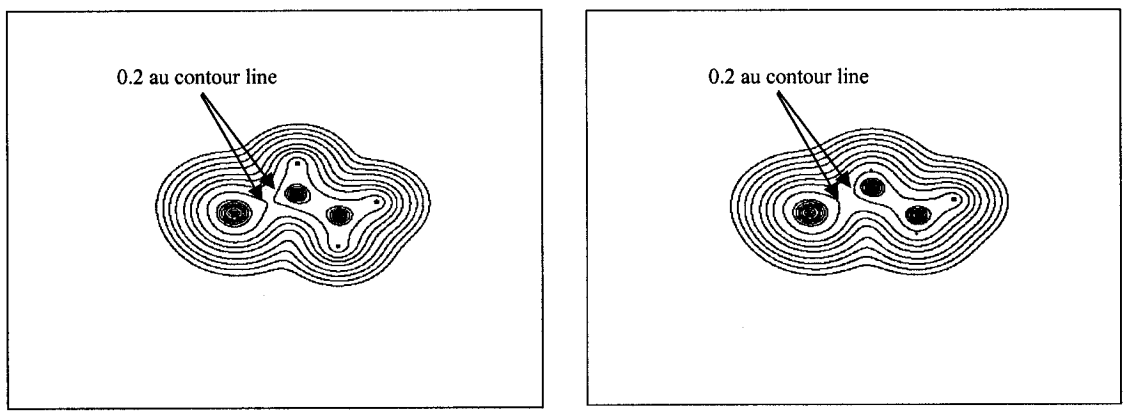

(a) (b)

Figure 9.3. Contour map of the electron density in the plane that contains chlorine and the two carbons. (a) Chloroethene. (b) Chloroethane.

The ring critical points were also analyzed for the cyclic systems. The three halogens do not produce any appreciable effects on ρ and $-\nabla^2\rho$ at the ring critical points. Their values are very similar to those of the non-halogen systems. Therefore, the presence of the halogens in the systems does not make any appreciable difference in the characteristics of the ring critical points whether the resonance effect exists or not.

9.4.5 Population analysis.

Table 9.7 lists the populations of the halogen and their adjacent carbons in series two and series three. Clearly the populations of chlorine and bromine in series two are smaller than in series three, whereas the population of fluorine remains constant at 9.62 au. Notice that the populations of chlorine and bromine are still greater than their respective atomic numbers (17 and 35). This suggests that the electron withdrawing inductive effect of the halogens is stronger than the donor resonance effect. However, the fluorine systems do not follow the same behavior.

Table 9.7. Populations of the halogens and their adjacent carbons in series two and series three.[a]

Population				
Molecule	Atoms	Fluorine	Chlorine	Bromine
2-1	Halogen	9.62	17.21	35.07
	Carbon	5.56	5.97	6.11
3-1	Halogen	9.62	17.28	35.18
	Carbon	5.49	5.88	5.99
2-2	Halogen	9.62	17.22	35.08
	Carbon	5.55	5.96	6.10
3-2	Halogen	9.62	17.30	35.20
	Carbon	5.52	5.89	5.994
2-3	Halogen	9.62	17.22	35.08
	Carbon	5.55	5.96	6.10
3 -3	Halogen	9.62	17.30	35.21
	Carbon	5.46	5.96	6.00
2-4	Halogen	9.62	17.22	35.08
	Carbon	5.55	5.96	6.10
3-4	Halogen	9.62	17.30	35.20
	Carbon	5.519	5.89	5.99

a- Populations in atomic units.

The populations of the carbons adjacent to the halogens are always greater in series two than in series three. This is an expected result and restates the donor character of the halogen resonance effect. The resonance effect produced by the delocalization of one non-bonded maximum charge concentration of the VSCC of the halogens in series two donates charge to the adjacent carbon, increasing its population. It makes the populations of the carbons adjacent to the halogen in series two greater than the respective carbons in series three where only the electron withdrawing inductive effect is present.

9.4.6 Delocalization indexes.

As explained above, δ (X,C) measures the sharing of electrons between a halogen and carbon. δ (X,C) is clearly greater in series two than in series three for chlorine and bromine (Table 9.8).

Table 9.8. Delocalization indexes for the bonded halogen-carbon (δ (X,C)) in series two and series three.[a]

Molecule	Fluorine	Chlorine	Bromine
2-1	0.850	1.125	1.158
3-1	0.813	1.028	1.051
2-2	0.826	1.092	1.121
3-2	0.787	0.985	1.003
2-3	0.823	1.087	1.114
3 -3	0.784	0.980	0.989
2-4	0.825	1.092	1.122
3-4	0.786	0.984	1.001

a- Delocalization indexes in atomic units.

The same behavior is observed in the case of fluorine, although the difference is not as great. These facts support the donor character of the halogen resonance effect in series two which produces a higher sharing of electrons between the three halogens and their bonded carbon than in series three. On the other hand, fluorine and bromine exhibit the lowest and largest values of δ (X,C), respectively. In fact, the sharing of electrons between halogens and their bonded carbons in our systems is inversely related to the eletronegativity difference between the halogen and its bonded carbon. For example, δ (Br,C) is greater than δ (F,C) and δ (Cl,C) in both series and the electronegativity difference increases from Br-C to F-C.

9.4.7 Electrophilic Aromatic Substitution in the α and β-halonaphthalenes.

In their study of electrophilic aromatic substitution, Bader and Chang [146] showed that the Laplacian values at the saddle points, which link the carbon-carbon bonded charge concentration in substituted benzenes, predict the observed directing and activating-deactivating effects. These so-called link points exhibit the second highest charge concentration of the VSCC of the atoms (second to the maximum charge concentration). In benzene these points are above and below the plane of the ring. Therefore, it is reasonable to think of them as possible sites for electrophilic attack. The location of these link points in benzene is illustrated in Figure 9.4. In this study a similar study of electrophilic aromatic substitution in the α and β-halonaphthalenes is carried out.

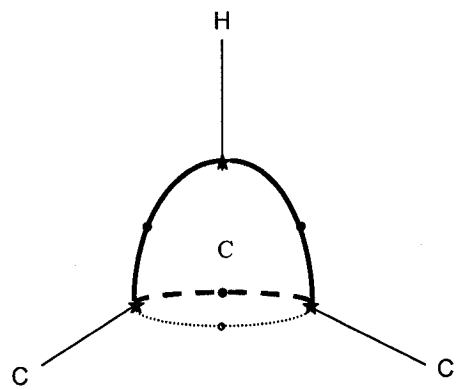

Figure 9.4. Atomic graphs describing the VSCC of a carbon in benzene. The maximum charge concentrations and link points are denoted by stars and dots, respectively. The solid link line is in the plane, the dashed link line is above the plane and the gray link line is below the plane.

As in the benzene case, there are two saddle points that link the two carbon-carbon bonded charge concentrations in the halonaphthalenes (one above and another below the plane of the ring). However, the saddle points which link the hydrogen-carbon maximum

bonded charge concentrations are not always in the plane of the ring as in benzene (Figure 9.4). All carbons of the ring except the bridging carbons in the halonaphthalenes exhibit one hydrogen-carbon link point in the plane of the ring. Also, they exhibit two hydrogen-carbon link points out of the plane of the ring, one above and one below. It can be understood that one of the hydrogen-carbon link points that is in the plane in benzene is split into two hydrogen-carbon link points in the halonaphthalenes due to the lower symmetry. The location of the split of the link points alternates along the carbon chain. For example, there are four hydrogen-carbon link points in the region between C_1 and C_2 (the split of hydrogen-carbon link points for each carbon), and it repeats in the region between C_3 and C_4, C_6 and C_7 and C_8 and C_9. On the other hand, there are two hydrogen-carbon link points in the region between C_2 and C_3 (the hydrogen-carbon link point in the plane for each carbon), and it repeats in the region between C_7 and C_8. Figure 9.5 illustrates the location of the link points in the α and β-halonaphthalenes and Table 9.9 provides $-\nabla^2\rho$ values of the carbon-carbon link points for the α and β-halonaphthalenes.[†,‡]

[†] The analysis of the hydrogen-carbon link points is not reported because it does not provide further insight. Their properties do not change appreciably throughout the ring, and also, they are generally similar to those of naphthalene for each halogen. Furthermore, their $-\nabla^2\rho$ values are noticeably lower than those for carbon-carbon link points. Thus, it is focused on the carbon-carbon link points because they should play a major role as sites for electrophilic attack.

[‡] Our analysis is performed in terms of $-\nabla^2\rho$ to be consistent with the common practice in the literature, but it must be noted that the opposite convention was used by Bader and Chang [146].

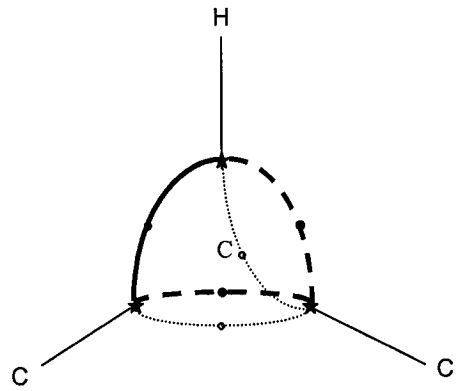

Figure 9.5. Atomic graphs describing the VSCC of a carbon in the halonaphthalenes. The maximum charge concentrations and link points are denoted by stars and dots, respectively. The solid link line is in the plane, the dashed link line is above the plane and the gray link line is below the plane.

Table 9.9. Values of $-\nabla^2\rho$ for carbon-carbon link points in α and β-halonaphthalene.[a]

α-halogen	F	Cl	Br	β-halogen	F	Cl	Br
C_2	0.159	0.150	0.149	C_1	0.165	0.156	0.154
C_3	0.135	0.136	0.136	C_3	0.150	0.146	0.146
C_4	0.145	0.139	0.136	C_4	0.136	0.136	0.137

a- $-\nabla^2\rho$ in atomic units.

Experimental studies of electrophilic aromatic substitution [147] indicate that halogens at the α-position (C_1) in naphthalene are C_2 and C_4 directing, whereas halogens at the β-position (C_2) are C_1 and C_3 directing. As can be seen in the table, the link points with the largest values of $-\nabla^2\rho$ are in the VSCCs of C_2 and C_4 in the case of the α-halonaphthalenes. The α-fluoronaphthalene exhibits the greatest values, 0.159 for C_2 and 0.145 for C_4, whereas the α-bromonaphthalene exhibits the lowest values 0.149 for C_2 and 0.136 for C_4. Thus, the electrophilic attack will preferentially occur at C_2 and C_4, following the trend F>Cl>Br as demonstrated by experiment. However, our results are

not absolutely consistent with experiment [147] because they predict that the electrophilic attack will be more preferentially directed to position C_2 than to position C_4 in the α-halonaphthalenes. Also, they predict a similar tendency of electrophilic aromatic substitution at the C_3 and C_4 positions except for the case of fluorine where there is a noticeable preference of C_4 over C_3. The analysis for β-halonaphthalenes indicates a preference for C_1 over C_3 with the same trend as observed in the α-halonaphthalenes (F>Cl>Br). These results are consistent with experiment. Furthermore, the results predict faster electrophilic aromatic substitution at the C_1 position of the β-halonaphthalenes than at the C_2 position of the α-halonaphthalenes. These results are also consistent with experiment [147].

9.5 Conclusions

The VSCCs of the halogens in compounds where the halogens are bonded to a carbon-carbon single bond exhibit three non-bonded maximum charge concentrations (series three). The location of these maxima can be considered to be tetrahedral. However, the VSCCs of the halogens bonded to a carbon-carbon double bond exhibit two non-bonded maximum charge concentrations in the sp^2 plane of the carbons (series two). This suggests an overlapping or delocalization of one of the non-bonded maximum charge concentrations of the halogen into the π cloud of the carbon-carbon double bond by a resonance effect. The systems with the halogen resonance effect exhibit smaller radii and larger values of $-\nabla^2\rho$ and ρ at the maximum charge concentrations of the halogens than those in the systems where only the electron withdrawing inductive effect of the halogen is acting.

In the case of the sp^2 carbons bonded to the halogen in series two, their maximum charge concentrations bonded to the halogen exhibit smaller radii and greater values of $-\nabla^2\rho$ and ρ than the sp^3 carbons bonded to the halogen in series three. Moreover, the maximum charge concentrations of the sp^2 carbons bonded to the other carbon that forms the carbon-carbon double bond in series two exhibit similar radii (in general slightly smaller) and greater values of $-\nabla^2\rho$ and ρ than the sp^3 carbons bonded to the halogen in series three. The values of $-\nabla^2\rho$ and ρ for these carbon-carbon bonded maximum charge concentrations in the four series of molecules follow the trend: 2>1>3>4.

The ellipticities, $-\nabla^2\rho$ and ρ at the bond critical points for the halogen-carbon bonds are greater in series two than in series three. Fluorine and chlorine produce the largest values of ρ and $-\nabla^2\rho$, respectively. These facts clearly show the delocalization of charge from the halogens to the sp^2 carbon. In the case of the carbon-carbon bond, the ellipticities at the bond critical point are greater in series two than in series one (also true for series three and series four). These results also suggest an overlapping or delocalization of one of the non-bonded maximum charge concentrations of the VSCC of the halogens into the π cloud of the carbon-carbon double bond by a resonance effect. The ρ and $-\nabla^2\rho$ values exhibit the same behavior.

The populations of chlorine and bromine in series two are smaller than in series three (larger than 17 and 35, respectively). This suggests that the electron withdrawing inductive effect of the halogens is larger than the donor resonance effect. However, the fluorine systems do not follow the same behavior. In the case of the carbon bonded to the halogens, the populations are always greater in series two than in series three, which is consistent with the donor character of the halogen resonance effect. Furthermore, the

delocalization indexes between the halogen and its bonded carbon are larger in series two than in series three, which shows that the halogen resonance effect contributes to the sharing of electrons between the halogens and their bonded carbon.

The locations of the carbon-carbon link points of the VSCC in α and β-naphthalene is slightly different than in benzene. The analysis of these link points in terms of $-\nabla^2\rho$ shows that electrophilic aromatic substitution is more favorable in α-fluoronaphthalene than in α-chloronaphthalene and α-bromonaphthalene. The same conclusion holds for the β-halonaphthalenes. Also, the results indicates a preference for C_1 over C_3 in the β-halonaphthalenes. All these results are consistent with experiment.

In summary, several observations are reported that are consistent with the presence of the halogen resonance effect in compounds where the halogen is bonded to a carbon-carbon double bond. These observations include the missing non-bonded maximum charge concentration in the VSCC of the halogens, the increase of $-\nabla^2\rho$ and ρ in the bonded maximum charge concentrations in the VSCC of the halogens and in the VSCC of their respective bonded carbons, the electronic properties at the BCPs, the atomic populations, and the delocalization indexes. Furthermore, these observations are consistent with experimental results for electrophilic aromatic substitution in halonaphthalenes.

Chapter 10 A Theoretical Study of the Thermolysis of β-hydroxyl Aldehydes.

10.1 Introduction.

The kinetics of the thermal decomposition have been characterized in many β-hydroxyl compounds. The first experimental studies were carried out by Yates and Smith [161] in 1965 and by Yates and Quijano [162] in 1969. The latter studied the thermal decomposition of β-hydroxy ketones and concluded that it is a first-order intramolecular reaction in which the hydrogen of the hydroxyl group interacts with the oxygen of the carbonyl group forming a six-membered cyclic transition state. Also, they analyzed the effect of replacing the hydrogens on the carbon adjacent to the hydroxyl group by methyl groups. The activation energies of alkyl β-hydroxy ketones were found to be about 30 kcal/mol, and the substitution of hydrogens by methyl groups was shown to accelerate the rate of the thermolysis.

Subsequent experimental and theoretical studies in the gas and solution phases have been reported for many β-hydroxy compounds such as β-hydroxyl ketones [163], β-hydroxyl esters [164-168], β-hydroxyl olefins [169] and β-hydroxynitriles [170-172]. All studies also included alkyl β-hydroxyl compounds and arrived at the same conclusions as that of the primary ketone cases.

In this chapter a theoretical study on the thermolysis of a group of β-hydroxyl aldehydes at the MP2(FC)/6-31G(d) and B3LYP/6-31G(d) levels is reported with the emphasis on the activation energies and rate constants obtained by using transition state theory (TST) [173]. Also, single-point calculations by both methods using the 6-311++G(d,p) basis set were performed for the reactants and transition states. Alkyl β-hydroxyl aldehydes and

chloro β-hydroxyl aldehydes were included in order to analyze substituent and electronic effects. Furthermore, the theory of atoms in molecules (AIM) [29,30] is used to study the topology of the electronic structure along the reaction path and to gain insight into this interesting mechanism. The thermolysis for β-hydroxyl aldehydes has not been reported previously.

10.2 Theoretical Background

10.2.1 Transition state theory.

The TST formula to calculate the rate constant is:

$$k = \kappa \frac{k_B T}{h} \frac{Q^{TS}}{Q^{\mathrm{Re}act}} \exp\left(-\frac{E_a}{RT}\right) \tag{10.1}$$

where E_a is the activation energy, κ is the tunneling factor, k_B, h and R are the Boltzmann, Planck and universal gas constants, respectively. Q is the partition function and T is the temperature.

The proposed mechanism for the thermolysis of β-hydroxyl aldehydes is unimolecular and does not involve radical species. Therefore, to calculate the partition function term it is only necessary to compute the rotational and vibrational partition functions because the electronic and translational partition functions [174] are the same for the reactant and transition state and therefore cancel out. The equations to calculate the rotational and vibrational partition functions are:

$$Q_R = \frac{1}{\sigma}\left(\frac{k_B T}{h}\right)^{3/2}\left(\frac{\pi}{ABC}\right)^{1/2} \tag{10.2}$$

$$Q_v = \prod_i \frac{1}{1-\exp\left(-\frac{h\nu_i}{k_B T}\right)} \tag{10.3}$$

where σ is the symmetry number (which is equal to unity in our systems [173]), A, B and C are the rotational constants and ν is the vibrational frequency.

The tunneling factor calculations were carried out by assuming unsymmetrical Eckart barriers [175,176]. In essence the calculation of the tunneling factor in terms of Eckart barriers (which mainly depend on the imaginary frequency of the transition state among other parameters such as the reaction temperature, activation energy and enthalpy of reaction) is an improved version of the simplest methods of Wigner [177] and the parabolic-type barrier tunneling corrections [178]. The Eckart barrier tunneling calculation is still widely used even though more sophisticated tunneling methods such as the multidimensional semiclassical zero and small-curvature methods [179] have been proposed. In 1997 Truong demonstrated the fairly good accuracy of the Eckart barrier tunneling calculation in his study of the hydrogen exchange reaction of methane in a zeolite [180,181].

10.2.2 NBO analysis.

Natural bond orbital (NBO) analysis is a powerful tool to characterize bonds, hyperconjugation effects, bond polarization, hybridization and atomic populations in molecules [168,182-184]. The NBO population analysis is carried out in terms of natural atomic orbitals (NAOs), which are the eigenvectors $\{\varphi_i\}$ obtained by the diagonalization of the atomic one-center blocks of the one-particle density operator expressed in an AO

basis $\{\phi_i\}$. Therefore the matrix representation of the one-particle density operator expressed in the basis of NAOs is a diagonal matrix whose diagonal elements are the orbital populations

$$p_i^{(A)} = \int \varphi_i^{(A)^*}(1)\hat{\gamma}(1|1')\varphi_i^{(A)}(1')d\tau_1 d\tau_{1'} \tag{10.4}$$

The NBO atomic populations are given by

$$p^{(A)} = \sum_i p_i^{(A)} \tag{10.5}$$

where the summation extends over all NAOs.

10.3 Computational Details

The optimization of the geometries of the reactants and products and the exploration of the potential energy hypersurface to determine the transition states and the reaction paths were carried out at MP2 (FC) and B3LYP/6-31G(d) levels of theory. Single-point calculations at MP2 (FC) and B3LYP/6-311++G(d,p) were also carried out. The ab initio calculations were performed by using the GAUSSIAN 03 computational package [53]. Intrinsic reaction coordinate (IRC) calculations were carried out to ensure the validity of the stationary points found (reactants, transition states and products). The energy barriers are corrected for the zero-point vibrational energy (ZPVE). A modified version of the numerical integration program of Brown [185] was used for the calculation of the tunneling factors.

The characterization of critical points was performed using the EXTREME program. The PROAIM program was used to compute the atomic populations, atomic dipole moments and atomic energies. Both programs belong to the AIMPAC package [54].

10.4 Results and Discussion

10.4.1 Transition state characterizations and determination of kinetic parameters.

The mechanism suggested for the thermolysis of the β-hydroxyl aldehydes is shown in Figure 10.1. It is very similar to those proposed for other β-hydroxyl compounds. Table 10.1 lists the bond distances in the reactants and the transition states at the MP2(FC)/6-31G(d) level for several β-hydroxyl aldehydes.

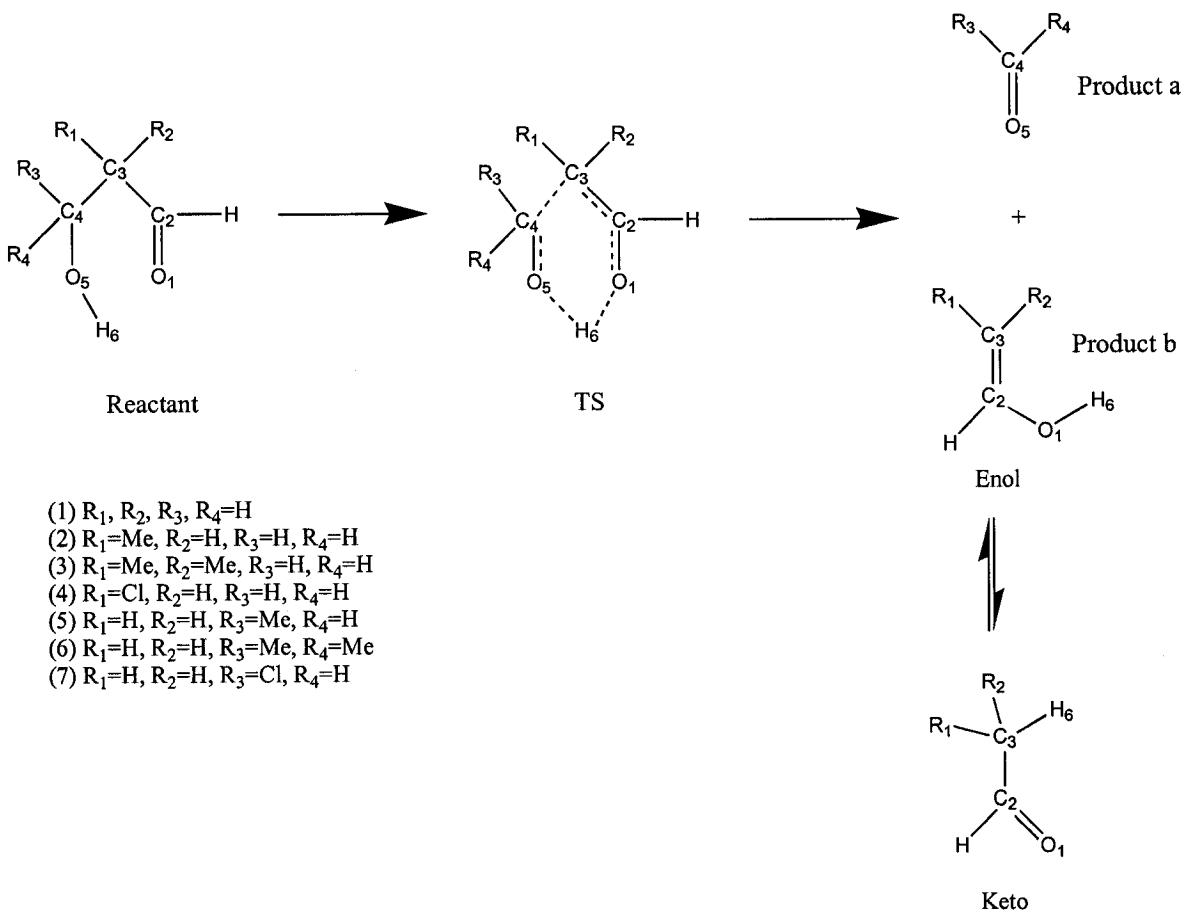

Figure 10.1. Mechanism for the thermolysis of β-hydroxyl aldehydes.

(1) β-hydroxyl aldehyde
(2) 3-methyl β-hydroxyl aldehyde
(3) 3,3-dimethyl β-hydroxyl aldehyde
(4) 3-chloro β-hydroxyl aldehyde
(5) 4-methyl β-hydroxyl aldehyde
(6) 4,4-dimethyl β-hydroxyl aldehyde
(7) 4-chloro β-hydroxyl aldehyde

Table 10.1. MP2(FC)/6-31G(d) bond distances (Å) of the optimized structures of reactants and transition states of β-hydroxyl aldehydes.

Structure	O_1-C_2	C_2-C_3	C_3-C_4	C_4-O_5	O_5-H_6	H_6-O_1
Reactant-1	1.223	1.508	1.525	1.428	0.973	3.535
TS-1	1.303	1.386	2.012	1.282	1.386	1.105
Reactant-2	1.223	1.510	1.526	1.426	0.973	3.485
TS-2	1.304	1.388	2.017	1.283	1.358	1.108
Reactant-3	1.223	1.515	1.532	1.425	0.972	3.718
TS-3	1.306	1.392	2.045	1.285	1.347	1.120
Reactant-4	1.220	1.515	1.526	1.420	0.973	3.464
TS-4	1.299	1.388	2.033	1.279	1.343	1.117
Reactant-5	1.223	1.508	1.529	1.432	0.974	3.440
TS-5	1.301	1.386	2.038	1.287	1.339	1.123
Reactant-6	1.225	1.507	1.542	1.437	0.975	3.039
TS-6	1.300	1.386	2.065	1.293	1.306	1.142
Reactant-7	1.222	1.512	1.521	1.392	0.976	3.369
TS-7	1.299	1.394	1.910	1.260	1.453	1.072

The O_1-C_2 distance and the C_4-O_5 distance increase and decrease, respectively, from the reactants to the transition states in all systems, representing the transition from a CO double bond to a CO single bond and from a CO single bond to a CO double bond, respectively. In all transition states, H_6 is closer to O_1 than to O_6, and therefore, they can be classified as late transition states. Furthermore, Table 10.1 shows that the C_3-C_4 distance increases from the reactants to the transition states for all systems, indicating the breaking of this bond.

Quijano et al. [169] observed nearly planar transition states in their study of β-hydroxyl-olefins, whereas the six-membered cyclic transition states in our systems are far from planarity. The dihedral angles of the transition states are shown in Table 10.2. The C_2-C_3-

C_4-O_5, C_4-O_5-H_6-O_1 and O_1-C_2-C_4-O_5 dihedral angles for system 7 are very different from the average values for the other β-hydroxyl aldehydes. This fact will be discussed below.

Table 10.2. MP2(FC)/6-31G(d) dihedral angles (in degrees) of transition states of β-hydroxyl aldehydes.

	Dihedral Angles (°)					
TS	O_1-C_2-C_3-C_4	C_2-C_3-C_4-O_5	C_3-C_4-O_5-H_6	C_4-O_5-H_6-O_1	O_1-C_2-C_4-O_5	C_2-C_4-O_5-H_6
TS-1	-61.0	58.8	-30.5	-9.2	7.4	-2.2
TS-2	-62.2	56.5	-27.9	-10.9	4.2	-0.1
TS-3	-67.9	60.6	-32.7	0.2	4.4	-2.5
TS-4	-60.5	58.6	-31.3	-2.7	6.9	-3.2
TS-5	-59.5	59.0	-32.2	-5.5	9.7	-4.2
TS-6	-58.8	58.8	-33.0	-2.3	10.7	-5.4
TS-7	-57.0	46.5	-12.9	-39.9	-2.5	10.2

In general the kinetics parameters of the ketones and aldehydes are very similar, which is not surprising because they are both classified as being carbonyl compounds. Experimental data for the thermolysis of β-hydroxyl aldehydes are unavailable. Therefore, the experimental activation energies and rate constants for β-hydroxyl ketones were used to compare with those of the β-hydroxyl aldehydes. In our work the activation energies and rate constants for some alkyl β-hydroxyl ketones [162] at 206.5°C were used for the comparison, thus, the rate constants for the β-hydroxyl aldehydes were calculated at this temperature.

The activation energies and the rate constants for the alkyl substituted β-hydroxyl ketones are about 31 kcal/mol and 10^{-4} sec^{-1}, respectively. The proposed mechanism (Figure 10.1) involves the interaction between the hydrogen of the hydroxyl group and an electron pair of the carbonyl oxygen to form a six-membered cycle. The β-hydroxyl ketones should

have lower activation energies and greater rate constants than the β-hydroxyl aldehydes because the electron pair on the carbonyl oxygen is more available in the ketone case due to the positive inductive effect of the methyl group. The chlorine substituted β-hydroxyl aldehydes were included to analyze the influence of the negative inductive effect in this mechanism. Furthermore, β-hydroxy aldehydes substituted at C_3 and C_4 were analyzed to determine which position produces a larger contribution.

Table 10.3 summarizes the activation energies and the rate constants (not corrected by the tunneling factor) for the thermolysis of β-hydroxy aldehydes at 206.5°C obtained with the MP2 (FC) and B3LYP/6-311++G(d,p)// MP2(FC) and B3LYP/6-31G(d) levels.

Table 10.3. MP2 (FC) and B3LYP/6-311++G(d,p)// MP2 (FC) and B3LYP/6-31G(d), respectively, activation energies and rate constants of β-hydroxyl aldehydes.

	Activation Energy (kcal mol^{-1})		Rate Constant (s^{-1})	
System	MP2	B3LYP	MP2×10^5	B3LYP×10^3
1	36.3	31.1	3.566	8.373
2	35.1	29.3	19.001	83.311
3	34.8	29.3	36.109	100.895
4	37.8	31.3	0.861	8.112
5	35.0	29.0	17.872	99.801
6	33.0	26.3	99.974	1641.995
7	36.0	30.0	5.476	31.859

The MP2 activation energies and rate constants are about 5 kcal/mol greater and one order of magnitude less, respectively, than the experimental results of similar β-hydroxyl ketones. Table 10.3 also illustrates the same trends for the substitution in every position except the case of chlorine at C_4 (system 7). The β-hydroxyl aldehyde with chlorine

substituted at C_4 has a lower activation energy and greater rate constant, respectively, than the unsubstituted β-hydroxyl aldehyde (this fact will be analyzed in detail below by use of AIM theory). These results suggest that a positive inductive effect accelerates the reaction.

The MP2 results in Table 10.3 show that the thermolysis of a β-hydroxyl aldehyde substituted at C_4 exhibits a lower activation energy than with the same substituent substituted at C_3. This result is expected because C_4 is bonded directly to the oxygen of the hydroxyl group which donates the hydrogen atom. When the oxygen atom begins to donate the hydrogen atom, the s character of the oxygen valence shell increases, and the oxygen atom becomes even more electronegative [31,186-189], withdrawing electron density from the carbon. Therefore, a positive inductive effect at C_4 plays a larger role in the thermolysis than at C_3 because the positive character at C_4 is greater than at C_3. This point is supported by the population analysis presented in the following section.

The B3LYP barriers are much lower (by as much as 6 kcal mol^{-1}) and therefore the B3LYP rate constants are much higher. This is similar to the results for β-hydroxyl olefins, for which Quijano et al. [169] concluded that B3LYP overestimates the rate constants.

Even though it is well known that the tunneling factor decreases as the temperature increases [178], the analysis of tunneling gives information about the barrier shape and also contributes to the analysis of substituents effects [190]. Table 10.4 reports the tunneling factors as well as the corrected rate constants for the thermolysis of the seven systems at 206.5°C at the MP2(FC)/6-311++G(d,p) // MP2(FC)/6-31G(d) level.

Table 10.4. MP2(FC)/6-311++G(d,p)// MP2(FC)/6-31G(d) tunneling factors and corrected rate constants of β-hydroxyl aldehydes.

System	Tunneling Factor (κ)	Rate Constant (s^{-1})$\times 10^5$
1	1.435	5.117
2	1.406	26.715
3	1.373	49.578
4	1.513	1.303
5	1.604	28.667
6	1.780	177.954
7	1.277	6.993

According to the tunneling criteria given by Bell,[a] the thermolysis of β-hydroxyl aldehydes exhibits small tunneling factors and does not produce changes in the order obtained from the uncorrected rate constants. Moreover, the tunneling factors show clearly the positional dependence of substituent effects. For instance, methyl at C_3 (systems 2 and 3) leads to tunneling factors smaller than the unsubstituted β-hydroxyl aldehyde, whereas at C_4 (systems 5 and 6) the tunneling factors are greater than in the unsubstituted aldehyde. However, when the substituent is chlorine the opposite effect is observed: system 4 and system 7 exhibit smaller and larger tunneling factors than the unsubstituted aldehyde, respectively.

[a] $1 < \kappa < 1.1$ - negligible tunneling, $1.1 < \kappa < 4$ - small to moderate tunneling, and $4 < \kappa$ - large tunneling.[18]

10.4.2 AIM analysis.

In order to determine if the reactions occur through a six-membered cyclic transition state, a topological study in terms of ring critical points was performed. Table 10.5 characterizes the ring critical points found for all the transition states. Figure 10.2 shows the molecular graphs and the location of the RCPs and their three respective eigenvectors for the seven systems.

Table 10.5. MP2(FC)/6-311++G(d,p) electron densities and eigenvalues at the ring critical points of β-hydroxyl aldehydes.

System	$\rho \times 10^2$	Eigenvalue$\times 10^2$		
		1	2	3
1	2.28	-1.91	6.63	8.94
2	2.32	-2.00	6.56	9.21
3	2.50	-2.26	6.59	10.00
4	2.27	-1.92	6.48	8.91
5	2.26	-1.84	6.53	8.67
6	2.28	-1.82	6.39	8.56
7	2.21	-1.72	6.88	8.53

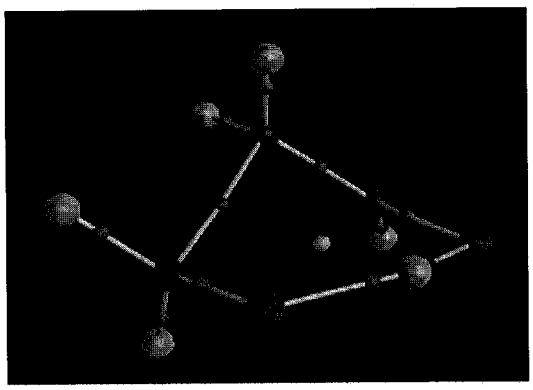

1(a)

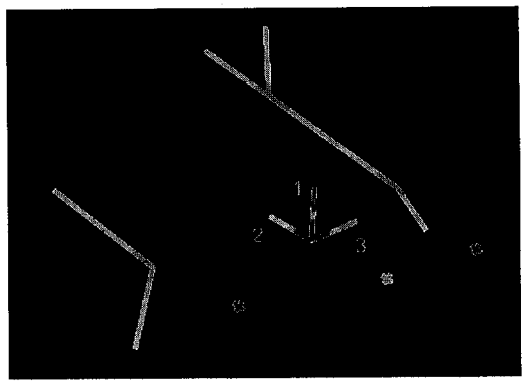

1(b)

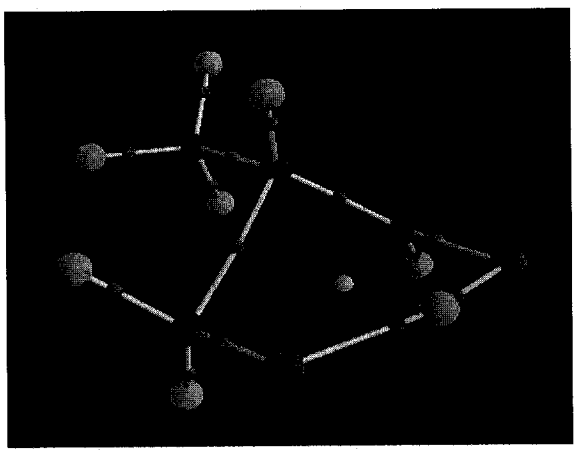

2(a)

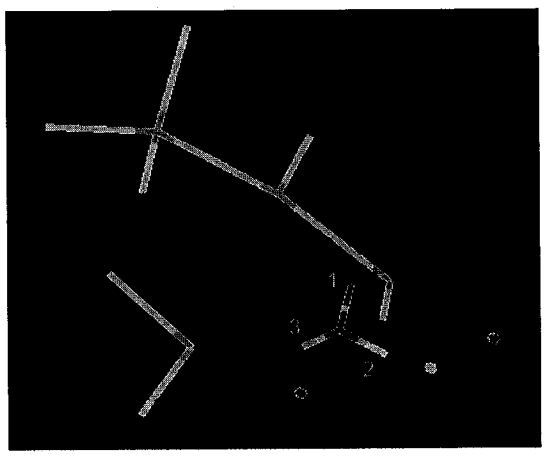

2(b)

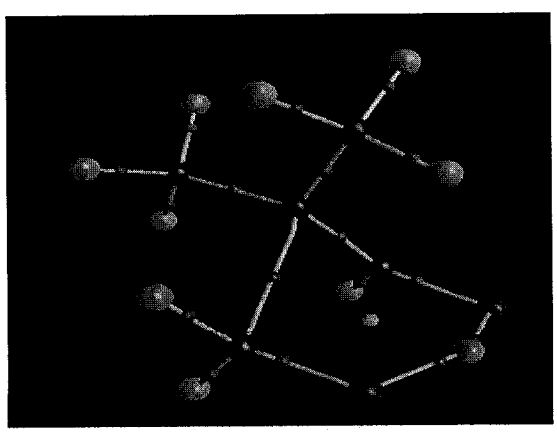

3(a)

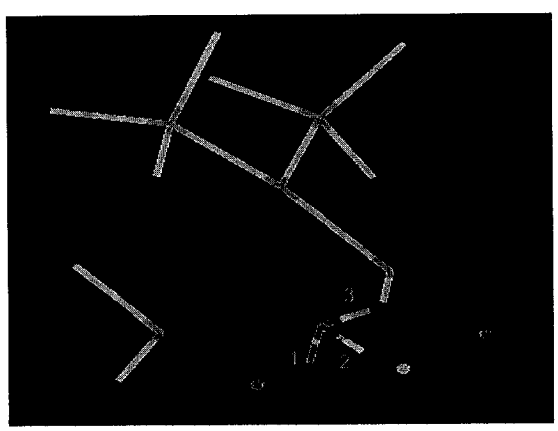

3(b)

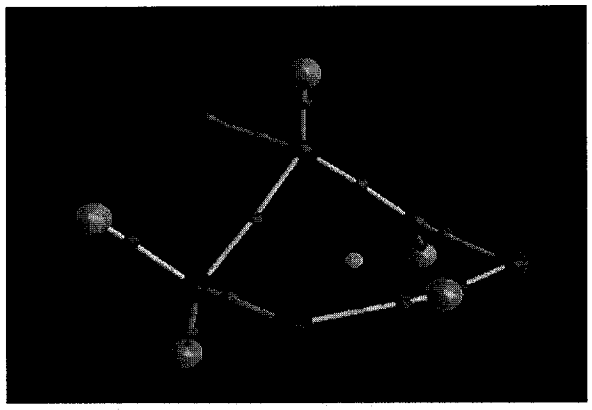

4(a)

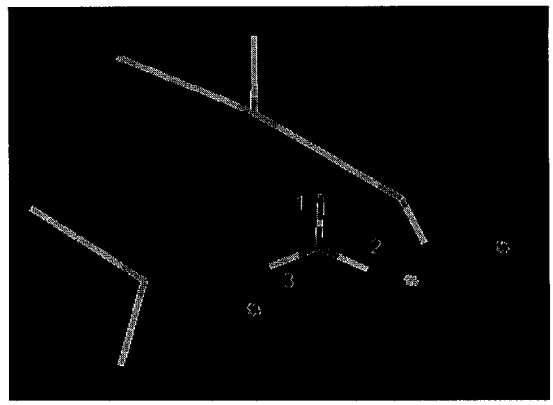

4(b)

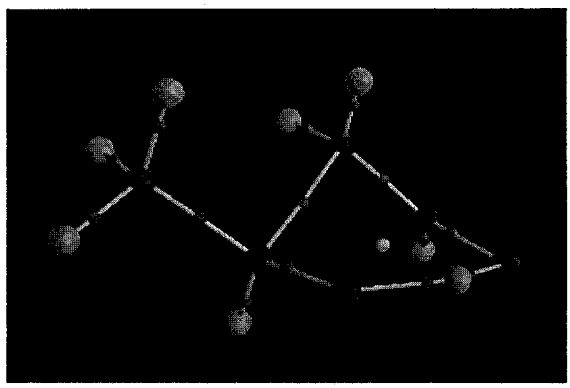

5(a)

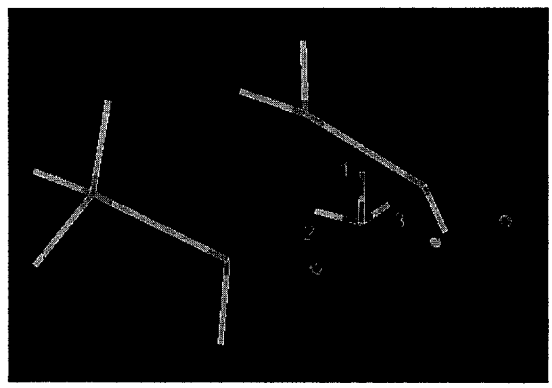

5(b)

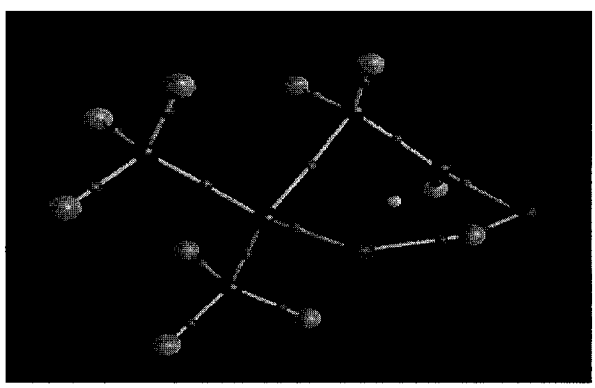

6(a)

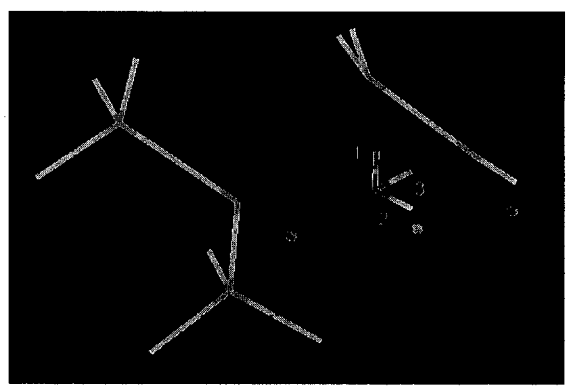

6(b)

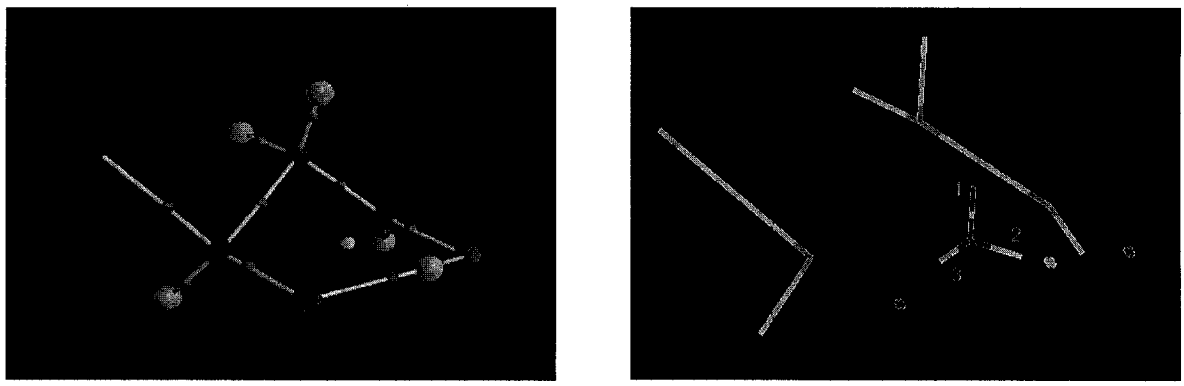

7(a) 7(b)

Figure 10.2. (a) Molecular graphs of the transition states of β-hydroxyl aldehydes, BCPs in red dots and RCP in yellow dot. (b) Characterization of the ring critical points and the eigenvectors in the transition states of β-hydroxyl aldehydes. The seven systems are defined in Figure 10.1 and eigenvectors are indicated in order of increasing eigenvalues in accordance with Table 10.5.

In all cases eigenvector 1 is nearly perpendicular to the six-membered ring. This shows that ρ is decreasing from the center of the ring in the perpendicular direction. Moreover substitution at C_4 decreases the curvature of ρ in the direction perpendicular to the ring (eigenvalue 1), indicating a greater accumulation of ρ in the perpendicular direction for systems 5, 6 and 7 than for the rest of the systems.

The electron density at the ring critical point (ρ_{RCP}) can be considered to be a criterion to measure how much a substituent stabilizes or destabilizes the transition state. For example, higher density at the RCP means stronger attractive interactions between the nuclei and the electron density which in effect reduces the repulsion between nuclei, and helps to stabilize the transition state. The ρ_{RCP} data yield the same trends as kinetics parameters for substituents at C_3. For example, system 3 exhibits the largest value of ρ at the ring critical point and the lowest activation energy while the opposite occurs with system 4. However, the same trend is not observed with substituents at C_4. Systems 5 and

6 exhibit very similar ρ_{RCP} to that of system 1 even though their activation energies are considerably lower. Also, system 7 exhibits lower ρ_{RCP} than system 1 even though its activation energy is lower. Moreover, this criterion does not reproduce the trends when the same substituent is at a different position (C_3 and C_4). For example, systems 2 and 3 exhibit larger ρ_{RCP} than systems 5 and 6, respectively, even though their activation energies are higher. These results also indicate that substituents at positions C_3 and C_4 play different roles in the thermolysis of β-hydroxyl aldehydes.

The electrostatic interaction between O_1 and H_6 in the reactants should contribute to the formation of the cyclic transition state. Therefore, it is reasonable to expect a greater electrostatic attraction between these two atoms would accelerate the reaction. For this reason, a point charge-interaction energy, $U_{PC} = \frac{q_{O_1} q_{H_6}}{d_{O_1-H_6}}$, from the NBO and AIM charges and the internuclear distance, was calculated as a first approximation (Figure 10.3). Table 10.6 lists the computed U_{PC} values.

Table 10.6. The point-charge contribution to the interaction energy (U_{PC}) in kcal/mol obtained by NBO and AIM analyses at the MP2(FC)/6-311++G(d,p) level.

System	NBO	AIM
1	-20.3	-55.0
2	-20.6	-56.0
3	-19.3	-52.6
4	-19.8	-55.7
5	-20.8	-56.1
6	-23.9	-63.7
7	-21.3	-58.9

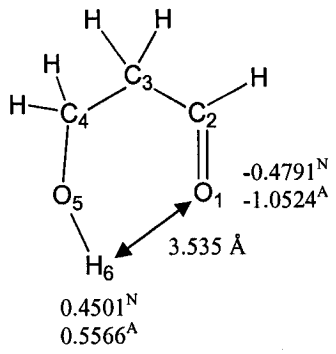

(1)

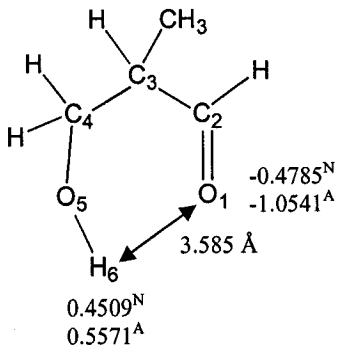

(2)

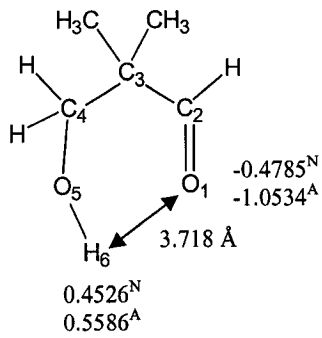

(3)

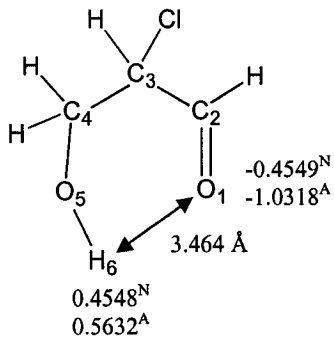

(4)

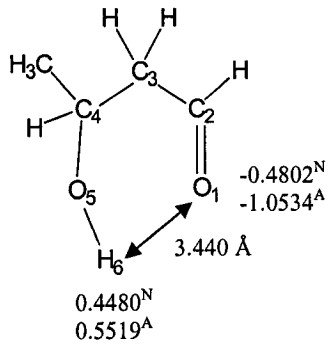

(5)

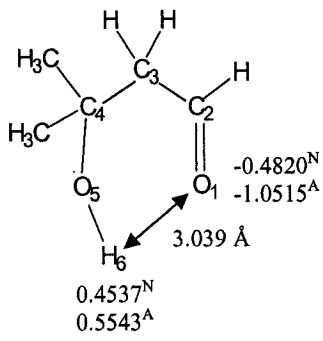

(6)

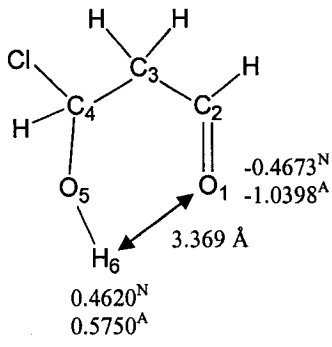

(7)

Figure 10.3. NBO (N) and AIM (A) atomic charges (au) as well as the interatomic distances (Å) between O_1 and H_6 for reactants of all the systems.

The NBO charges differ considerably from those calculated by AIM. For example, the NBO charges of O_1 are roughly half of the AIM values. However, both methods yield similar trends. The NBO U_{PC} values for β-hydroxyl aldehydes substituted at C_3 and C_4 follow the trends 2>1>4>3 and 6>7>5>1, respectively, whereas the AIM values yield 2>4>1>3 and 6>7>5>1, respectively. As suggested above, a larger negative value of U_{PC} indicates a greater attractive interaction, and therefore, it should correlate with faster thermolysis. The results shown in Table 10.6 reproduce the trend obtained by analyzing the kinetics parameters for β-hydroxyl aldehydes substituted at C_4 except that the thermolysis of system 5 (U_{PC} (NBO) = -20.8 kcal/mol, U_{PC} (AIM) = -56.1 kcal/mol) is faster than that of system 7 (U_{PC} (NBO) = -21.3 kcal/mol, U_{PC} (AIM) = -58.9 kcal/mol). Furthermore, the U_{PC} values for β-hydroxyl aldehydes substituted at C_4 are more negative than the respective ones substituted at C_3, and therefore, their thermolysis reactions are faster, which is consistent with the kinetics parameters (Table 10.3). The U_{PC} values for β-hydroxyl aldehydes substituted at C_3 do not reproduce the trend obtained by analyzing the kinetics parameters (Table 10.3).

As a second approximation, we calculated the dipole-moment interaction energy (U_{DM}) between the two atomic dipole moments of O_1 and H_6. Figure 10.4 indicates the direction of the atomic dipole moments of O_1 and H_6 in system 1. Similar directions were found for the other systems. The standard equation which describes the interaction energy between two dipole moments was used [191]:

$$U_{DM} = \frac{[\mathbf{M}_1(O_1)\cdot\mathbf{M}_1(H_6) - 3(\mathbf{M}_1(O_1)\cdot\hat{\mathbf{d}}_{O_1-H_6})(\mathbf{M}_1(H_6)\cdot\hat{\mathbf{d}}_{O_1-H_6})]}{d^3{}_{O_1-H_6}} \qquad (10.6)$$

where $\mathbf{M}_1$ (O_1) and $\mathbf{M}_1$ (H_6) are the atomic dipole moments of O_1 and H_6, respectively, $\hat{\mathbf{d}}_{O_1-H_6}$ is the unitary vector which defines the line connecting O_1 and H_6 and $d_{O_1-H_6}$ is the distance between O_1 and H_6. Table 10.7 lists U_{PC} and U_{DM} and the total interaction energies (U_{total}) for the seven systems.

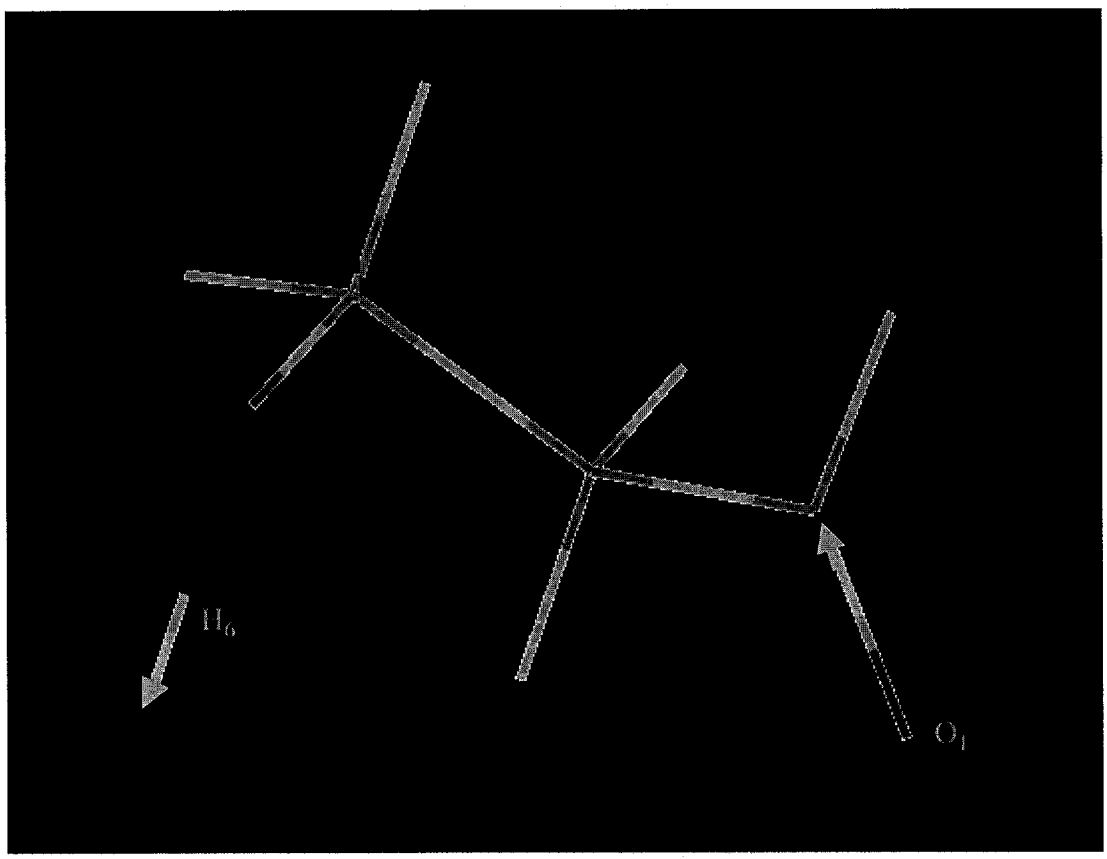

Figure 10.4. Directions of the atomic dipole moments of O_1 and H_6 in system 1.

Table 10.7. The point-charge contribution (U_{PC}) and the dipole-moment contribution (U_{DM}) to the total interaction energy (U_{total}) obtained by AIM at the MP2(FC)/6-311++G(d,p) level. The values are reported in kcal/mol.

System	U_{PC}	U_{DM}	U_{total}
1	-55.0	0.3	-54.7
2	-56.0	0.3	-55.6
3	-52.6	-0.5	-53.0
4	-55.7	0.3	-55.4
5	-56.1	0.2	-56.0
6	-63.7	0.0	-63.6
7	-58.9	-0.3	-59.2

The data in Table 10.7 show that U_{total} and U_{PC} lead to the same trend, and the inclusion of U_{DM} has no effect on the trend. This suggests that the inclusion of higher electric moments would have a negligible effect.

The theory of atoms in molecules partitions a molecule into atomic fragments and yields an atomic energy associated with each atom [29,30]. Changes in atomic energies can be used to determine the effect of substituents. Figure 10.5 illustrates the differences in atomic energies between transition states and reactants for all atoms that form the six-membered cyclic transition state. A negative value indicates a stabilization of the atom in the transition state with respect to the reactant, whereas a positive value indicates the opposite.

Comparison of systems 1, 2 and 3 indicates that the atomic energy of C_3 is lowered substantially by successive methyl substituents at C_3. In the case of system 4, the atomic energy of C_3 (4.8 kcal/mol) is similar to that of system 1 (8.5 kcal/mol), but the stabilization of C_2 in system 1 (-115.9) is greater by almost 9 kcal/mol than in system 4 (-107.1 kcal/mol). Therefore, chlorine at C_3 stabilizes C_2 less with respect to the unsubstituted β-hydroxyl aldehyde, and it accounts primarily for the overall destabilization of the transition state relative to the reactant introduced by the negative

inductive effect of chlorine. With respect to β-hydroxyl aldehydes substituted at C_4, the stabilization introduced by the positive inductive effect of the methyl group in system 5 relative to system 1 occurs mainly at O_5. Moreover, C_4 and O_5 are more stable in system 6 than in system 1. On the other hand, system 7 exhibits a very unstable C_4 with respect to system 1; the negative inductive effect of chlorine produces a large destabilization of C_4. It is interesting to note that system 7 exhibits a much greater stabilization of O_1 at the transition state relative to the reactant than the rest of the systems.

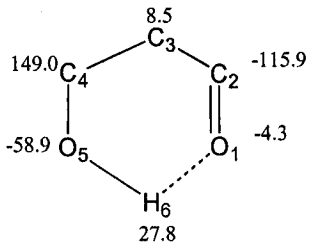

(1)

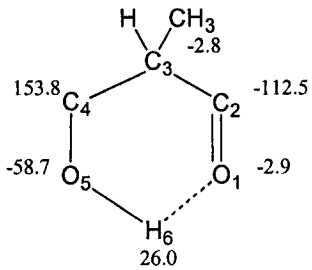

(2)

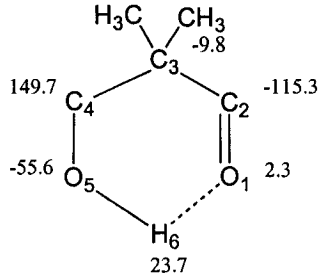

(3)

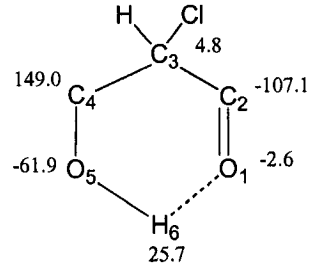

(4)

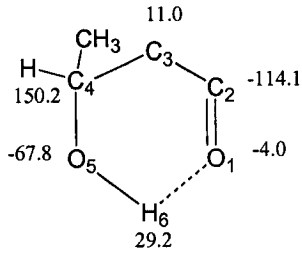

(5)

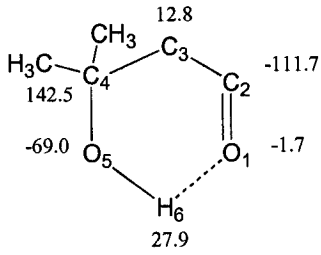

(6)

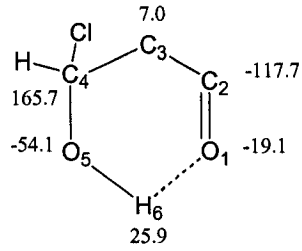

(7)

Figure 10.5. Differences in atomic energies (kcal/mol) between transition states and reactants for the atoms that form the six-membered cyclic transition state. For clarity the substituents have been removed except at C_3 for systems 2, 3 and 4, and at C_4 for systems 5, 6 and 7.

10.4.3 Anomalous behavior of 4-chloro β-hydroxyl aldehyde.

4-Chloro β-hydroxyl aldehyde behaves differently from the other six systems. For example, the dihedral angles of the transition state of 4-chloro β-hydroxyl aldehyde are very different from the average of the other systems. Also, the tunneling factor is very different. Moreover, it has the lowest ρ_{RCP} at the transition state, and it has larger U_{PC} values (NBO and AIM) as well as U_{total} (AIM) than the other systems with the exception of 4,4-dimethyl β-hydroxyl aldehyde. Finally, 4-chloro β-hydroxyl aldehyde exhibits a much greater stabilization of O_1 in the transition state relative to the reactant than the rest of the systems. All these results indicate clearly that a chlorine at C_4 plays a totally different role than a chlorine at C_3 in the thermolysis of β-hydroxyl aldehydes. The effect of chlorine at C_3 is very different from that at C_4, which is bonded to an oxygen that is transformed from a single to a double bond during the reaction. This produces a completely different type of chlorine-carbon interaction which constrains the geometry of the system along the reaction path (Table 10.2) and introduces new electronic effects that result in faster thermolysis than the unsubstituted β-hydroxyl aldehyde.

10.5 Conclusions.

The activation energies and rate constants for the thermolysis of β-hydroxyl aldehydes have been calculated at the MP2/6-311++G(d,p) // MP2(FC)/6-31G(d) level to be between 32 and 38 kcal/mol and 0.8×10^{-5} and 1×10^{-3} s^{-1}, respectively. These results indicate that the thermolysis of β-hydroxyl aldehydes is slower than the thermolysis of similar β-hydroxyl ketones. The B3LYP method with the same basis set underestimates

the activation energies and overestimates the rate constants for the thermolysis of the β-hydroxyl aldehydes, in agreement with previous results reported for β-hydroxyl olefins [169]. The inclusion of the effect of tunneling on the rate constants does not change the trend obtained from the uncorrected rate constants but shows clearly the different roles that C_3 and C_4 play in the thermolysis and the effects of substituents.

The AIM analysis in terms of ring critical points and the topology of the electron density shows that the transition state for the thermolysis of β-hydroxyl aldehydes is a six-membered cycle. Furthermore, ρ at the ring critical points is a good criterion for predicting the trends of the thermolysis rates in the β-hydroxyl aldehydes substituted at C_3. On the other hand, the analysis of the electrostatic interaction between O_1 and H_6 accounts for the trends of the thermolysis rates in the β-hydroxyl aldehydes substituted at C_4.

A positive inductive effect due to methyl groups, either at C_3 or C_4, accelerates the reaction with respect to the unsubstituted β-hydroxyl aldehyde; the effect at C_4 is greater than at C_3. A negative inductive effect due to chlorine at C_3 retards the thermolysis. However, with chlorine at C_4, the rate of thermolysis is accelerated and some anomalous results are exhibited.

Chapter 11 Global Conclusions

The theory of atoms in molecules (AIM) shows in a clear and accessible way the connection between first principles (Hamiltonians, wave functions and the concepts of quantum mechanics) and experiment (chemical processes and molecular systems). The main concepts in chemistry as a science such as atoms, molecules, chemical bonds, valence shells, and functional groups, are defined in a remarkable way by AIM. Furthermore, the theory of atoms in molecules provides theoretical support for the extremely useful valence shell electron pair repulsion model, a model which is inseparable from the way of thinking of both experimental and theoretical chemists and constitutes the basis for interpreting reaction mechanisms and developing new synthetic schemes.

The results presented in this thesis in areas as diverse as NMR, kinetics and organic chemistry, are just a small group of examples of the areas where the theory of atoms in molecules can be applied. It really has no limits in the area of applications. Furthermore, the theory of atoms in molecules can be very useful and has a strong impact in material science, inorganic and coordination chemistry, and biochemistry which are the main directions for future research.

The main conclusion of this thesis is that the theory of atoms in molecules is a very valuable interpretative tool in chemistry, and it should be introduced to all students irrespective of their area of specialization.

All the results presented in this thesis have been published in journals of high impact: Chemical Physics Letters (Chapters 4, 7, and 8), the Journal of Chemical Information and

Modeling (Chapter 5), the Journal of Physical Chemistry A (Chapters 6 and 10) and the Journal of Chemical Theory and Computation (Chapter 9).

11.1 Future Directions

11.1.1 The Negative Divergence of the Quantum Stress Tensor and Conductivity.

The discovery of conducting plastics in the 1970s was a very significant event [192,193]. These plastic materials are polymers that possess very long chains of alternating single and double bonds, and become conductors when reduced or oxided. This process is called p-doping when electrons are removed from the material and n-doping when electrons are inserted into the material [192,193].

The first reported plastic conductor was polyacetylene in 1977, for which Heeger, MacDiarmid and Shirakawa were awarded the Nobel Prize in 2000. Polyacetylene is a semiconductor in its natural state. The trans isomer exhibits a higher conductivity than the cis isomer. They have been studied experimentally and theoretically, and have played a dominant role in the comprehension of the conduction properties of these types of materials.

In an effort to shed light on the electronic origin of the conductivity an AIM study based mainly on the negative divergence of the quantum stress tensor of the *cis* and *trans*-$C_{10}H_{12}$ is being carried out. Also, systems such as *cis* and *trans*-C_6H_8 and cis and trans-$C_{14}H_{16}$ are included to analyze the effect of increasing the chain length. To study the effect of substituents on the conducting properties of the systems, which is one of the main challenges in the synthesis of new conducting materials, *cis* and *trans* isomers of $C_{10}H_{12}$ substituted with F, Cl, Br, NO_2, CN, NH_2 and CH_3 are being considered. All

systems exhibit chains of alternating single and double bonds in a plane (assumed to be the XY plane) and therefore, application of an electric field along the chain will give rise to conductivity.

As was demonstrated in Chapter 3, the equation of motion for any observable $\hat{\mathbf{A}}(\mathbf{r})$ in an open system (assuming a stationary state) is given by equation 3.23:

$$\left\langle \Psi \middle| \left[\hat{H}, \hat{A}\right] \middle| \Psi \right\rangle_{\Omega} = -i\hbar \oint dS(\Omega, \mathbf{r}) \mathbf{j}_A \cdot \mathbf{n}(\mathbf{r}) \tag{11.1}$$

where $\mathbf{j}_A$, the quantum mechanical current density for an observable $\hat{A}$, is defined by equation 3.24.

The choice of $\hat{\mathbf{A}}(\mathbf{r})$ as the electronic momentum operator yields the Ehrenfest force (F(Ω)), which is the force exerted on an open system [29,30,194]:

$$\mathbf{F}(\Omega) = -\oint d\mathbf{S}(\mathbf{r}_S) \cdot \vec{\sigma}(\mathbf{r}) \tag{11.2}$$

where $\vec{\sigma}(\mathbf{r})$, the quantum stress tensor, and is defined by equation 3.55. The quantum stress tensor is a symmetric tensor and it is not incorrect to say that its analogue in classical electrodynamics is the very well known Maxwell stress tensor [191].

Applying Gauss' theorem to equation 11.2 yields:

$$\mathbf{F}(\Omega) = -\int_{\Omega} d\tau \nabla \cdot \vec{\sigma}(\mathbf{r}) \tag{11.3}$$

The local form of this force law is:

$$\mathbf{F}(\mathbf{r}) = -\nabla \cdot \vec{\sigma}(\mathbf{r}) \tag{11.4}$$

F(**r**) is the force exerted on an electron at every point **r** in the charge distribution by the remaining particles in the system.

The basic idea of this project consists of analyzing the direction and values of F(**r**) at several points over the nuclei and bond critical points in the Z direction. Figure 11.1

illustrates the molecular graphs as well as the directions of $F(\mathbf{r})$ at 2 au above the carbon nuclei and carbon-carbon bond critical points in *cis* and *trans*-$C_{10}H_{12}$.

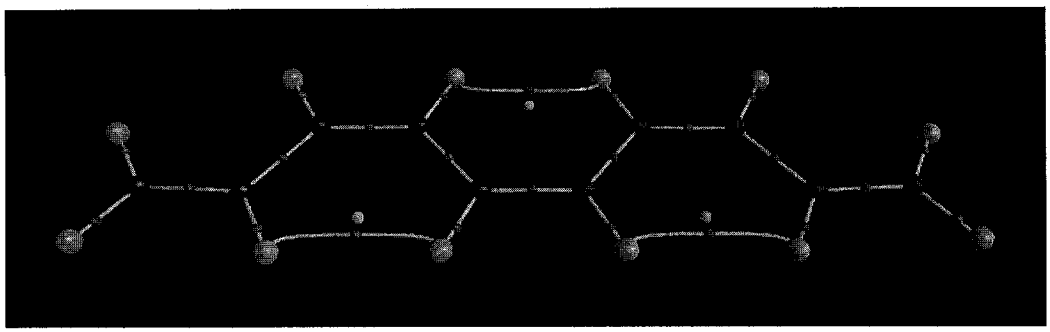

(a)

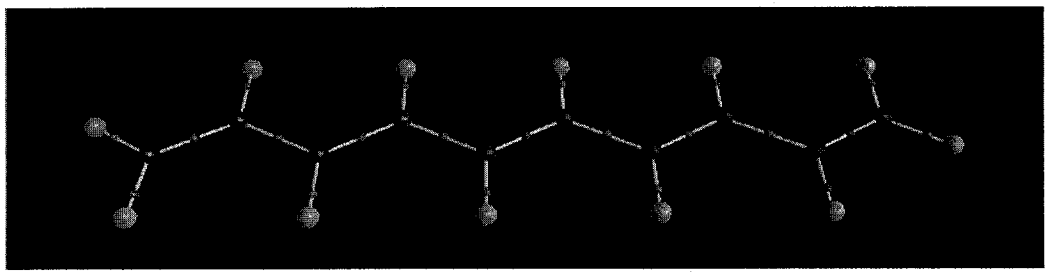

(b)

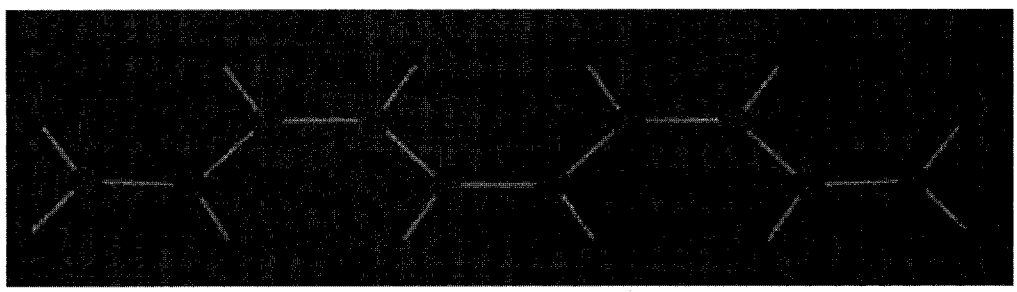

(c)

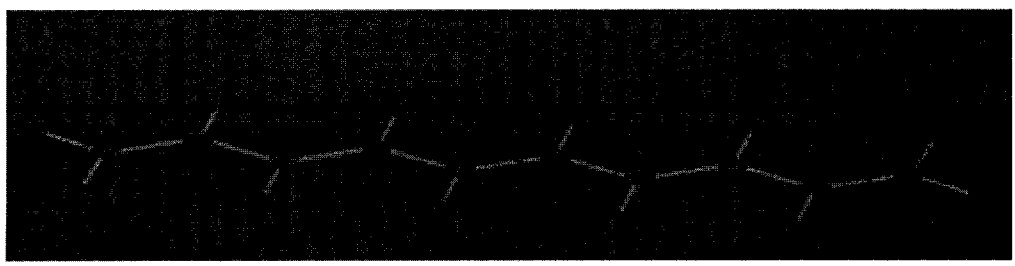

(d)

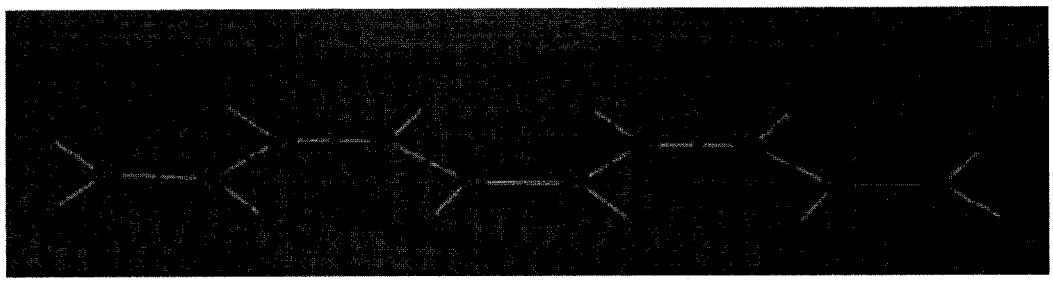

(e)

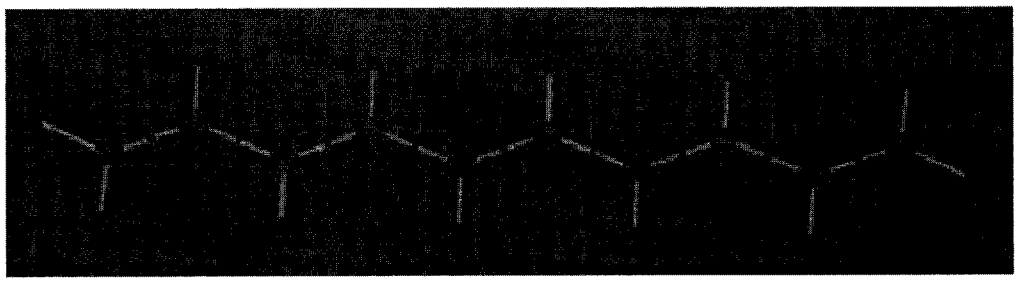

(f)

Figure 11.1. Molecular graphs (a and b) and the directions of F(**r**) at 2 au over the carbon nuclei (c and d), and carbon-carbon bond critical points (e and f) in the *cis* and *trans*-$C_{10}H_{12}$, respectively.

As can be seen in Figure 11.1, the direction of F(**r**) at 2 au above the carbon nuclei and the carbon-carbon BCPs in cis and trans-$C_{10}H_{12}$ is perpendicular to the XY plane. The same direction was found for the force at 0.5, 1.0, 1.5, 2.5 and 3.0 au above the carbon nuclei and carbon-carbon BCPs in all systems. Therefore, it is reasonable to think that the electron mobility generated by an electric field along the chains of alternating single and double bonds is greater when the value of the perpendicular forces on points above the XY plane are smaller. Electron mobility is directly proportional to the conductivity, and therefore, molecules which exhibit smaller values of these perpendicular forces can be considered to have higher conductivity.

The calculations of these perpendicular forces in *cis* and *trans*-C_6H_8, *cis* and *trans*-$C_{10}H_{12}$ and *cis* and *trans*-$C_{14}H_{16}$ as well as in *cis* and *trans*-$C_{10}H_{12}$ substituted with F, Cl, Br,

NO_2, CN, NH_2 and CH_3 are being carried out. A new version of the EXTREME program belonging to the AIMPAC program package is being used to perform the calculation [54]. The available version of the EXTREME program has some inconsistencies in the calculation of the negative of the divergence of stress tensor and reorientation of the molecular geometries. These problems were fixed to develop the new version.

11.1.2 Bond Length and the Electron Density at the Bond Critical Point: X-X, Z-Z, and C-Z Bonds (X = Be-F, Z = Na-Cl)

The estimation of bond properties from parameters at the critical points in the electron density distributions of molecules has become a very popular area of research in the last 25 years. Specifically, the estimation of bond length from parameters at the bond critical point (BCP) has received much attention. In particular, the electron density (ρ) at the bond critical point has been used to estimate bond lengths.

There are several reports in the literature showing correlations of ρ_{BCP} and bond length. One of the first correlations was reported by Bader and co-workers in 1982 where the authors showed a linear correlation between bond length and ρ_{BCP} for C-C bonds in ethane, benzene, ethylene and acetylene [195] at HF/STO-3G level. The linear relationship was $\rho_{BCP} = -0.184 d_{C-C} + 0.777$ and it is a generalization of the bond order-bond length relationship. Five years later Boyd and Choi carried out the same type of analysis of heterobonds for the first time [196], namely, C-N bonds (HF/6-31G(d)) and complexes of the type of R-C≡N---HF and R-C≡N---HCl (HF/6-31G(d)). Specifically in the analysis of CN bonds, Boyd and Choi included systems with simple, double and triple CN bonds as Bader did in the CC case, expecting the fulfillment of the bond order-bond

length relationship in the CN case. All the analyses exhibited a linear correlation with a correlation coefficient greater than 0.98. Therefore, the bond order-bond length relationship was also established in the CN case.

However, a linear correlation cannot be true for a more complete set of systems because it predicts negative electron densities for long bond lengths. Therefore, a power fit should be more realistic than the linear fit, as shown by Knop, Boyd and Choi in a more general study (HF/6-31G(d)) [197] with the following title: "S-S Bond Lengths, or Can Bond Length Be Estimated by a Single Parameter?" in 1988. They analyzed S-S, O-O, Al-F and Be-Cl and also re-fitted the data proportioned by the above reports of Bader and Boyd. The correlation analysis showed a considerably better power fit between bond length and ρ_{BCP} than the linear fit. The main conclusion of this work was that deviations from the power-law correlation depend on sampling problems, and that better designed and more complete sample sets can be expected to vindicate the essential validity of the power-law correlation.

In 1998 Alkorta and co-workers reported a similar correlation study between the electron density at the BCP and the bond lengths to that of Bader about ethane, benzene, ethylene and acetylene but at higher level of theory [198]. The systems were optimized at HF/6-311++G(d,p) and single point calculations at B3LYP/6-311++G(d,p) were carried out to calculate ρ at the BCP. A linear fit was again obtained ($\rho_{BCP} = -2.87 d_{C-C} + 2.23$) with a correlation coefficient of 0.995. Furthermore, they included an analysis on complexes such as R-C≡N----HF and R-C≡N----HCl at the same level of theory used for the hydrocarbons, where 10 and 7 systems were analyzed, respectively. A linear fit was obtained for both cases with a correlation coefficient of 0.98.

Two years later, Alkorta and coworkers [199] considered a broad range of compounds such as a van der Waals and hydrogen bond interactions as well as typical covalent bonds. Also, they divided the sets into types of chemical bonds, for example, H-H (n=12), C-H (n=33), O-H (n=26), N-H (n=24), F-H (n=12), Cl-H (n=25), Br-H (n=12), C-C (n=21), C-O (n=12), C-N (n=11), C-S (n=6), C-Br (n=10), Br-N (n=14) and S-S (n=19). The geometry and ρ at the BCP was either taken from experiment and ab initio calculations (B3LYP/6-311++G(d,p) and MP2/6-311++G(d,p)). The authors had demonstrated previously in two reports in 1998 and 1999, that the use of different ab initio methods does not produce any significant loss statistically [200,201]. The statistical analysis in terms of square correlation coefficient[1], standard deviation[2] and the Durbin-Watson[3] test shows that the power and exponential fits properly correlate ρ at the BCP and the bond lengths for each type of chemical bonds. Slightly better results were observed for the exponential model.

In 2001, Knop, Rankin and Boyd reported a correlation study between the bond length and ρ at the BCP in N'-H---N'' hydrogen bonds [202]. The study was carried out at the HF/6-31G(d,p) level for 63 compounds and MP2/6-31G(d,p) for 19 compounds. The correlation analysis was performed on the logarithmically transformed functions, and it showed acceptable correlations for both power and exponential fits at the two different levels. The square correlation coefficients and standard deviations for power-HF and

---

[1]Coefficient of determination ($0 \leq r^2 \geq 1$) is a measure of the degree of association between two variables. Its maximum value corresponds to 1.

[2]Standard deviation (SD) is the square root of the mean of the squared deviations of member of a population from their mean measures. It provides an idea of the average deviation of the fitted values to the original set of data.

[3]The Durbin-Watson test (DW) measures the association of between successive residuals. For example, a value of 2 signifies that the residuals are not correlated to each other.

power-MP2 were 0.768 & 0.0159 and 0.967 & 0.0139. In the case of the exponential fit, they were 0.770 & 0.0150 and 0.972 & 0.0127, respectively. However, significantly better fits were obtained at the two levels of calculations when two separate regression functions of the same type were used:

$$\text{Power fit} \longrightarrow \ln(\rho'/\rho'') = a + b\ln d'' + c\ln(d''/d') \qquad (11.5)$$

$$\text{Exponential fit} \longrightarrow \ln(\rho'/\rho'') = a + bd'' + c(d''/d') \qquad (11.6)$$

where ρ' and d' are the electron density at the BCP and bond length for the N'-H bond, whereas ρ'' and d'' are the electron density at the BCP and bond length for the H---N'' bond. For example in the case of MP2/6-31G(d,p), the values of R^2 and SD were 0.999 and 0.0393 for the power fit, and 0.999 and 0.0454 for the exponential fit. The authors stated that the universality of this finding has to be tested at higher levels of calculation as well as by experiment. This result is remarkable because it shows that the parameter of both bonds N'-H (covalent) and H---N'' (hydrogen bond) are correlated. Grabowsky [203] reached a similar conclusion for several types of hydrogen bonds X-H---Y (X=O and F, Y=O and N) and showed that the hydrogen bond energy can be estimated from the parameters of the X-H bond.

One year later, Knop, Rankin and Boyd carried out a detailed study about correlation between parameters of both bonds to gain more insight in the correlation between N'-H and H---N'' bonds [204]. They reported a strong linear correlation between ρ' and ρ'' for a set of 54 molecules at the MP2/6-31G(d,p) level (R^2=0.983). Also, they reported a strong exponential correlation between $\nabla^2\rho_{BCP}$' and $\nabla^2\rho_{BCP}$'' (R^2=0.982).

In this project, a broader study and at a higher level of theory than that of Knop, Boyd and Choi [197] is underway for all the homonuclear combinations of the first (Li-Li, Be-

Be, B-B, C-C, N-N, O-O and F-F) and second rows (Na-Na, Mg-Mg, Al-Al, Si-Si, P-P, S-S and Cl-Cl) of the periodic table with the exception of the noble gases. The objective of the study is to generalize the correlation between bond lengths and ρ_{BCP}. Furthermore, a comparison between power, exponential and linear fits for all combinations will be carried out. An extension of the study to the analysis of heteronuclear combinations (C-S, C-Cl, N-S, N-Cl, O-S, O-Cl, etc) is planed. Moreover, a multilinear relationship between bond length and the formal molecular orbital electron occupancies in diatomic molecules will be investigated.

References

[1] A. Messiah, Quantum Mechanics, John Wiley, New York, 1961.

[2] A. Szabo, N. S. Ostlund, Modern Quantum Chemistry, Introduction to Advanced Molecular Structure Theory, McGraw-Hill, New York, 1989.

[3] W. J. Hehre, L. Radom, P. v. R. Schleyer, J. A. Pople, Ab initio Molecular Orbital Theory, John Wiley and Sons, 1986.

[4] C. C. J. Roothaan, Rev. Mod. Phys. 23, 69, 1951.

[5] J. C. Slater, Phys. Rev. 36, 57, 1930.

[6] S. F. Boys, Proc. Roy. Soc. (London), A200, 542, 1950.

[7] P.-O. Löwdin, Adv. Chem. Phys.2, 207, 1959.

[8] I. N. Levine, Quantum Chemistry, Allyn and Bacon, Boston, 1974, p190.

[9] R. E. Watson, Phys. Rev. 119, 170-177, 1960.

[10] O. Sinanoglu, Many-electron Theory of Atoms, Molecules, and Their Interactions, Adv. Chem. Phys. 6, 315, 1964.

[11] R. K. Nesbet, Electronic Correlation in Atoms in Molecules. Adv. Chem. Phys. 9, 321, 1965.

[12] J. Cizek and J. Paldus, Coupled-cluster Approach, Physica Scripta 21, 251, 1980.

[13] R. G. Parr and W. Yang, Density-Functional Theory of Atoms in Molecules. Oxford University Press. New York, 1989.

[14] E. V. Ludena, J. Chem. Phys. 79, 6174, 1983.

[15] J. P. Perdew, Phys. Rev. Lett. 55, 1665, 1985.

[16] W. Kohn and L. J. Sham, Phys. Rev. 140, A 1133, 1965.

[17] J. P. Perdew and Y.Wang, Phys. Rev. B45, 13244, 1992.

[18] A. D. Becke, J. Chem. Phys., 98, 5648, 1993.

[19] J. B. Foresman, Exploring Chemistry with Electronic Structure Methods, 2nd Ed, 1996.

[20] (a) W. J. Hehre, Practical Strategies for Electronic Structure Calculations, Wavefunctions Inc., Irvine, 1995. (b) H. B. Schlegel, Encycl. Comput. Chem, 2, 1136, 1998. (c) T. Schlick, Encycl. Comput. Chem. 2, 1143, 1998.

[21] E. B. Wilson, J. C. Decius, P. C. Cross, Molecular Vibrations, McGraw-Hill: New York, 1955.

[22] D. E. Sands, Introduction to Crystallography. New York: Dover Publications, Inc. 1975.

[23] G. Rhodes, Crystallography Made Crystal Clear: A Guide for Users of Macromolecular Models. San Diego: Academic Press, Inc, 1993.

[24] C. F. Matta, Applications of the Quantum Theory of Atoms in Molecules to Chemical and Biochemical Problems. Ph.D. Thesis, McMaster University. Hamilton, Canada: 2002.

[25] P. Coppens, X-Ray Charge Densities and Chemical Bonding. New York: Oxford University Press, Inc, 1997.

[26] B. M. Carven, H. P. Weber, X. M. He, The POP Least-Squares Refinement Procedure, Technical Report, Department of Crystallography, University of Pittsburgh, USA, 1987.

[27] N. K. Hansen, P. Coppens, Acta Crystallogr. A34, 909, 1978.

[28] T. S. Koritsanszky, P. Coppens, Chem. Rev. 101, 1583, 2001.

[29] R. F. W. Bader, Atoms in Molecules-A Quantum Theory (Oxford University Press, New York, 1990).

[30] R. F. W. Bader, Chem. Rev. 91, 893, 1991.

[31] R. J. Gillespie, I. Bytheway, R. S. DeWitte, R. F. W. Bader, J. Inorg. Chem., 33, 2115, 1994.

[32] R. F. W. Bader, P. J. MacDougall, C. D. H. Lau, J. Am. Chem. Soc. 106, 1594, 1984.

[33] R. F. W. Bader, P. M. Beddall, J. Chem. Phys. 56, 3320, 1972.

[34] (a) E. Schrödinger, Ann. D. Phys. 79, 361, 1926. (b) E. Schrödinger, Ann. D. Phys. 81, 109, 1926.

[35] S. Srebrenik, R. F. W. Bader, J. Chem. Phys. 63, 3945, 1975.

[36] R. F. W. Bader, Can. J. Chem. 76, 973, 1998.

[37] R. F. W. Bader, Phys. Rev. B. 49, 13348, 1994.

[38] R. F. W. Bader, P. L. A. Popelier, T. A. Keith, Angew. Chem. Int. Ed. Engl. 33, 620, 1994.

[39] CRC Handbook of Chemistry and Physics, 62nd Ed. (CRC Press, Inc. Boca Raton, Florida, 1982).

[40] J. Huheey, E. Keiter, and R. Keiter, Inorganic Chemistry: Principles of Structure and Reactivity, 4th ed. (HarperCollins College, 1993).

[41] F. A. Cotton and G. Wilkinson, Basic Inorganic Chemistry (New York: Wiley, 1988).

[42] R. J. Gillespie and I. Hargittai, The VSEPR Model of Molecular Geometry (Boston, Allyn and Bacon 1991).

[43] F. B. Mallory, J. Am. Chem. Soc. 95, 7747, 1973.

[44] J. Mason, Multinuclear NMR (Plenum Press, New York, 1987).

[45] S. Berger, S. Braun, and H. Kalinowski, NMR Spectroscopy of the Non-Metallic Elements, (New York, John Wiley & Sons, 1997).

[46] J. Hilton and L. H. Sutcliffe, Progr. NMR Spectrosc. 10, 27, 1975.

[47] R. P. Sagar, A. C. T. Ku, V. H. Smith, and A. M. Simas, J. Chem. Phys. 88, 4367, 1988.

[48] Z. Shi and R. J. Boyd, J. Chem. Phys. 88, 4375, 1988.

[49] R. P. Sagar, A. C. T. Ku, V. H. Smith and A. M. Simas, Can. J. Chem. Eng. 66, 1005, 1988.

[50] W. Chan, I. P. Hamilton, J. Chem. Phys. 108, 2473, 1998.

[51] R. J. Gillespie, I. Bytheway, T. Tang, and R. F. W. Bader, Inorganic Chemistry, 35, 3954, 1996.

[52] A. A. Oliferenko, S. A. Pisarev, V. A. Palyulin, and N. S. Zefirov, Vestnik Moskovskogo Universiteta, Seriya 2: Khimiya, 41, 325, 2000.

[53] M. J. Frisch, G. W. Trucks, H. B. Schlegel, G. E. Scuseria, M. A. Robb, J. R. Cheeseman, Jr., J. A. Montgomery, T. Vreven, K. N. Kudin, J. C. Burant, J. M.

Millam, S. S. Iyengar, J. Tomasi, V. Barone, B. Mennucci, M. Cossi, G. Scalmani, N. Rega, G. A. Petersson, H. Nakatsuji, M. Hada, M. Ehara, K. Toyota, R. Fukuda, J. Hasegawa, M. Ishida, T. Nakajima, Y. Honda, O. Kitao, H. Nakai, M. Klene, X. Li, J. E. Knox, H. P. Hratchian, J. B. Cross, C. Adamo, J. Jaramillo, R. Gomperts, R. E. Stratmann, O. Yazyev, A. J. Austin, R. Cammi, C. Pomelli, J. W. Ochterski, P. Y. Ayala, K. Morokuma, G. A. Voth, P. Salvador, J. J. Dannenberg, V. G. Zakrzewski, S. Dapprich, A. D. Daniels, M. C. Strain, O. Farkas, D. K. Malick, A. D. Rabuck, K. Raghavachari, J. B. Foresman, J. V. Ortiz, Q. Cui, A. G. Baboul, S. Clifford, J. Cioslowski, B. B. Stefanov, G. Liu, A. Liashenko, P. Piskorz, I. Komaromi, R. L. Martin, D. J. Fox, T. Keith, M. A. Al-Laham, C. Y. Peng, A. Nanayakkara, M. Challacombe, W. P. M. Gill, B. Johnson, W. Chen, M. W. Wong, C. González and J. A. Pople, Gaussian03, Revision B.03. Gaussian Inc.: Pittsburgh PA, 2003.

[54] F. W. Biegler-König, R. F. W. Bader, and T. J. Tang, Comput. Chem. 3, 317, 1982.

[55] G. Schaftenaar and J. H. Noordik, J. Comput.-Aided Mol. Design, 14, 123, 2000.

[56] Y. G. Gakh, A. A. Gakh, A. M. Gronenborn, Magn. Reson. Chem. 38, 551, 2000.

[57] N. F. Ramsey, Phys. Rev. 91, 303, 1953.

[58] M. J. Stephen, Proc. Roy. Soc. (London) A, 243, 274, 1957.

[59] S. J. Wilkens, W. M. Westler, J. L. Markley, F. Weinhold, J. Am. Chem. Soc. 123, 12026, 2001.

[60] T. Helgaker, M. Jaszuński, K. Ruud, Chem. Rev. 99, 293, 1999.

[61] M. A. Watson, P. Salek, P. Macak, M. Jaszuński, T. Helgaker, Chem. Eur. J. 10, 4627, 2004.

[62] I. Alkorta, J. Elguero, Int. J. Mol. Sci. 4, 64, 2003.

[63] T. Helgaker, M. Jaszuński, K. Ruud, A. Górska, Theor. Chim. Acc. 99, 175, 1998.

[64] J. E. Peralta, R. H. Contreras, J. P. Zinder, J. Chem. Soc., Chem. Commun., 2025, 2000.

[65] J. E. Peralta, V. Barone, R. H. Contreras, D. G. Zaccari, J. P. Snyder, J. Am. Chem. Soc. 123, 9162, 2001.

[66] J. San Fabián, A. J. A. Westra Hoekzema, J. Chem. Phys. 121, 6268, 2004.

[67] L. Ernst, K. Ibrom, Angew. Chem. Int. Ed. Engl. 34, 1881, 1995.

[68] F. B. Mallory, C. W. Mallory, K. E. Butler, M.-B. Lewis, A. Qian Xia, E. D. Jr. Luzik, L. E. Fredenburgh, M. M. Ramanjulu, Q. N. Van, M. M. Francl, D. A. Freed, C. C. Wray, C. Hann, M. Nerz-Stormes, P. J. Carroll, L. E. Chirlian, J. Am. Chem. Soc. 122, 4108, 2000.

[69] I. Alkorta, J. Elguero, Struct. Chem. 15, 117, 2004.

[70] R. F. W. Bader, M. E. Stephens, J. Am. Chem. Soc. 97, 7391, 1975.

[71] X. Fradera, M. A. Austen, R. F. W. Bader, J. Phys. Chem. A, 103, 304, 1999.

[72] C. F. Matta, J. Hernández-Trujillo, R. F. W. Bader, J. Phys. Chem. A, 106, 7369, 2002.

[73] J. A. Pople, W. G. Schneider, H. J. Bernstein, High-Resolution Nuclear Magnetic Resonance. New York: McGraw-Hill Book Co. Inc., 1959.

[74] W. Kohn, L. J. Sham, Phys. Rev. A, 140 (4A), 1133, 1965.

[75] J. Poater, M. Solà, M. Duran, X. Fradera, Theor. Chem. Acc. 107, 362, 2002.

[76] C. F. Matta, AIMDELOC: Program to calculate AIM localization and delocalization indices (QCPE0802). 2001, Quantum Chemistry Program Exchange, Indiana University: IN. (http://qcpe.chem.indiana.edu/)

[77] Minitab. *MINITAB, Release 13 for Windows.*Minitab Inc.: PA, U.S.A, 2000.

[78] Microcal. Origin v.6.0. Microcal Software, Inc.: MA, USA, 1999.

[79] C. F. Matta, J. Hernández-Trujillo, J. Phys. Chem. A, 107, 7496, 2003.

[80] M. A. Austen, A New Procedure for Determining Bond Orders in Polar Molecules, with Applications to Phosphorus and Nitrogen Containing Systems. Ph.D. Thesis, McMaster University. Hamilton, Canada: 2003.

[81] F. B. Mallory, C. W. Mallory, M. B. Baker, J. Am. Chem. Soc. 112, 2577, 1990.

[82] S. Berger, S. Braun, H. Kalinowski, NMR Spectroscopy of the Non-Metallic Elements. New York: John Wiley & Sons, 1997.

[83] F. B. Mallory, C. W. Mallory, W. M. Ricker, J. Org. Chem. 50, 457, 1985.

[84] P. Murray-Rust, W. C. Stallings, C. T. Monti, R. K. Preston, J. P. Glusker, J. Am.

Chem. Soc. 105, 3206, 1983.

[85] J. A. R. P. Sarma, G. R. Desiraju, Acc. Chem. Res. 19, 222, 1986.

[86] S. L. Price, A. J. Stone, R. S. Rowland, A. E. Thornley, J. Am. Chem. Soc. 116, 4910, 1994.

[87] N. Ramasubbu, R. Parthasarathy, P. Murray-Rust, J. Am. Chem. Soc. 108, 4308, 1986.

[88] G. R. Desiraju, R. Parthasarathy, J. Am. Chem. Soc. 111, 8725, 1989.

[89] L. Shimoni, H. L. Carrell, J. P. Glusker, M. M. Coombs, J. Am. Chem. Soc. 116, 8162, 1994.

[90] L. Pauling, The Nature of the Chemical Bond, 3rd ed., Cornell University Press: Ithaca, N.Y., 1960.

[91] V. Tsirelson, P. F. Zou, T.-H. Tang, R. F. W. Bader, Acta Cryst. A, 51, 143-153, 1995.

[92] A. Bach, D. Lentz, P. Luger, J. Phys. Chem. A, 105 , 7405, 2001.

[93] S. J. Grabowski, A. Pfitzner, M. Zabel, A. T. Dubis, M. Palusiak, J. Phys. Chem. B, 108, 1831, 2004.

[94] I. Alkorta, I. Rozas, J. Elguero, J. Phys. Chem. A, 102, 9278, 1998.

[95] N. Castillo, C. F. Matta, R. J. Boyd, J. Chem. Inf. Mod. 45, 354, 2005.

[96] R. J. Boyd, S. C. Choi, Chem. Phys. Letters. 120, 80, 1985.

[97] R. J. Boyd, S. C. Choi, Chem. Phys. Letters. 129, 62, 1986.

[98] R. J. Boyd, K. E. Edgecombe, J. Am. Chem. Soc. 110, 4182, 1988.

[99] R. J. Boyd, S. L. Boyd, J. Am. Chem. Soc. 114, 1652, 1992.

[100] D. Cremer, E. Kraka, Angew. Chem. Int. Ed. Engl. 23, 627, 1984.

[101] T. A. Keith, R. F. W. Bader, Y. Aray, Int. J. Quantum Chem. 57, 183, 1996.

[102] C. F. Matta, J. Hernández-Trujillo, T. H. Tang, R. F. W. Bader, Chem. Eur. J. 9, 1940, 2003.

[103] F. Cortés-Guzmán, J. Hernández-Trujillo, G. J. Cuevas, Phys. Chem. A, 107, 9253, 2003.

[104] F. W. Biegler-König, J. Schönbohm, D. J. Bayles, Comput. Chem. 22, 545, 2001.

[105] F. W. Biegler-König, J. Schönbohm, and D. Bayles, AIM2000 program can be downloaded from Internet at http://gauss.fh-bielefeld.de/aim2000.

[106] M. Shacham, M. B. Cutlip, M. Elly, POLYMATH 5.1; CACHE Corporation, The University of Connecticut, Ben Gurion University of the Negev, and University of Michigan.

[107] K. N. Robertson, O. Knop, T. S. Cameron, Can. J. Chem. 81, 727, 2003.

[108] C.-C. Wang, T.-H. Tang, L.-C. Wu, Y. Wang, Acta Cryst. A, 60, 488, 2004.

[109] P. L. A. Popelier, J. Phys. Chem. A, 102, 1873, 1998.

[110] S. J. Grabowski, J. Phys. Chem. A, 104, 5551, 2000.

[111] S. J. Grabowski, J. Phys. Chem. A, 105, 10739, 2001.

[112] M. Calhorda, J. Chem. Commun. 801, 2000.

[113] I. Alkorta, I. Rozas, Elguero, J. Chem. Soc. Rev. 27, 163, 1998.

[114] M. T. Carroll, R. F. W. Bader, Mol. Phys. 65, 695, 1988.

[115] J. R. Cheeseman, M. T. Carroll, R. F. W. Bader, Chem. Phys. Lett. 143, 450, 1988.

[116] U. Koch, P. L. A. Popelier, J. Phys. Chem. 99, 9747, 1995.

[117] O. Knop, K. N. Rankin, R. J. Boyd, J. Phys. Chem. A, 105, 6552, 2001.

[118] O. Knop, K. N. Rankin, R. J. Boyd, J. Phys. Chem. A, 107, 272, 2003.

[119] E. A. Zhurova, V. G. Tsirelson, A. I. Stash, A. A. Pinkerton, J. Am. Chem. Soc. 124 , 4574, 2002.

[120] R. Bianchi, G. Gervasio, D. Marabello, Inorg. Chem. 39, 2360, 2000.

[121] R. F. W. Bader, C. F. Matta, Inorg. Chem. 40, 5603, 2001.

[122] N. Castillo, C. F. Matta, R. J. Boyd, Chem. Phys. Lett. 409, 265, 2005.

[123] R. F. W. Bader, J. Phys. Chem. A, 102, 7314, 1998.

[124] A. R. Choudhury, U. K. Urs, T. N. Guru Row and K. Nagarajan, J. Mol. Struct. 605, 71, 2002.

[125] R. Choudhury and T. N. Guru Row, Cryst. Growth Des. 4, 47, 2004.

[126] R. Bayón, S. Coco and P. Espinet, Chem. Eur. J. 11, 1079, 2005.

[127] C. F. Matta, N. Castillo and R. J. Boyd, J. Phys. Chem. A. 109, 3669, 2005.

[128] P. L. A. Popelier, Atoms in Molecules: An Introduction (Prentice Hall, London, 2000).

[129] P. L. A. Popelier, Comp. Phys. Comm. 93, 212, 1996.

[130] P. L. A. Popelier, MORPHY98: A topological analysis program. UMIST, England, EU, 1998.

[131] R. F. W. Bader , Y. Tal, S. G. Anderson and T. T. Nguyen-Dang, Israel J. Chem. 19, 8, 1980.

[132] A. Villiers, Compt. Rend.112, 536, 1891.

[133] J. Szejtli, Chem. Rev. 98, 1743, 1998.

[134] H. Schneider, F. Hacket, V. Rüdiger, Chem. Rev. 98, 1755, 1998.

[135] K. Lipkowitz, Chem. Rev. 98, 1829, 1998.

[136] T. Fujimoto, A. Nakamura, Y. Inoue, Y. Sakata, T. Kaneda, Tetrahedron Lett. 42, 7987, 2001.

[137] V. Balzani, A. Credi, M. Venturi, Curr. Opin. Chem. Biol. 1, 506, 1997.

[138] F. L. Dickert, R. Sikorski, Mater. Sci. Eng. C. 10, 39, 1999.

[139] S. Tommasini, M. L. Calabrò, P. Donato, D. Raneri, G. Guglielmo, P. Ficarra, R. Ficarra, J. Pharm. Biomed. Anal. 35, 389, 2004.

[140] A. M. El-Kosasy, M. A. Shehata, N. Y. Hassan, A. S. Fayed, B. A. El-Zeany, Talanta, 66, 746, 2005.

[141] J. Yang, H. Lin, H. Huang, Anal. Chim. Acta. 530, 213, 2005.

[142] D. A. El-Hady, M. M. Seliem, R. Gotti, N. A. El-Maali, Sensors and Actuators B Chemical, 113, 978, 2006.

[143] Y. Song, Y. Chen, Y. Liu, J. Photochem. Photobiol. A: Chem. 173, 328, 2005.

[144] V. Ferancová, M. Bucková, E. Korgová, O. Korbut, P. Gründler, I. Wärnmark, R. Štepán, J. Barek, J. Zima, J. Labuda, Bioelectrochemistry, 67, 191, 2005.

[145] S. Muraka, O. Matsuzaka, S. Kamitori, K. Okuyama, Carbohydr. Res. 320, 261, 1999.

[146] R. F. W. Bader and C. Chang, J. Phys. Chem. 93, 2946, 1989.

[147] R. Taylor, Electrophilic Aromatic Substitution (John Wiley & Sons Ltd, England, 1990).

[148] M. J. S. Dewar, Mol. Struct. Energ. 6, 1, 1988.

[149] R. F. W. Bader, A. Streitwieser, A. Neuhaus, K. E. Laidig, P. Speers, J. Am. Chem. Soc. 118, 4959, 1996.

[150] M. J. González, R. Mosquera, J. Phys. Chem. A. 107, 5361, 2003.

[151] N. Okulik, N. M. Peruchena, P. M. Esteves, C. J. A. Mota, A. Jubert, J. Phys. Chem. A. 103, 8491, 1999.

[152] N. B. Okulik, L. G. Sosa, P. M. Esteves, C. J. A. Mota, A. H. Jubert, N. M. Peruchena, J. Phys. Chem. A. 106, 1584, 2002.

[153] S. J. Grabowski, J. Mol. Struc. 562, 137, 2001.

[154] S. J. Grabowski, J. Phys. Org. Chem. 16, 797, 2003.

[155] P. Gilli, V. Bertolasi, L. Pretto, A. Lycka, G. Gilli, J. Am. Chem. Soc. 124, 13554, 2002.

[156] O. Y. Borbulevych, R. D. Clark, A. Romero, L. Tan, M. Y. Antipin, V. N. Nesterov, B. H. Cardelino, C. E. Moore, M. Sanghadasa, T. V. Timofeeva, J. Mol. Struc. 604, 73, 2002.

[157] R. F. W. Bader, R. J. Gillespie, P. J. MacDougall, J. Am. Chem. Soc. 110, 7329 1988.

[158] R. F. W. Bader, G. L. Heard, J. Chem. Phys. 111, 8789, 1999.

[159] N. Castillo, R. J. Boyd, Chem. Phys. Lett. 403, 47, 2005.

[160] P. L. A. Popelier, J. Burke, N. O. Malcolm, J. Int. J. Quantum Chem. 92, 326, 2003.

[161] G. G. Smith, B. L. Yates, J. Org. Chem. 30, 2067, 1965.

[162] B. L. Yates, J. Quijano, J. Org. Chem. 34, 2506, 1969.

[163] A. Rotinov, G. Chuchani, R. A. Machado, C. Rivas, J. Quijano, M. S. Yepes, I. Restrepo, Int. J. Chem. Kinet. 24, 909, 1992.

[164] B. L. Yates, J. Quijano, J. Org. Chem. 35, 1239, 1970.

[165] A. Viola, J. H. MacMillan, R. J. Proverb, B. L. Yates, J. Am. Chem. Soc. 93, 6967, 1971.

[166] R. Notario, J. Quijano, J. C. Quijano, L. P. Gutiérrez, W. Suárez, C. Sánchez, L. León, E. Chamorro, J. Phys. Chem. A. 106, 4377, 2002.

[167] J. Quijano, R. Notario, E. Chamorro, L. A. León, C. Sánchez, G. Alarcón, J. C. Quijano, G. Chuchani, J. Phys. Org. Chem. 15, 413, 2002.

[168] R. Notario, J. Quijano, L. A. León, C. Sánchez, J. C. Quijano, G. Alarcón, E. Chamorro, G. Chuchani, J. Phys. Org. Chem. 16, 166, 2003.

[169] J. Quijano, J. David, C. Sánchez, E. Rincón, D. Guerra, L. A. León, R. J. Notario, J. Mol. Struc. 580, 201, 2002.

[170] E. Chamorro, J. Quijano, R. Notario, C. Sanchez, L. A. León, G. Chuchani, Int. J. Quant. Chem. 91, 618, 2003.

[171] R. Dominguez, A. Rotinov, G. Chuchani, J. Quijano, C. Valencia, B. Vicente, D. Franco, Actualidades de Físico-Química Orgánica, [based on the Latin American Conference on Physical Organic Chemistry], 4th, Florianopolis, Brazil, Aug., 1998 (1999), Meeting Date 1998, 348-355.

[172] G. Chuchani, R. Dominguez, A. Rotinov, J. Quijano, C. Valencia, B. Vicente, D. Franco, J. Phys. Org. Chem. 12, 19, 1999.

[173] K. J. Laidler, Chemical Kinetics, 3rd ed.; Harper Collins Publishers, New York, 1987.

[174] P. W. Atkins, Physical Chemistry, 6th ed.; Oxford University Press, New York, 1998.

[175] C. Eckart, Phys. Rev. 35, 1303, 1930.

[176] H. J. Shin, Chem. Phys. 39, 2934, 1963.

[177] E. J. Wigner, Chem. Phys. 5, 720, 1937.

[178] R. P. Bell, The Tunnel Effect in Chemistry; Chapman and Hall Ltd., New York, 1980.

[179] D. G. Truhlar, A. D. Isaacson, R. T. Skodje, B. C. Garrett, J. Phys. Chem. 86, 2252, 1982.

[180] T. N. Truong, D. G. Truhlar, J. Chem. Phys. 93, 1761, 1990.

[181] T. N. Truong, J. Phys. Chem. 101, 2750, 1997.

[182] A. E. Reed, L. A. Curtiss, F. Weinhold, Chem. Rev. 88, 899, 1988.

[183] I. V. Alabugin, M. Manoharan, S. Peabody, F. Weinhold, J. Am. Chem. Soc. 125, 5973, 2003.

[184] P. Mitrasinovic, Can. J. Chem. 81, 1, 2003.

[185] R. L. Brown, J. Res. Natl. Bur. Stand. (U.S.), 86, 357, 1981.

[186] T. W. G. Solomons, Organic Chemistry; Wiley, New York, 1980.

[187] M. B. Smith, March, J., March's Advanced Organic Chemistry: Reactions, Mechanisms and Structure, 5th ed.; Wiley, New York, 2001.

[188] R. F. W. Bader, A. Larouche, C. Gatti, M. T. Carroll, P. J. MacDougall, K. B. Wiberg, J. Chem. Phys. 87, 1142, 1987.

[189] K. B. Wiberg, R. F. W. Bader, C. D. H. Lau, J. Am. Chem. Soc. 109, 1001, 1987.

[190] N. Mora-Diez, J. R. Alvarez-Idaboy, R. J. Boyd, J. Phys. Chem. A. 105, 9034, 2001.

[191] D. J. Griffiths, Introduction to Electrodynamics (Prentice Hall, New Jersey, 1999).

[192] H. Shirakawa, E. J. Louis, A. G. MacDiarmid, C. K. Chiang, A. J. Heeger, J. Chem. Soc., Chem. Commun. 578, 1977.

[193] H. Shirakawa, A. G. MacDiarmid, A. J. Heeger, J. Chem. Soc., Chem. Commun., 1, 2003.

[194] J. Hernandez-Trujillo, R. F. W. Bader, J. Phys. Chem. A. 104, 1779, 2000.

[195] R. F. W. Bader, T. H. Tang, Y. Tal, F. W. Biegler-Köning, J. Am. Chem. Soc. 104, 946, 1982.

[196] R. J. Boyd, Stud. Org. Chem. (Amsterdam) 31, 485, 1987.

[197] O. Knop, R. J. Boyd, S. C. Choi, J. Am. Chem. Soc. 110, 7299, 1988.

[198] I. Alkorta, I. Rozas, J. Elguero, Struc. Chem. 9, 243, 1998.

[199] I. Alkorta, L. Barrios, I. Rozas, J. Elguero, J. Mol. Struc. 496, 131, 2000.

[200] I. Alkorta, I. Rozas, J. Elguero, B. Bunsen-Gesellschaft, Phys. Chem. 102, 429, 1998.

[201] I. Alkorta, J. Elguero, J. Phys. Chem. A. 103, 272, 1999.

[202] O. Knop, K. N. Rankin, R. J. Boyd, J. Phys. Chem. A 105, 6552, 2001.

[203] S. J. Grabowski, J. Phys. Chem. A 105, 10739, 2001.

[204] O. Knop, K. N. Rankin, R. J. Boyd, J. Phys. Chem. A 107, 272, 2003.